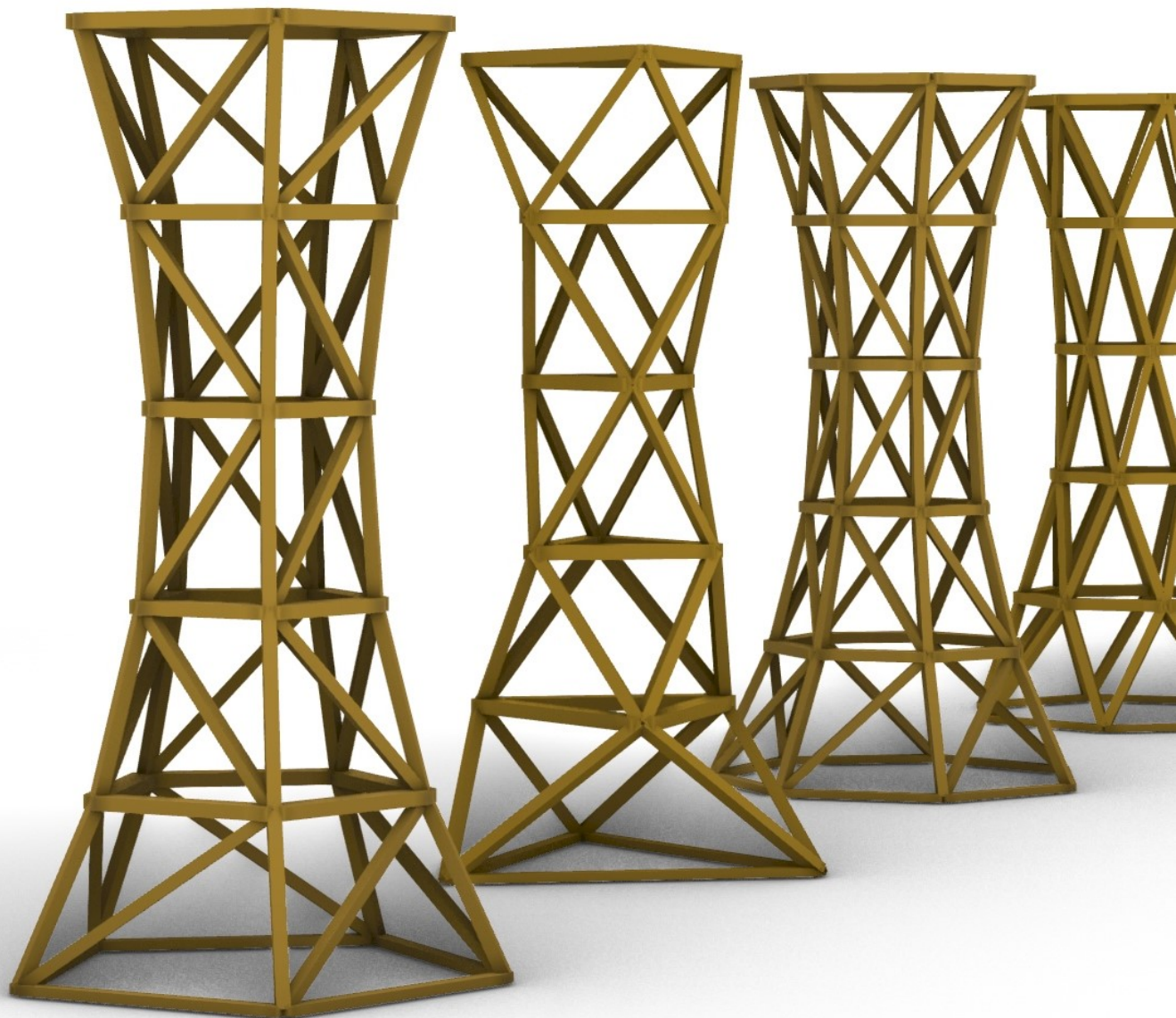


# Design and Optimization of Hyperboloid Lattice Structures for Timber Towers: A Study on Stiffness and Material Efficiency

MSc Master's Thesis  
Dominykas Acas



Delft University of Technology



# Design and Optimization of Hyperboloid Lattice Structures for Timber Towers: A Study on Stiffness and Material Efficiency

by

Dominykas Acas

to obtain the degree of Master of Science  
at the Delft University of Technology,  
to be defended publicly on Thursday March 28, 2024 at 16:00 PM.

Student number:	5630525
Project duration:	April 6, 2023 – March 28, 2024
Thesis committee:	Dr. Ir. G.J.P. Ravenshorst    TU Delft, Chair
	Dr. F. Kavoura,                    TU Delft
	Dr. Ir. H.R. Schipper            TU Delft
	Dr. Ir. R. Oval,                    TU Delft
	Dr. Ir. D. Veenendaal          Summum Engineering

*This thesis is confidential and cannot be made public until December 31, 2024.*

An electronic version of this thesis is available at <http://repository.tudelft.nl/>.

# Acknowledgements

This Master's Thesis has been developed at TU Delft for a duration of over a year. Just as evidently as my name is written on the cover of this report, it represents far more than my efforts alone.

Firstly and most importantly, I'd like to thank my family whose unwavering support and love allowed me to achieve one of the most excellent educations as well as a profound opportunity to explore the world and myself.

My gratitude extends to my academic mentors and committee members for providing me with a chance to work on this project. Their knowledge and insights have guided me through the path to graduation while invaluabley challenging me along the way.

I am grateful to my friends, whose invaluable input has greatly contributed to this project. I thank Luka and Luuk for their unparalleled knowledge in detailing as well as report writing, Santiago for his excellence in architectural visualization and aesthetics, Valerio for demonstrating what great storytelling truly is and Iliana for being an incredibly supportive friend. Outside academia, my time in the Netherlands has been enriched with precious and bright memories, thanks to my friends, for which I am deeply grateful.

***Dominykas Acas***  
*Delft, March 2024*

# Abstract

The presented research aims to design and optimize a timber observation tower, with a primary focus being the influence of topological and curvature parameters on its stability and lateral stiffness in resistance to non-uniform wind load profiles.

Having recognised the environmental benefits and urgency to find other alternatives, there's a clear necessity to incorporate wood as the main construction material into the infrastructure projects, like observational towers. By conducting a study on hyperboloid towers implemented in the last 100 years, this project questions the necessity of in plane stiff platforms, flexurally stiff rings and continuous vertical members as being pivotal to the stability and lateral stiffness of the global structure when subjected to non-uniform wind loads. In addition, the study intends to investigate how the narrowness of the hyperboloid might affect the lateral stiffness of the structure. Thus, by utilizing parametric tools (Grasshopper, Karamba3D and Beaver plug-in), the study aims to design a timber tower structure comprised of fully segmented members as well as incorporation of circular (flexurally stiff) rings, aiming to address the questions raised. In terms of structural member arrangement, the study will investigate two topologies: one featuring a diagrid pattern that emulates a geometrical shape of an antiprism, and a custom pattern inspired by the post and beam approach, which resembles a regular prism shape. The study emphasizes the tower's multi-functionality and adaptability throughout its lifespan. Tower's main structural framework is a pivotal element in providing required stiffness and strength by excluding the need for in-plane reinforcement provided by arbitrarily placed platforms.

The key realisation of this research was the kinematic behaviour exhibited by the segmented, triangular tower, adversely impacting its stability characteristics. The study used a combination of analytical and graphic kinematics techniques, along with a physical mock-up model, to confirm the kinematic behavior of the tower given that even sided polygons for rings are incorporated. This revelation would have an impact on how a structure like that would perform as well the way it would be built. Further research unveils the strong influence of ring type on structural stiffness showing that segmented rings render tower structures less stiff than ones employing curved ring members, regardless of the pattern. In terms of the direct comparison between tower patterns, custom one demonstrated a more consistent and stable performance in general, particularly achieving higher stiffness levels when employing segmented rings. As regards the triangular pattern, the stiffest response against wind loads has been exhibited through the use of curved rings. In addition, the study validates that adopting a hyperboloid shape along with smaller shape factors for the global tower geometry yields more favorable lateral stiffness characteristics. Finally, the study navigates through the exploration of the most optimal connection design, illustrating how considerations related to detailing have necessitated a re-evaluation of the most optimal tower configuration, which initially was chosen to be a triangular one equipped with curved rings. A qualitative assessment of a potential joint within this specific tower variant has confirmed that designing such a connection is significantly more complex. This is due to the necessity of ensuring the continuous flow of the curved ring, emergence of a kink within the insertion of the plate and how that is needed to be addressed.

Alternatively, these considerations have motivated the design process to converge into a new hybrid design, integrating segmented rings with a curved top ring defined by the custom pattern. This choice has been made by conducting a separate parametric study of the new tower design and ensuring that the new connection design fulfills elastic slipping modulus and ultimate strength requirements. The final topology that showed higher stiffness metrics was the custom one. It's also highlighted that maintaining the top of the tower constrained leads to favorable effects on stability and stiffness, irrespective of the chosen topology. The resulting structure is optimized for mass by strategically reducing member cross-sections in accordance with connection scheming while adhering to both SLS and ULS criteria.

# Contents

<b>Preface</b>	<b>i</b>
<b>Abstract</b>	<b>ii</b>
<b>1 Introduction</b>	<b>1</b>
<b>2 State-of-the-art</b>	<b>3</b>
2.1 Timber as a structural material	3
2.1.1 Timber against traditional building materials	3
2.1.2 Wood Products	4
2.1.3 Solid timber products	5
2.1.4 Curved glulam members	7
2.1.5 Joints in Timber Structures	8
2.2 Timber Lattice Towers	12
2.3 Hyperboloid Lattice Structures in Research Domain	25
2.4 Grid Structures	28
2.4.1 Patterns in Structural Design	28
2.4.2 Tessellations	29
2.5 Kinematic Analysis of Grid Structures	33
2.5.1 The singular value decomposition of the equilibrium matrix	34
2.5.2 Graphic kinematics for 3D pin-jointed trusses	38
<b>3 Research Question and Objectives</b>	<b>41</b>
3.1 Research Question	41
<b>4 Parametric Framework</b>	<b>43</b>
4.1 Software to be utilized	43
4.1.1 Grasshopper	43
4.1.2 Karamba3d	43
4.1.3 Beaver	44
4.1.4 Ansys FEA	46
4.1.5 IDEAS StatiCA	47
4.2 Developing geometry and parameters	48
4.2.1 Curvature	48
4.2.2 Topology	49
4.3 Structural model	51
4.3.1 Joints and degrees of freedom	51
4.3.2 Wind loads	52
4.4 General workflow	55
<b>5 Kinematic Nature of the Triangular Pattern</b>	<b>59</b>
5.1 Topological influences	59
5.1.1 Confirmation of mechanisms through mock-up models	62
5.1.2 Theoretical (analytical) confirmation of mechanisms	62
5.1.3 Graphic kinematics confirmation of mechanisms	66
5.1.4 Karamba3D confirmation of mechanisms with 'Eigen Modes' component	68
5.1.5 Overview of methods utilized	70
5.2 Discussion	72
<b>6 Stiffness Studies of the Triangular Pattern</b>	<b>74</b>
6.1 Curvature	74
6.1.1 Tower stiffness in response to the proposed wind load profile	74

6.1.2	Tower stiffness in response to simplified point loads	79
6.2	Curved ring elements	81
6.3	Elaboration on results and discussion	85
<b>7</b>	<b>Stiffness Studies of the Custom Pattern</b>	<b>92</b>
7.1	Curvature Influences	92
7.2	Curved Rings	95
7.3	Discussion and elaboration on findings	98
<b>8</b>	<b>Materialization</b>	<b>104</b>
8.1	Feasibility Study of the Initial Connection Design	104
8.2	Alternative Connection Design Explorations	108
8.2.1	Triangular Topology	111
8.2.2	Custom topology	113
8.3	Determining the final design and optimizing member sizes	116
8.4	Connection detailing	121
8.4.1	Stiffness Considerations and Geometry of the Connection	121
8.4.2	Analytical Assessment of the connection in SLS and ULS in accordance with Eurocode 5	124
8.4.3	Finite Element Analysis of the steel part of the connection	130
8.5	Construction considerations	131
8.6	Discussion	133
<b>9</b>	<b>Conclusions</b>	<b>139</b>
9.1	Conclusions and Recommendations	139
9.2	Future Work	141
	<b>References</b>	<b>143</b>
<b>A</b>	<b>Grasshopper scripts</b>	<b>148</b>
<b>B</b>	<b>Singular Value Decomposition Code in Python</b>	<b>149</b>
<b>C</b>	<b>Equilibrium matrices</b>	<b>151</b>
<b>D</b>	<b>Graphic kinematics of other tower configurations</b>	<b>158</b>
<b>E</b>	<b>Beaver plug-in reports for member groups in the final design.</b>	<b>160</b>
E.1	The most critical vertical member	160
E.2	The most critical vertical member	169
E.3	The most critical ring member	177
<b>F</b>	<b>IDEASTatiCA analysis outputs of the first connection design</b>	<b>186</b>

# List of Figures

2.1	Sawn timber square elements where knots are visibly present (Woodubuy 2022) . . . . .	5
2.2	Stages of glulam production (Ong 2015). . . . .	6
2.3	Squared glulam cross-section (a) and the removal of sections containing in-grown defects (b) (Blaß and Sandhaas 2017). . . . .	7
2.4	Non-linear bending stress distribution in a curved glulam beam due to the bent shape (Doe 2021). . . . .	8
2.5	Transversal tension and compression in the curved glulam beam (Doe 2021). . . . .	9
2.6	Failure modes of a timber-to-timber single and double shear plane fastener connection with a single dowel (Steer 2001). . . . .	10
2.7	Load - deformation diagram concerning the doweled connection (Jockwer and Jorissen 2018). . . . .	12
2.8	Ismaning transmitter tower. . . . .	13
2.9	Gliwice radio station (Ebielmaj 2014). . . . .	13
2.10	Responses to vertical and wind loads depending on the global silhouette (Cajmatz 2017). . . . .	14
2.11	St Venant and Vlaslov torsion (Cajmatz 2017). . . . .	15
2.12	Shukov tower in Polibino (1896). . . . .	16
2.13	The initial design of the Shabalovka tower (left) in relation to the Eiffel tower and the one that is realised (right). . . . .	16
2.14	Resulting effects of horizontal nodal loads: applied loads (a), axial forces within helical members (b) and axial forces within circumferential members (c). Red colour indicates members in tension, while blue relates to members in compression (Beckh 2015). Green dashed line indicate the neutral axis for the hyperboloid tower. . . . .	17
2.15	Given that hyperbolic segments are employed, the change of angle at abutting vertical members causes the increase in the normal force within them at the point of the main ring (Beckh 2015). . . . .	18
2.16	The tower in Drenthe, The Netherlands by Tentech: architectural preliminary draft of the tower (a) and the realized tower (b) (P. d. Vries 2005). . . . .	19
2.17	Connection implemented for the tower in Drenthe, The Netherlands by Tentech (P. A. d. Vries and Gard 2006). . . . .	19
2.18	Responses to horizontal loads of the hyperboloid through employment of bipod vertical element grouping (Beckh 2015). . . . .	20
2.19	The East Strand Tower in London, UK: the hyperboloid shape of the tower (a), as well as the inside of the tower (b) (Lorusso 2012). . . . .	20
2.20	Hyperboloid segmented tower in Kootwijkerzand, the Netherlands (Cindy and Janneke 2024). . . . .	22
2.21	Seljord observation tower designed by Rintala Eggertsson Architects: the tower at night (a) and the interior of the tower showcasing the post and beam system (Jenssen 2012). . . . .	22
2.22	The Pyramidenkogel tower (a) and its construction highlighting the post and beam system comprised of glulam posts, elliptical steel rings and diagonal steel rods (b). . . . .	23
2.23	Antiprisms (Tomruen 2006). . . . .	24
2.24	The general system and parameters of a lattice structure (Vasiliev, Barynin, and Rasin 2001). . . . .	25
2.25	Stress distributions (Mpa) of lattice structures subjected to bending of 100 kNm. (a) Cylindrical. (b) Hyperboloid (Shitanaka, Aoki, and Yokozeki 2019). . . . .	26
2.26	The load-bearing structure of the China Comic and Animation Museum (a) and the schematic illustration of the RGHLs (b) (Guo et al. 2018). . . . .	28
2.27	Configurations of three 2D lattice plates (from top to bottom): hexagonal, Kagome and triangular lattice plates (Y. Zhang et al. 2009)). . . . .	29

2.28	Trial gridshell, which is defined as a compression-only structure. It was built on a super-elliptical plan by Frei Otto in Essen, 1962 (Liddell 2015). . . . .	30
2.29	Three types of regular tessellations: rectangular, equilateral triangular and regular hexagonal (Cicerone et al. 2021). . . . .	30
2.30	Eight types of semi-regular tessellations (Grünbaum et al., 1987). . . . .	31
2.31	Regular and semi regular tessellation applications in practice. . . . .	32
2.32	Deformation of a simply supported rectangle. It should be noted that forces are transmitted through member bending and nodal rotations. Triangulation (or introduction of diagonal bracing) ensure the structure is transmitting forces in a more efficient manner (compression and tension). . . . .	32
2.33	Polyhedras. . . . .	33
2.34	Two frames which satisfy Maxwell's rule $b = 2j - 3$ : a simply stiff assembly (a) and a part redundant and part mechanism one (b) (Calladine 1978). . . . .	34
2.35	An example 2-D pin-jointed truss. . . . .	35
2.36	Resulting equilibrium matrix $\mathbf{A}$ of a given 2-D pin-jointed truss presented in Figure 2.35. . . . .	35
2.37	Graphical representation of the derivation of the kinematic mechanism variable $m$ by subtracting the rank of the equilibrium matrix $r$ from the number of rows $n_r$ . . . . .	36
2.38	Graphical representation of the SVD of the equilibrium matrix $\mathbf{A}$ along with highlighting the first $r$ left singular vectors and the first $r$ right singular vectors (Pellegrino 1993). . . . .	37
2.39	Graphical representation of the kinematic sense behind the parameter $m$ and the remaining $n_r - r$ equations which represent strain-free, or zero-energy, displacement modes. (Pellegrino 1993). . . . .	38
2.40	Two frames along with their reciprocal, polyhedral force diagrams. The face perpendicular to each bar and the applied force creates a closed nodal force cell indicating equilibrium. Lastly, the pipe diagram in c indicates the magnitude of each force within the bar and the force vector (Akbarzadeh, Van Mele, and Block 2015). . . . .	39
2.41	Two frames along with their reciprocal, polyhedral force diagrams. The face perpendicular to each bar and the applied force creates a closed nodal force cell indicating equilibrium. Lastly, the pipe diagram in c indicates the magnitude of each force within the bar and the force vector (Akbarzadeh, Van Mele, and Block 2015). . . . .	40
4.1	A typical 'Karamba3D' set up involving the provision of geometry, definition of member cross-sections, material in use, loading, support and joint conditions. Additionally, the script is able to provide maximum bending moment, shear, normal forces as well as critical stress among all members. . . . .	44
4.2	'Beaver' plug-in provides the user a functionality to re-adjust partial load factors in relation to combination factors. In this case, presented outputs are relating to ones detailed in EN 1990, cl. 6.4.3.2(3) and cl. A1.3.1. . . . .	45
4.3	In case of ULS assessment, Beaver plug-in is able to provide report for calculations in accordance with Eurocode 5. . . . .	46
4.4	'Beaver' plug-in provides the user a functionality to re-adjust partial load factors in relation to combination factors. In this case, presented outputs are relating to ones detailed in EN 1990, cl. 6.4.3.2(3) and cl. A1.3.1. . . . .	47
4.5	Steps to be taken in order to retrieve control vertices of the tower. . . . .	48
4.6	Triangular (or diagrid) pattern. Circumferential members can be identified as those currently taking a horizontal direction. . . . .	49
4.7	The logic behind the development of triangular (diagrid) pattern for both segmented and curved (circular rings). . . . .	50
4.8	Custom made pattern. . . . .	51
4.9	The logic behind the development of custom pattern for both segmented and curved (circular rings). . . . .	51
4.10	The taxonomy of tower variants following custom topology. It categorizes these towers by two critical dimensions: the shape factor, indicated by $N$ , which refers to the count of vertex (or sides) within the ring, and the curvature, symbolized by $C$ , that measures the tapering of the hyperboloid structure. . . . .	52
4.11	The resulting structural model of the tower following the triangular and custom topology. . . . .	53

4.12	Pitch angle $\alpha$ and the peripheral angle $\phi$ as provided by NEN-EN 13782:2015. . . . .	54
4.13	Pressure coefficient $c_p$ values in relation to pitch angle $\alpha$ and the peripheral angle $\phi$ as provided by NEN-EN 13782:2015. . . . .	55
4.14	Corresponding wind force profile imposed on a tower with a triangular configuration in accordance with NEN-EN 13782:2015. Image (a) reflects on the change of pressure coefficient moving along the diameter of the tower as referred in Figure 4.13, while (b) indicates the influence of height on the magnitude of the wind load. . . . .	56
4.15	. . . . .	56
4.16	Representation of areas where live and dead loads are applied on tower's ring elements.	57
4.17	General workflow of the thesis project. . . . .	58
5.1	Global displacement of the tower (in mm) versus the change of the shape factor $N$ . Note that the y axis is a logarithmic one. Corresponding shapes relating to the shape number $N$ are presented as well. . . . .	60
5.2	The deformed shape of the tower following a triangular (diagrid) pattern and equipped with segmented (polygonal) rings. Associated shape factors are (from left): $N = 3$ , $N = 4$ , $N = 5$ , $N = 6$ , $N = 7$ . . . . .	60
5.3	Simplified representations of triangular single level component subjected to point load on alternating nodes. As it can be observed, even sided polygons (displayed in c, d, g and h) exhibit significant displacements relating to certain point load combinations while odd sided polygons (displayed in a, b, e and f) deem tower segment to respond to any point load variation in a rigid way. . . . .	61
5.4	A mock-up model representing a single-level component of the antiprism tower following a triangular topology and its variations differing in the shape factor $N$ . It can be observed that for configurations having odd sided polygons, the response to point loads is always rigid no matter the placement of forces. However, for towers exhibiting even sided polygons the response to certain loading conditions tend to show instability and, thus, kinematic mechanisms occur. . . . .	63
5.5	Corresponding equilibrium matrices $\mathbf{A}$ for single-level tower assemblies exhibiting shape factors $N = 3$ , $N = 4$ and $N = 5$ . . . . .	64
5.6	Strain-free, or zero-energy displacement modes relating to single-level tower components taking shape factor values $N$ relating to assemblies exhibiting kinematic mechanisms. On the right hand side displacement vectors are visualized for each node of the assembly which correspond to the matrix on the left. . . . .	67
5.7	A graphic kinematics approach utilizes Rankine reciprocal force cells and their sliding in relation to one another in order to confirm and analyze the potential deformation of a given assembly within a kinematic mechanism. For (b) and (c), red arrows represent zero-strain deformation vectors obtained through the method of SVD and displayed in Figure 5.6. For other arrows, those were constructed manually as to closely replicate ones from before. . . . .	69
5.8	By utilizing the 'Eigen Modes' component in the Karamba3D plug-in for Grasshopper, it becomes feasible to identify assemblies that exhibit kinematic mechanisms based on their initial geometry. The outputs incrementally reveal how nodal displacements can occur in towers with even-sided polygons while no strain is induced on their members (a and e). Additionally, this can also be noticed in output eigenvalue list (b, d, f). . . . .	70
6.1	Towers with the triangular topology and different shape factors $N$ and their response to wind loads whenever curvature $C$ is adjusted. Results are displayed as global lateral displacements (in mm) against the curvature $C$ (in m). . . . .	75
6.2	Illustration of the deformed tower variant employing a shape factor $N = 7$ with its curvature variable $C$ being increased (tower is widening). It can be observed that when the structure is subjected to the proposed wind profile, its deformed shape is quite rapidly approaching global buckling, while becoming less hyperbolic with just a little increase in curvature. It is of essence to note that the depicted deformations are on a 1:1 scale with actual displacements. Sub captions inform about the employed curvature variable $C$ along with the corresponding global displacement $\delta$ . . . . .	76

- 6.3 Illustration of the deformed tower variant employing a shape factor  $N = 7$  with its curvature variable  $C$  being decreased (tower is narrowing). It can be observed that when the structure is subjected to the proposed wind profile, its deformed shape is very rapidly approaching global buckling, while becoming more hyperbolic with just a little decrease in curvature. It is of essence to note that the depicted deformations are on a 1:1 scale with actual displacements. Sub captions inform about the employed curvature variable  $C$  along with the corresponding global displacement  $\delta$ . . . . . 77
- 6.4 Illustration of towers with varying shape factors. These variants represent the structure that has shown stiffest response to wind loads. It can be seen that as the shape factor  $N$  grows, the stiffest response is associated with tower shapes that become increasingly more cylindrical with their respective curvature  $C$  values increasing. . . . . 77
- 6.5 Towers variants showcasing the stiffest response to wind loads and different shape factors  $N$  and their respective strain energy (kNm). Findings inform about the most efficient design as strain energy indicate how much structure is affected by external loads. Lowest strain energy correspond to an efficient design. After adjusting structures to maintain constant mass for varying  $N$ , discrepancies in efficiency become even more apparent. . . . . 78
- 6.6 Illustration of the nodal point loads applied to the tower. . . . . 80
- 6.7 Tower variants with different shape factor  $N$  after being subjected to horizontal nodal point loads. The curvature  $C$  is varied for every design variant and displacements are recorded. It can be observed that all design variants exhibit a stable and stiff response to this simplified loading case. . . . . 80
- 6.8 Tower variants with different shape factor  $N$  after the implementation of curved ring members while maintaining constant mass. The curvature  $C$  is iterated for every design variant and displacements are recorded. It can be observed that all design variants exhibit a stable and stiff response to this loading case. As curvature ( $C$ ) grows, there appears to be a trend of decreasing tower stiffness, which then converges to a consistent level. Markers indicate the lowest displacement recorded for towers with different shape factors  $N$ . Note that the  $y$  - axis (displacements) is scaled logarithmically. . . . . 82
- 6.9 Illustration of towers (constant mass) with varying shape factors after the implementation of curved rings. These variants represent the structure that has shown stiffest response to wind loads. It can be seen that as the shape factor  $N$  grows, the stiffest response is associated with tower shapes that steadily converge into a hyperboloid with a curvature value  $C = -3.61$  (also described in Table 6.3). . . . . 82
- 6.10 Deformed shape of the tower with curved rings, after exposure to the proposed wind profile (as indicated by the red arrows). It can be seen that that global shape does not tend to any instabilities and tower deforms laterally as a unit. This is due to immense in-plane stiffness facilitated by the solid ring, which resists loading in bending. Blue colour indicates members in tension while red represents members in compression. It is important to state that the illustrated deformation has been magnified 400 times compared to the actual values. . . . . 83
- 6.11 Displacements and strain energy plotted against the shape factor  $N$ . Each marker represent the stiffest tower with curved rings shape for every  $N$  derived from Table 6.3 while the mass is kept constant at  $m = 65.14 t$ . Additionally, for comparative purposes the mass of the tower has been reduced to  $m = 44.23 t$  and metrics were recorded again. Findings indicate that regardless of the mass, the most efficient behaviour has been exhibited by the tower design characterised by  $N = 6$  as strain energy and displacements are lowest in this case. . . . . 84
- 6.12 In the this plot, displacements and strain energy are graphed against the shape factor  $N$ . Each data point represents the configuration with the highest stiffness for a given  $N$ , adhering to a triangular topology with curved and segmented rings, as detailed in Tables 6.3 and 6.2. This analysis maintains a constant mass of approximately  $m \approx 66t$  for each tower configuration, facilitating a direct comparison of the impact of curvature  $C$  on displacement and strain energy characteristics. It can be seen that after the implementation of curved rings into tower design, strain energy and displacement drops down by on average a factor of 5 to 7. . . . . 84

6.13	Illustration of restorative bending moments within curved rings to counter-act the squeezing action exerted by the wind load. Red arrows indicate wind load profile for each face of the tower. . . . .	85
6.14	Simplification of the hyperboloid by projecting it to a 2D plane as an arch. Horizontal posts represent ring (circumferential) members, which in this case can be perceived as springs with a certain stiffness. . . . .	86
6.15	A more elaborate explanatory arch beam model providing representative ring elements that do re-adjust in orientation and length in accordance with the shape factor $N$ utilized. Note that loads are applied directly and perpendicular to the shape of the tower arch. Note that green arrows and a purple circle indicate degrees of freedom of simple pinned supports. . . . .	87
6.16	Representative spring models for tower rings taking different shape factors. All units are in m. . . . .	88
6.17	A more elaborate explanatory arch beam model providing representative ring elements that do re-adjust in orientation and length in accordance with the shape factor $N$ utilized. Note that loads are applied directly and perpendicular to the beam. . . . .	89
6.18	Set up of a beam model with ring elements relating to $N = 3$ . . . . .	90
6.19	Set up of a beam model with curvature $C = -2.1$ m. . . . .	90
6.20	Set up of a beam model with curvature $C = -2.1$ m. . . . .	90
6.21	Set up of a beam model with curvature $C = -2.1$ m. . . . .	90
6.22	A more elaborate explanatory arch beam model providing representative ring elements that do re-adjust in orientation and length in accordance with the shape factor $N$ utilized. Note that loads are applied directly and perpendicular to the beam. . . . .	90
6.23	Given the implementation of curved (circular) rings, the spring model relies on bending of curved elements. All units are in m. . . . .	91
7.1	The plot examines tower variants adhering to a custom topology, characterized by varying shape factors ( $N$ ), while maintaining a constant mass and segmented rings. The curvature ( $C$ ) of each design variant is iteratively changed, and the associated displacements are recorded. Similar to observations in the triangular topology, lower curvature values ( $C$ ) tend to result in dramatically increased displacements. The stiffest tower response to the proposed wind profile was identified at curvatures ranging from $C = -4$ meters to $C = -3$ meters. Markers on the graph indicate the lowest displacement recorded for towers with different shape factors ( $N$ ). It is important to note that the y-axis, representing displacements, is scaled logarithmically. . . . .	94
7.2	The figure presents a deformed tower variant, distinguished by a custom topology that incorporates a shape factor $N = 9$ . This variant undergoes a change in its curvature variable $C$ , resulting in a narrowing structure. It can be observed that when the structure is subjected to the proposed wind profile, its deformed shape is very rapidly approaching global buckling, while becoming more hyperbolic with just a little decrease in curvature. A crucial aspect of this illustration is the true-to-scale representation of deformations, mirroring the actual displacements. Additionally, sub-captions are provided to indicate the employed curvature variable ( $C$ ) and the corresponding global displacement ( $\delta$ ). . . . .	95
7.3	This illustration displays a custom topology tower variant characterized by a shape factor ( $N = 9$ ), where the curvature variable ( $C$ ) is increased, causing the tower to widen. When this structure is exposed to the proposed wind load profile, it demonstrates stable behavior, as indicated by relatively low displacements. As the tower adopts a more cylindrical shape, it presents a flatter surface to the oncoming wind, which appears to facilitate easier displacement. This effect becomes more pronounced in a fully cylindrical form, where the wind profile's squeezing action is markedly noticeable. It's important to highlight that the deformations shown here are illustrated at a scale of 1:30 compared to the actual displacements. Sub-captions provide details about the used curvature variable ( $C$ ) and the associated global displacement ( $\delta$ ). . . . .	96

- 7.4 In the this plot, displacements and strain energy are graphed against the shape factor  $N$ . Each data point represents the configuration with the highest stiffness for a given  $N$ , adhering to a triangular topology with curved and segmented rings as well as custom topology with segmented rings. This analysis maintains a constant mass of approximately  $m \approx 66.5t$  for each tower configuration, facilitating a direct comparison of the impact of curvature  $C$  on displacement and strain energy characteristics. Newly studied tower design following a custom top. appears to exhibit more advantageous stiffness and strain energy characteristics compared to what has been observed in designs following a triangular top. (featuring segmented rings). . . . . 97
- 7.5 Custom topology (light brown) and triangular topology (orange) towers equipped with curved rings and the corresponding shape with the configuration that is narrowing ( $C = -3.9 m$ ) and widening ( $C = -2.2 m$ ) overall shape. It should be noted that the scale of the model is magnified 5 times in relation to real calculated displacements. It is observable how custom topology tower does not permit any ring deformations for a wider range of curvatures as the overall tubular configuration of the tower remains even and linear from bottom to top. In contrast, the tower with an antiprism composition, following a triangular topology, seems to provide more freedom of movement for the topmost rings. . . . . 98
- 7.6 The plot examines tower variants adhering to a custom topology equipped with curved rings, characterized by varying shape factors ( $N$ ), while maintaining a constant mass. The curvature ( $C$ ) of each design variant is iteratively changed, and the associated displacements are recorded. As expected, all tower variants respond to wind profile in a stiff and stable manner with displacements showing a rather minimal variation. The stiffest tower response was identified at curvatures ranging from  $C = -3.5$  meters to  $C = -2.5$  meters. Markers on the graph indicate the lowest displacement recorded for towers with different shape factors ( $N$ ). It is important to note that the y-axis, representing displacements, is scaled logarithmically. . . . . 99
- 7.7 Illustration of force distribution within the structure defined by the custom top. (with curved rings). Following the application of wind load, the front side of the tower dealing with the positive pressure undergoes tension (indicated in blue), meanwhile the opposite side, facing the negative pressure, experiences compression (highlighted in red). Additionally, it can be observed that the lower part of the tower is undergoing larger forces than the top. . . . . 99
- 7.8 In the this plot, displacements and strain energy are graphed against the shape factor  $N$ . Each data point represents the configuration with the highest stiffness for a given  $N$ , adhering to a triangular topology with curved and segmented rings as well as custom topology with segmented and curved rings. This analysis maintains a constant mass of approximately  $m \approx 66t$  for each tower configuration, facilitating a direct comparison of the impact of curvature  $C$  on displacement and strain energy characteristics. Newly studied tower design following a custom top. with curved rings (green and dark green curves) appears to exhibit less advantageous stiffness and strain energy characteristics compared to what has been observed in designs following a triangular top. (featuring curved rings) indicated by red and orange curves. . . . . 100
- 7.9 In the this plot, displacements and strain energy are graphed against the shape factor  $N$ . Each data point represents the configuration with the highest stiffness for a given  $N$ , adhering to a triangular topology with curved ringa as well as custom topology with segmented and curved rings. This plot serves as a closer examination in of the three curves representing the most stiff and efficient designs, enabling a more accurate assessment of their relation. . . . . 101
- 7.10 Illustration of members being in stress within structures characterized by the custom topology equipped with curved rings (right) along with the triangular topology also featuring curved rings (left). Both structures are characterised by  $C = -2 m$  and  $N = 7$  while mass is kept the same for both. A clear distinction can be noticed between the distribution of stresses in these assemblies as vertical members do take disproportionately higher amount of loads compared to the diagonal ones in case of the custom top. A more uniform force distribution is evident in case of the triangular topology. . . . . 101

7.11	Average stresses against the variance in curvature $C$ in vertical and respective diagonal members for towers following custom and triangular topology. The uneven distribution of loads in assemblies of custom pattern leads to excessive stress on vertical members and diagonal ones under-utilized. This is not the case for triangular topology as the average stress amount in its diagonals are less than that defined by the light green curve. This feature allows tower structures defined by the triangular topology to experience lower strains and resist loads in a more stiff manner. . . . .	102
7.12	The tower stiffness is influenced by the arrangement of rings for different topologies, particularly when considering diverse shape factors denoted by $N$ . . . . .	102
8.1	The lowest set of nodes experiences compressive forces. In this case live, permanent and wind loads are applied with relevant safety factors. . . . .	105
8.2	Illustration of an altered tower configuration in terms of curvature as to allow upper and lower diagonal members to connect to the ring in a straight line in relation to one another.	106
8.3	Due to certain curvature of the tower silhouette, diagonals do not abut at the node in the same plane, thus a kink in the connecting plate should be introduced. . . . .	107
8.4	Drafted representation of the steel timber connection employing a longer steel plate accommodating timber diagonals via drilled bolts. Dimensions of members are taken to be arbitrary as the strength of the steel plate is to be investigated. It should be noted that this connection relates to lowest platform ring node, where force magnitude was evident to be the highest. . . . .	107
8.5	Comparison of torsional effects on towers with curved and segmented rings. It should be noted that the scale of moment lines on 'Karamba3D' component 'Beamview' is set to 0.1. . . . .	109
8.6	'Beaver' plug-in outputs displaying critical failure modes in which certain glulam sections throughout the tower might fail. It can be seen that ring elements are highly susceptible to failure in torsion as utilization for that failure mechanism is the highest. . . . .	110
8.7	Watch tower in Kootwijkerzand and the connection design employed to join 6 steel members (NatureScanner 2024). . . . .	110
8.8	A sample tower following the triangular topology having segmented rings and a curved ring at the top. This configuration has a shape factor $N = 6$ and a curvature $C = -4 m$ . . . . .	112
8.9	The plot examines tower variants adhering to a triangular topology equipped with segmented rings with a curved ring at the apex, characterized by varying shape factors ( $N$ ), while maintaining a constant mass. The curvature ( $C$ ) of each design variant is iteratively changed, and the associated displacements are recorded. It is important to note that the y-axis, representing displacements, is scaled logarithmically. Markers indicate the stiffest response for every shape factor. . . . .	112
8.10	In the this plot, displacements are graphed against the shape factor $N$ . Each data point represents the configuration with the highest stiffness for a given $N$ , adhering to a triangular topology with a curved ring at the top as well all the other configurations that showed favorable stiffness metrics. This analysis maintains a constant mass of approximately $m \approx 65t$ for each tower configuration, facilitating a direct comparison of the impact of curvature $C$ on displacement. . . . .	113
8.11	A sample tower following the custom topology having segmented rings and a curved ring at the top. This configuration has a shape factor $N = 5$ and a curvature $C = -4 m$ . . . . .	114
8.12	The plot examines tower variants adhering to a custom topology equipped with segmented rings with a curved ring at the apex, characterized by varying shape factors ( $N$ ), while maintaining a constant mass. The curvature ( $C$ ) of each design variant is iteratively changed, and the associated displacements are recorded. Markers indicate the stiffest response for every shape factor. . . . .	114
8.13	In the this plot, displacements are graphed against the shape factor $N$ . Each data point represents the configuration with the highest stiffness for a given $N$ , adhering to a custom topology with a curved ring at the top as well all the other configurations that showed favorable stiffness metrics. This analysis maintains a constant mass of approximately $m \approx 65t$ for each tower configuration, facilitating a direct comparison of the impact of curvature $C$ on displacement. . . . .	115

8.14	Applied live and dead loads stemming from a platform at every ring level. Red areas indicate the potential placement of platforms and where live and dead loads are distributed initially. . . . .	116
8.15	Illustration and annotation of forces acting on the most critical node. In this instance, $N = 6$ , $C = -3.5 m$ . It should be noted that in all cases there are 6 members joining at the node. This annotation is utilized to represent forces at nodes for towers with different $N$ in Table 8.3. It should be noted that green colour indicates axial forces while colour yellow indicates shear forces imposed upon the connection. . . . .	117
8.16	Division of members for optimization. . . . .	119
8.17	ULS unity check for all timber members within the final design of the tower. . . . .	121
8.18	SLS (local) unity check for all timber members within the final design of the tower. . . . .	121
8.19	Illustration of members based on their critical and governing failure category in ULS. . . . .	122
8.20	Front view of the connection. All values are in mm. . . . .	123
8.21	Perspective view of the proposed connection design. Red blocks indicate glulam members . . . . .	124
8.22	Resulting distances and spacing of the connection. $\alpha$ direction denotes compressive force orientation which is aligned with the grain direction in this case. All values are in mm. . . . .	126
8.23	Decomposition of the connection with four shear planes into connections with two shear planes (Sandhaas et al. 2018). . . . .	127
8.24	Set-up of the connection model by enforcing restraints and loading conditions. . . . .	131
8.25	Resulting buckling shapes of the steel component after being subjected to compressive member forces. Each image corresponds to a different buckling factor. The scale is 1:200. . . . .	136
8.26	Equivalent (von-Mises) stresses occurring within the steel component after being subjected to compressive member forces. Image in (b) shows the section with higher stress concentrations developing at the onset of two lower plates, which are exposed to highest compressive loads transmitted from member . . . . .	137
8.27	Split ring segments and dimensions of the largest segment. All values are in m. . . . .	138
8.28	Split ring segments and their respective joint placement in relation to sagging and hogging moments. Joints are placed at points of inflexion. . . . .	138
8.29	Bending moments around the local z-axis (in-plane) within the top ring before (a) and after (b) splitting the ring at said joint locations. The scale of the moment line is 0.13 kNm to m in the 'BeamView' component. Notice the points of zero moment within the member as these are represented by the placement of joints where splices meet. . . . .	138
C.1	Equilibrium matrix of the tower defined by the triangular pattern and $N = 3$ while having 4 rings in total. . . . .	151
C.2	The rank and resulting values of numbers of kinematic mechanisms and states of self-stress related to tower defined by the <b>triangular pattern</b> and $N = 3$ while having 4 rings in total. This outcome confirms that this structure is <b>kinematically determinate</b> . . . . .	152
C.3	Equilibrium matrix of the tower defined by the <b>triangular pattern</b> and $N = 4$ while having 4 rings in total. . . . .	153
C.4	The rank and resulting values of numbers of kinematic mechanisms and states of self-stress related to tower defined by the <b>triangular pattern</b> and $N = 4$ while having 4 rings in total. This outcome confirms that this structure is <b>kinematically indeterminate</b> . . . . .	154
C.5	Equilibrium matrix of the tower defined by the <b>custom pattern</b> and $N = 3$ while having 4 rings in total. . . . .	155
C.6	The rank and resulting values of numbers of kinematic mechanisms and states of self-stress related to tower defined by the <b>custom pattern</b> and $N = 3$ while having 4 rings in total. This outcome confirms that this structure is <b>kinematically determinate</b> . . . . .	156
C.7	Equilibrium matrix of the tower defined by the custom pattern and $N = 4$ while having 4 rings in total. . . . .	157
C.8	The rank and resulting values of numbers of kinematic mechanisms and states of self-stress related to tower defined by the <b>custom pattern</b> and $N = 4$ while having 4 rings in total. This outcome confirms that this structure is <b>kinematically determinate</b> . . . . .	157

---

D.1	Reciprocal cells of the tower defined by the triangular topology and $N = 3$ . At the top-most ring the cells are unable to shift without separation or overlapping to their adjacent counterpart. Thus, the structure is kinematically determinate. . . . .	158
D.2	Reciprocal cells of the tower defined by the triangular topology and $N = 4$ . At the top-most ring the cells are able to shift without separation or overlapping to their adjacent counterpart. Thus, the structure is kinematically indeterminate. . . . .	159
E.1	Vertical members for which Beaver calculation reports are generated. . . . .	160
E.2	The most critical diagonal member for which Beaver calculation reports are generated. . . . .	169
E.3	The most critical ring member for which Beaver calculation reports are generated. . . . .	177
F.1	Structural analysis of the steel plate connection and results relating to strength capacity and stability. . . . .	187
F.2	Structural analysis of the steel plate connection and results relating to strength capacity and stability after implementing a stiffener plate. . . . .	188

# List of Tables

2.1	Wood Construction Products with Their Associated Components (Blaß and Sandhaas 2017) . . . . .	4
2.2	Based on the type of the fastener, the contribution of the 'rope effect' to the load bearing capacity of the dowel type timber to timber connection. . . . .	11
5.1	Structural analysis results through deployment of SVD of an equilibrium matrix $\mathbf{A}$ of single-level components having different shape factors $N$ . . . . .	65
6.1	Stiffest shape of towers taking different shape factors $N$ and their respective results relating to global displacement, strain energy and mass. It should be noted that mass is not constant as same size members are used to construct the ring and diagonal elements. 78	
6.2	Stiffest shape of towers taking different shape factors $N$ and their respective results relating to global displacement, strain energy and mass. It should be noted that mass is being kept constant. This measurement does inform about the design variant exhibiting the most efficient structural behaviour. . . . .	78
6.3	Stiffest shape of towers taking different shape factors $N$ and their respective results relating to global displacement, strain energy and mass after the implementation of curved ring members. It should be noted that mass is being kept constant. This measurement does inform about the design variant exhibiting the most efficient structural behaviour. It can be observed that these results indicate that this design variant significantly more efficient in comparison to the results relating to designs with segmented rings (see Table 6.2 . . . . .	83
7.1	Stiffest shape of towers taking different shape factors $N$ and their respective results relating to global displacement, strain energy and mass. It should be noted that mass is being kept constant. This measurement does inform about the design variant exhibiting the most efficient structural behaviour. . . . .	93
7.2	Stiffest shape of towers (custom top. with curved rings) taking different shape factors $N$ and their respective results relating to global displacement, strain energy and mass. It should be noted that mass is being kept constant. This measurement does inform about the design variant exhibiting the most efficient structural behaviour. . . . .	97
8.1	Stiffest shape of towers (triangular top. with segmented rings and a curved ring at the top) taking different shape factors $N$ and their respective results relating to global displacement, strain energy and mass. It should be noted that mass is being kept constant. This measurement does inform about the design variant exhibiting the most efficient structural behaviour. . . . .	111
8.2	Stiffest shape of towers (custom top., with segmented rings and a curved ring at the top) taking different shape factors $N$ and their respective results relating to global displacement, strain energy, and mass. It should be noted that mass is being kept constant. This measurement does inform about the design variant exhibiting the most efficient structural behaviour. . . . .	115
8.3	Representation of forces being transmitted to the most critical connection within different tower assemblies. Compressive forces are negative, while tensile are positive. It can be seen that there is a significant jump in compressive forces occurring in vertical member $V_{x1}$ when shape factor $N = 4$ is adopted. . . . .	118
8.4	The recommended range of limiting values of deflections for beams with span $l$ provided in Table 7.2 from Eurocode 5 (Steer 2001). . . . .	118

---

8.5	Limits for horizontal displacements (for characteristic combinations of actions) as detailed in EN 1990, cl. A1.4.2 (Snijder and Steenbergen 2020). . . . .	118
8.6	A comprehensive overview of tower's specifications relating to dimensions, strength and SLS characteristics (local and global), final geometrical parameters and materials of choice. . . . .	120
8.7	Fastener Specifications . . . . .	125
8.8	Material properties for GL28h class in accordance with EN 14080:2013. . . . .	125
8.9	Minimum values of spacing and edge and end distances for bolts as detailed in Table 8.4 from Eurocode 5. . . . .	126
8.10	Summary of failure modes, stiffness, design requirements, and utilization. . . . .	129
8.11	Structural Performance Metrics for the Tower after implementing split ring at the top. . .	132
8.12	Normalized areas of platforms provided by different shape factors $N$ . . . . .	135

# 1

## Introduction

In light of the current ecological challenge on a global scale, the need to limit average temperatures to 1.5 degrees Celsius above pre-industrial temperatures warns that carbon emissions should be reduced significantly across all sectors (Paris Agreement 2015). The civil engineering industry has emerged as one of the leading contributors to human-induced carbon dioxide (CO<sub>2</sub>) emissions, accounting for a significant 38% of global energy-related emissions (IEA 2020). It is projected that with the rapid growth of the population in the upcoming century (United Nations 2020), there will be an increased demand for infrastructure. In terms of construction materials, concrete has been extensively utilized for the development of infrastructure as it displays excellent economic applicability and durability. Literature suggests that the annual global consumption of concrete has reached 25 Gt (Gursel et al. 2014). In relation to other construction materials, concrete is the leading one that generates 73% of global warming effects associated with the construction industry (Thiel et al. 2013). In terms of steel, the blast furnace process used in iron production is the primary source of carbon dioxide emissions in the steel industry, accounting for approximately 997 kg per ton of steel and contributing to a significant 4-5% of global CO<sub>2</sub> emissions (Nidheesh and Kumar 2019). Having observed these effects of the built environment, it is of essence to explore more sustainable, alternative means for the ever so necessary infrastructure development.

Timber as a construction material poses a viable solution to offset environmental effects related to the use and production of concrete and steel. Timber construction products are known to physically embody carbon that, before trees' intervention, was present in the form of atmospheric CO<sub>2</sub>. This feature builds an argument that the combination of forestry, wood products and integrated construction systems can play a crucial part in even mitigating climate change via the carbon sequestration strategy (Hart and Pomponi 2020). Additionally, timber members display a high level of manual and digital prefabrication, a feature that has been thoroughly researched within the context of academia and engineering projects (Eversmann, Gramazio, and Kohler 2017). This characteristic is a clear indicator of timber's high construction efficiency, demonstrated by its ability to minimize both construction time and material waste.

Thus, modern designers ought to consider timber as an alternative to supplement their infrastructure or residential projects. While traditional design strategies mostly focus on obtaining cost minimization, a more sustainable design should bring forward the concept of material optimization within given structural design standards/codes in order to reduce the embodied energy related to construction (Yoon

et al. 2018).

As urban populations continue to grow, exemplified by the urgent need to deliver around 845,000 homes in the Netherlands within the next ten years, there's is a pressing need to also build tall (efficient in space) while finding means to maintain wood as the primary material (environmentally responsible) (Capital Value 2020). Bearing in mind that wood does not match the strength characteristics of more conventional construction materials (steel and concrete), the manipulation of global form and geometry in attempts to find structurally efficient solutions becomes an imperative design aspect.

In the construction industry, the concept of the lifespan and utility of structures is evolving. By utilizing solid timber and engineered wood products for prolonged periods of time without the need to change its purpose through disassembly, replacement and demolition, this material remains at the peak level of the value chain (Jockwer, Öberg, et al. 2023). The need for devising a design practice that accentuates material efficiency and ensures functional versatility and longevity of infrastructural units cannot be understated.

From a structural design perspective, civil engineering discipline can draw knowledge of aerospace industry and realize benefits of lattice structures as regards its material efficient application in residential or industrial construction projects. In recent decades, lattice structures have been increasingly used in the construction of aircraft and spacecraft components due to their exceptional material efficiency and stiffness. These characteristics hold a great potential to push boundaries in architectural design, allowing to incorporate light-weight, resilient hyperboloid grid structures into larger scale infrastructural and residential projects, like observational towers.

The subsequent chapter will examine the latest literature to showcase the properties and use of such structures in both civil and aerospace contexts. Thus, it can be affirmed that the research provided in this proposal aims to understand hyperboloid lattice structures and their integration as the main load-bearing system within residential infrastructure while utilizing timber as the main construction material.

# 2

## State-of-the-art

### 2.1. Timber as a structural material

In this chapter a comprehensive literature study of timber as a viable tower construction material is conducted. Relevant topics cover timber manufacturing, properties, dimensioning methods as well as connections. By applying gathered information, a more informed structural model with representative material properties can be developed to complement established research goals.

#### 2.1.1. Timber against traditional building materials

Timber as a construction material poses a viable solution to offset environmental effects related to the use and production of concrete and steel. Timber construction products are known to physically embody carbon that, before trees' intervention, was present in the form of atmospheric ( $\text{CO}_2$ ). This feature builds an argument that the combination of forestry, wood products and integrated construction systems can play a crucial part in even mitigating climate change via the carbon sequestration strategy (Arehart et al. 2021). It should be noted that over the past few decades, the Earth's forests have played a crucial role in absorbing a significant portion of the annual global anthropogenic ( $\text{CO}_2$ ) emissions, approximately equivalent to the amount absorbed by the oceans, which amounts to approximately 30% of the total. The carbon sequestration strategy is occurring on a global level while the global carbon cycle can be enhanced by various means, including the prevention of deforestation, the cultivation of new forests, and the greater utilization of wood in durable construction products. Forests and vegetation, as well as the ocean and various products, serve as reservoirs for carbon dioxide ( $\text{CO}_2$ ). By halting deforestation, engaging in reforestation efforts, and promoting the use of wood in long-lasting construction materials, respective industries can contribute to the overall improvement of the global carbon cycle (Versteeg Conlledo 2022).

Category	Associated Components	
	Wood Product	Component
Solid Timber Products	Logs	Stems
	Sawn Timber	Squared Timber, Planks and Boards
	Glued Laminated Timber (Glulam)	Boards
	Cross Laminated Timber (CLT)	
Wood-Based Products	Laminated Veneer Lumber (LVL)	Veneers
	Plywood	Veneers or Sawn Timber
	Parallel Strand Lumber (PSL)	Veneer Strands
	Particleboards	Particles (Chips)

**Table 2.1:** Wood Construction Products with Their Associated Components (Blaß and Sandhaas 2017)

### 2.1.2. Wood Products

What concerns wood taxonomy, quite a broad although important distinction can be made between softwoods and hardwoods that encapsulate various species amongst them. As Arets et al. (2011) recognised around 80% of timber products are composed of softwood. While hardwood may exhibit higher strength characteristics, it does not necessarily possess the same level of stiffness. Therefore, due to its lower density, significant workability, and fast growth rate, softwood emerges as a more favored choice when considering construction elements and their manufacturing (Arets et al. 2011). However, durability concerns should be recognised of softwood in relation to hardwood products. Many hardwoods contain natural oils that allow them resistant to rot, decay, and insect infestation, improving their suitability for outdoor use. On the contrary, softwoods are less dense and, thus, can be prone to microbes and moisture effects (Ranger Truss 2024).

In terms of engineering practice and wood utilization, two categories arise that more sufficiently characterize wood's properties and potential in the construction industry: solid wood products and wood-based products. Through manufacturing and machining techniques, these items leverage the desirable attributes of wood and present themselves as viable choices for integration into timber constructions. For different engineering utilization, Table 2.1 overviews these wood product categories and present associated components. As a long time ago, the occurrence of certain tree types in forests would determine structural timber and its purpose. Nowadays, as structural requirements for large member dimensions are ever so prevalent, construction industry has faced timber innovation that allows multiple pieces of wood to be combined to make a single member, which is the case with glued laminated timber, for example (Blaß and Sandhaas 2017). This feature allows to offset the considerable variance in strength properties of timber due to the natural growth process of trees as knots and similar growth related aspects impact the strength quite considerably. Thus, as portrayed in Table 2.1 wood products are listed in a way to represent reduced variance of relevant properties.

### 2.1.3. Solid timber products

Whenever solid wood term is used, one should refer to structural members that are composed of wood in its original configuration or form. This is quite in contrast to engineered wood products or wood-based panels, which are created through the process of dismantling and reassembling individual components.

#### Sawn timber

These structural members are obtained by sawing logs longitudinally. Therefore, such a technique means that sawn timber elements are composed of wood in its most natural structural arrangement. Products that are usually obtained from sawn timber include boards, planks, battens and square timbers, while their cross-sectional dimensions are usually standardized (Blaß and Sandhaas 2017). Sawn timber products are available in "stress grades" which provide restrictions on knot dimensions and the extent of sloping grain. Once the wood has reached the desired moisture content through the drying process, the sawn timber undergoes either visual inspection or machine grading. It is then categorized and assigned to a specific strength class (Blaß and Sandhaas 2017). Notably, knots that occupy a significant portion of the wood's cross-section result in localized changes in the grain direction, leading to weakened areas due to the fact that the perpendicular-to-the-grain strength of timber is only one-tenth of its parallel-to-the-grain strength (Milner 2009). In order to extend its length, sawn timber elements can be finger jointed, as highlighted by Blaß and Sandhaas (2017). Figure 2.1 displays rectangular sawn timber elements.



**Figure 2.1:** Sawn timber square elements where knots are visibly present (Woodubuy 2022)

#### Glued Laminated Timber

Glulam, also known as glue laminated timber, is created by joining softwood lumber end to end with an adhesive in a face-laminating process, aligning the joints parallel to the grain direction. The first stage in the manufacturing procedure usually is the drying of sawn timber in a kiln-dryer where pieces

are aligned and stacked to give way to air circulation. This is followed by strength grading by utilizing a strength grader, while any strength reducing flaws (knots, pitch pockets or bark in-growths) are eliminated with cross-cut saw. The timber pieces undergo a process where they are first cut using a finger-joint cutter, then joined together with adhesive to achieve the desired length, and subsequently left for curing. Afterwards, the timber pieces are planed and adhesive is evenly applied to the flat surfaces that need to be bonded. The glued timbers are then clamped and left for further curing. This process is illustrated in Figure 2.2 with each respective step outlined (Ong 2015). Additionally, Figures 2.3a and 2.3b depict square glulam cross-section and the removal of defects within elements respectively. One can observe that a glulam square cross-section does not contain as many or any in-grown flaws in comparison to the sawn timber elements.

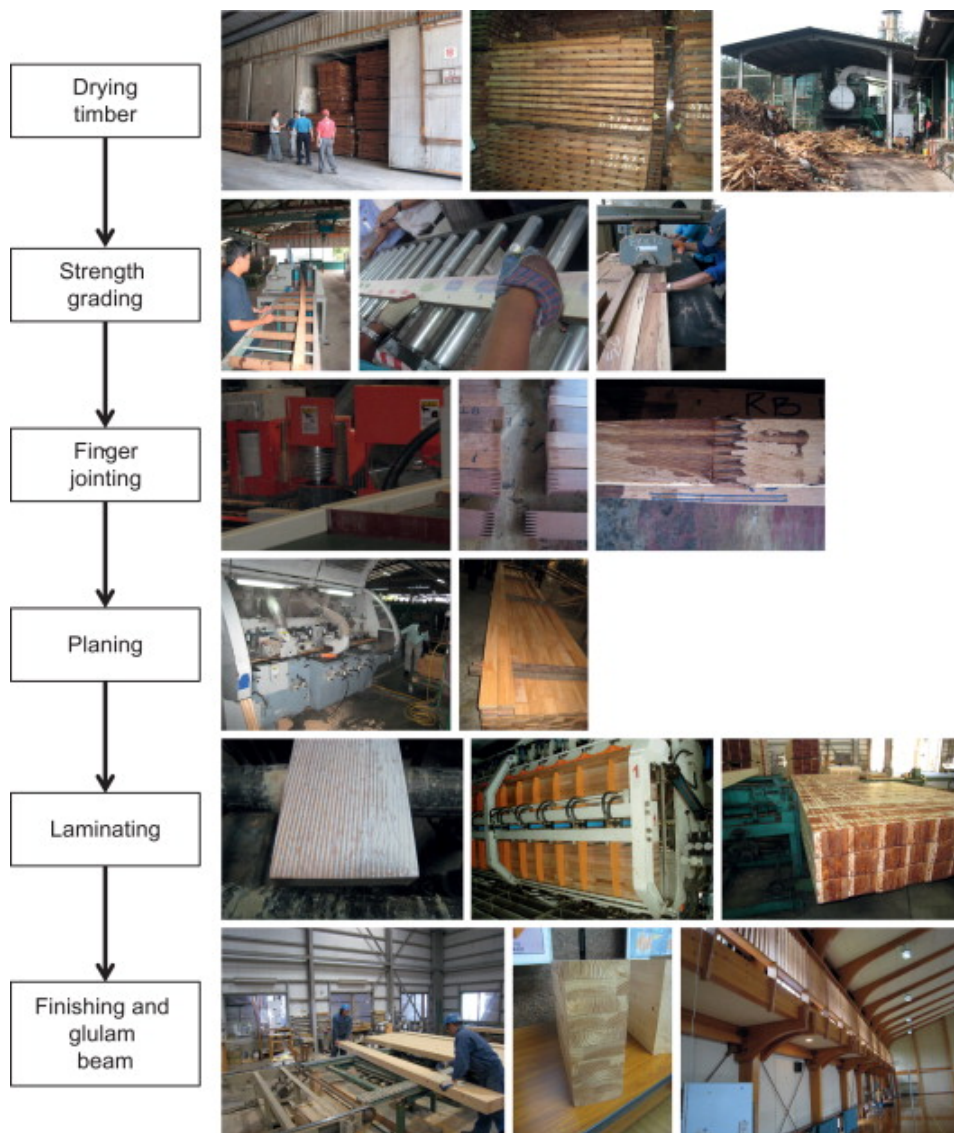


**Figure 2.2:** Stages of glulam production (Ong 2015).

This fabrication process allows manufacturers to create structural columns and beams that are longer, wider, and deeper compared to sawn timber elements. Moreover, it enables the production of more intricate geometries, including curves, arches and twisted elements (Smulski 2004). The breakthrough



**Figure 2.3:** Squared glulam cross-section (a) and the removal of sections containing in-grown defects (b) (Blaß and Sandhaas 2017).

and development of waterproof and mildew-proof synthetic resin adhesives have propelled glue laminated timber as a revolutionary "engineered wood product." These adhesives enable the creation of much larger cross-sections, leading to significant advancements in the field (Blaß and Sandhaas 2017). Thus, it is not common to view glulam member length spanning up to 30.5 m as well as depths going as far as 1 m. When designing glulam elements, an efficient utilization of wood is obtained by strategically placing the highest-grade laminations in sections where in-service stresses are most significant. Subsequently, the remaining sections of the members are positioned with lower-grade laminations, which corresponds to lower stress levels (Smulski 2004). What concerns the design of connections of glulam members, their large dimensions warrant connection type to be accompanied with through-bolts and steel gusset plates as well as framing anchors. Although glued laminated timber elements have a low initial moisture content (amounting to around 12%), connections have to be designed to accommodate shrinkage and swelling of glulam members freely (Smulski 2004). In terms of strength classes, two types of glulam elements can be distinguished: homogeneous and combined. For the latter, GL28h, for example, all the lamellae encapsulate boards of the same strength. In combined glulam, like GL28c, the outer layers are stronger than the inner ones. A combination allows to mix different wood types, which is indeed more cost-effective as it may include less expensive wood without compromising the beam's overall strength (Blaß and Sandhaas 2017).

#### 2.1.4. Curved glulam members

When producing glulam, certain tree species like Siberian larch, Douglas fir, spruce, and oak are highlighted as viable options for the laminates of wood. The thickness of wood layers highly depend on the size of the glulam member to be manufactured whereas the thickness of laminates for curved beams is derived by taking into account the radius by which the laminates are required to be bent. In terms of design considerations of curved beams, special attention is required due to its unique shape and the manufacturing process. In contrast to straight beams, the stress due to bending in curved glulam cross-sections does not distribute uniformly along the depth of the beam. In addition, the manufacturing process give way for stresses as wood laminations were bent into shape and wood fibers on the inner side are compressed. By taking into account Hooke's law, the resulting stresses are indeed larger at

the inner side (Figure 2.4). In addition, given that the bending moment causes the radius of curvature to grow, the occurring transverse stresses are evident as portrayed in Figure 2.5. Usually these stresses cannot be detected by assessing a single dimensional beam (1D), thus, FEA or analytical solutions are derived to determine critical stress values. Typically, the stresses that occur along the neutral axis of a beam, which can lead to cracking. In order to prevent this, tensile reinforcements in the form of fully threaded screws, for example, are incorporated as they take up resulting transversal tensile stresses (Doe 2021). A more elaborate tensile stress perpendicular to the grain evaluation is given in Section 6.4.3 of Eurocode 5.

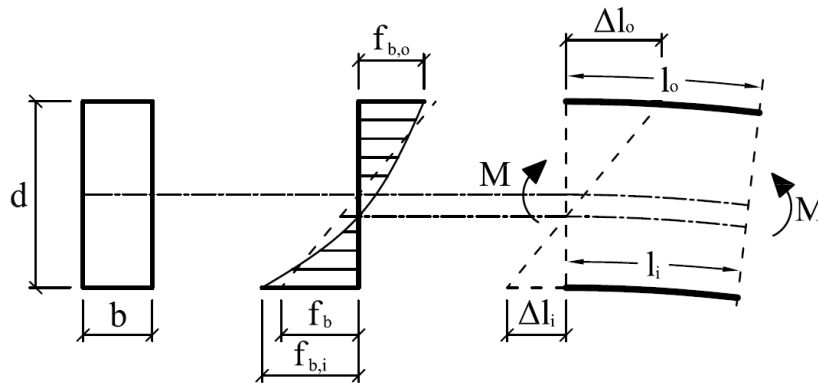


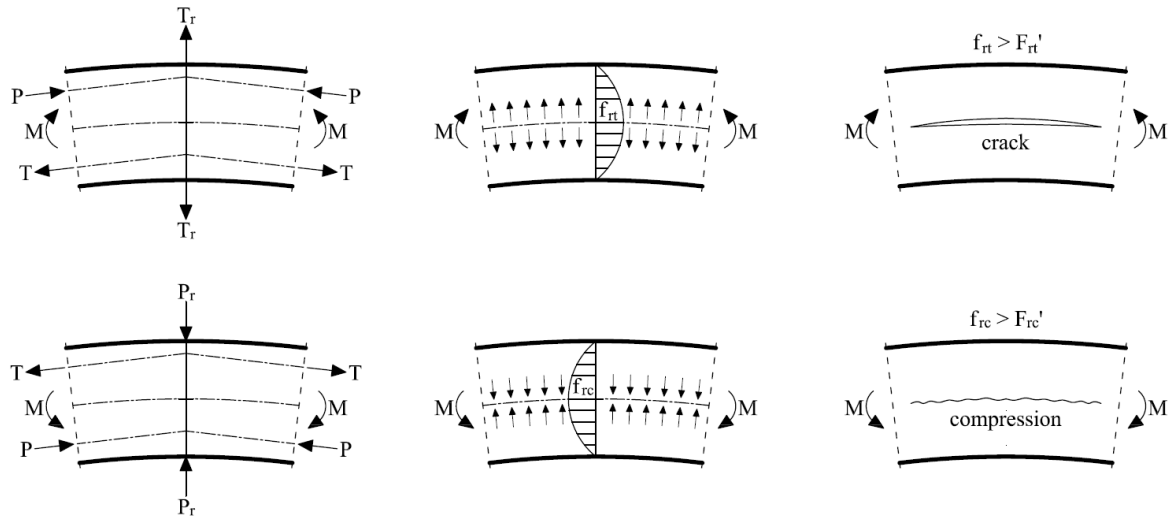
**Figure 2.4:** Non-linear bending stress distribution in a curved glulam beam due to the bent shape (Doe 2021).

### 2.1.5. Joints in Timber Structures

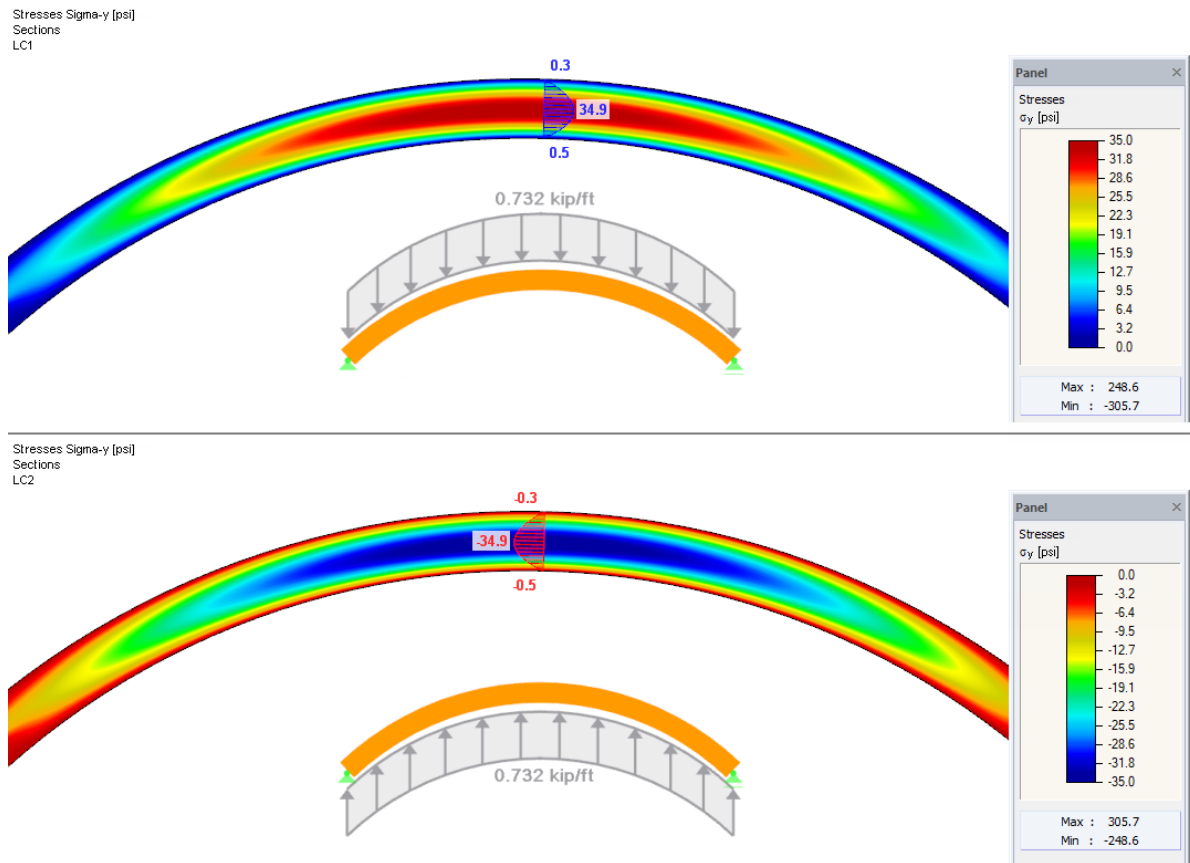
In timber construction, joints play a vital part. Unlike the solid timber pieces they connect, joints often have a lower strength, thus, it makes the design of this component quite crucial. Essential aspects besides the load and the bearing capacity of the joint include cost efficiency, production processes as well as the assembly method. That being said, the objective of joint design is to maintain simplicity while using the least amount of fastener types within the component (Blaß and Sandhaas 2017).

Mainly there are three types of joints: glued joints, which include techniques like gluing steel rods into wood and creating finger joints for glulam beams; carpentry joints that rely on wood pressing against wood to transfer forces through contact and friction; and joints using metal fasteners for added strength. For this research, mechanical fastener joints are of relevance due to a high complexity that hyperboloid structures encapsulate. These structures have varying angles between members, making the role of mechanical fasteners crucial for their realization.

Thus, it's crucial to keep in mind that these joints with mechanical fasteners can deform substantially when subjected to lateral loads. An aspect, which is required to be accounted for in the design process. Timber joints with mechanical fasteners, especially the doweled type connectors exhibit a blend of elasticity and ductility, largely due to how the metal fasteners slightly bend and the wood compresses or embeds around them. This occurs when the joints are designed with specific guidelines in mind regarding the minimum distances from the edges, ends, and between the fasteners themselves. By



(a) Emergence of transversal tension and compression in a curved beam.



(b) FEA outputs of transversal stresses in tension (upper) and compression (lower) of a curved beam.

**Figure 2.5:** Transversal tension and compression in the curved glulam beam (Doe 2021).

adhering to these guidelines, it is possible to prevent brittle failures such as wood splitting, enabling the joint to behave in a ductile way. The main components determining the strength of the fastener connection are: the embedment strength of timber, the yield moment of the fastener and the joint

geometry (comprising edge, end and fastener spacing). It is also of essence to highlight the impact of grain direction in relation to that of the force. Ductile behaviour might be lost whenever the force is applied perpendicular to the grain, which results in timber splitting prematurely as this material is highly anisotropic (Blaß and Sandhaas 2017). More detailed and elaborate design guidelines of dowel type connectors for timber are provided in Eurocode 5: Design of timber structures (Steer 2001).

### Types of failure modes

Given a simple double shear plane timber to timber fastener connection as displayed in Figure 2.6, the lateral load imposed upon the component might result in several failure mechanisms. Johansen (1949) was credited as the pioneer for investigating those failure modes in more detail and deriving methods of calculating the load bearing capacity of the joint via force and method equilibrium conditions. As displayed in Figure 2.6, failure modes g and h relate to the embedment strength of the side and middle member respectively, while failure modes j and k are marked by the fastener deforming due to one or more plastic hinges forming. For two latter modes, that is where the "rope effect" becomes effective. This phenomenon enables the fastener to act in tension throughout its shank, which in turn determines how much timber members are pressed against each other through the anchorage of the dowel while friction force also contributes. Based on the type of the fastener, the contribution of the 'rope effect' to the load bearing capacity of the joint can be realized and displayed in Table 2.2. Taking into account all the failure modes, by enforcing the equilibrium of forces and moments, the load bearing capacity  $F_{v,R}$  per shear plane and fastener can be derived.

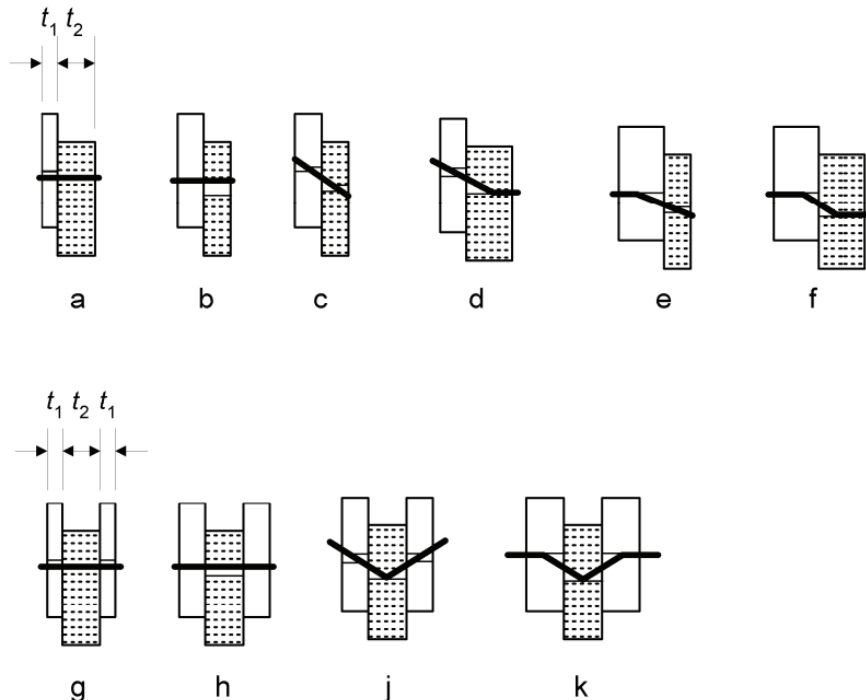


**Figure 2.6:** Failure modes of a timber-to-timber single and double shear plane fastener connection with a single dowel (Steer 2001).

In order to transmit forces of substantial magnitude, especially when it's needed to connect structural

Fastener Type	Percentage
Round, smooth shank nails	15%
Square, smooth shank nails	25%
Ringed shank or spiral nails	50%
Screws	100%
Bolts	25%
Dowels	0%

**Table 2.2:** Based on the type of the fastener, the contribution of the 'rope effect' to the load bearing capacity of the dowel type timber to timber connection.

elements of the same size, it is quite beneficial to increase the amount of shear planes in the dowel-type connection. Given that the double shear plane connection reaches failure modes j or k (the development of plastic hinges in a dowel), by merely increasing the thickness of timber members will not further enhance the strength capacity of the connection. Consequently, the limit where larger cross-sections cannot provide cost-effective outcomes is reached. Thus, in order to boost the strength load-bearing capacity of the connection, a solution to increase the number of shear planes emerges. According to paragraph 8.1.3 in Eurocode 5, the multiple shear plane connection model is necessitated to be taken as a series of three-member connection, where each shear plane has a certain resistance. In addition, the paragraph states that in case of a multiple shear plane connection, the respective shear planes should work together and exhibit compatibility. Thus, governing failure mechanisms cannot be occurring with a mix of modes (a), (b), (g), and (h) and modes (e), (f), and (j) alongside other ones (Figure 2.6) (Sandhaas et al. 2018).

### Stiffness

A robust connection design necessitates attention to more than just the strength capacity of it. The stiffness of the component becomes imperative especially when connections have to exhibit sufficient flexibility and absorb and dissipate energy, for example, in case of an earthquake. To put it more clearly, by obtaining the stiffness value of the connection, the designer is able to predict how much a joint will deform under various loads. This characteristic significantly influences the overall deformation of the frame structure, for instance, under lateral wind loads. Yet, for timber multiple shear connections, it is quite common to see the stiffness decrease as the load is growing. The loss of stiffness of the joint can be attributed to non-linear material behaviour (timber compaction, crushing), fastener bending or yielding as well as slippage and loosening of the bolt once it is beyond the point of friction holding it in place (Jockwer and Jorissen 2018). Figure 2.7 illustrates a characteristic load-deformation diagram of a doweled connection. The slip modulus in the serviceability limit state per shear plane per fastener is denoted as  $K_{ser}$ .

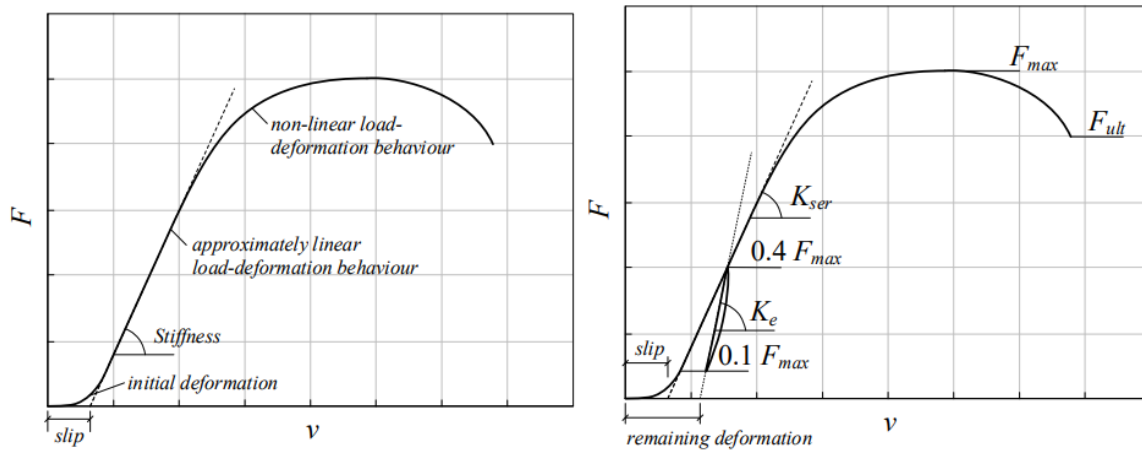


Figure 2.7: Load - deformation diagram concerning the doweled connection (Jockwer and Jorissen 2018).

## 2.2. Timber Lattice Towers

After providing a broad overview on timber as a building material, it's crucial to delve into the specific structures that can be realized with it. This section reviews a variety of timber towers, examining their design principles, global shape, member configuration, construction methods as well as challenges they address.

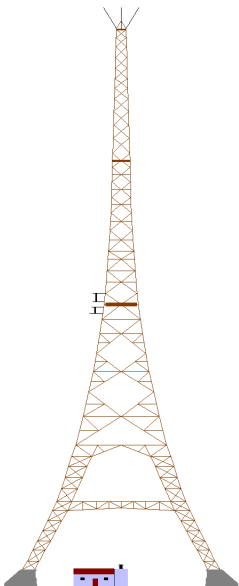
In general, observational timber towers often share a similar component layout, comprising a rectangular or triangular plan configuration, an outer skin that remains consistent from top to bottom, and a central staircase leading to the viewing platform at the apex. By maintaining these characteristics, throughout modern history, various tower configurations have been realized. The first notable design has to be recognised as the array of truss towers were built before the period of World War II in the form of radio masts, especially in Germany and Poland. In 1932 the transmitter mast in Ismaning, Germany was realized with a height of 115 m, which later on was re-adjusted to 165 m (Figure 2.8). While having a square 20 m wide base, the tower exhibited a truss paraboloid silhouette that resembles that of an Eiffel tower currently. The structure is assembled through the use of timber rectangular sections with the largest one being 140 x 240 mm, while joint design was employing Kübler dowelled connections, which can bear significant loads without showing the same degree of slip as a standard screwed or bolted joint. Unfortunately, high costs of refurbishment related to heightened construction requirements which rendered the structure ill-conditioned. Thus, the tower was demolished in 1983 (Herzog et al. 2004).

The other similar and noteworthy tower design was realized in Poland in 1935, the Gliwice radio tower (Figure 2.9). This tower boasts a height of 111.1 m, while having four platforms located at various heights. The paraboloid silhouette of the tower is assembled with unimpregnated larch wood members that form the truss configuration. The tower also utilized brass connectors (Kuśnierz 2003).

By observing the global paraboloid shape of such towers, one can explore the engineering decisions made to accommodate imposed loads. The fact that the overall width of the tower is not consistent from top to bottom as well as the fact that it varies non-linearly is particularly intriguing. The overall shape is associated to the load it is primarily subjected to and especially by taking into account horizontal loads stemming from the wind it is quite evident as to why. The tower in its most global sense acts as



(a) (Zimmer 1950)



(b) (Vakarel 2006).

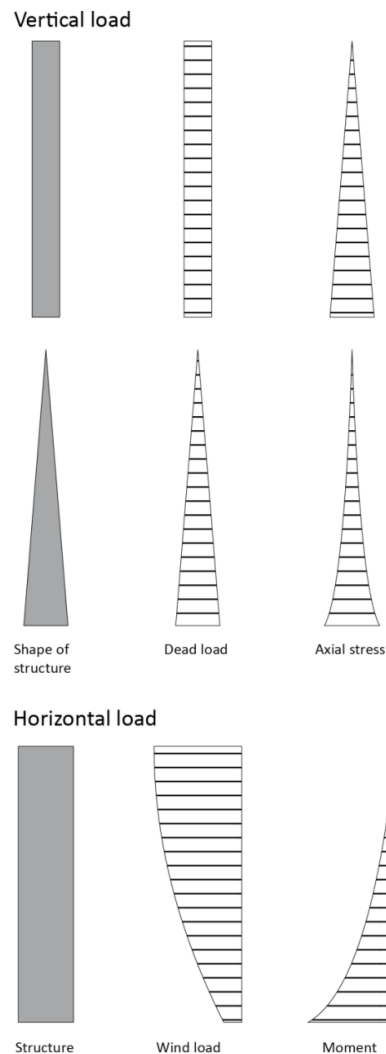
Figure 2.8: Ismaning transmitter tower.



Figure 2.9: Gliwice radio station (Ebielmaj 2014).

a cantilever resisting loads, and in turns develops high bending moments at its base. By adopting a tower shape that closely emulates that of the resulting bending moment, the structure becomes innately better at resisting imposed loading. By inspecting Figure 2.10, one can comprehend the axial stress

and bending moments incurred on a structure based on its global silhouette. In addition, it is of essence to compose a rotated or at least symmetric face of the structure, which prepares it to withstand winds from all different directions. Thus, the composing elements within the structure have to be prepared to transmit both tensile and compressive forces from top to bottom. Involving platforms at different levels facilitates a more uniform distribution of horizontal forces within the structure, which in turn increases global lateral stiffness enormously. In addition to that, given a non-centrally applied wind load, the structure forms an outer layer composed of a truss and is able to resist torsion by virtue of St. Venant principle. This principle (as portrayed in Figure 2.11 in relation to Vlaslov principle) allows resulting forces to spirally traverse through the outer skin down towards supports. (Cajmatz 2017).



**Figure 2.10:** Responses to vertical and wind loads depending on the global silhouette (Cajmatz 2017).

Increasing the level of complexity of built towers, the doubly curved silhouette of the structure involves not trusses per se, but grid shells, which form a smoother surface of the outer skin. Thus, this configuration is required to be analyzed in a three dimensional space. Famous samples of a doubly curved tower structure include the works of a russian engineer Vladimir Shukov (1853-1939). Built in 1896 at the All-Russia Fair in Polibino, Lipetsk Oblast, Russia, his 37 m tall first hyperboloid lattice tower is still standing today (Figure 2.12). Shukov identified the impeccable structural strength to self-weight

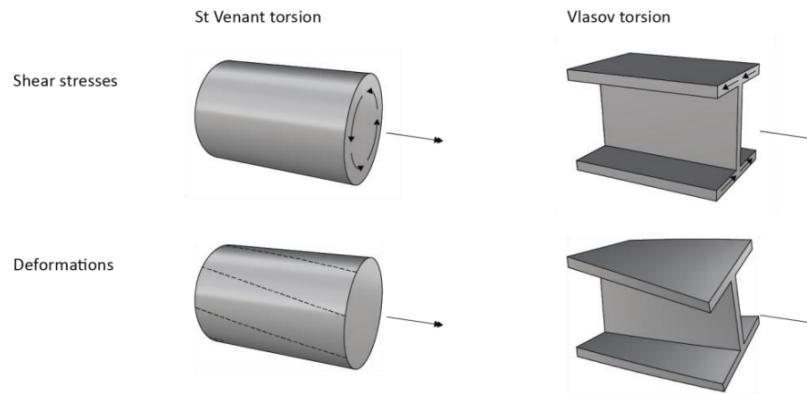
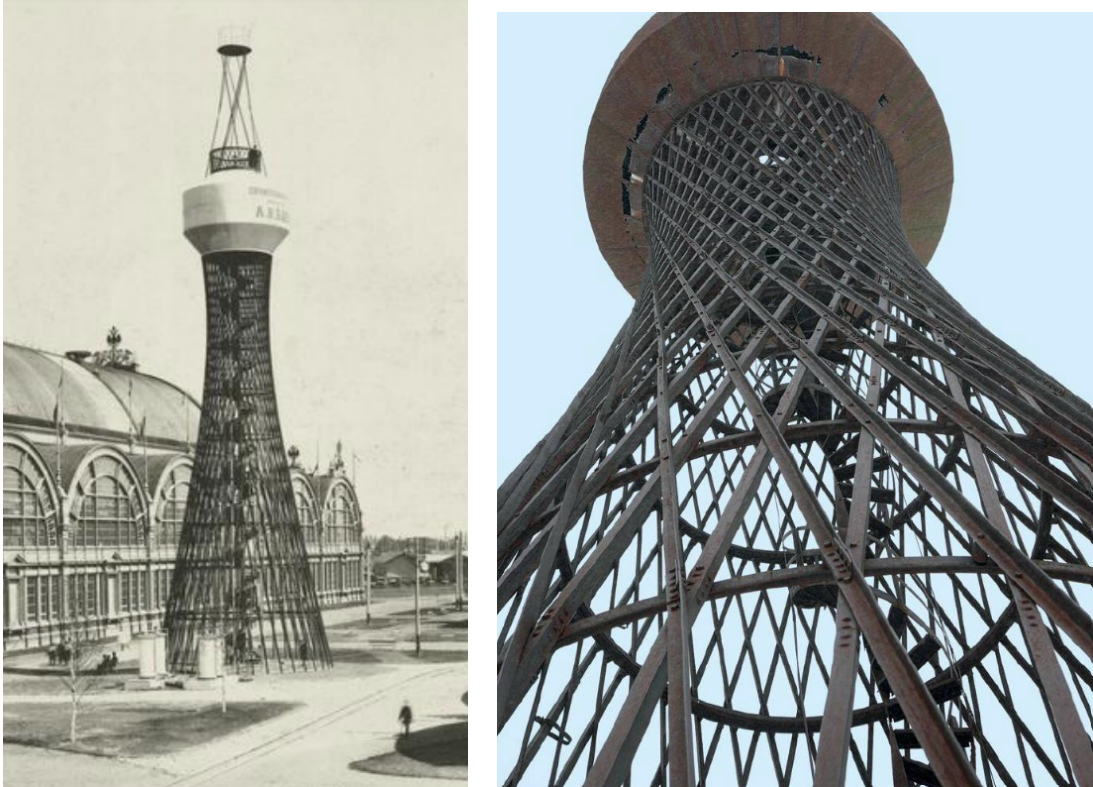


**Figure 2.11:** St Venant and Vlasov torsion (Cajmatz 2017).

ratio that lattice structures possess. In addition to that characteristic, Shukov hyperboloid towers were quite easy to transport and erect as well due to smaller member cross-sections. Thus, in 1922, the Shabalovka tower was designed with a height that exceeded the Eiffel Tower by 50 meters (350 m), while utilizing less than a quarter of the material required for the latter's construction (English 2005). This structure utilized segmented hyperboloids that were stacked on top of each other (Figure 2.13). The grid of the structure is composed of helical and circumferential members. The former essentially are two sets of straight and continuous strips that are rotated around a vertical axis and define the hyperboloid silhouette. These sets of straight lines are rotated in opposite directions. In case of the towers presented, circumferential ring elements are designed to be flexurally stiff as to avoid kinematic displacement (Beckh 2015).

Given that horizontal loads, which, for this instance is taken to be point loads subjected to flexurally stiff rings throughout the height of the tower, the force will be distributed by each ring into the adjacent straight members depending on their geometric stiffness as portrayed in Figure 2.14. The resulting force distribution within the tower means that circumferential members on the windward side are loaded in compression, while the ones on the leeward side are experiencing tension. The opposite is true for helical members: windward side is mostly loaded in tension, while leeward side is in compression. The magnitude of force within each member is becoming less from top to the bottom of the tower. Imagining this tower as a cantilever being subjected to bending, at the neutral axis, supports experience lowest amount of force as detailed in Figure 2.14b. In case of a tower, composed of separate segments (Shabalovka tower, for example), the vertical load increases step-wise (non-linearly) in vertical members at main rings. This is due to the change of slope and the direction of those vertical members as they arrive at the main ring. Knowing that the vertical force that need to be transferred down remains the same, the increase of the angle of vertical members in relation to the ones above does expose them to larger axial forces as portrayed in Figure 2.15. Through employment of flexurally stiff rings, the structure is able to showcase high stiffness characteristics under horizontal nodal loads.

It should be noted that for this example, which has been researched more thoroughly by Beckh (2015), the wind loads are applied as nodal point loads without expressing considerations for shielding factors or the fact that current standards did not take into account more intricate three dimensional lattice structures. This is particularly of significance for this loading type, as sides of the tower should experience less loading due to tightly packed vertical (helical) members. In addition, the current research did not



(a) (Arsenev 2009).

(b) (Beckh 2015).

Figure 2.12: Shukov tower in Polibino (1896).

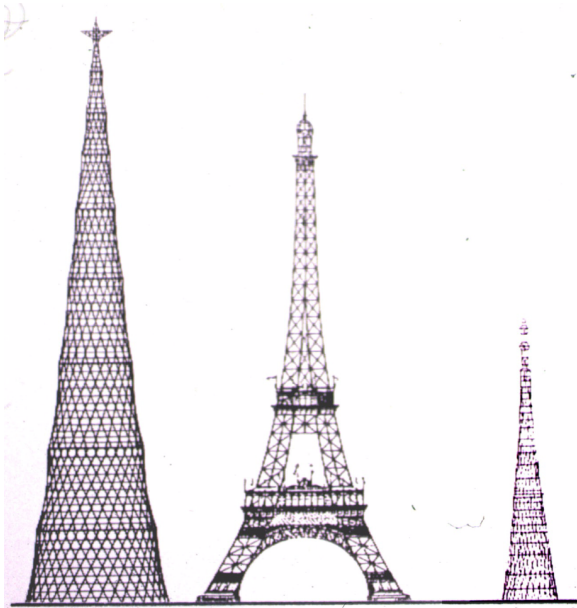
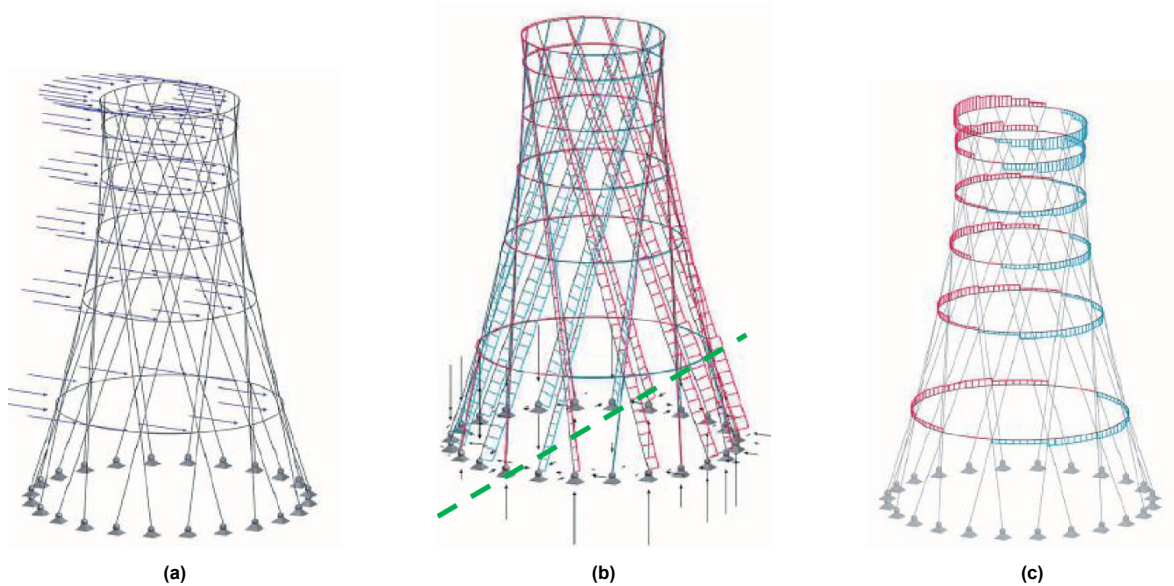


Figure 2.13: The initial design of the Shabalovka tower (left) in relation to the Eiffel tower and the one that is realised (right).

particularly dive into the loading case which would consider a hyperboloid lattice tower that would be clad with a solid surface. The research highlights the advantages of the hyperboloid tower silhouette in enhancing stiffness and stability characteristics under vertical loads. However, it does not explicitly mention that this shape provides optimal benefits for stability and stiffness when being subjected to

horizontal nodal loads.



**Figure 2.14:** Resulting effects of horizontal nodal loads: applied loads (a), axial forces within helical members (b) and axial forces within circumferential members (c). Red colour indicates members in tension, while blue relates to members in compression (Beckh 2015). Green dashed line indicate the neutral axis for the hyperboloid tower.

In terms of the proposed silhouette being realised with timber, it can be found Shukov himself admitting (regarding the patent of a new hyperboloid tower): 'A lattice-form tower characterised in that its load-bearing structure consists of straight wooden beams, iron tubes or angle profiles which cross over one another and lie on the directrix of a solid of revolution and that takes the form of a tower' (Beckh 2015). Thus, this quote does illuminate the notion that the global shape and member configuration does not depend on the material and, thus, the hyperboloid tower can be quite confidently realized in timber.

A more recent timber hyperboloid tower structure has been implemented in the nature reserve of Helemlers - Halkenbroek in Drenthe province, The Netherlands (Figure 2.16). This 15 meters tall observational tower, designed by Tentech, employs a system of two components: the vertical members that connect to platforms that primarily bear vertical loads and the hyperboloid outer diagonal structure that supports its own self-weight, some of the floor loading of the top platform and all incoming horizontal loads (lateral wind as well as torsion). The structure boasts a material efficient design through employment of slender diagonal elements with the diameter of 140 mm at the ground level while the rest of the floors utilize members with a diameter of only 120 mm (P. A. d. Vries and Gard 2006).

The design could not solely rely on continuous straight elements to define the hyperboloid shape. Instead, long vertical members are comprised of shorter elements that are connected in the node. Vertical members as well as ring members do not meet at one point, instead the node accommodates those members in different layers, thus, eccentricity at the joint is occurring. Structural analysis needed to consider this factor, and the design of connections had to incorporate it as well (P. A. d. Vries and Gard 2006). The implemented connection is displayed in Figure 2.17.

Differently from the variants designed by Shukov, this tower does not incorporate flexurally stiff rings,

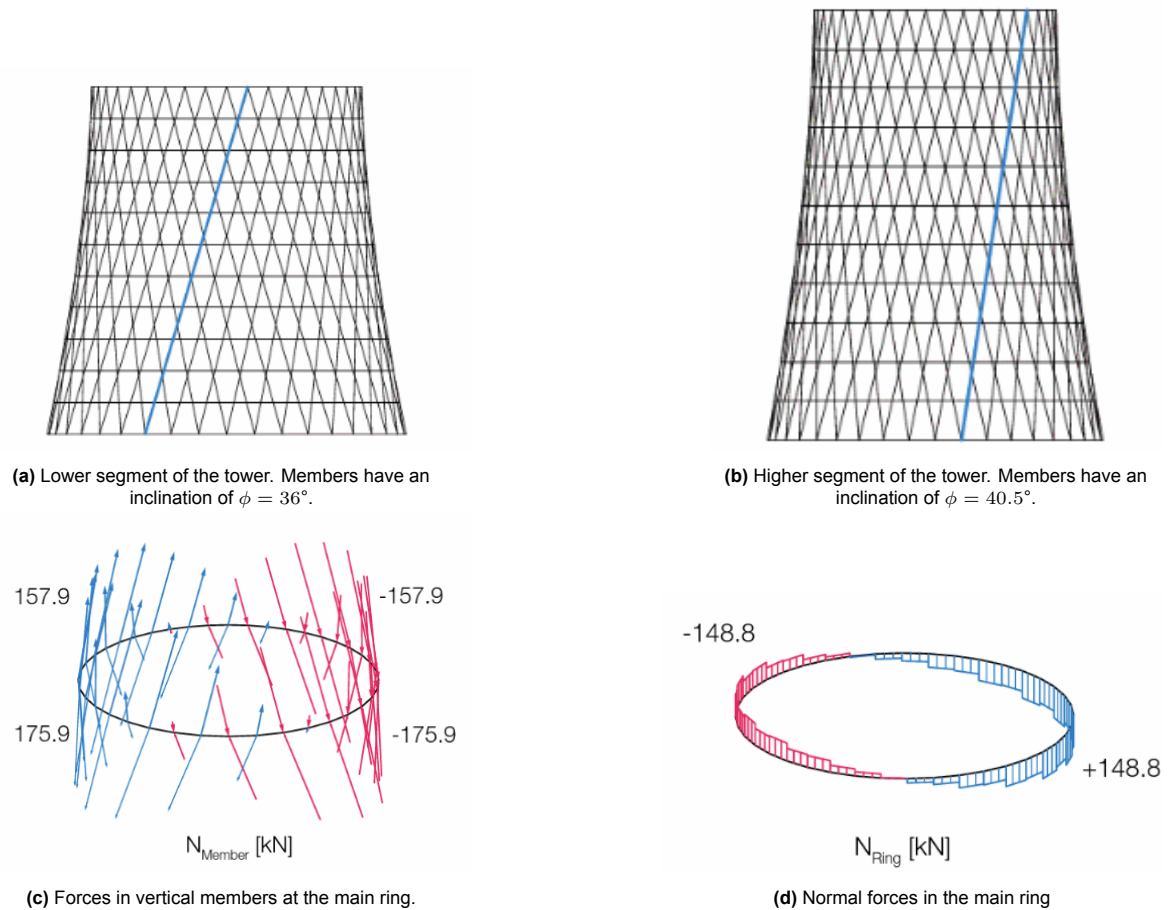


**Figure 2.15:** Given that hyperbolic segments are employed, the change of angle at abutting vertical members causes the increase in the normal force within them at the point of the main ring (Beckh 2015).

instead the configuration relies on segmented or polygonal ring elements. This design choice brings up an interesting point: the presence of a platform connected to each nearby node leads to question whether it's really isolated from contributing to the tower's overall lateral stiffness, given the immense in-plane stiffness of this element and how its integration facilitates horizontal load distribution within the structure. Understanding how flexurally stiff rings behave is key, especially considering the significant axial forces they encounter from wind loads (Figure 2.14c). When observing the hyperboloid observational tower designed by Tentech, the inclusion of platforms becomes even more critical within segmented rings under the impact of lateral wind loads, particularly at the tower's top where axial forces in rings are at their most intense. Thus, the triangulated platform does indeed facilitate the horizontal load transfer within the structure under lateral wind loads. However, the use of straight vertical members within the structure allows them to also resist lateral loads by forming pairs (or bipods) that exhibit different geometrical stiffness (Figure 2.18). The placement of the bipod subjected to the highest load is determined by its rotational angle: specifically, the bipod whose connecting line, when viewed in plan, forms the narrowest angle with the force's direction, supports the most significant load. Through employment of ring and platform elements, the buckling lengths of the bipod members are reduced and stability is not governing the design. Finally, the tower forms an approximate tubular section which in turn resists torsion through St Venant's principle.

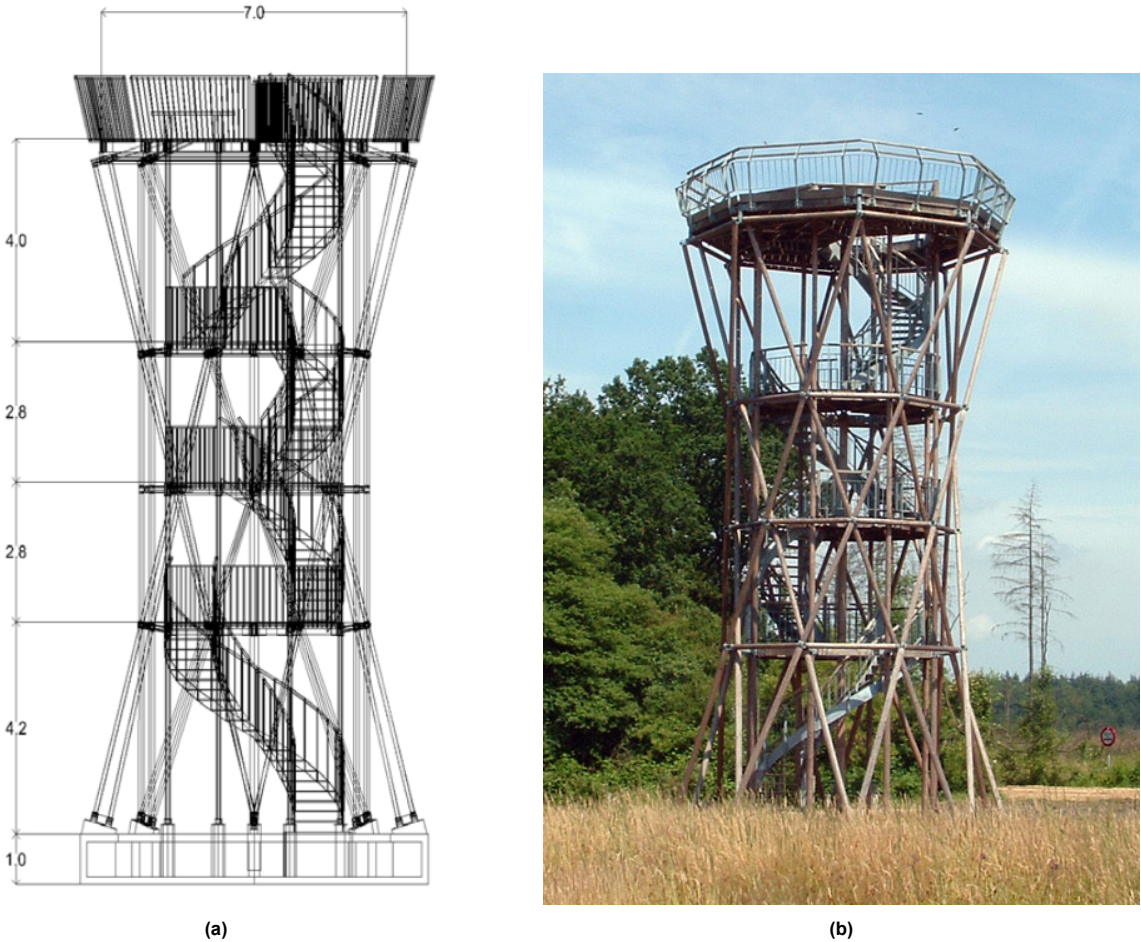
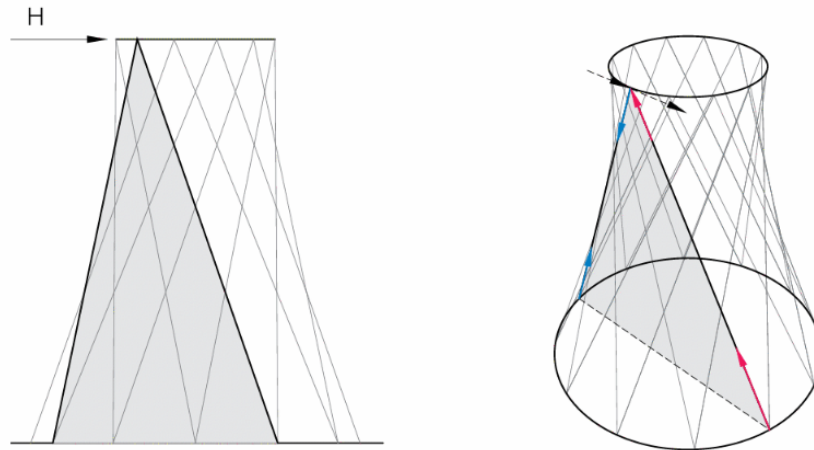


Figure 2.16: The tower in Drenthe, The Netherlands by Tentech: architectural preliminary draft of the tower (a) and the realized tower (b) (P. d. Vries 2005).



Figure 2.17: Connection implemented for the tower in Drenthe, The Netherlands by Tentech (P. A. d. Vries and Gard 2006).

Another structure to be inspected is the Strand East Tower located in London, UK. A monumental 40 m high sculpture boasts a slender shape comprised of a grid of crossed timber laths and 16 flexurally stiff galvanized steel rings (Figure 2.19). The structure has been designed by 'ARC-ML' architects in collaboration with 'eHRW' engineers and finished in 2012. The first 3.5 meters of the structure

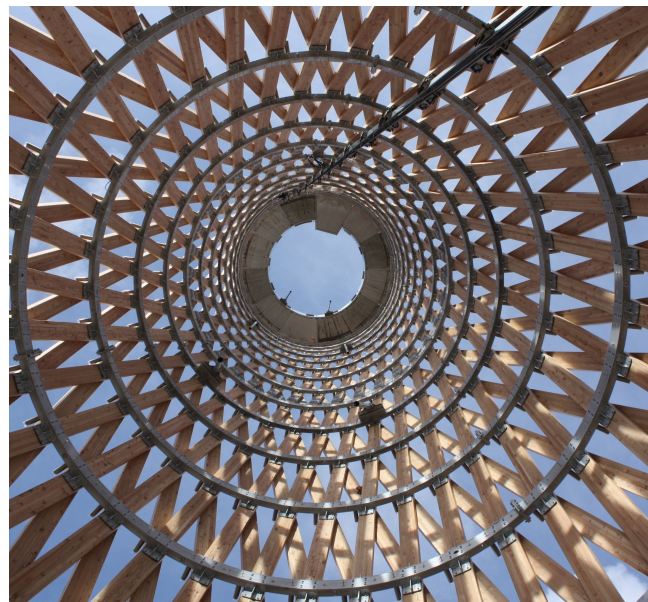


**Figure 2.18:** Responses to horizontal loads of the hyperboloid through employment of bipod vertical element grouping (Beckh 2015).

is composed of steel members, while the rest of the vertical members are wooden. By employing rectangular timber cross-sections and rotating two layers of vertical members around the tower's skin — each layer in opposite directions to achieve a total twist of  $80^\circ$  — and reinforcing this structure with steel rings, the distinctive hyperboloid shape of the tower is defined. Given that each ring is flexurally stiff, the tower structure is able to resist lateral wind loads by itself and function as a hollow sculpture without the need of in-plane reinforcement (platform). An important characteristic of the tower is the possible disassembly and re-use for different projects (Lorusso 2012).



(a)



(b)

**Figure 2.19:** The East Strand Tower in London, UK: the hyperboloid shape of the tower (a), as well as the inside of the tower (b) (Lorusso 2012).

These examples illustrate how hyperboloid tower designs can effectively manage lateral forces using different strategies: through incorporation of flexurally rigid rings, utilization of straight vertical members forming a bipod, and integrating in-plane stiff platforms that facilitate horizontal load transfer. In addition to that, the use of timber has been prevalent throughout many similar projects, which basically confirms that such structural systems rely heavily on geometrical structural properties rather than material dependencies. A review of relevant literature reveals that such structures are often constructed using straight, continuous, and rotated vertical members. The use of segmented members in order to define the hyperboloid is seldom used due to kinematic motion concerns, which have to be resolved either through flexurally stiff rings or implementation of platforms that stabilize nodes in the ring (Beckh 2015). A noteworthy example of a hyperboloid steel construction, characterized by segmented rings and vertical members that are neither continuous nor straight, is the observation tower located in Kootwijkerzand, the Netherlands (Figure 2.20). Here the platform stabilize the 13.5 m tall structure by disallowing any nodal movement to occur as vertical members do not maintain its continuous shape (the bipods are not formed) and nodal eccentricities are introduced. Thus, the structure resembles more of a grid shell through discrete members abutting at nodes. The grid shell implementation in this case necessitates the inclusion on platforms at every nodal level and functional versatility is not at a high level. These design aspects spur an exploration whether a specific gridshell or hyperboloid configuration exists that inherently achieves sufficient lateral stiffness without relying on a stabilizing platform, given both gridshells and hyperboloids achieve their stability from the geometry. The challenge lies in identifying a gridshell shape that naturally provides the desired level of lateral stiffness, potentially simplifying construction, material re-usability and functional tower versatility. The primary concern given the grid shell configuration of the tower is the kinematic motion of nodes as identified by Beckh (2015). For Shukov towers this issue is resolved through employment of flexurally stiff rings. However, certain geometrical silhouettes and member configurations could yield stable responses of discretized hyperboloid towers without the need of platforms or flexurally stiff rings as indicated by Cajmatz (2017).

Considering the challenge of obtaining fully rigid joints in timber construction, the inherent stability concerns are thoughtfully addressed in post and beam towers through their specific design approach. These systems are comprised mainly of horizontal members and vertical posts while in between having a diagonal bracing which in turn provides the capability to resist lateral wind loading. The example of Seljord observation tower by Rintala Eggertsson Architects is a 12 meter tall glulam timber construction built in 2011 (Figure 2.21). The tower maintains a rectangular tubular plan which allows to resist torsion quite efficiently. The cladding exposes the tower to more critical wind loading as the projected area increases compared to completely transparent skeleton. Diagonal bracing is implemented at every rectangular component.

A more famous post and beam construction was realized in 2013 in Austria, the Pyramidenkogel tower, whose structural design was undertaken by engineers 'Lackner + Raml' (Figure 2.22). The composition of 16 curved glulam posts interconnected by 10 elliptical steel rings and braced by 80 steel struts gives rise to a laterally stiff and stable 100 m tall lighthouse. Given its stature as the tallest wooden observation tower in the world, its substantial height and width were expected to expose it to significant wind loads, making lateral loading a governing one. This lead the design team to resort to wind tunnel testing as the structure could not be classified by the Standard 1991 - 1 - 4 (Lackner and Vodicka 2013). The post and beam configuration allows the structure to form a closed cross-section and resist torsional by St. Venant principle. By not relying on in-plane stiff diaphragm acting as stiffeners (lateral stiffness and



Figure 2.20: Hyperboloid segmented tower in Kootwijkerzand, the Netherlands (Cindy and Janneke 2024).



(a)



(b)

Figure 2.21: Seljord observation tower designed by Rintala Eggertsson Architects: the tower at night (a) and the interior of the tower showcasing the post and beam system (Jenssen 2012).

overall stability is ensured through the use of elliptical steel rings and bracing of steel rods), the tower is able to accommodate technical installations, stairs, landings as well as a long slide all down to the ground within its cross-section. To reduce the effects of lateral forces, the structure incorporates glulam

columns oriented with their rigid side facing the direction of the wind (long side against the projected wind force). These structural characteristics ensures maximum functional versatility and adaptability of this tower throughout its lifetime (Frame 2013). In the construction of this specific structure, it's designed in a way that glulam columns are kept uninterrupted, and steel components are affixed to them. Naturally, the connections between glulam elements occur at distinct locations, separate from the points where the steel sections are connected.



(a) (Fine Stay Slovenia 2024)



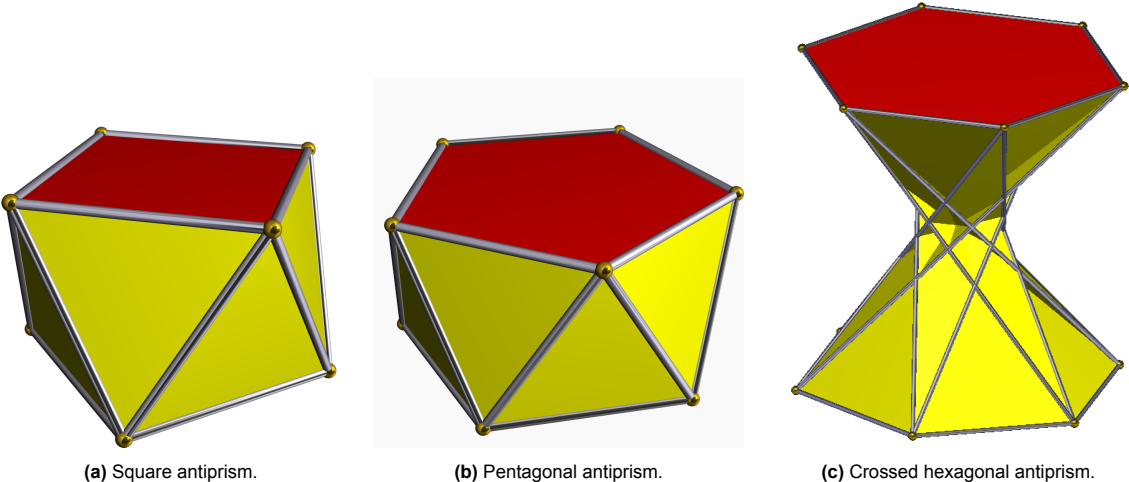
(b) (hsbcad 2024)

**Figure 2.22:** The Pyramidenkogel tower (a) and its construction highlighting the post and beam system comprised of glulam posts, elliptical steel rings and diagonal steel rods (b).

The distinct geometrical difference between the post and beam and previous hyperboloid towers reviewed is the member configuration or the pattern (topology). By visually inspecting the pattern of the tower in Drenthe (by Tentech), the tower in Kootwijkerzand the predominant topology is the one resembling closely a diagrid configuration. Cylindrical or hyperboloid shapes defined by this topology is often referred to as the antiprism (Figure 2.23). This geometric structure is formed by two congruent polygons, each with  $n$  sides, arranged in parallel. These polygons are joined by a sequence of  $2n$  triangles that alternate around the perimeter, creating a seamless linkage. The main characteristic of an antiprism is that base polygons are twisted relatively to each other (Cromwell 1997). In the context of Shukhov's designs, the foundational geometric figure is notably the crossed antiprism, distinguished by its crossed isosceles triangles forming the sides (refer to Figures 2.23c). The rotation of connected vertices of each base polygon forms a hyperboloid silhouette. Incorporating stiff rings or platforms into structures based on geometrical shapes like antiprisms is seen as a strategy to counter their tendency to display kinematic behaviour. This approach prompts an investigation into the structural stability of antiprisms and the specific conditions under which they might exhibit instability. Currently no literature covers or mentions the kinematic behaviour of antiprism structures.

In terms of the composition of post and beam structures, the arrangement of members—specifically four vertices lying in a single plane (comprising two posts, two beams, and a diagonal brace) — enables the

structure to maintain a consistent (and un-rotated) base or ring at every level of its height. The stability of the structure is ensured through bracing and the exoskeleton is in no need of internal stabilizing components.



(a) Square antiprism.

(b) Pentagonal antiprism.

(c) Crossed hexagonal antiprism.

Figure 2.23: Antiprisms (Tomruen 2006).

## 2.3. Hyperboloid Lattice Structures in Research Domain

According to literature to be presented, lattice structures have been extensively researched and implemented in the realm of aerospace engineering, while their utilization and understanding in civil engineering applications have received comparatively limited attention. As described by Vasiliev, Barynin, and Rasin (2001), lattice structures are typically composed in the form of thin-walled cylindrical or conical shells and they are comprised of helical and circumferential ribs that form a system at an angle in respect to the shell axis. Generally, the most basic lattice structure does not entail a skin, although in some configurations in accordance to certain design specifications, this structure can be constructed with one-side or two-side skins. Figure 2.24 displays the typical system and parameters of a Kagome topology lattice structure. Vasiliev, Barynin, and Rasin (2001) details that applications of lattice structures include aircraft fuselage sections, wing boxes, ribs, load carrying tanks and fairings of launch vehicles. In general, composite lattice cylindrical shells are substantially utilized in whenever the design of load-carrying spacecraft tubular bodies are considered.

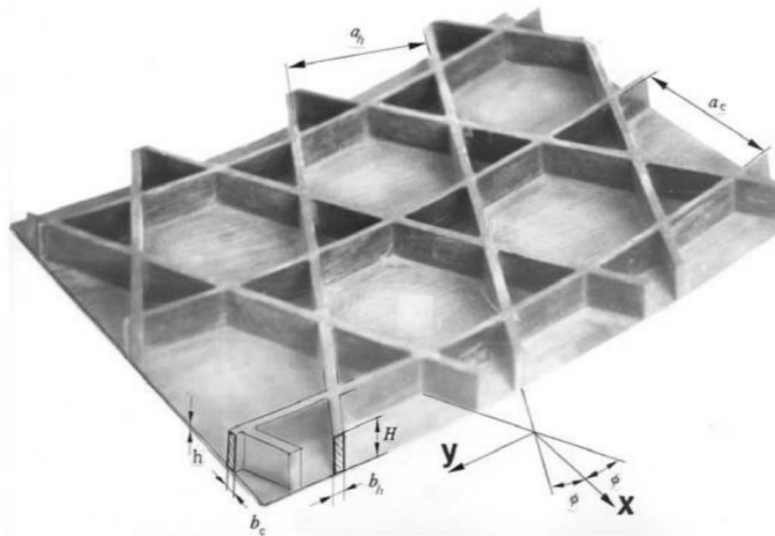


**Figure 2.24:** The general system and parameters of a lattice structure (Vasiliev, Barynin, and Rasin 2001).

According to recent research, lattice structures hold tremendous promise for attaining lightweight properties and sought-after structural attributes, such as exceptional shock resistance (Elnasri et al. 2007), energy absorbency (Xiao et al. 2020) and specific stiffness (Xia and Breitkopf 2015). Whenever the shortcomings of lattice structures are considered, unstiffened lattice structures cannot demonstrate satisfactory stiffness at certain locations whenever concentrated loads are involved. This flaw is often compensated by combining both lattices and stiffeners within the structure (Yang et al. 2023). However, stiffeners result in unwanted addition of mass, which denounces the sought after efficiency of the lattice structure.

Aerospace industry has conducted extensive investigations on the structural characteristics of cylindrical and hyperboloid lattice configurations. In the context of aircraft fuselage sections, Vasiliev, Barynin, and Rasin (2001) theoretically evaluated lattice structures' weight efficiency (maximum design load

divided by the weight of the structure) to be much higher than those for traditional structures (sandwich and stringer cylindrical shells). This effect can be explained by the high degree of membrane and bending stiffness provided by the ribs in the lattice configuration despite their low mass in comparison to uniform skins. This neglects the need to introduce stiffeners or a core. Additionally, lattice structures exhibit self stabilizing attributes, which significantly augment their capacity to resist buckling. The self stabilization stems by virtue of rigidly connected helical and circumferential members and the conversion of compressive force located in helical ribs into circumferential tension of the circumferential ribs. This phenomenon bears a resemblance to the effect caused by internal pressure that reduces the shell sensitivity to shape imperfections.

Whenever different curvatures of lattice structures are considered, Shitanaka, Aoki, and Yokozeki (2019) explored the axial stress distribution and buckling loads of hyperboloid (negative curvature) and conventional cylindrical lattice structures by subjecting them to compression force and bending. By utilizing finite element method software, the author concluded that buckling loads of hyperboloid lattice structures are smaller than that of cylindrical ones in both loading cases. However, it was also observed that the hyperboloid lattice structure exhibited lower maximum stress levels compared to its cylindrical counterpart as portrayed in Figure 2.25. The stress distributions varying by the order of two at max in this research does signify about stiffness capabilities of a hyperboloid, which are quite promising.

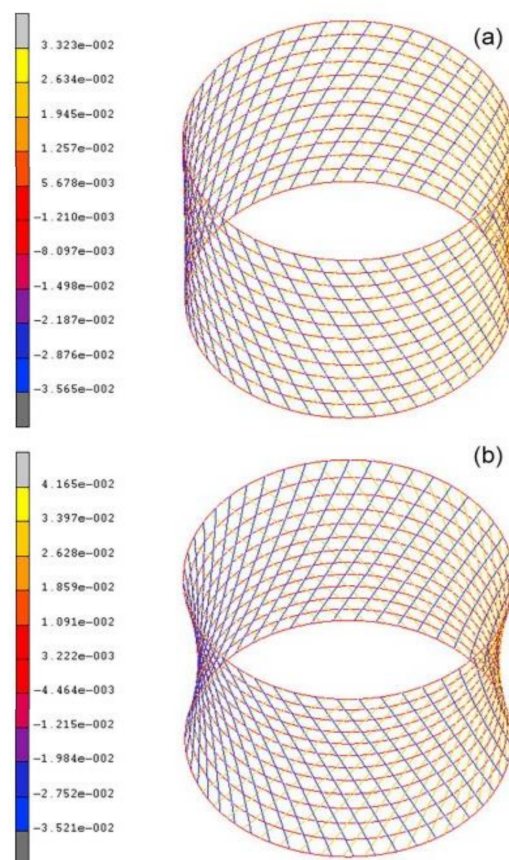


**Figure 2.25:** Stress distributions (Mpa) of lattice structures subjected to bending of 100 kNm. (a) Cylindrical. (b) Hyperboloid (Shitanaka, Aoki, and Yokozeki 2019).

Within the realm of civil engineering, a hyperboloid structure known as the Rhombic grid hyperboloid-latticed shell (RGHLS) stands out, particularly for its incorporation at The China Comic and Animation Museum (CCAM) in Hangzhou, China. This structure is used as a sub-structure designed to bear the weight of the museum's upper levels as illustrated in Figure 2.26. As highlighted by Guo et al. (2018), whenever high-rise buildings incorporate a diagrid structure and an internal core, the diagrid is mainly responsible for handling the forces stemming from wind or seismic events, providing remarkable stability against lateral movements. Even more, the integration of floor slabs serves to tie the diagrid and the core, improving the building's ability to distribute these forces effectively. The RGHLS utilized straight members rotated around the vertical axis without any circumferential members being present. The governing failure mechanism for this type was identified as the out-of-plane multi-column interaction instability under vertical loads due to rhombic grids, absence of circumferential members (except the stiff ring at the apex) and lateral braced in the radial direction. The introduction of openings (adhering to the architectural function) within a dense grid worsened structure's lateral stiffness after being subjected to horizontal loads. Considering the need to maintain diagonal members in plane it was imperative to construct two types of bidirectional columns that would form an X joint. The first type, referred to as primary columns, extended continuously from the base to the top. In contrast, the secondary columns were divided by the primary ones, creating a segmented structure. Thus, the structural strength of X joint and the ratio of stiffness between the secondary and primary columns becomes a significant design concern. Given the ease of connecting steel members through welding, this geometrical feature is highly challenging to obtain with timber without layering. Thus, to realize such a structure in timber, the segmentation of members is a concern which would be addressed in joint and connection design phase.

These findings yield a notion of how much more hyperboloid lattice structures are subject to failures in global buckling compared to cylindrical ones given that helical members do extend a bit to reach circumferential members and buckling lengths increase. Notably, the present study underscores the need for further research to be conducted on lattice structures with shapes that deviate from the hyperboloid configuration. Alternative shapes such as 'negative hyperboloids' or barrel-shaped structures warrant investigation as they may possibly enhance the buckling load capacity of lattice configurations. In addition, current studies concerning the hyperboloid silhouette do not emphasise the narrowness or skewness and its effect on lateral stiffness after being subjected to horizontal loads.

Finally, Y. Zhang et al. (2009) systematically investigated lattice cylindrical shells with various core topologies in attempts to minimize the weight for a given stiffness or load carrying capacity. The results of this study reveal that the maximum specific stiffness of the Kagome lattice cylindrical shell is slightly greater than that of the triangular one. Furthermore, the axially loaded Kagome and triangular (diagrid) lattice cylindrical shells exhibit equivalently high load-carrying efficiency, which is substantially greater than that of the hexagonal lattice cylindrical shell. Various lattice topologies are presented in Figure 2.27. Evidently, the author solely focused on vertical load implementation.

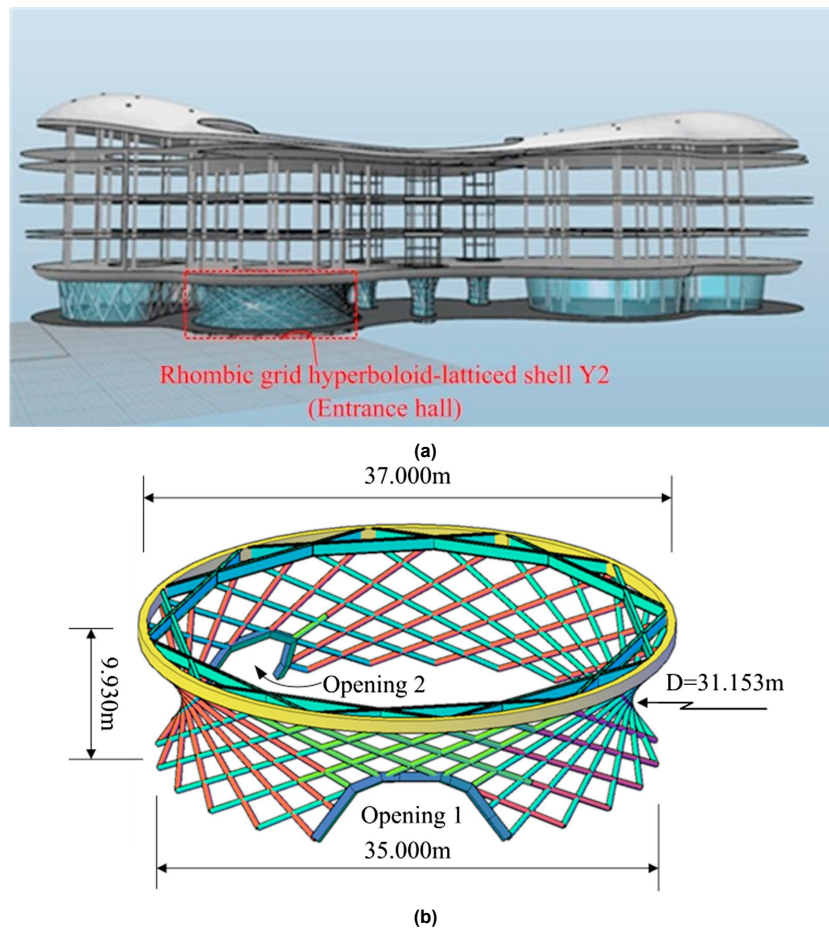


**Figure 2.26:** The load-bearing structure of the China Comic and Animation Museum (a) and the schematic illustration of the RGHS (b) (Guo et al. 2018).

## 2.4. Grid Structures

### 2.4.1. Patterns in Structural Design

For this graduation research project, it is of essence to approach and describe the element of pattern of the topology as it does define the principal behaviour of selected structural systems. The pattern, as specified by Oval (2019), can represent various structural elements, such as beams, walls or slabs. As the focus of this thesis is tied to the design of cylindrical towers, it is of essence to theoretically review the pattern and geometry of grid shells and vaults in general as these entities share similarities fundamentally, especially if the project focus shifts to segmented hyperboloid towers composed of discrete and separated members.

Grids and patterns can be utilized to enable the assembly and construction of the load bearing or cladding element systems. In these systems, the pattern can be composed from nodes, beams, ribs or voussoirs. It is of importance to realize that the final design of these patterns ultimately determine the overall structural performance, efficiency, ease of construction, manufacturing as well as costs (Oval 2019). Regarding the structural design, patterns are usually modelled to present the equilibrium of forces within the structure. Forces can be perceived as acting in full compression or full tension

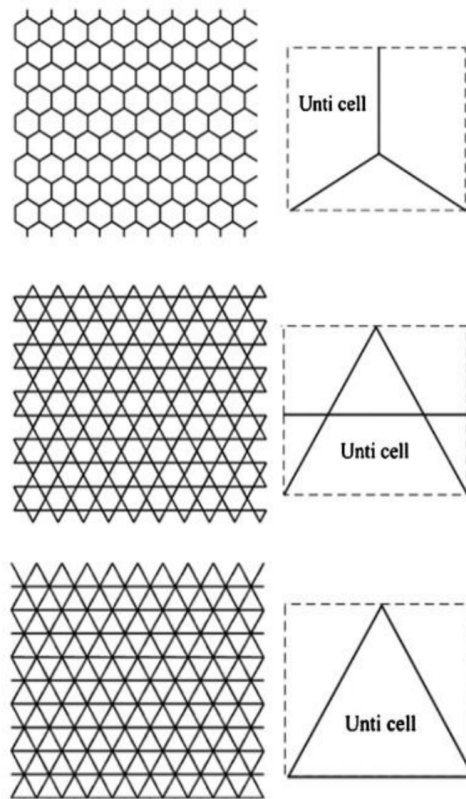


**Figure 2.27:** Configurations of three 2D lattice plates (from top to bottom): hexagonal, Kagome and triangular lattice plates (Y. Zhang et al. 2009).

throughout respective structural elements. For modelling purposes, various strategies can be employed to realize grid structures within given design space. Additionally, a strut-and-tie model was presented by Jorg Schlaich and Schafer (1991) as a design strategy to trace internal forces in complicated concrete details. This technique utilizes struts to represent concrete stress fields with predominant compression in the strut's direction while ties indicate areas of tensile reinforcement. Finally, Liew et al. (2018) detailed how they utilized the load-path of a thrust network to establish compression-only structures with doubly-curved shapes that have the least volume possible for a set of given boundary conditions such as point loads situated on a common plane. For example, a standard compression-only structure in a more real-life setting can be observed in Figure 2.28.

### 2.4.2. Tessellations

The world of tessellations is a vast field that explains the basic unit in a pattern. This element enforces logic, structure upon the pattern and therefore they can be identified by a high level of regularity. According to Schoenberg (2011), a way to define a tessellation is by dividing a space or plane into regions that are convex polygons. As it was previously proposed by geometers from centuries ago, the term has been associated with dividing the plane into regular polygons of equal size, whereas most sources now refer to tessellations as a technique that encompasses configurations of shapes that do not overlap, and also divisions of metric spaces. As tessellations are characterized by regularity in terms of the adjacency of their elements, they object to any unstructured patterns that exhibit irregularity in these



**Figure 2.28:** Trial gridshell, which is defined as a compression-only structure. It was built on a super-elliptical plan by Frei Otto in Essen, 1962 (Liddell 2015).

aspects. In terms of the taxonomy of this term, one can regard regular tessellations where each polygon is the same, where each face of the polygon corresponds to the same number of vertices within the tessellation. According to Grünbaum and Shephard (1987), there only three regular tessellations exist, and they are created using squares, equilateral triangles, or regular hexagons (Figure 2.29).

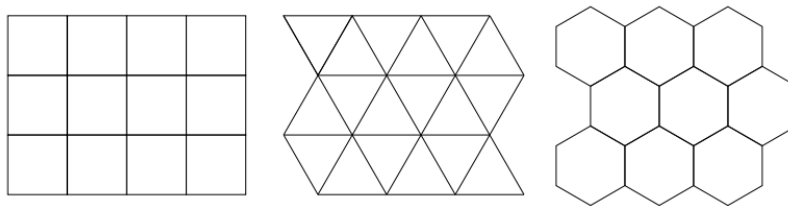


**Figure 2.29:** Three types of regular tessellations: rectangular, equilateral triangular and regular hexagonal (Cicerone et al. 2021).

On the other hand, semi-regular tessellations comprise two or more regular polygons that do not overlap in the tessellation space. As Grünbaum and Shephard (1987) highlighted, there are eight configurations of semi-regular tessellations as visualized in Figure 2.30. These combinations incorporate triangles, squares, hexagons. In addition, other shapes like dodecagons as well as octagons may be included.

For the reference project, one can be directed to view the Great Court Roof of the British Museum in London. This steel grid shell has a pattern that is based on a regular triangular tessellation (Figure 2.31b). By closely inspecting the structure, members are predominantly discretized and segmented by starting and ending at the joint. Triangular mesh renders each joint to accommodate 6 members, which adds to the complexity of the assembly of the structure. In terms of semi-regular tessellation applications, the Centre Pompidou timber grid shell in Metz, France exhibits a pattern composed of triangles and hexagons, more frequently in literature referred to as the Kagome pattern (Figure 2.31a). This grid shell retains continuity of its members (curved glulam sections). These beams are layered over each other and connected using dowels - quite a prevalent assembly technique in timber construction, as exemplified by the Mannheim Multihalle, designed by Frei Otto.

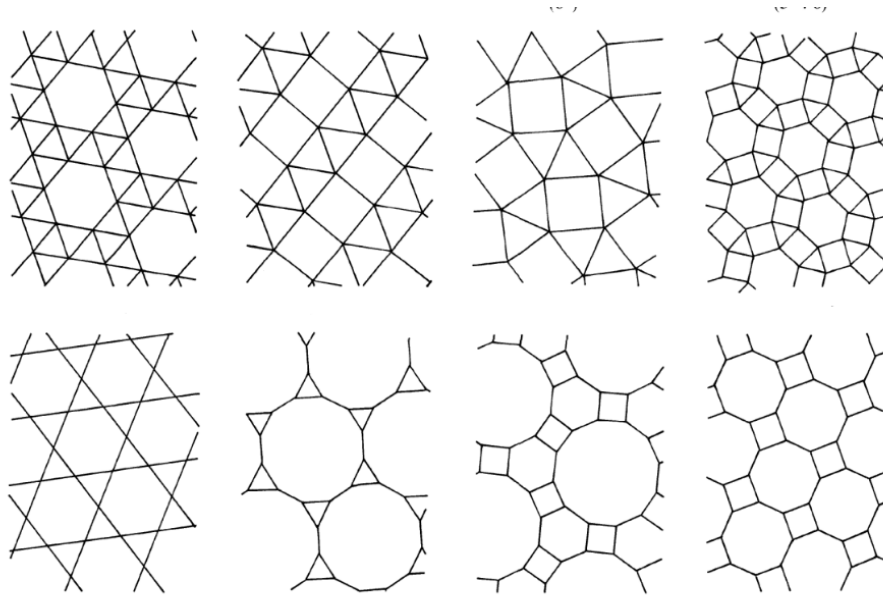


**Figure 2.30:** Eight types of semi-regular tessellations (Grünbaum et al., 1987).

When determining the mesh type to define a shell surface, the primary options to consider are either quadrangular or triangular types. Regarding its use in structural design, literature presents several advantages and disadvantages of both quadrangular and triangular mesh compositions when compared to each other. As it is theoretically presented, shell structures ideally should be able to carry loads without bending in surface elements only via tension and compression. When it comes to grid shells, according to Jörg Schlaich and Schober (2005), only configurations with triangular pattern can yield membrane forces to be transmitted purely as theory predicts (triangular elements are only subjected to axial compression or tension), which can be attributed to the stability of triangles. In contrast, quadrangle meshes are dependent on node and member bending capacities in order to transfer forces within the grid shell as portrayed in Figure 2.32. Thus, the lack of structural stability is offset by in plane bracing or stiff nodes. This characteristic is implemented in post and beam tower configurations to maintain its stability and omit joint necessity to exhibit rotational stiffness.

However, in terms of the practicality and manufacturing, According to Jörg Schlaich and Schober (2005), quadrangular mesh components necessitate considerably less machining since each node is connected to four edges, as opposed to six in triangular mesh components. This feature yields considerably lower costs associated with the construction of quadrangular grid shell structures. Additionally, as to what concerns visibility, the use of a quadrangular grid shell configuration allows for more daylight entry and imparts a sense of aesthetic lightness to the overall structure.

By going into the three dimensional realm, the tessellations can be extended into polyhedrons: a three-dimensional shape, distinguished by its flat, polygonal surfaces, straight sides, and distinct, angular vertices. There are many types of polyhedrons, the main ones are the following (Cromwell 1997):

- **Regular polyhedra** (Platonic solids): these are characterized by faces that are congruent regular polygons, with an equal number of faces meeting at each vertex.
- **Semi-regular polyhedra** (Archimedean solids): these consist of faces that are regular polygons,

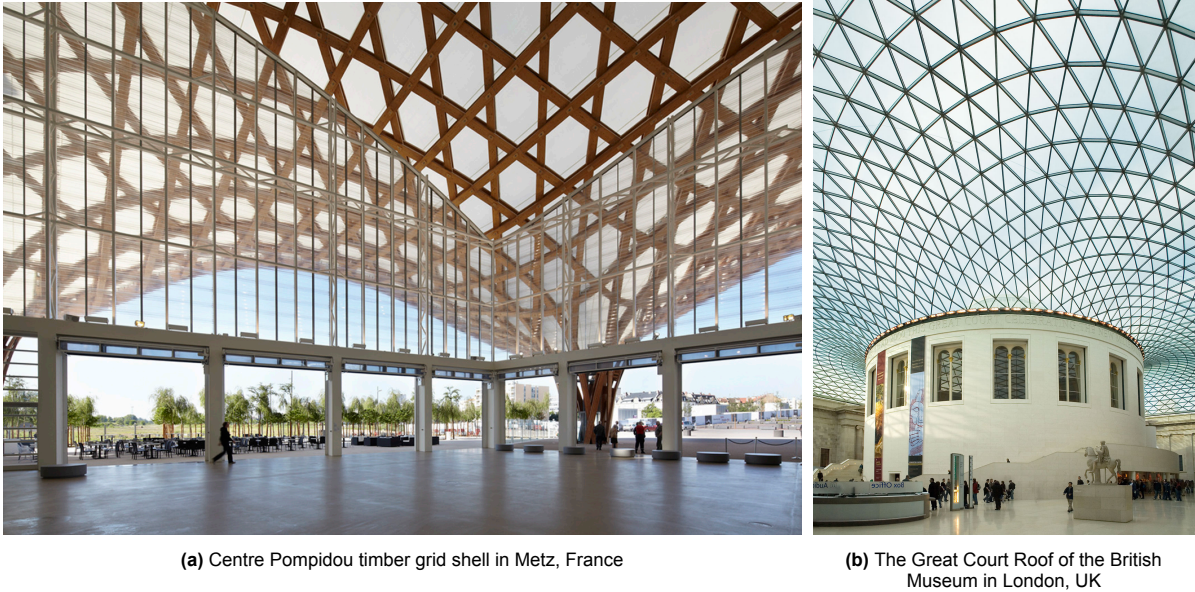


**Figure 2.31:** Regular and semi regular tessellation applications in practice.

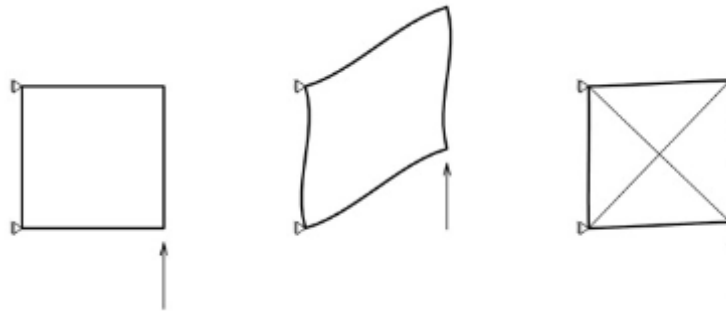


**Figure 2.32:** Deformation of a simply supported rectangle. It should be noted that forces are transmitted through member bending and nodal rotations. Triangulation (or introduction of diagonal bracing) ensure the structure is transmitting forces in a more efficient manner (compression and tension).

but more than one type of polygon is used, and the same arrangement of polygons meets at each vertex.

- **Prisms and antiprisms:** prisms have two congruent polygonal faces in parallel planes and rectangular faces joining them. Antiprisms are similar but have two sets of identical faces that are twisted relative to each other, and their other faces are triangles.

Figure 2.33 displays polyhedron types. In this research, as it was observed and related to hyperboloid towers, characterised by a diagrid (or triangular) topology, the relevant polyhedron is the antiprism (Figure 2.33d). As it was mentioned before, studies concerning structural stability and stiffness characteristics of these geometrical bodies whenever implemented in construction are quite limited, the forthcoming study shall delve into analyzing these specific aspects.

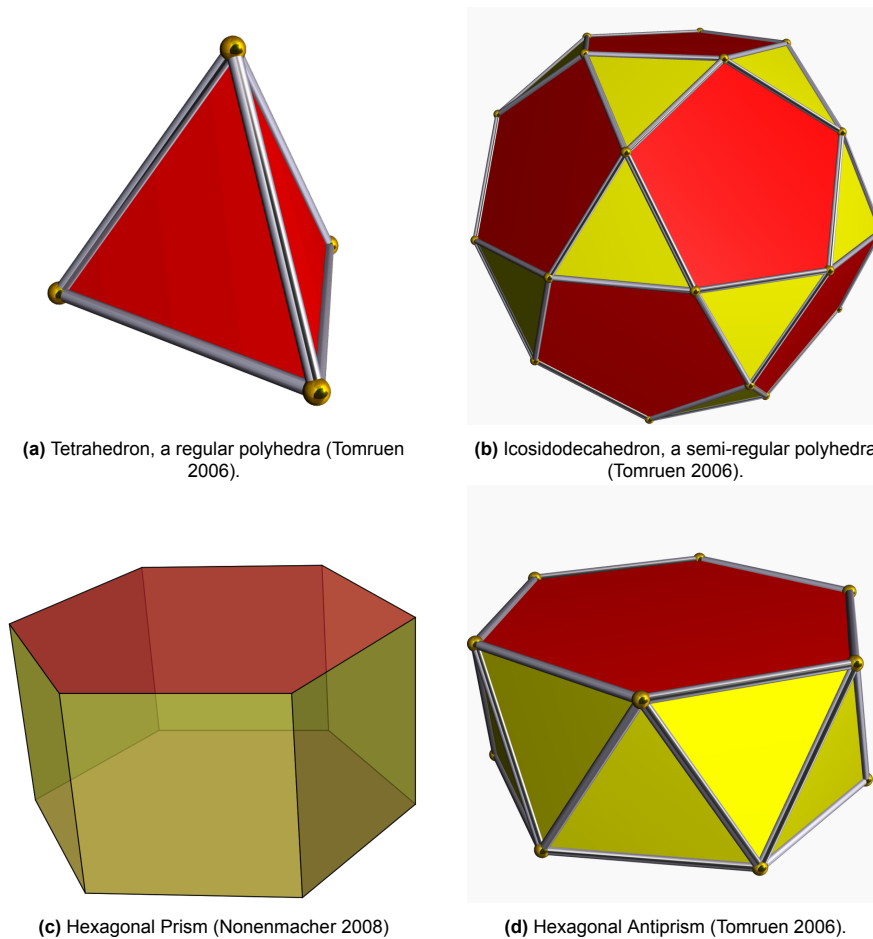


Figure 2.33: Polyhedras.

## 2.5. Kinematic Analysis of Grid Structures

Following the exploration of the realm of segmented hyperboloid structures and their relations to complex geometries, such as antiprisms, this inquiry delves into their stability analysis. The literature offers methodologies to understand and articulate the kinematic nature of various three-dimensional grid structures. Knowing the necessity to avoid any reliance on nodal rotational stiffness in the context of timber grid structures, the search for a self-sustained segmented kinematically stable hyperboloid structure becomes imperative.

For starters, it is of essence to approach the extended Maxwell's rule by examining the relationship between the number of bars ( $b$ ), the number of joints ( $j$ ), and the conditions under which the structure can either remain stable or exhibit flexibility. The classic Maxwell's criterion states that in order for 3D structures to be rigid (not too rigid and not too flexible) the number of bars  $b$  shall be equal to  $3j - 6$ . The first component in the last expression highlights the fact that in a three dimensional space, each joint has three degrees of freedom (translational displacements in  $x$ ,  $y$  and  $z$  axis). Thus, the structure in question is termed as statically determinate and stable whenever the number of constraints given by the bars is equal to the number of degrees of freedom while subtracting the six global rigid body movements (three translations and three rotations) that do not affect the internal stability of the structure.

For further categorization, given that the number of bars  $b$  is larger than  $3j - 6$ , the structure is termed as over-constrained, meaning that there are more bars than necessary for reaching stability. This scenario leads to states of self-stress, where certain members are experiencing either tension or compression even with external loads being absent. On the contrary, if the number of bars  $b$  is lower than  $3j - 6$ , the structure is rendered as not rigid and has mechanisms, or free movements due to insufficient number of members being present to constrain all the degrees of freedom. In this case, this configuration might lead to total collapse of the structure if not supported properly (Maxwell 1870).

However, the application of suggested equation does not always precisely predict the kinematic type of certain assemblies. Given the example in Figure 2.34, the satisfaction of the equation  $b = 6j - 3$  solely does not inform about the number of mechanisms or states of self-stress. In addition, for certain frames satisfying Maxwell's rule, an infinitesimal mode of deformation means there's a corresponding state of self-stress, which involves tension in the bars (Calladine 1978). Thus, more accurate methods are required to determine the kinematic nature of the structure.

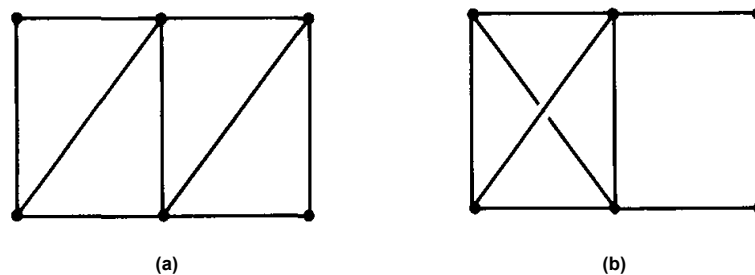


**Figure 2.34:** Two frames which satisfy Maxwell's rule  $b = 2j - 3$ : a simply stiff assembly (a) and a part redundant and part mechanism one (b) (Calladine 1978).

### 2.5.1. The singular value decomposition of the equilibrium matrix

According to the insights provided by Pellegrino (1993) on structural analysis, the equilibrium matrix (often denoted as  $\mathbf{A}$ ) of a pin-jointed truss, whether in two or three dimensions, encapsulates a wealthy array of invaluable information. Not only it could be utilized for the well established force method proposed by Przemieniecki (1968), but to also assess the static/kinematic nature of the structure. To provide the meaning behind the equilibrium matrix  $\mathbf{A}$ , this element typically establishes a connection between the vector  $\sigma$ , which denotes stresses in individual truss members, and the vector  $\mathbf{I}$ , representing generalized loads or global loads acting on the structure. The following indicates this relationship being as such (Pellegrino 1993):

$$A\sigma = I. \quad (2.1)$$

In essence, the equilibrium matrix  $\mathbf{A}$  shows geometrical relationships between each node, its adjacent connected members and the global coordinate system (x,y,z). Each node (except the ones connected to supports) contribute to the equilibrium matrix  $\mathbf{A}$ . Support nodes are not considered as support reactions imposed on these nodes are not part of the internal force matrix. A simple example can be provided in order to illustrate the innate idea that this matrix holds. Figure 2.35 shows a simple pin-jointed 2-D truss

with 2 pin-jointed supports. Knowing that only two nodes (B and C) are considered for the generation of **A**, three members in total (1, 2 and 3) are connected to them, thus, the size of the matrix shall be 4 x 3 (number of rows represent the node count per each coordinate while the number of columns - the member count). It should be noted that if a given assembly was constructed in a 3-D space, an additional z coordinate would yield an extra row per each node. As provided in Figure 2.36, the derived equilibrium matrix **A** provides information on the connection of a particular member to its corresponding node, considering both the angles of connection and the direction in which each member is facing.

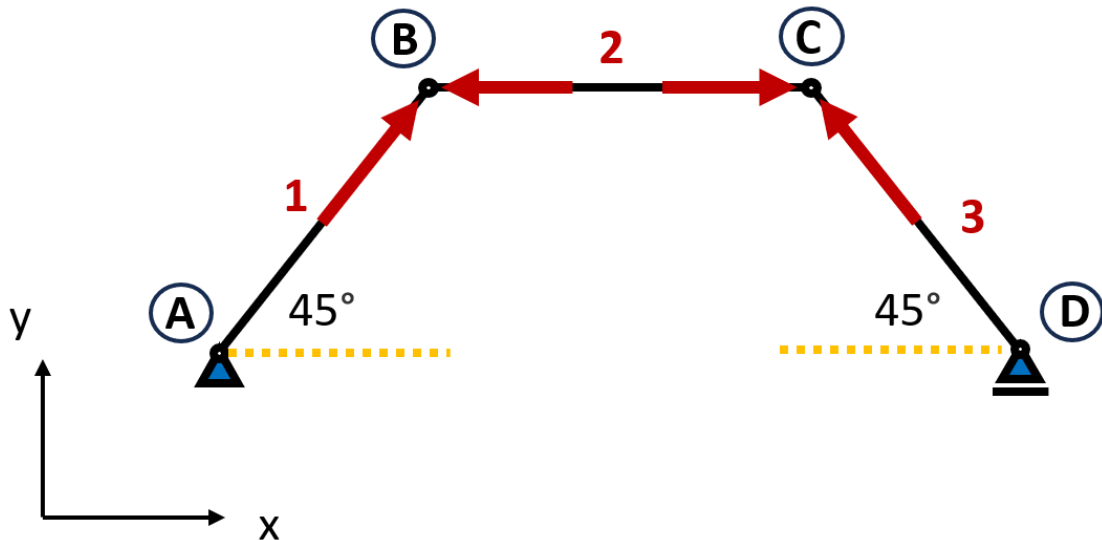


Figure 2.35: An example 2-D pin-jointed truss.

The utilization of Singular Value Decomposition (SVD) mathematical operation (more in detail described by Stewart (1973)) for an equilibrium matrix **A** proves instrumental in computing essential parameters that determine the behavior of structural assemblies. In essence, SVD is a technique in linear algebra employed to decompose a matrix into three simpler matrices. The key aforementioned parameters that are later derived from this operation are as follows:

*m* the number of independent zero-energy deformation modes.

*s* number of independent states of self-stress.

Structures that are associated with  $m = 0$  can be termed as *kinematically determinate*. Additionally, assemblies characterised by having  $s = 0$  are known to be *structurally determinate*. Parameter *m* and

	Member 1	Member 2	Member 3		Member 1	Member 2	Member 3	
$B_x$	$\cos(45)$	-1	0	=	$B_x$	0.7071	-1	0
$B_y$	$\sin(45)$	0	0		$B_y$	0.7071	0	0
$C_x$	0	1	$-\cos(45)$		$C_x$	0	1	-0.7071
$C_y$	0	0	$\sin(45)$		$C_y$	0	0	0.7071

Figure 2.36: Resulting equilibrium matrix **A** of a given 2-D pin-jointed truss presented in Figure 2.35.

s can be derived from presented equations as well as Figure 2.37:

$$m = n_r - r \quad (2.2)$$

$$s = n_c - r \quad (2.3)$$

Where:

$r$  the rank of the equilibrium matrix.

$n_r$  the number of rows in the equilibrium matrix

$n_c$  the number of columns in the equilibrium matrix

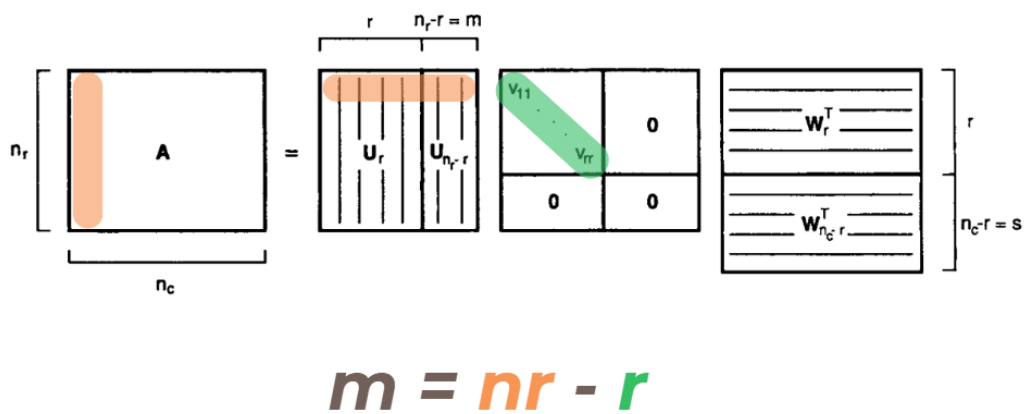


**Figure 2.37:** Graphical representation of the derivation of the kinematic mechanism variable  $m$  by subtracting the rank of the equilibrium matrix  $r$  from the number of rows  $n_r$ .

As stated by Pellegrino (1993) the concrete value of  $m$  does not matter so much as the fact whether it is non-zero in order to determine the nature of a pin-jointed truss. As regards the computation of SVD of the equilibrium matrix  $\mathbf{A}$ , the resulting three matrices are presented to be as such:

$$\mathbf{U} = [u_1, \dots, u_{n_r}] \quad \text{orthogonal matrix of size } n_r \times n_r.$$

$$\mathbf{W} = [w_1, \dots, w_{n_c}] \quad \text{orthogonal matrix of size } n_c \times n_c.$$

$\mathbf{V}$  diagonal matrix of size  $n_r \times n_c$ . This matrix has  $v_{ii}$  ( $i = 1, \dots, r$ ) on the leading diagonal, while the rest of the elements have zero values.

Coefficients  $v_{11}$  represent the singular values of the equilibrium matrix  $\mathbf{A}$ , while the vectors  $u_i$  and  $w_i$  are the  $i$ th *left singular vector* and the  $i$ th *right singular vector*, respectively. These three matrices result in such a way that satisfies the proposed expression:

$$A = UVW^T \quad (2.4)$$

According to the author's suggestion, matrices  $\mathbf{U}$  and  $\mathbf{W}$  can be divided into partitions. For ease of reference, it is found convenient to adhere to the following arrangement of sub-matrices:

$$U_r = [u_1, \dots, u_r], \quad U_{n_r-r} = [u_{r+1}, \dots, u_{n_r}] \quad (2.5)$$

and

$$W_r = [w_1, \dots, w_r], \quad W_{n_c-r} = [w_{r+1}, \dots, w_{n_c}] \quad (2.6)$$

The visual explanation of each resulting matrix from the SVD operation can be viewed in Figure 2.38.

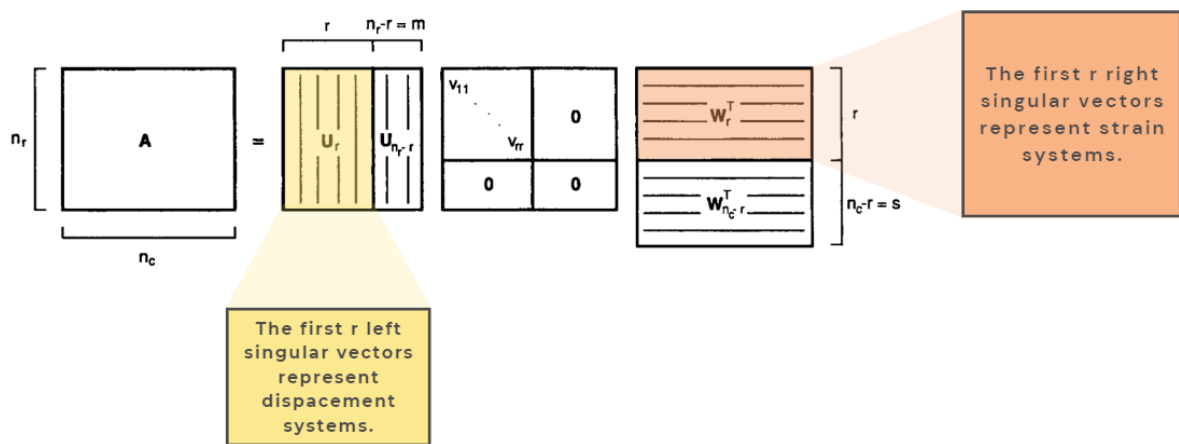


**Figure 2.38:** Graphical representation of the SVD of the equilibrium matrix  $\mathbf{A}$  along with highlighting the first  $r$  left singular vectors and the first  $r$  right singular vectors (Pellegrino 1993).

Whenever the SVD operation of the equilibrium matrix  $\mathbf{A}$  has been computed, the rank  $r$  has to be determined. It should be noted that for some computations, the number (which is  $\min(n_r, n_c)$ ) of non-zero elements in the matrix  $\mathbf{V}$  can seem to be non-trivial as some values in it can be of very small magnitude although not equal to zero. Some threshold  $\alpha$  can be established to delineate that values smaller than this proposed  $\alpha$  should not be contributing to the rank  $r$ . Thus, it is advised that for most structures the  $\alpha$  value should be set to  $10^{-3} \times v_{11}$ .

In terms of the physical interpretation provided by the output matrices, the first  $r$  equations assert that the first  $r$  left singular vectors represent displacement systems that align with the strain systems found in the corresponding right singular vectors, divided by their respective singular values. Consequently,  $r$  orthogonal sets of displacements are obtained with their corresponding orthogonal strains. The remaining  $m = n_r - r$  equations signify that the last  $m$  left singular vectors represent strain-free, or zero-energy, displacement modes. Finally, it can be indicated that the last few  $m$  left singular vectors are load conditions which the structure cannot react in its current layout. These last vectors, in essence, provide displacement coordinates for each node given the occurrence of a kinematic mechanism. For a visual explanation one should be referred to Figure 2.39. Thus, for retrieved values of  $m$  being non-zero, the corresponding structural assembly is known to have occurring kinematic mechanisms.

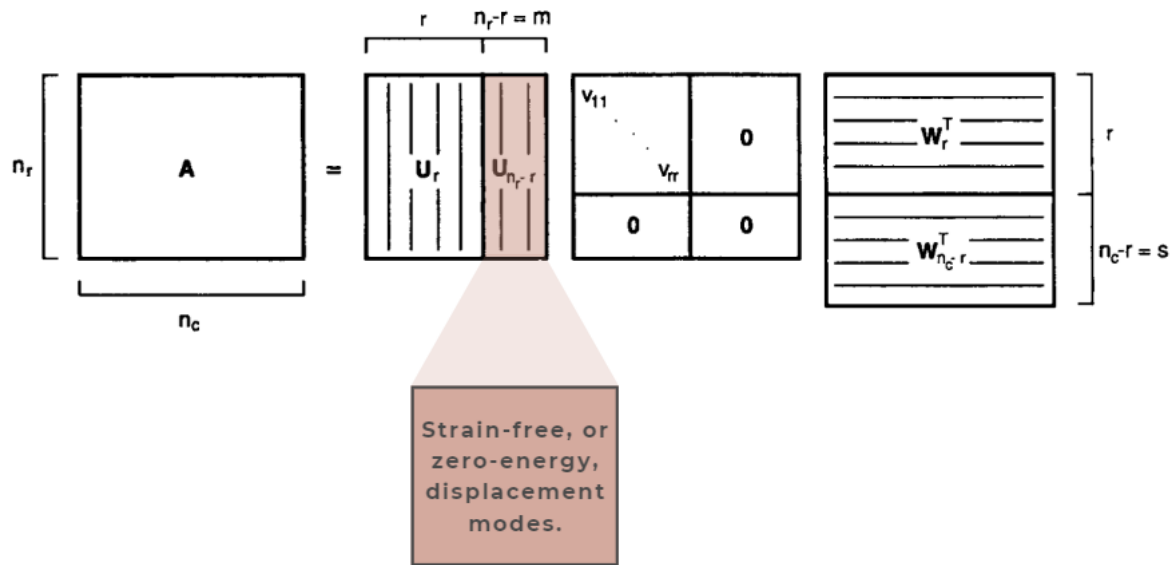


**Figure 2.39:** Graphical representation of the kinematic sense behind the parameter  $m$  and the remaining  $n_r - r$  equations which represent strain-free, or zero-energy, displacement modes. (Pellegrino 1993).

### 2.5.2. Graphic kinematics for 3D pin-jointed trusses

When evaluating assemblies for kinematic determinacy, it is of importance to elaborate on the analysis and elaborate on the information concerning the exact nodal displacement in instances of zero-strain deformation in the assembly (mechanisms). In this case, one shall refer to graphic statics that introduce more intuitive ways to realise and understand the nature of the truss structure. This method has been extensively studied and standardized in terms of the structural analysis of 2D and 3D trusses by the likes of Maxwell (1870) and Rankine (1864). To be more specific, Rankine introduced the *Principle of equilibrium of polyhedral frames*, asserting that forces exerted on a given point, which are both perpendicular and proportional to the areas of the faces of a closed polyhedron, are indeed in a state of equilibrium. As detailed by Akbarzadeh, Van Mele, and Block (2015) the stated polyhedral diagram of a given truss contains certain number of vertices, edges, faces and cells. The form (truss geometry) and force diagrams are thought to be dual if the following points are satisfied:

- Each edge of the form diagram corresponds to one and only one face of the force diagram.
- Each vertex in the form diagram corresponds to a closed polyhedral cell in the force diagram.
- Each open/closed polyhedral cell of the form diagram corresponds to one and only one vertex of the force diagram.
- Each bounded/unbounded face in the form diagram corresponds to one and only one edge in the force diagram.

The corresponding reciprocal force diagram conditions for a given node within a truss are displayed in Figure 2.40.

While the method proposed by Pellegrino (1993) for utilizing the equilibrium matrix and its Singular Value Decomposition (SVD) offers insights into the structural kinematics and statics within an analytical framework, an analogous methodology for achieving the same purely within the domain of geometrical

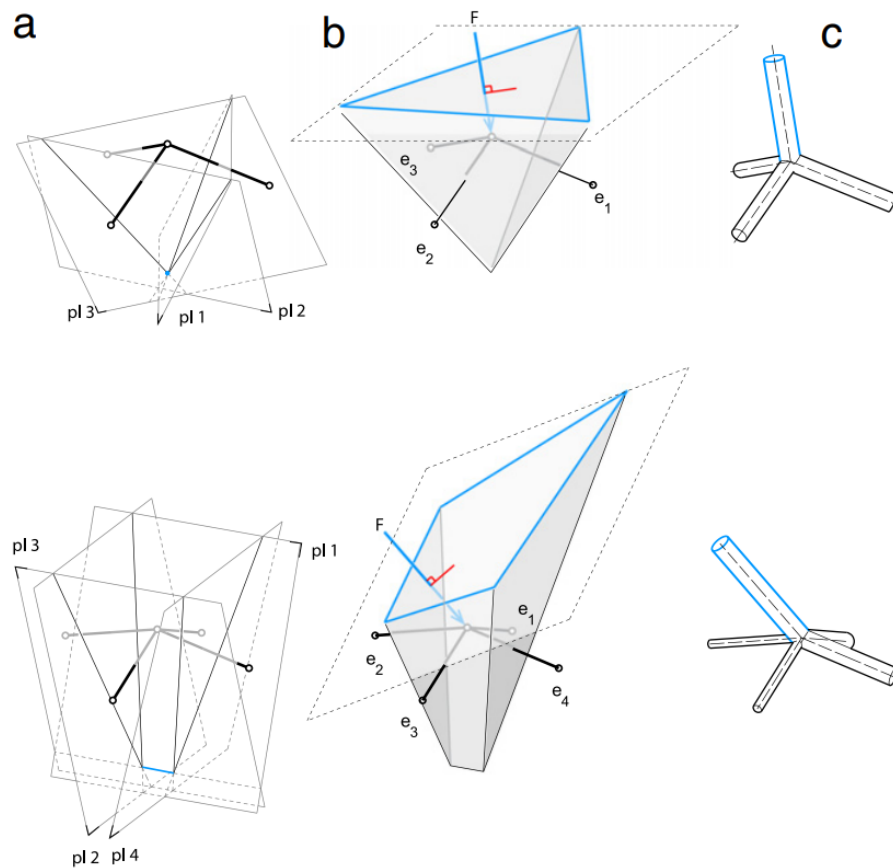


**Figure 2.40:** Two frames along with their reciprocal, polyhedral force diagrams. The face perpendicular to each bar and the applied force creates a closed nodal force cell indicating equilibrium. Lastly, the pipe diagram in c indicates the magnitude of each force within the bar and the force vector (Akbarzadeh, Van Mele, and Block 2015).

graphic statics was non-existent, until recently. According to McRobie et al. (2017), structural mechanisms become apparent when three-dimensional Rankine reciprocal force cells are translated in a way that allows their common faces to slide across each other without disconnecting. An example is displayed in Figure 2.41 that indicates a 'spoked cube' truss, which shows that there exists a number of infinitesimal mechanisms that cannot be termed as rigid body motions. In this case, the Rankine reciprocal is a spoked octahedron that can be viewed in Figure 2.41b that encapsulates 8 tetrahedra representing individual nodes within the spoked cube. Thus, in Figure 2.41c and Figure 2.41d it can be viewed that individual tetrahedra can be translated without their adjacent faces being separated within the same plane in relation to one another. Sliding blocks represent associated displacement vectors of representative nodes. In case some reciprocal cells slide with their adjacent faces separating, this would indicate that the movement is due to extension or contraction of some members and such a displacement would not be related to a kinematic truss mechanism.

Therefore, the review of analysis methods shall accompany the following research and assist in explorations that perhaps shall identify a segmented hyperboloid frame that is able to individually exhibit favorable stability and lateral stiffness characteristics.

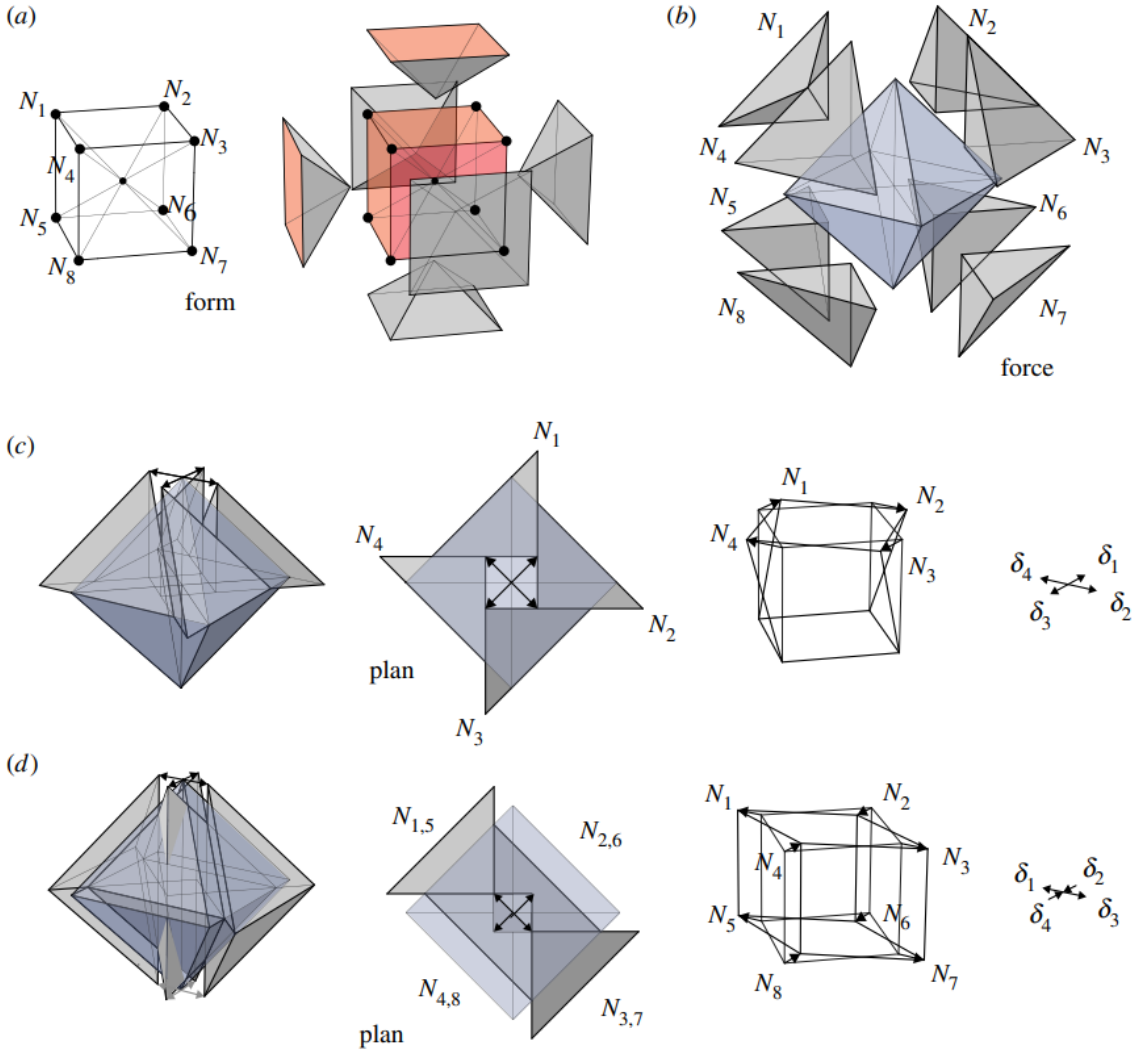


**Figure 2.41:** Two frames along with their reciprocal, polyhedral force diagrams. The face perpendicular to each bar and the applied force creates a closed nodal force cell indicating equilibrium. Lastly, the pipe diagram in c indicates the magnitude of each force within the bar and the force vector (Akbarzadeh, Van Mele, and Block 2015).

# 3

## Research Question and Objectives

### 3.1. Research Question

Stability aspects of antiprism structures are notably absent in existing literature. In addition, the effect of hyperboloid skewness on a tower's lateral stiffness, especially when facing non-uniform wind load profiles, remains a question unanswered according to studies reviewed. Finally, through a review on hyperboloid towers implemented in the last 100 years, this project questions the necessity of in plane stiff platforms, flexurally stiff rings and continuous vertical members as being pivotal to the stability and lateral stiffness of the global structure when subjected to non-uniform wind loads. By omitting the need of these elements and devising a tower structure self-sustained via its own through its external framework of grid elements, it is possible to significantly improve both the functional adaptability and the ease of construction.

Hence, by highlighting noted points, a research question can be formed:

***What are the hyperboloid lattice structure parameters that lead to the most favorable tower designs in terms of its stability, global (lateral) stiffness and adaptability under non-uniform wind loads?***

In order to answer this question, several objectives will lead the course of the research:

Design a preliminary tower geometry that entails geometrical design variables: the **curvature** of the global shape and **topology** (pattern):

- The 'Summum Engineering' project is focused on the examination of a timber lookout tower in the Netherlands, with a stature of 30 meters. The goal is to obtain a geometric model that will provide a comprehensive example for study, from which a structural model will be assembled and analysed. The design will feature both prism and antiprism geometries, described through diagrid and custom topologies. The basis of this study shall aim to analyse their stability and stiffness

characteristics. The important bit is to introduce geometrical variables that allow to adjust the global shape and its curvature (hyperboloid skewness) as well as density of the grid. In addition, the study will incorporate the introduction of circular, flexurally stiff circumferential rings as key structural elements next to segmented (polygonal) ones.

Assess the effect that the change in **topological parameters** might have on tower's **stability** and **stiffness**.

- The study will examine how antiprism and prism hyperboloid structures, defined by two topologies, react to non-uniform wind load profiles. By varying the density of the grid, the resulting stiffness and stability behaviour shall be documented and investigated.

Find the most optimal design in terms of **global lateral stiffness** whenever the **curvature** (hyperboloid skewness) of the tower silhouette is adjusted:

- Investigate the curvature and its effect on lattice structure's global (lateral) stiffness. Achieve the most suitable curvature of the lattice tower that would provide the most material efficient design variant.

Find the most optimal design in terms of **stiffness** and **ultimate limit state** requirements whenever the **member size** distribution within the tower structure is adjusted.

- Finally, an optimal distribution of member sizes is set to be determined, ensuring adherence with the criteria for structural strength and stiffness. This feature is anticipated to result in a tower design that ultimately satisfies established building standards. The aim is to gain insights into optimization methodologies that can be utilized to determine optimal sizes of structural members and to understand how the distribution of certain members along the skeleton of the structure affects the overall stiffness and strength.

After creating a lattice structure that has been fully optimized by taking into account curvature, topology, and member size variables, the focus shifts towards gaining insight into how the **lateral stiffness** and the **final tower geometry** is affected by the design of **connections** within the structure.

- Gain understanding of joint stiffness parameters and transmit this knowledge into the optimized structure as another variable to be adjusted. Learn about the way this parameter influences the structure in terms of global (lateral) stiffness and attempt to find most suitable lateral stiffness that would still satisfy global serviceability limit state requirements. Questions regarding the possibility of achieving feasible connection given the pre-determined tower geometry shall be raised too. Ultimately, if resources allow, attempt to provide a preliminary connection design containing achieved stiffness and required strength parameters.

# 4

## Parametric Framework

This chapter reviews the methodology in more depth with discussing the tools employed and their roles within the overarching context of the study.

### 4.1. Software to be utilized

#### 4.1.1. Grasshopper

'Grasshopper 3D' (or just 'Grasshopper') which was developed by David Rutten at Robert McNeel Associates, serves as an intuitive visual programming language integrated into the Rhinoceros 3D CAD software. It offers a user-friendly interface for complex design variants and modeling tasks (Tedeschi 2011). Visual programming has been increasingly becoming a vital tool within the realm of Civil Engineering, whether that would entail utilizing 'Grasshopper' or 'DynamoBIM' (an 'Autodesk' parametric design feature). These tools are leading the charge as ways for engineers to provide and analyze more intricate geometries with a higher rate of iterations and adjustments made via introductions of variables.

For this project, the parametric applicability seems of essence as the tower entails a more complex geometry to be realised. Iterations that reflect design changes adhering to performance criteria and standards can be executed efficiently, with the entire design space responding to modifications in near real-time. With 'Grasshopper' programming language, the geometry of the tower is generated by way of lines and nodes at which they are connected. The global configuration of the tower could be altered by adjusting design parameters which shall be defined in later subsections of the report.

#### 4.1.2. Karamba3d

'Karamba3D' is a plug-in integrated into Grasshopper environment. It facilitates structural analysis through the Finite Element Method (FEM). This method is extensively employed in engineering to address complex issues by breaking down a vast system into smaller, more manageable units known as

finite elements. The development of this tool is a collaborative effort involving a team of architecture and engineering enthusiasts, working in conjunction with Bollinger+Grohmann.

For this project, 'Karamba3D' tool shall serve as a mean to create a structural design assessment space that would allow to define model's physical parameters relating to material of choice, dimensions of members, support, joint and loading conditions etc. Additionally, the software shall yield relevant performance results that inform about the total mass, global displacements, on-going stresses as well as forces within members. A typical 'Karamba3D' set-up that has been utilized by Johan et al. (2019) to design a simple truss is presented in Figure 4.1.

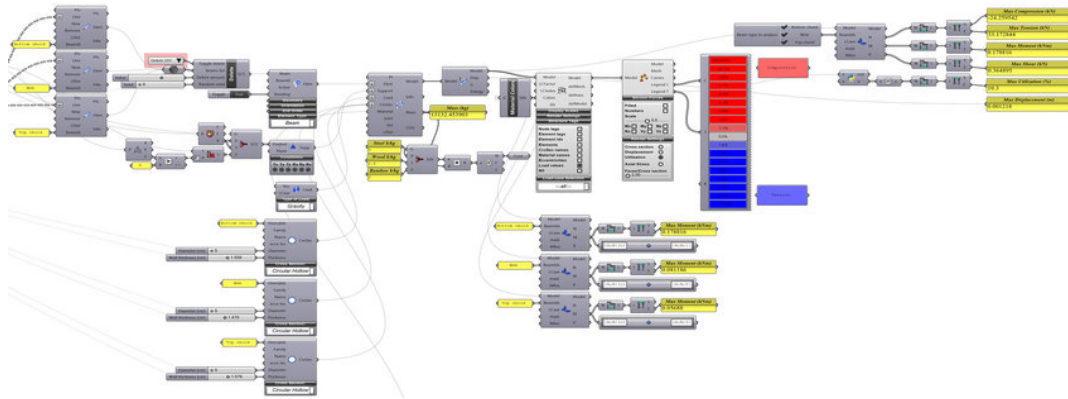


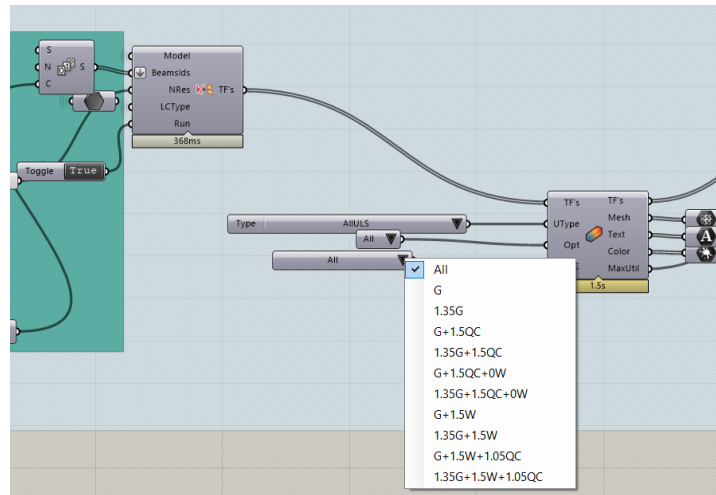
**Figure 4.1:** A typical 'Karamba3D' set up involving the provision of geometry, definition of member cross-sections, material in use, loading, support and joint conditions. Additionally, the script is able to provide maximum bending moment, shear, normal forces as well as critical stress among all members.

### 4.1.3. Beaver

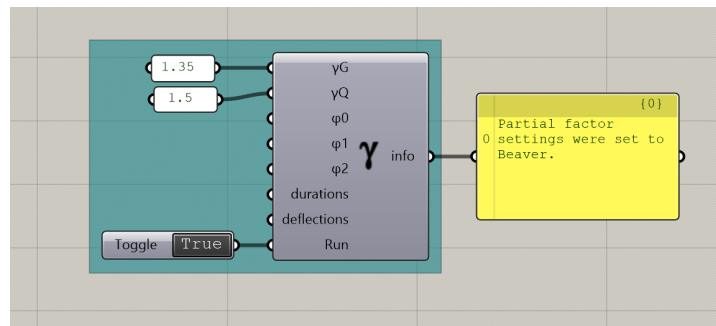
While a plethora computational tools exist for managing intricate geometry, timber engineering design still faces challenges in the interdisciplinary design-to-production process, particularly concerning data exchange as described by Apolinarska (2018). Beaver, a Grasshopper plug-in, has been developed to analyse and determine the necessary safety of structural elements according to Eurocode 5. This tool assists in designing viable timber-framed structures and facilitates the exploration of optimal solutions in terms of topology, aesthetics, and overall structural performance (Prandini, Pini, and Souza 2023). More precisely, the plug-in allows to define elements and their span lengths, buckling lengths, service classes and other necessary parameters needed for standard assessment of the structure. Additionally, working in conjunction with Karamba3D plug-in, Beaver allows to generate load combinations in accordance with equations (1.9) and (1.10) with specific values  $\gamma_G$  as well as  $\gamma_Q$  as referred in EN 1990, cl. 6.4.3.2(3) and cl. A1.3.1. Safety factors are easily manipulated and adjustable to the ones dictated by the standards as portrayed in Figure 4.2.

A representative output showing the Ultimate Limit State (ULS) behaviour within a sample structure is displayed in the accompanying Figure 4.4a, highlighting areas corresponding to members with strength parameters exceeding permissible limits. Furthermore, the plug-in is able to recognise the specific mode or type of failure which might fall into one of the categories as standardized and detailed in Eurocode 5. Those categories are visualized for a sample structure in Figure 4.4b and are as follows:

- ULS: Tension parallel to the grain.



(a) 'Beaver' plug-in component 'TimberFrameView', which takes in load combinations for ULS analysis as presented.



(b) 'Beaver' plug-in component 'CombinationSettings', which sets partial factor values in relation to combination factors.

**Figure 4.2:** 'Beaver' plug-in provides the user a functionality to re-adjust partial load factors in relation to combination factors. In this case, presented outputs are relating to ones details in EN 1990, cl. 6.4.3.2(3) and cl. A1.3.1.

- ULS: Compression parallel to the grain.
- ULS: Biaxial Bending.
- ULS: Shear.
- ULS: Torsion.
- ULS: Combined Tension and bending.
- ULS: Combined Compression and bending.
- ULS: Flexural Compression Buckling.
- ULS: Lateral Torsional Buckling.
- ULS: Combined shear and torsion (not ECS).
- SLS: Instantaneous deflection.
- SLS: Net final deflection.
- SLS: Final deflection.

To reflect the assessment in terms of the ULS, a comprehensive reports are generated and provided by the plug-in. These documents itemize the calculations for each structural member, associating them with their respective failure categories as outlined previously. A sample from the report is given in Figure 4.3.

```

{0;0}
0 Tension along the grain acc. to EC5 6.1.2 | N = 0.00; sigN = 0.00; Kmod = 0.90; Ym =
1.25; ft0d = 14.04; R0 = 0.00
1 Compression along the grain acc. to EC5 6.1.4 | N = 0.00; sigN = 0.00; Kmod = 0.90; Ym =
1.25; fc0d = 17.64; R1 = 0.00
2 Bending acc. to EC5 6.1.6 | Wy = 0.01; Wz = 0.02; fmk = 32.00; Myd = 0.00; Mzd = 0.00;
sigMy = 0.00; Kmod = 0.90; Ym = 1.25; fmd = 23.04; Km = 0.70; R2y = 0.00&R2z = 0.00
3 Shear acc. to EC5 6.1.7 | kcrit = 0.67; Vy = 3590.55; Vz = -4214.15; A = 0.22; sigVy =
0.02; sigVz = -0.03; R3y = 0.01&R3z = 0.01
4 Torsion acc. to EC5 6.1.8 | ; It = 0.01; Kshape = 1.11; Mt = 0.00; sigMt = 0.00; Kmod =
0.90; Ym = 1.25; fvd = 2.52; R4 = 0.00
5 Combined Bending and Axial Tension acc. to EC5 6.2.3 | A = 0.22; Wy = 0.01; Wz = 0.02;
Nd = 0.00; Myd = 0.00; Mzd = 0.00; sigN = 0.00; sigMy = 0.00; sigMz = 0.00; Kmod = 0.90;
Ym = 1.25; ft0d = 14.04; fmd = 23.04; Km = 0.70; R5y = 0.00&R5z = 0.00
6 Combined Bending and Axial Compression acc. to EC5 6.2.4 | A = 0.22; Wy = 0.01; Wz =
0.02; Nd = 0.00; Myd = 0.00; Mzd = 0.00; sigN = 0.00; sigMy = 0.00; sigMz = 0.00; Kmod =
0.90; Ym = 1.25; fc0d = 17.64; fmd = 23.04; Km = 0.70; R6y = 0.00&R6z = 0.00
7 Compression or combined Compression and Bending acc. to EC5 6.3.2 (buckling about both
axes considered) | A = 0.22; Wy = 0.01; Wz = 0.02; Nd = 0.00; Myd = 0.00; Mzd = 0.00;
sigN = 0.00; sigMy = 0.00; sigMz = 0.00; ly = 5.47; lz = 5.47; ry = 0.12; rz = 0.16;
lampi = 0.01; lamy = 47.39; lamz = 34.47; lamyrel = 0.71; lamzrel = 0.51; ky = 0.77; kz =
0.64; kyc = 0.93; kzc = 0.97; Kmod = 0.90; Ym = 1.25; fc0d = 17.64; fmd = 23.04; Km =
0.70; R7y = 0.00&R7z = 0.00
8 Bending or combined Bending and Compression acc. to EC5 6.3.3 (lateral torsional
buckling considered) | A = 0.22; Wy = 0.01; Wz = 0.02; Nd = 0.00; Myd = 0.00; Mzd =
0.00; sigN = 0.00; sigMy = 0.00; sigMz = 0.00; ly = 5.47; lz = 5.47; ry = 0.12; rz =
0.16; lampi = 0.01; lamy = 47.39; lamz = 34.47; lamyrel = 0.71; lamzrel = 0.51; ky =
0.77; kz = 0.64; kyc = 0.93; kzc = 0.97; ltb = 5.47; lefy = 5.47; lefz = 5.47; sigMcrity =
1207.28; sigMcritz = 464.41; lammy = 0.16; lammz = 0.26; kcrity = 1.00; kcritz = 1.00;
Kmod = 0.90; Ym = 1.25; fc0d = 17.64; fmd = 23.04; Km = 0.70R8y = 0.00&R8z = 0.00
9 Combined Torsion and Shear - Not specified in EC5 (Maximum Shear Utilization Ratio +
Torsion Utilization Ratio) | R9 = R3max + R4 = 0.01

```

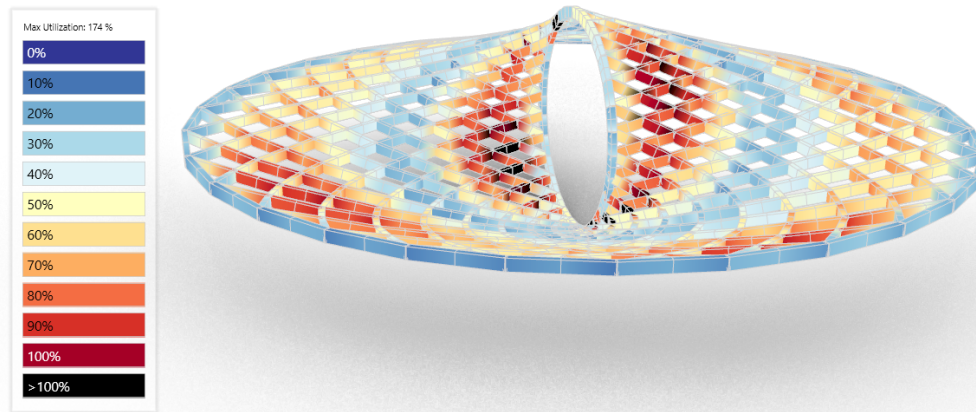
**Figure 4.3:** In case of ULS assessment, Beaver plug-in is able to provide report for calculations in accordance with Eurocode 5.

This plug-in, however, is not without limitations. At the moment, it is noted that the SLS utilization values, at present, do not yield precise deflection measurements in millimeters, while the output is limited to unity checks with values between 0 and 1. Additionally, SLS assessment is only limited to the corresponding mean values acquired from the Table 7.2 found in Eurocode 5, thus, global displacement assessment is not part of the software's analysis workflow. For this aspect, one is left to rely on stiffness and global displacement results obtained through 'Karamba3D' plug-in. It is also worth mentioning that the plug-in is only limited in taking trapezoidal timber cross-section and does not support deviations such as circular cross-sections.

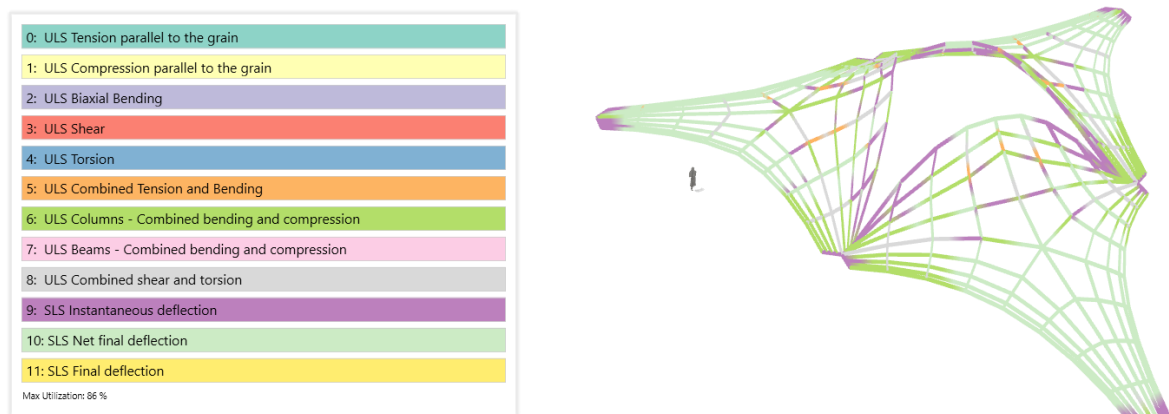
Coordination with developers of the 'Beaver' plug-in aimed to identify and refine these values for a more comprehensive structural assessment of timber assemblies. Despite these aspects, the plug-in and its outputs are known to be valuable in the later stages of this research, offering a standardized approach and providing the most representative results alongside a comprehensive report.

#### 4.1.4. Ansys FEA

'Ansys FEA' is a computer-aided engineering simulation tool utilized to analyze and predict how defined geometries of pre-determined material react to forces, vibration, heat, fluid flow effects. For this project, software's functionality concerning linear, non-linear analysis of structural elements in order to determine internal stresses, deformations and stability characteristics (buckling) is of essence. The Finite Element Method (FEA) is incorporated in this software. This process allows to discretize the structural element into smaller elements (known as finite elements) and through employment of differential equations each element is assessed individually. This is followed by combining all these elements and their solutions into a coherent system and observing how it reacts to pre-determined boundary conditions as well as external effects. FEM is highly versatile and may be employed for analyzing more unconventional and complex geometries and shapes (ANSYS, Inc. 2023).



(a) 'Beaver' plug-in component 'TimberFrameView' output indicating members with different strength capacity in relation to ULS guidelines provided by Eurocode 5 (Prandini, Pini, and Souza 2023).



(b) 'Beaver' plug-in component 'VisualizeCriticalCheck' output indicates members and categorises them according to potential failure modes they may encounter (Prandini, Pini, and Souza 2023).

**Figure 4.4:** 'Beaver' plug-in provides the user a functionality to re-adjust partial load factors in relation to combination factors. In this case, presented outputs are relating to ones details in EN 1990, cl. 6.4.3.2(3) and cl. A1.3.1.

#### 4.1.5. IDEASTatiCA

For more conventional geometries and especially those of connections involving steel and timber elements, IDEASTatiCa emerges as a viable tool. Its function allows for a detailed examination of the connections' performance under diverse load scenarios, while also guaranteeing adherence to standards and regulations. Given the use of timber elements in this project, 'IDEASTatiCa' can be utilized to explore and realize steel - timber joints through implementation of welded or bolted plates. Detailed reports including stiffness and buckling characteristics can be retrieved as well (IDEA StatiCa 2023).

## 4.2. Developing geometry and parameters

The development of the global geometry. Presentation of triangular and custom topology, highlighting governing geometrical parameters and illustration of tower design taxonomy.

### 4.2.1. Curvature

The curvature of the tower defines the global shape that the assembly takes and how much it resembles the hyperboloid or a cylinder. For the generation of geometry, the control points have to be acquired. These points serve as connectivity vertices lines. In order to obtain these geometrical elements, the following steps are taken:

1. Sketch two circles: the first one at the bottom symbolizes the tower's ground level, and the second one above represents the highest platform. The bottom circle has a radius of 8 meters, and the top circle's radius is 6 meters. The vertical distance between two rings is 30 m, which reflects the actual height of the structure (Figure 4.5a).
2. Draw a connecting line between two circles. Take the midpoint in it and offset it by a certain distance at a right angle from the curve towards the centre of each circle. This distance is to be referred from now as the curvature  $C$  parameter, which is quantified in meters. This is followed by drawing an arch which goes through the start and end points of the connecting line as well as the offset point. In Figure 4.5b the green line indicates this distance. Negative  $C$  values indicate a narrowing hyperboloid, while  $C = 0\text{ m}$  means that the arch has become the connecting curve and the shape of the tower exhibits a cylinder.
3. By taking the arch and rotating it certain times around the centre point at the base, a hyperboloid frame is achieved (Figure 4.5c).
4. By dividing each arch into a certain number of segments (which is effectively the number of platforms in the structure) and taking start and end points of those segments, control points (or vertices) are obtained (Figures 4.5d and 4.5e).

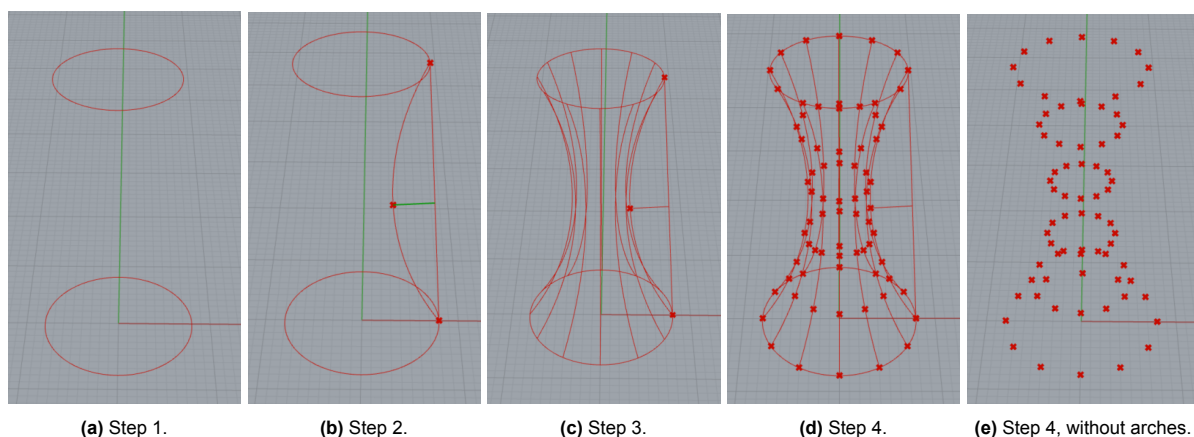


**Figure 4.5:** Steps to be taken in order to retrieve control vertices of the tower.

The acquisition of control vertices allows the designer to define the connectivity and distribution of lines that ultimately define the topology of the grid structure.

## 4.2.2. Topology

### Triangular pattern

The initial design topology adopted for the tower is triangular. The choice for such a configuration is relevant as this specific pattern has been researched within the context of lightweight hyperboloid lattice structures by Y. Zhang et al. (2009) and results were promising in terms of strength and stiffness capacities. In contrast to hyperboloid timber towers that were reviewed in Chapter 2, this configuration relies on segmented vertical members that do not span undisturbed from the bottom to top ring. From the first glance in Figure 4.7, the resulting three dimensional geometrical shape is that of a pentagonal antiprism. Thus, this research gives a valuable opportunity to explore stiffness and stability characteristics of this geometrical body.

The pattern is presented in 2D space in Figure 4.6. In order to apply this configuration within the hyperboloid geometry of the tower, at each level vertical members are erected at an angle and connected via ring (circumferential) elements as displayed in Figure 4.7. An additional point to consider is the introduction of curved circumferential members instead of the segmented ones. This design choice is inspired by examples in hyperboloid tower construction, such as those by Shukov and The East Strand Tower. These structures exhibited that curved, flexurally stiff rings can indeed substantially enhance stability by preventing any free kinematic nodal motion. However, the question of how and to what degree these curved members affect the tower's overall resistance to sideways forces, like wind, remains open. This presents a valuable opportunity to investigate their impact on the tower's lateral stiffness.

It is of essence to highlight another geometrical variable determining the structure's topology, known as the shape factor, indicated by  $N$ . This variable represents the number of vertices that connect diagonal members within the ring (or the number of sides given that the ring is segmented and polygonal). The tower in Figure 4.7 is, for instance, characterised by the shape factor  $N = 5$  and curvature  $C = -3.5 m$ .

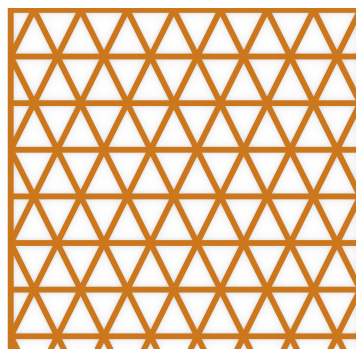


**Figure 4.6:** Triangular (or diagrid) pattern. Circumferential members can be identified as those currently taking a horizontal direction.

### Custom made pattern

To create the custom pattern that characterizes the tower and its structural elements, the linear components and their connections to control points are adjusted in the 'Grasshopper' algorithm. This pattern

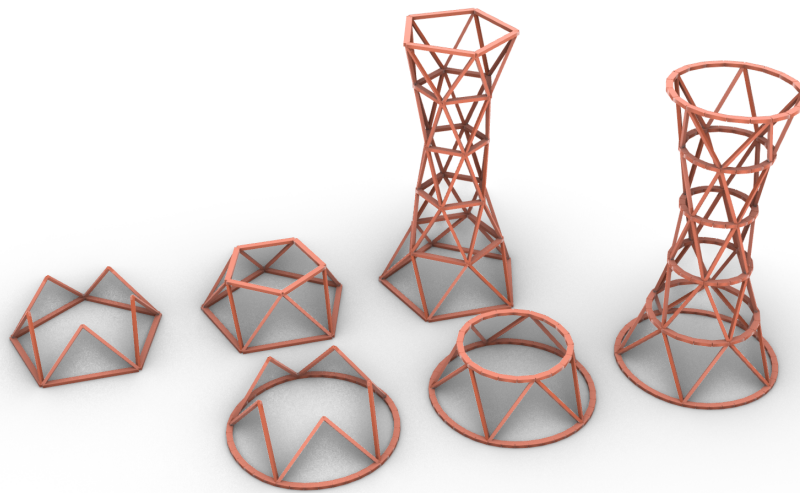


**Figure 4.7:** The logic behind the development of triangular (diagrid) pattern for both segmented and curved (circular rings).

(Figure 4.8) aims to emulate the post and beam configuration observed in Chapter 2. Thus, by employing vertical posts, horizontal beams and diagonal bracings, the tower with segmented rings can be realized as portrayed in Figure 4.9. In addition, the structure employs curved rings, similarly as it was done for towers characterised by the triangular (diagrid) topology. From the first glance it is evident that this configuration is representative of a regular prism as sides are connecting ring vertices while being parallel to each other. At the outset, the prism is characterized by its rectangular side faces. The resulting quadrangular mesh would mean that there is a dependency on node and member bending capacities in order to transmit forces within the tower, which is a highly unfavorable for timber structures. Thus, in plane bracing is provided by diagonal members.

This is the second pattern to be employed upon the tower structure and it is done so to conduct a comparative study in relation to assemblies employing the triangular topology and draw insights into the stability of such structures, which seems to exhibit no kinematic behaviour based on observed structures in Chapter 2. In Figure 4.9, the tower presented is defined by geometrical variables  $N = 5$  and  $C = -3.5 m$ . In order to grasp the relationship between the shape factor  $N$  and curvature  $C$ , Figure 4.10 displays a taxonomy of hyperboloid towers designed with a custom topology, classified by these two essential parameters that whose influence will be studied throughout this project.

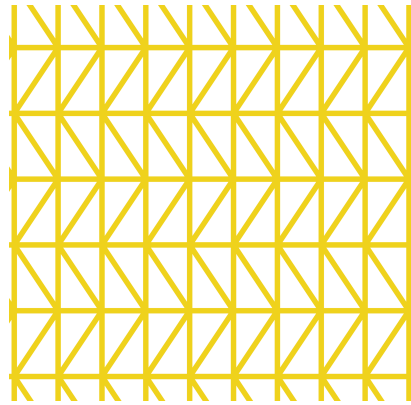


**Figure 4.8:** Custom made pattern.

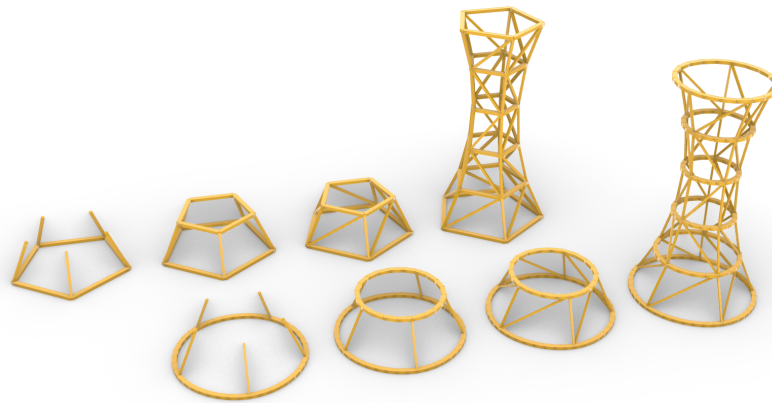


**Figure 4.9:** The logic behind the development of custom pattern for both segmented and curved (circular rings).

## 4.3. Structural model

This section discusses the definition of the structural model of towers following both proposed topologies. The material of choice throughout the structural analysis for the tower is taken to be GL28h. This material is a glued-laminated timber with 40 mm lamination thickness, which shall be assumed throughout the analysis process. Additionally, for the current stage, all members are taken to be rectangular in their cross-section.

### 4.3.1. Joints and degrees of freedom

This section discusses the definition of the structural model of towers following both proposed topologies. As what relates to detailing of nodes and joints of the tower, the structure is assumed to be fully hinged, which means that degrees of freedom related to rotations around local element z and y axes is released. Such a joint definition is relevant for towers characterised by segmented rings. However, when incorporating curved circumferential elements, each element is taken to be fully fixed to another

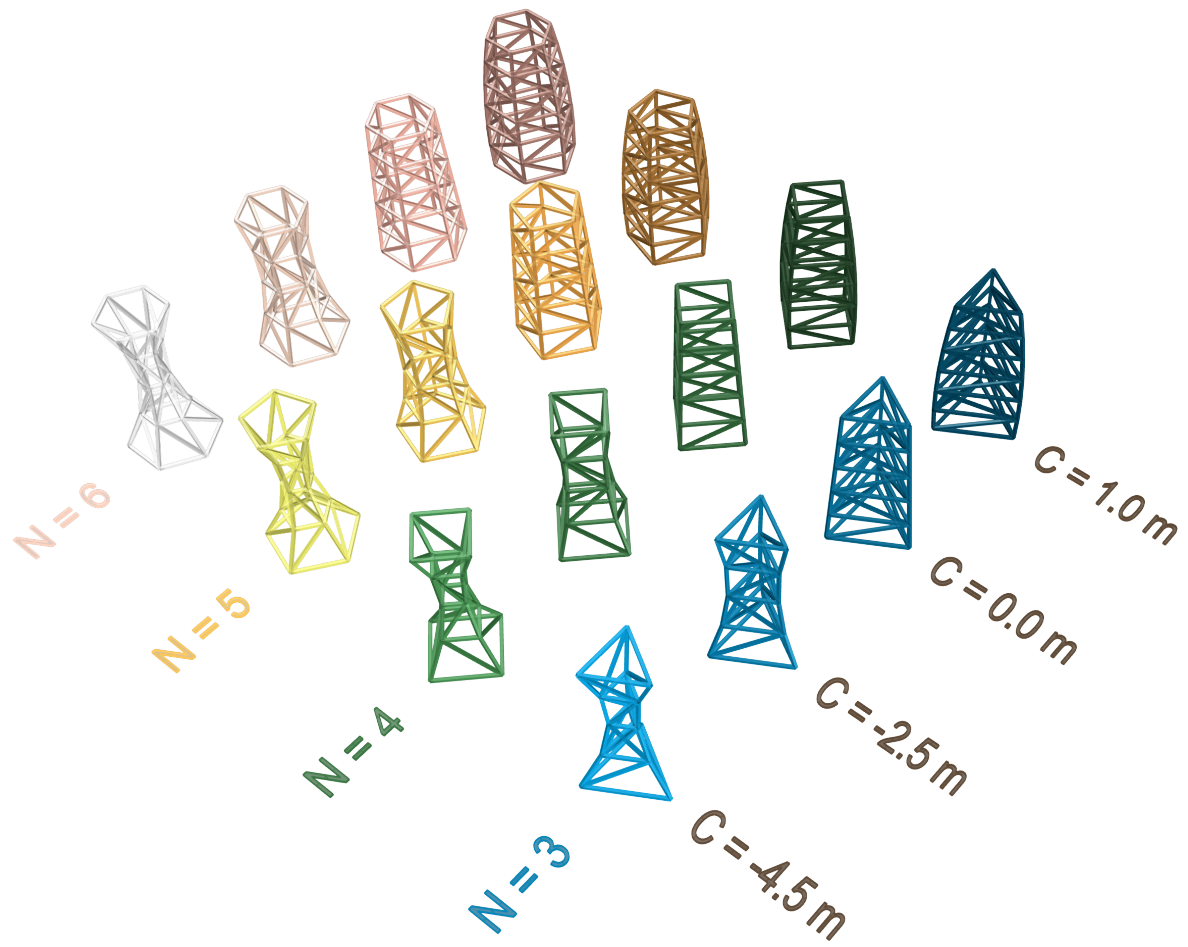


**Figure 4.10:** The taxonomy of tower variants following custom topology. It categorizes these towers by two critical dimensions: the shape factor, indicated by  $N$ , which refers to the count of vertice (or sides) within the ring, and the curvature, symbolized by  $C$ , that measures the tapering of the hyperboloid structure.

curved circumferential element, forming a solid glulam ring. In that case, degrees of freedom linked to rotation around all axes for circumferential elements attached to one another are constrained. A fully hinged cylindrical lattice tower is of great benefit knowing that the steel timber connection design would be requiring to consider the occurrence of moments within the joint. The development of moments within the solid ring would not be an issue as well knowing that no connections are needed in between each and every curved circumferential element. Figure 4.11 displays two possible variants of the triangular configuration: all straight ring elements and all curved (solid) ring elements. These three variants will be analysed and tested against proposed permanent, wind and live load combinations in the further stages of the research. One should bear that no active bending occurs in curved (solid) ring elements.

### 4.3.2. Wind loads

Wind load implementation poses a crucial aspect of this research project as stability of the tower is investigated and it forms the central focus. The generation and modelling of wind loads on this structure depend on assumptions made about how the structure is enclosed. Assuming a solid cladding for the tower, with glass panels placed between diagonals, implies a less favourable case for wind action due

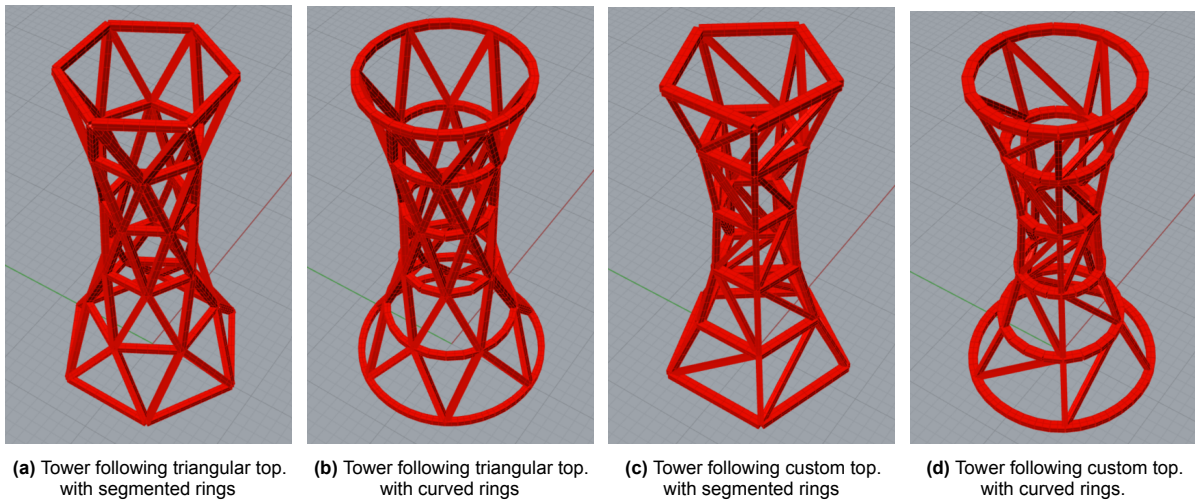
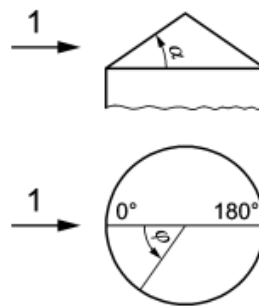


**Figure 4.11:** The resulting structural model of the tower following the triangular and custom topology.

to the absence of transparency in the lattice of the tower. In this case, the engineer is required to consult the Dutch building code NEN-EN 13782:2015, titled "Temporary structure - Tents Safety." According to this standard, the code assumes a solid tent with a pitch angle, signifying the angle of inclination of the tent wall relative to the horizontal surface. The pitch angle shall be referred in this case as  $\alpha$ . Another parameter important in this wind analysis is the peripheral angle  $\phi$ . This angle indicates the angle between the normal vector of the tent surface and the vector representing the wind direction. Both the pitch angle  $\alpha$  and the peripheral angle  $\phi$  are portrayed in the Figure 4.12. With these two angles known, a pressure coefficient  $c_p$  can be obtained for each face unit of the tent surface through interpolation, following the requirements as displayed in Figure 4.13 from NEN-EN 13782:2015.

To implement the proposed approach into the Grasshopper environment, the surface enclosing the tower is generated by creating a mesh that is divided into individual faces characterized by peripheral and pitch angles. Subsequently, each face is assigned a force per unit area value determined by the retrieved pressure coefficient ( $c_p$ ). A force vector perpendicular to the mesh face is applied to each mesh face. Finally, the height of the mesh face dictates the final peak velocity pressure values  $q_p(z)$  as dictated by EN 1991-1-4, cl. 4.5. This is implemented in the model using Karamba3D's 'Loads' component, with the 'MeshLoad Const' setting selected. This component facilitates the distribution of mesh area loads to truss members within the structure. The resulting wind pressure profile is illustrated in the Figure 4.15.

It is also important to note that wind directions shall vary in conjunction with changes in tower configurations. For different shape factors  $N$  that describe the ring shape or number of vertices within it, the most governing wind direction shall be applied in order to simulate the most unfavorable loading scenario on the tower. To quantify and describe the direction of the wind, Figure 8.25c illustrates and relates wind load direction angle to its wind profile's position in the global axis. The angle itself is the one between the main wind direction vector (corresponding to the peripheral angle  $\phi = 0^\circ$ ) and the opposite of the global vector of y-axis within Rhino graphic environment.



#### Key

- 1 direction of wind
- $\varphi$  peripheral angle
- $\alpha$  angle of the pitch (45° or 22° or 90° (wall))

**Figure 4.12:** Pitch angle  $\alpha$  and the peripheral angle  $\phi$  as provided by NEN-EN 13782:2015.

### Live Loads

For live loads, ring elements are selected to take up live loads resulting from tower visitors. According to EN 1991-1-1, cl. 6.3.1.2 category C5 (large crowds) for the characteristic value for distributed load  $q_k$  is assumed, which amounts to  $5 \text{ kN/m}^2$ . This load is distributed on a circular area represented in Grasshopper environment as a line load which gets transferred to a adjacent ring element.

### Permanent Loads

In terms of permanent loads, the elements of the tower are recognized to carry their self-weight. In addition, the tower platform, although its geometry is absent in the Grasshopper environment, will impose a permanent load on the relevant ring elements. This platform self-weight is assumed to be around  $5 \text{ kN/m}^2$  as a primarily CLT floor. This is determined in accordance to DIN 1055-2002 titled 'Action on structures - Part 1: Densities and weights of building materials, structural elements and stored materials'. The distribution of loads on platforms is represented in Figure 4.16. A point to consider is the fact that an increase in the ring area correlates with a higher loading experienced by the rings. It should be noted that the platform shall be placed on the ring on its centre-line position as to avoid significant torsional effects. This is ensured by placing rubber bearings below the platform application point and distributing loads rather uniformly.

### Safety Factors

For safety factors, the structure is assumed to be CC2, category C: congregation areas. Factors  $\psi$  are retrieved from the Dutch National Annex EN 1990, cl. A1.2.2, table A1.1. For load combinations, equations (1.9) and (1.10) shall be implemented with specific values  $\gamma_G$  as well as  $\gamma_Q$  as referred in EN 1990, cl. 6.4.3.2(3) and cl. A1.3.1.

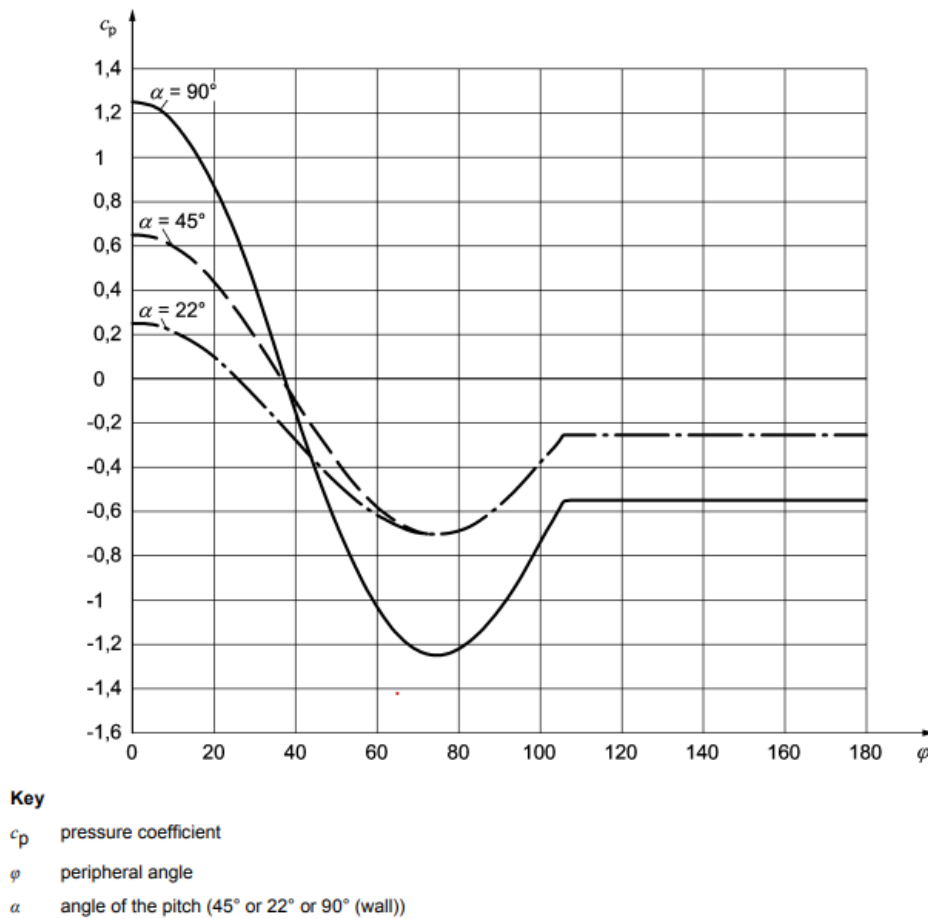


**Figure 4.13:** Pressure coefficient  $c_p$  values in relation to pitch angle  $\alpha$  and the peripheral angle  $\phi$  as provided by NEN-EN 13782:2015.

## 4.4. General workflow

The general workflow encapsulates the use of the proposed software tools in order to generate the geometry, build a structural model, perform kinematic and stiffness studies. The performed studies will inform about geometrical parameters and topology that perform in the most optimal way in terms of stiffness and stability. In terms of 'Grasshopper' scripts for the generation of both topologies, relevant files can be found in Appendix A.

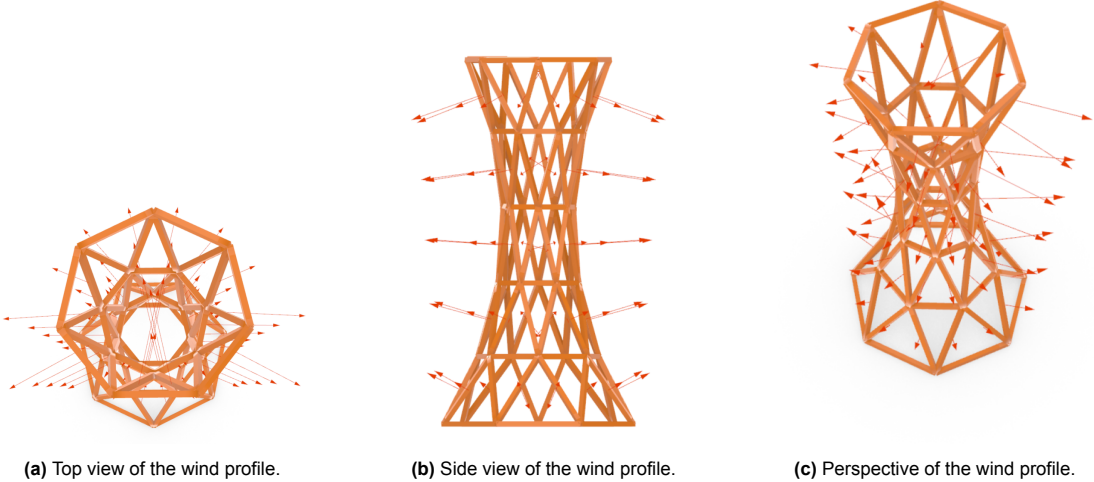


**Figure 4.14:** Corresponding wind force profile imposed on a tower with a triangular configuration in accordance with NEN-EN 13782:2015. Image (a) reflects on the change of pressure coefficient moving along the diameter of the tower as referred in Figure 4.13, while (b) indicates the influence of height on the magnitude of the wind load.

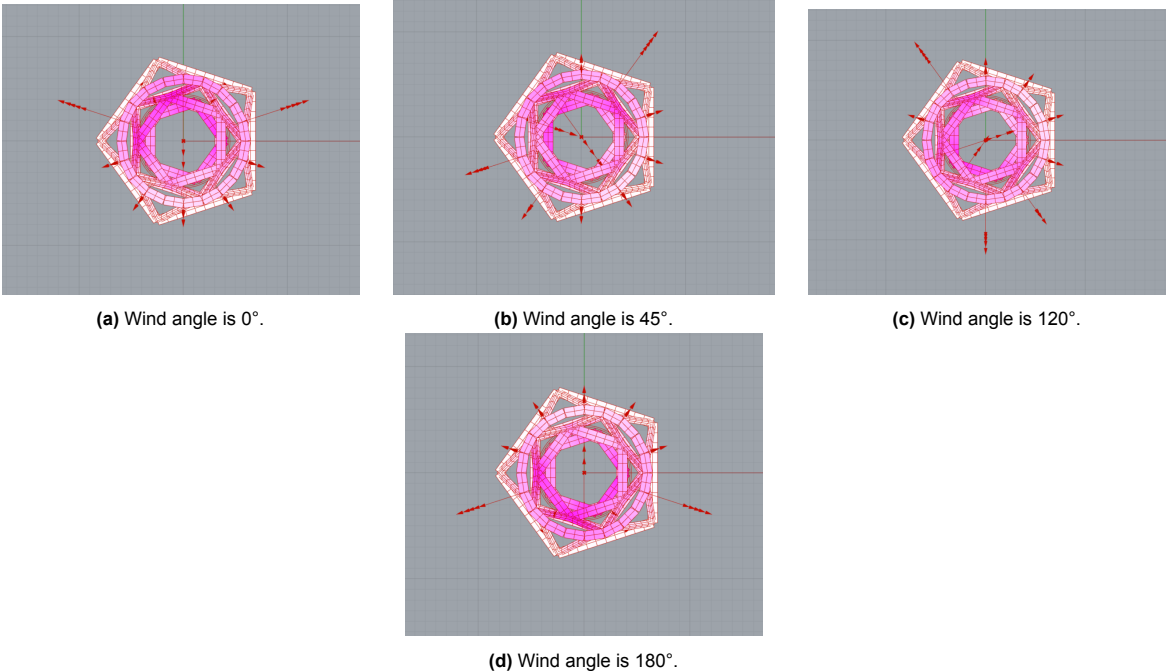


**Figure 4.15**

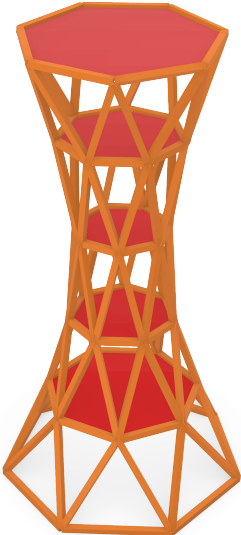


**Figure 4.16:** Representation of areas where live and dead loads are applied on tower's ring elements.

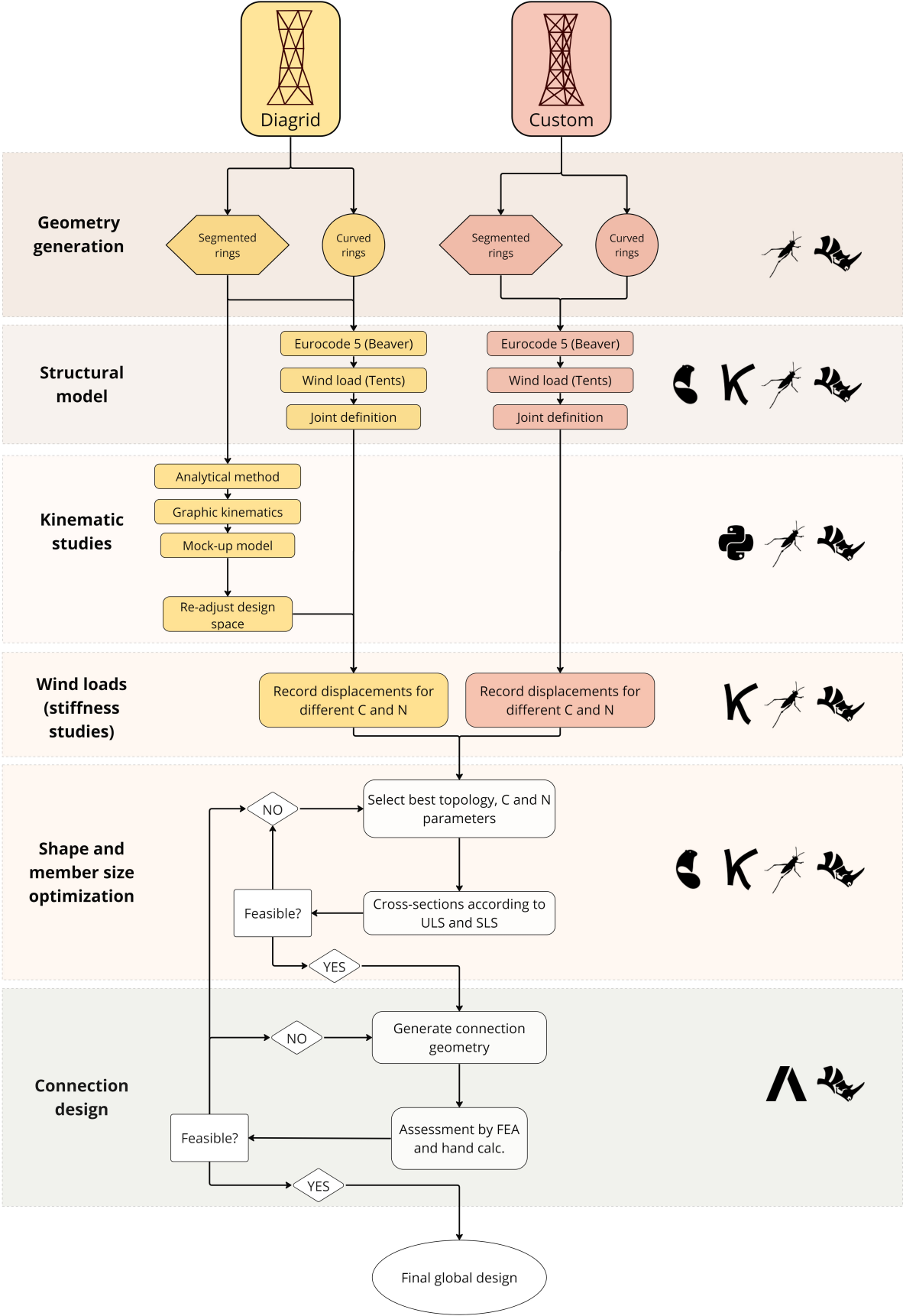


Figure 4.17: General workflow of the thesis project.

# 5

## Kinematic Nature of the Triangular Pattern

In this chapter, the analysis of the tower is presented, considering a triangular pattern equipped with segmented rings. This chapter investigates the impact of excluding flexurally stiff rings, which were previously incorporated to ensure stability of hyperboloid towers designed by Shukov. The research focuses on whether a segmented tower, comprised of straight, pin-jointed elements, can achieve stability without the direct reliance on a stabilizing components when subjected to the presented wind profile. It should be noted as analysis solely focuses on comparative study and how do performances fare within a set frame of reference, orders of magnitude of resulting values do not necessarily need to reflect or satisfy standards as the best and most optimum result is the goal of the research.

### 5.1. Topological influences

For the global structural behaviour considerations, SLS (global) output shall inform the design process regarding the overall stiffness of the assembly, thus, in this study it shall provide insights regarding topological influences.

For this topology, an initial geometry having its representative parameters being set to  $d = 5$  (number of levels) as well as the curvature parameter being set to  $C = -3.5 m$ , while the variable parameter in this case being  $N$  (the polygon shape factor). This set of geometry has been subjected to the proposed wind load profile relative to the one indicated in Chapter 4. Figure 5.1 indicates findings relating to global displacement of the structure (in mm) versus the change of the shape factor  $N$ . It becomes evident that towers exhibit disproportionately high displacements when their shape factor ( $N$ ) takes even values, meaning that the ring polygon is even sided. These results do present the idea that for certain polygon configurations, the tower tends to exhibit instability behaviour relating to possible kinematic mechanisms i.e. nodes are free to translate without inducing strains on respective members. By inspecting the deformed shape in Figure 5.2 of the tower, it becomes apparent that these displacements occur at the topmost ring since nodes there are unrestrained. Although this occurrence was initially also

pondered to happen due to boundary conditions of nodes (each member in the analysis software was allowed to freely rotate in all directions, while translations in all directions were turned off or restricted) or software related issues of the Karamba3D plug-in for the Grasshopper environment.

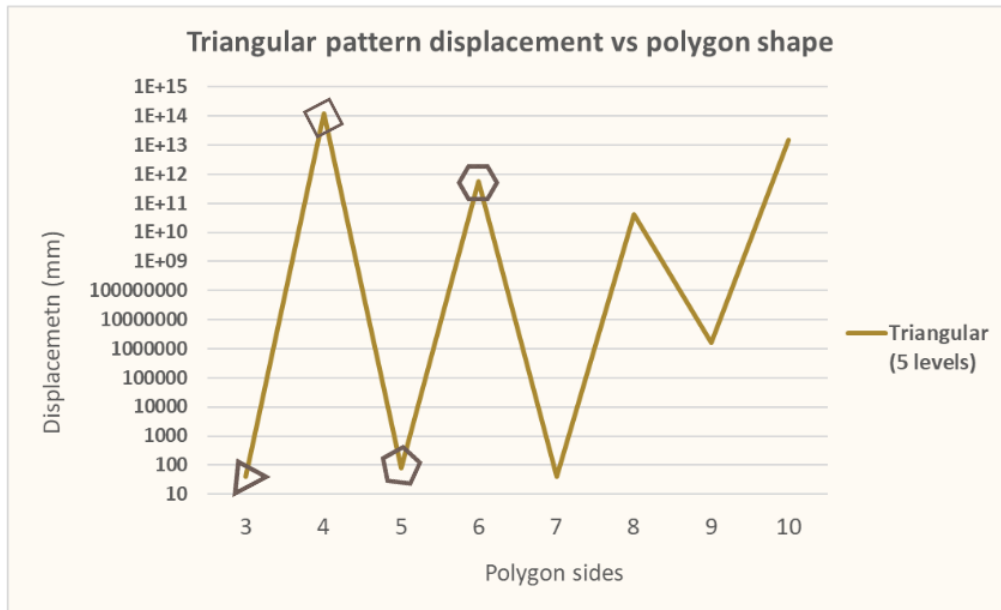


**Figure 5.1:** Global displacement of the tower (in mm) versus the change of the shape factor  $N$ . Note that the y axis is a logarithmic one. Corresponding shapes relating to the shape number  $N$  are presented as well.

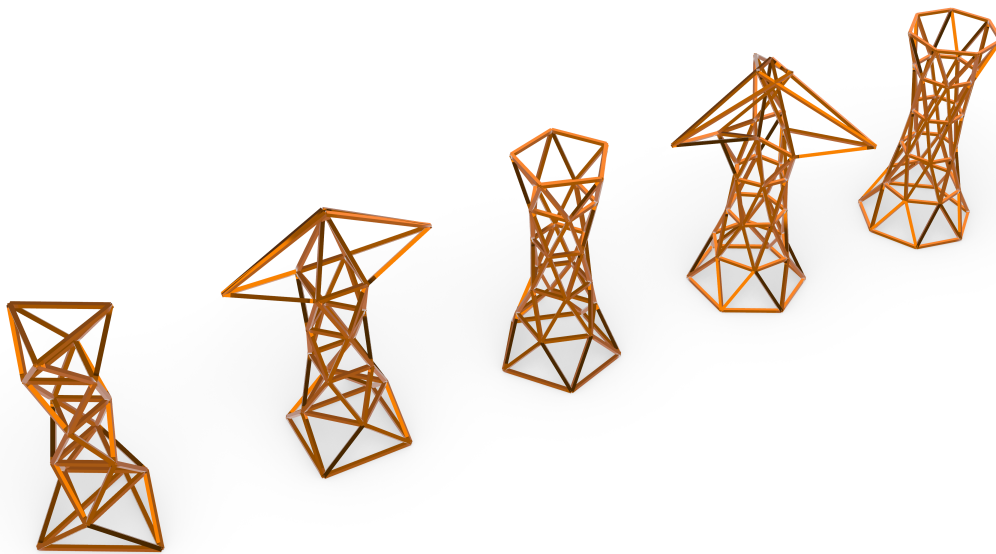


**Figure 5.2:** The deformed shape of the tower following a triangular (diagrid) pattern and equipped with segmented (polygonal) rings. Associated shape factors are (from left):  $N = 3$ ,  $N = 4$ ,  $N = 5$ ,  $N = 6$ ,  $N = 7$ .

In order to clear doubts and tackle the uncertainty behind obtained results, a single level component of the tower has been extracted and subjected to simple point loads as given in Figure 5.3. This approach does simplify the model that was previously was subjected to a rather complex wind load profile and the structural behaviour of the tower was more challenging to comprehend and inspect. Certainly, it's apparent that in the case of polygon shapes with an even number of sides (or  $N$  assuming an even

number), certain load combinations lead the assembly toward kinematic mechanisms characterized by unusually significant displacements, while odd sided polygons imposed upon the assembly signify an always consistent rigid response.

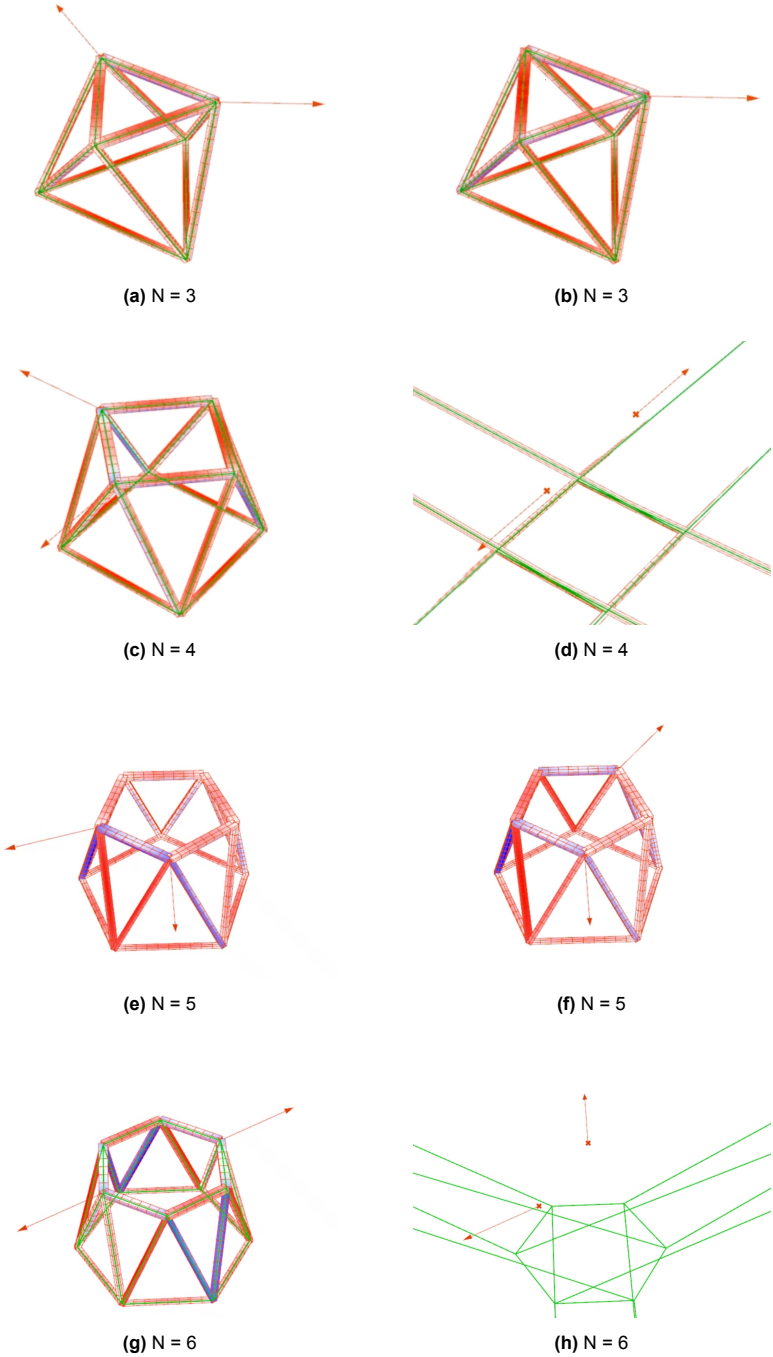


**Figure 5.3:** Simplified representations of triangular single level component subjected to point load on alternating nodes. As it can be observed, even sided polygons (displayed in c, d, g and h) exhibit significant displacements relating to certain point load combinations while odd sided polygons (displayed in a, b, e and f) deem lower segment to respond to any point load variation in a rigid way.

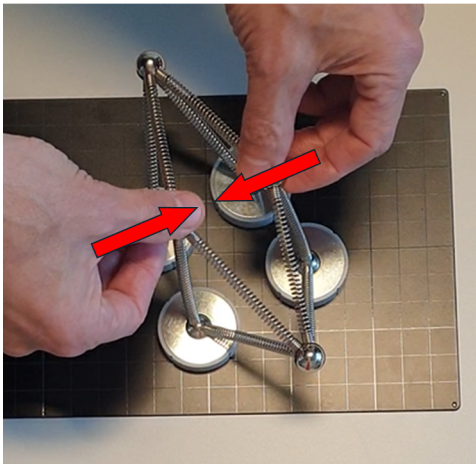
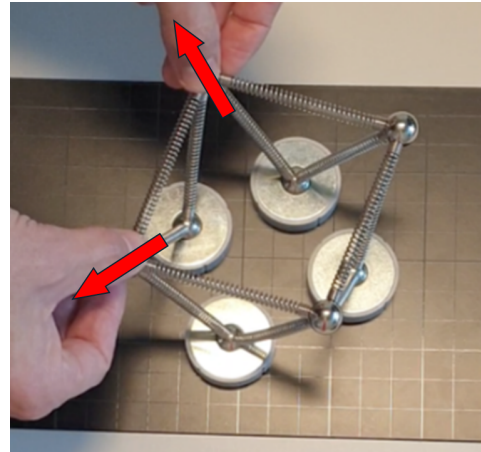
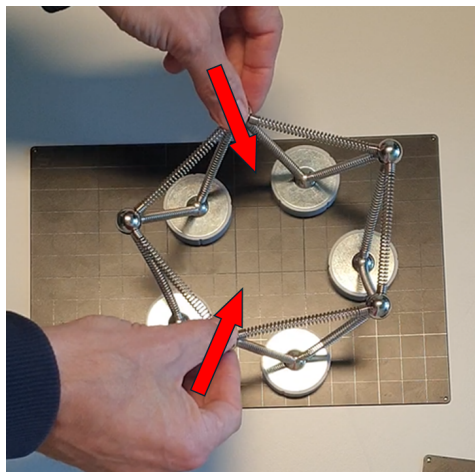
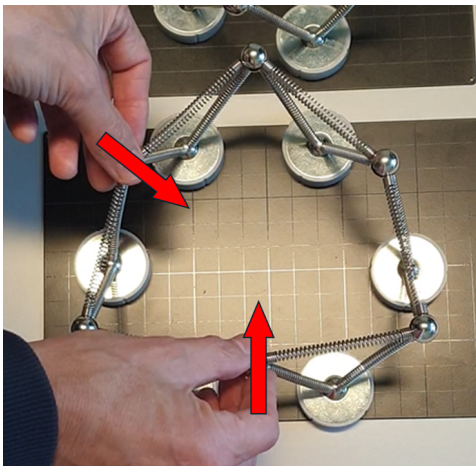
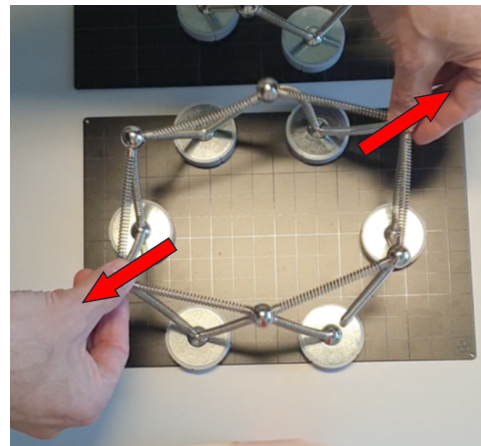
### 5.1.1. Confirmation of mechanisms through mock-up models

As this response was intended to be apparent or anticipated by the designer intuitively, a reasonable level of understanding can be achieved by assembling a real, representative mock-up model to confirm the observed structural analysis software results. Thanks to the resources provided by the Faculty of Civil Engineering of TU Delft, the assembly of given single-level even and odd polygon tower components was realized as displayed in Figure 5.4. Observations relating to the behavior of the model (composed of metal springs connected to each other by virtue of magnetic capsules and steel ball serving as a pinned joint) showed corresponding responses as portrayed in Figure 5.3. For instance, for shape factors taking a value equal to and  $N = 6$ , kinematic mechanisms take place at certain loading conditions (radial point loads) which seem to have an anti-symmetric configuration (Figure 5.4d), while the structure seems to respond rigidly when point loads have a symmetric placement (Figure 5.4e). On the other hand, assemblies showing a shape factor taking an odd number  $N = 5$  showcase a rigid response at any point load placement. Cases of a rigid response can be pondered to be relating to the structure reaching a state of self-stress that in turn stabilizes the structure, while the unstable response indicates the presence of a zero-strain kinematic mechanism. Therefore, the development and testing of mock-up models do substantiate the observations made in the models generated by the structural analysis software Karamba3D.

### 5.1.2. Theoretical (analytical) confirmation of mechanisms

As both, mock-up and structural software models, seem to agree on the occurrence of specific structural behaviour relating to a certain geometry or assembly of a truss, a thorough theoretical basis shall be established to confirm and possibly interpret the observed results. Referring to Pellegrino (1993) and the method of SVD of the equilibrium matrix  $\mathbf{A}$ , every single-level triangular topology tower segment shall be investigated for its geometry while varying its shape factor  $N$ . In order to set up an equilibrium matrix  $\mathbf{A}$  for a given truss geometry, one shall take each node of the assembly and separately assess the members connected to that node following the method provided in the Subsection 2.5. The members in question shall have their vector projections in all three x, y and z directions. The resulting matrix should assist in solving force equilibrium problems for a given set of forces on the assembly. One should mind that nodes directly connected to supports do not contribute to the equilibrium matrix and shall not be considered as support reactions imposed on these nodes are not part of the internal force matrix. Additionally, members of the lower ring are also not taken into account as the pin-jointed nature of the truss does not permit these bars to have an effect on overall stability. Thus, it can be stated that a single storey triangular topology tower with a triangular shape for a ring ( $N = 3$ ) characterised by having  $b = 9$  number of bars and  $j = 3$  number of nodes. Thus, the resulting equilibrium matrix  $\mathbf{A}$  would be of size  $9 \times 9$ . By performing the SVD operation on such a matrix, three resulting matrices are retrieved, while the middle one denoted as  $V$  and its rank  $r$  are of importance as the equilibrium dimension parameter  $n_r$  is already known for the retrieval of  $m$ . An example equilibrium matrices  $\mathbf{A}$  of a single level tower component with shape factors  $N = 3$ ,  $N = 4$  and  $N = 5$  is displayed in Figure 5.5.

For varying shape factors  $N$ , Table 5.1 presents the resulting output values from the SVD operation of the equilibrium matrix  $\mathbf{A}$ : rank  $r$ , dimensional matrix values  $n_r$  and  $n_c$ , number of mechanisms  $m$  and number of states of self-stress  $s$ . It can be observed that even-sided polygons tend to exhibit states

(a)  $N = 4$ , symmetric loading, kinematic mechanism.(b)  $N = 4$ , anti-symmetric loading, rigid response.(c)  $N = 5$ , rigid response, always.(d)  $N = 6$ , anti-symmetric loading, kinematic mechanism occurs.(e)  $N = 6$ , symmetric loading, rigid response (a member breaks from the node).

**Figure 5.4:** A mock-up model representing a single-level component of the antiprism tower following a triangular topology and its variations differing in the shape factor  $N$ . It can be observed that for configurations having odd sided polygons, the response to point loads is always rigid no matter the placement of forces. However, for towers exhibiting even sided polygons the response to certain loading conditions tend to show instability and, thus, kinematic mechanisms occur.



$N$	$r$	$n_r$	$n_c$	$m$	$s$	Type
3	9	9	9	0	0	Kinematically <b>determinate</b>
4	11	12	12	1	1	Kinematically <b>indeterminate</b>
5	15	15	15	0	0	Kinematically <b>determinate</b>
6	17	18	18	1	1	Kinematically <b>indeterminate</b>
7	21	21	21	0	0	Kinematically <b>determinate</b>
8	23	24	24	1	1	Kinematically <b>indeterminate</b>

**Table 5.1:** Structural analysis results through deployment of SVD of an equilibrium matrix  $\mathbf{A}$  of single-level components having different shape factors  $N$ .

of instability, approaching kinematic zero-strain mechanisms. In these configurations, the number of independent zero-energy deformation modes ( $m$ ) is consistently non-zero. This observation similarly applies to the associated number of states of self-stress ( $s$ ), classifying the structure as structurally indeterminate as certain load configurations cause the structure to self-stabilize and remain rigid. On the contrary, whenever the essential parameters  $m$  and  $s$  are observed to take zero values, the assembly is termed as kinematically determinate and nodal displacements appear only by virtue of member elongation or contraction (stiff response). This approach firmly establishes the foundation by demonstrating the alignment between real-world mock-up models and software Karamba3D observations with the theoretical framework. It highlights the impact that both even-sided and odd polygons exert on the overall stability of pin-jointed truss towers following the adopted triangular topology and how that should inform the design practice of representative structural assemblies.

Finally, as the occurrence of mechanisms have been confirmed for certain polygon shapes in the tower, the last  $m$  left singular vectors (derived from the resulting matrix  $\mathbf{U}$ ) representing strain-free, or zero-energy displacement modes (illustrated in Figure 2.39) can in fact inform about the precise nodal deformation relating to a kinematic mechanism. Figure 5.6 shows  $n_r \times 1$  matrix (or a vector) for single-level tower components taking a different shape factor  $N$ . Interestingly, as it was highlighted in Table 5.1, the method of taking an SVD of an equilibrium matrix  $\mathbf{A}$  does give only one mechanism for a kinematically indeterminate assembly as the parameter  $m$  is always equal to 1. Thus, zero-strain deformation matrices are always composed of one column. Thus, it can be seen that if the resulting data from the zero-strain deformation modes are applied in the form of displacement vectors on the corresponding node, the resulting configuration precisely resembles zero-strain kinematic mechanisms observed from the mock-up model testing (Figure 5.4). More precisely, zero-strain deformation is only realized by the alternating fashion in which each node undergoes displacement. This explains the scenario in which a single-level mock-up tower component with a hexagon ( $N = 6$ ) shape for a ring did respond rigidly to symmetric loading conditions, which in turn restrained nodes to move in an alternating way, thus, members were subjected to internal tensile and compressive stresses.

Thus, a comprehensive analytical verification has been obtained, in turn confirming the kinematic nature

of tower assemblies following a triangular topology. This feat provides a fundamental understanding of circumstances and loading conditions under which observed instabilities of the tower structure (marked by substantial deformations displayed in Figure 5.1) does occur. The following section shall present an alternative approach to address this question. The code used for implementing SVD is given in Appendix B while equilibrium matrices and further kinematic analysis relating to more complex tower geometries can be found in Appendix C.

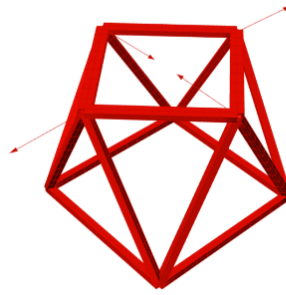
### 5.1.3. Graphic kinematics confirmation of mechanisms

Analytical method involving the SVD of an equilibrium matrix  $\mathbf{A}$  does inform one as to whether and how assemblies with certain shape factors tend to exhibit kinematic mechanisms in their structural response. However, an alternative paradigm for a structural analysis of spacial structures is provided by graphic kinematics which is extensively discussed in Subsubsection 2.5.2. This method allows a more intuitive and interactive way to realise in which way the tower structure can experience structural mechanisms by virtue of simply sliding force cells. The exploration includes inspecting the potential occurrence of linked zero-strain deformation modes, indicated as  $m$ , within an assembly for having a specific shape factor  $N$ .

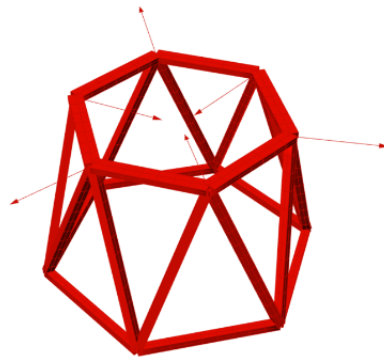
As previously presented graphic kinematics method of deploying Rankine reciprocal force cells for a given pin-jointed truss (presented in Chapter 2) would provide a clear indication of not only whether but also how the assembly deforms in a zero-strain manner. Thus, in terms of towers following a triangular topology reciprocal force polyhedras are generated as to follow the definition presented by Akbarzadeh, Van Mele, and Block (2015). However, the assembly in this case deviates from the one documented in the literature and as presented in Subsubsection 2.5.2. The key distinction lies in the fact that the existing tower structure is configured as an antiprism, contrasting with the prism structure depicted in Figure 2.41.

Reciprocal force polyhedras are developed by utilizing Grasshopper component 'Voronoi Cell' that takes nodal points of the assembly and generates Voronoi surfaces in 3D that quite precisely replicate those equivalent of the Rankine reciprocal force diagrams. As the geometrical features that are relevant for this analysis are faces of adjacent (also the underneath and above) cells and whether they separate in case of cell translation, the scale, the total size of the area of a cell or outer faces are not significant. Thus, in Figure 5.7 one can observe the resulting reciprocal cells for given single level tower assemblies following different shape factors  $N$ . For the movement of cells associated to towers with an even valued  $N$  (even sided polygons) displayed in Figures 5.7b and 5.7d, the translational vectors from Figure 5.6 are utilized in this case to move the respective nodal cell in that specific direction and inspect whether the adjacent cell walls are separating or not. These specific translational vectors obtained through the analytical SVD method do correspond to a zero-strain deformation mode exhibited by tower structures having an even valued shape factor  $N$ . The resulting possibility to shift force cells when neighboring walls are sliding within a single plane reinstates the notion of their kinematic nature being *indeterminate*, thereby confirming the existence of a mechanism. It is noteworthy to highlight the strong and remarkable correlation between both methods, as the data generated by the SVD approach reveals Rankine force cells sliding precisely without a single overlap.

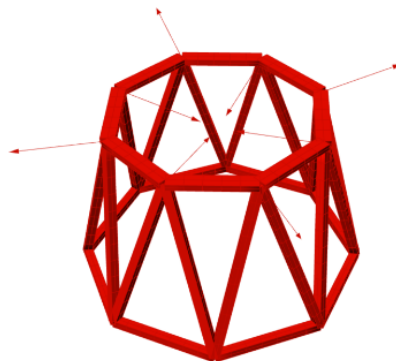
$$\begin{array}{l}
 \text{Node 1} \\
 \text{Node 2} \\
 \text{Node 3} \\
 \text{Node 4}
 \end{array}
 \begin{array}{l}
 x \\
 y \\
 z \\
 x \\
 y \\
 z \\
 x \\
 y \\
 z \\
 x \\
 y \\
 z
 \end{array}
 \begin{bmatrix}
 0 \\
 -0.4997 \\
 0.0171 \\
 -0.4997 \\
 0 \\
 -0.0171 \\
 0.4997 \\
 0.0171 \\
 0.4997 \\
 0 \\
 -0.0171
 \end{bmatrix}$$

(a)  $N = 4$ 

$$\begin{array}{l}
 \text{Node 1} \\
 \text{Node 2} \\
 \text{Node 3} \\
 \text{Node 4} \\
 \text{Node 5} \\
 \text{Node 6}
 \end{array}
 \begin{array}{l}
 x \\
 y \\
 z \\
 x \\
 y \\
 z
 \end{array}
 \begin{bmatrix}
 -0.2033 \\
 -0.352 \\
 -0.0377 \\
 -0.2033 \\
 0.352 \\
 0.0377 \\
 0.4065 \\
 0 \\
 -0.0377 \\
 -0.2033 \\
 -0.352 \\
 0.0377 \\
 -0.2033 \\
 0.352 \\
 -0.0377 \\
 0.4065 \\
 0 \\
 0.0377
 \end{bmatrix}$$

(b)  $N = 6$ 

$$\begin{array}{l}
 \text{Node 1} \\
 \text{Node 2} \\
 \text{Node 3} \\
 \text{Node 4} \\
 \text{Node 5} \\
 \text{Node 6} \\
 \text{Node 7} \\
 \text{Node 8}
 \end{array}
 \begin{array}{l}
 x \\
 y \\
 z \\
 x \\
 y \\
 z
 \end{array}
 \begin{bmatrix}
 0.2476 \\
 0.2476 \\
 0.0487 \\
 0 \\
 -0.3502 \\
 -0.0487 \\
 -0.2476 \\
 0.2476 \\
 0.0487 \\
 0.3502 \\
 0 \\
 -0.0487 \\
 -0.2476 \\
 -0.2476 \\
 0.0487 \\
 0 \\
 0.3502 \\
 -0.0487 \\
 0.2476 \\
 -0.2476 \\
 0.0487 \\
 -0.3502 \\
 0 \\
 -0.0487
 \end{bmatrix}$$

(c)  $N = 8$ 

**Figure 5.6:** Strain-free, or zero-energy displacement modes relating to single-level tower components taking shape factor values  $N$  relating to assemblies exhibiting kinematic mechanisms. On the right hand side displacement vectors are visualized for each node of the assembly which correspond to the matrix on the left.

Thus, if an attempt is made to move two adjacent cells within an assembly characterized by an even polygonal shape, it no longer implies that nearby faces slide along each other in the same plane. Instead, they become separated. In turn, a zero-strain response is not related to this scenario. This explains that certain point loads imposed upon single level even polygon assemblies did not trigger mechanisms as illustrated in Figure 5.3.

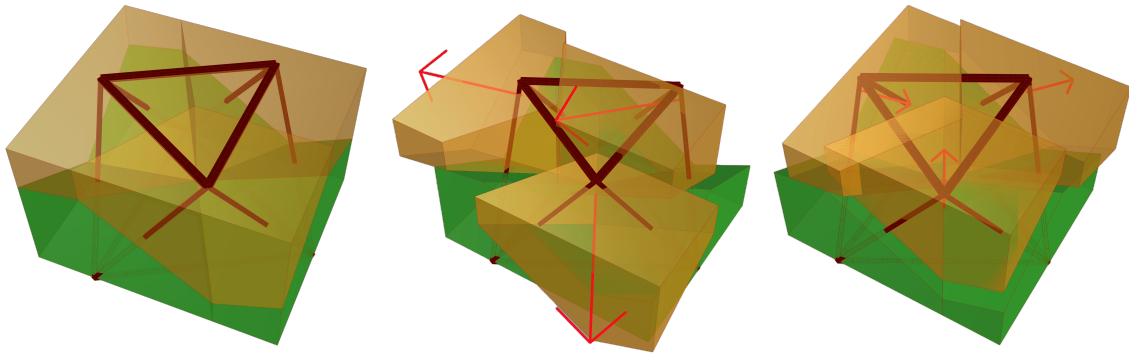
It is also noteworthy to highlight the distinction between the antiprism tower configuration under consideration and the regular prism configuration discussed by Akbarzadeh, Van Mele, and Block (2015) and depicted in Figure 2.41. This distinction shows that lower level cells (indicated in green) do present a valley (a sharper cut) which allows only a specific translation of a cell above it. This unique characteristic associated only to the antiprism configuration does provide the rationale behind the resulting single ( $m = 1$ ) kinematic mechanism pertaining to assemblies with even sided polygons. Meanwhile for regular prisms, which can be viewed in Figure 2.41, upper cells lie on a flat surface provided by lower cells. Consequently, there are numerous ways for translating these cells relative to each other without connecting walls separating. This results in a higher number of kinematic mechanisms occurring for each assembly following a regular prism configuration.

On the other hand, for structures employing odd sided polygons for rings (as portrayed in Figures 5.7a and 5.7c), the sliding of cells is possible only if the separation of adjacent faces is occurring, thus, these assemblies can be defined as inherently being *kinematically determinate* as such nodal displacements are permitted by virtue of member elongation or shortening (strains).

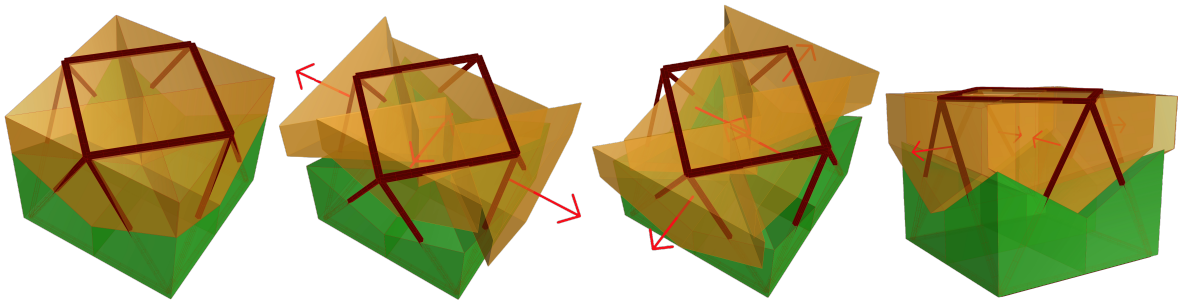
Thus, theoretical numerical and graphical outputs do establish consistency with observed results from mock-up models and structural analysis software. Graphic kinematic analysis relating to more complex tower geometries can be found in Appendix D.

#### 5.1.4. Karamba3D confirmation of mechanisms with 'Eigen Modes' component

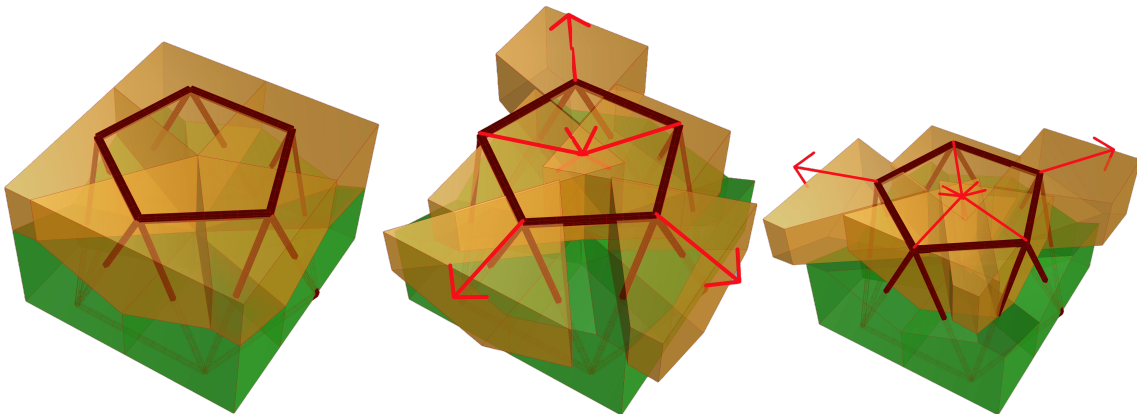
For the final step that involves a more precise estimation of structural behaviour of 3D kinematically indeterminate trusses, Karamba3D software does encompass a component called 'Eigen Modes' which calculated the eigenmodes of a given defined structural model according to the special eigenvalue problem. The resulting model presents the computed eigenmodes as result cases. This showcases their superimposition using the "ModelView" component. Each eigenmode corresponds to a specific global shape or pattern, indicating how the truss structure would deform under a critical load that could potentially induce buckling or instability. If the investigated triangular topology single level tower component's model is plugged into this component the outputs are as displayed in Figure 5.8. By increasing the 'Deformation' slider in the 'Model View' component one can observe how a kinematically indeterminate assembly tends to a zero-energy, zero-strain mechanisms and what exact shape the structure takes in case of that. It is noteworthy to highlight that observed shapes in case of a mechanism exactly resemble ones provided by all the other methods utilized from before (SVD, graphic kinematics and a mock-up model). It is also noteworthy to highlight the fact that resulting extremely low eigenvalues ( $5.0e-9$ ) even for kinematically determinate structures relate to members being torsionally unrestrained and, thus, exhibiting instability of members rotating longitudinally. Extremely low values are not contributing to the rank  $r$  after the implementation of SVD for kinematic analysis by enforcing a multiplier



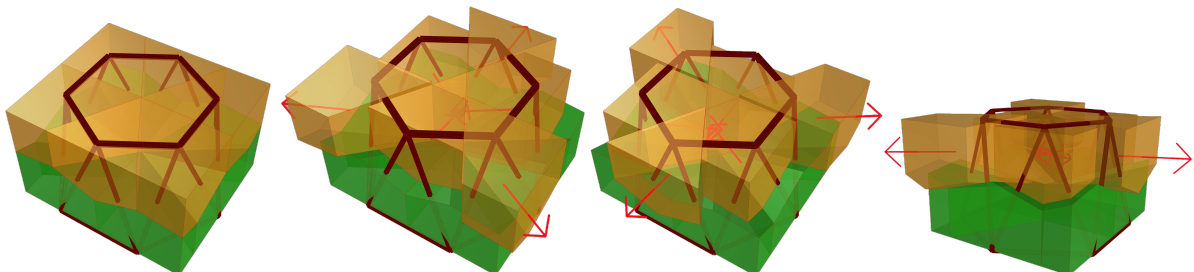
(a)  $N = 3$ , force cells cannot be shifted in any way without separation from the adjacent one (kinematically determinate).



(b)  $N = 4$ , it is possible to shift force cells when neighboring walls are sliding within a single plane (kinematically indeterminate).



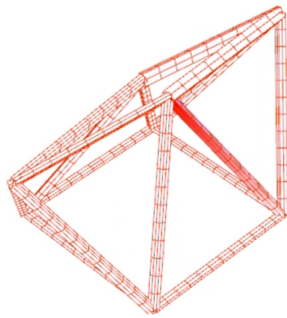
(c)  $N = 5$ , force cells cannot be shifted in any way without separation from the adjacent one (kinematically determinate).



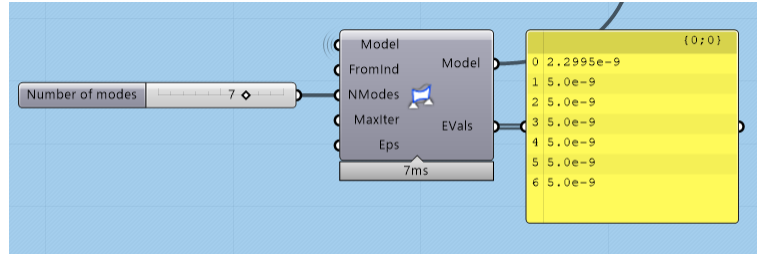
(d)  $N = 6$ , it is possible to shift force cells when neighboring walls are sliding within a single plane (kinematically indeterminate).

**Figure 5.7:** A graphic kinematics approach utilizes Rankine reciprocal force cells and their sliding in relation to one another in order to confirm and analyze the potential deformation of a given assembly within a kinematic mechanism. For (b) and (c), red arrows represent zero-strain deformation vectors obtained through the method of SVD and displayed in Figure 5.6. For other arrows, those were constructed manually as to closely replicate ones from before.

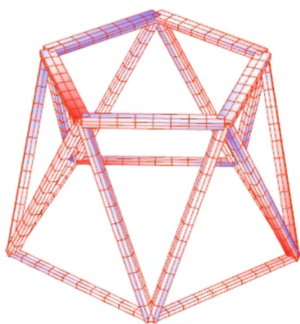
$\alpha$  being  $10^{-3} \times$



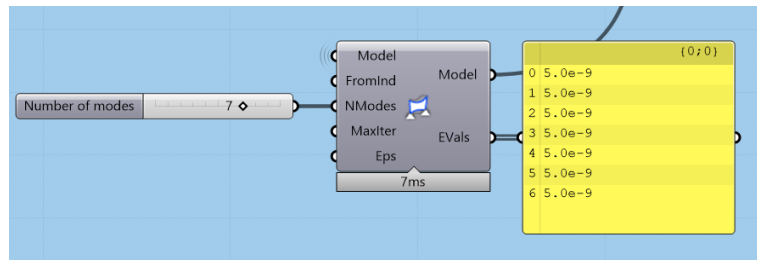
(a) N = 4



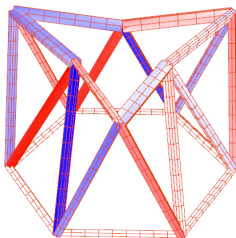
(b) N = 4



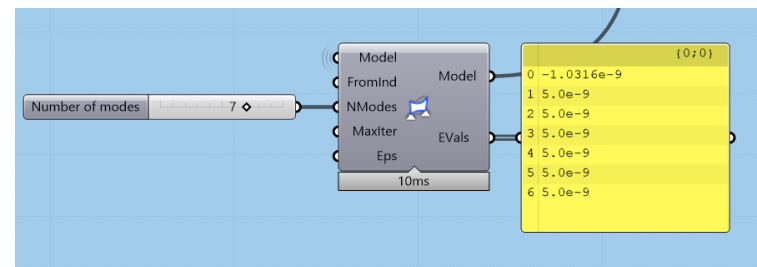
(c) N = 5



(d) N = 5



(e) N = 6



(f) N = 6

**Figure 5.8:** By utilizing the 'Eigen Modes' component in the Karamba3D plug-in for Grasshopper, it becomes feasible to identify assemblies that exhibit kinematic mechanisms based on their initial geometry. The outputs incrementally reveal how nodal displacements can occur in towers with even-sided polygons while no strain is induced on their members (a and e). Additionally, this can also be noticed in output eigenvalue list (b, d, f).

### 5.1.5. Overview of methods utilized

The innate benefit stemming from the utilization of the mock-up model is the interactive nature available to the engineer. This feature allows an instant grasp and intuition of how the structure behaves and reacts to different loading conditions. In the of this research there were doubts surrounding modelled

tower's response to loading within the realm of structural analysis software (reasons were potentially associated with the incorrect set up of the model or software related issues). The construction of a representative mock-up model dispelled these doubts as one could observe first-hand the influence certain geometrical configurations (topology) hold on tower's stiffness or even kinematic nature. One drawback relating to this method is the expense of acquiring these building sets and their availability to practising engineers. Additionally, as these sets rely on straightforward spring bars of uniform length as well steel spheres as joints, the realization of more intricate and complex geometries becomes more challenging within the constraints of such building sets.

Furthermore, the method of performing the Singular Value Decomposition (SVD) of the equilibrium matrix  $\mathbf{A}$  of a certain structural assembly within the 3D space has demonstrated itself as a robust analytical technique. It is able to describe the kinematic nature of the structure and predict its behaviour quite precisely. The acquisition of zero-strain deformation mode vectors from the matrix  $\mathbf{U}$  accurately predicts nodal displacement of certain assemblies given that their associated number of mechanisms are  $m = 1$ . A solid mathematical foundation allows a robust analysis even for more complex geometries having more diverse arrangement of nodes and member connectivities, which cannot be said about the mock-up model. However, the main limitation of this method relates to the required computational effort in order to set up required parameters relating to the geometry of the pin-jointed assembly. The main parameter being the equilibrium matrix  $\mathbf{A}$ , which requires one to develop an algorithm to transfer the geometrical data into its corresponding mathematical expression. Additionally, the SVD operation additionally incurs some computational effort in Python programming. Finally, as the working mathematical principles governing the SVD of an equilibrium matrix may not be instantaneously evident to practicing engineer or designer, its results might be greeted with scepticism given the entire method operates rather in a way that is not apparent and immediately comprehensible.

The approach of graphic kinematics combines the benefits of the two methods discussed previously. The innate interactive nature of simply shifting associated nodal force cells in relation to one another facilitates a sudden and rather intuitive comprehension of circumstances under which the kinematic mechanism might occur. Similar to what has been demonstrated with a mock-up model of the tower, the engineer is able to engage with Rankine reciprocal cells individually and assess the structure purely within the graphical domain. This method holds significance, especially because of the widespread use of graphical software nowadays in engineering and architecture practices in efforts to visualize and engage with structural form. Overall, graphic kinematics provides a more streamlined way to inspect the structure for multiple potential zero-strain modes or mechanisms. Concerning the drawbacks of the approach is again a rather considerable computational effort needed to generate associated nodal force cells by virtue of boundary representation (or BREP). However, this effort is not as high compared to the SVD approach.

Lastly, 'Eigen Modes' is a powerful feature of the Karamba3D as it allows a more involved understanding and comprehension of the nature that kinematically indeterminate structure might entail. Typically, with other structural analysis software, giving the input geometry of a tower characterized by an even-sided polygon (or when its shape factor  $N$  takes even numbers) often leads to error messages stating singularity or an algorithm's inability to assess the structure. Therefore, these messages often lack further clarification on the specific reasons behind such occurrences. By combining engineering intuition, more in depth and thorough assessment and results given by Karamba3D software, designer can

gain further insights and understanding of the effect geometrical features might have on the kinematic nature of a given structural assembly.

## 5.2. Discussion

This chapter has delved into the kinematic aspect of the tower design defined by the triangular topology. Initial parametric studies investigated the assembly comprised of straight pin-jointed elements and its lateral stiffness against proposed wind loads that had a non-uniform force profile acting upon the structure. First results demonstrated discrepancies in global displacements of structures characterised by different shape factors  $N$ . Quite a stable and predictable behaviour is observed with structures employing an odd valued shape factor  $N$ , while even valued  $N$  was associated with substantial displacements caused by the wind. It is noteworthy to highlight that significant deformations related to latter are observable to occur at the apex of the structure where nodes are not restrained as no members are connected above them. Freedom of movement of these joints rely completely on the shape of the ring and the topology of the tower. Proposed triangular topology replicates one of a uniform antiprism (a semi-regular polyhedron) defined by regular  $N$  - gons at every ring level and  $2N$  isosceles triangles for every segment of the tower. It has been observed that this configuration does allow an increased level of freedom in terms of nodal movement as the level rises, which can be associated with a strain-free displacements. In other words, kinematic mechanisms are observed. However, certain number of vertices within the ring polygon has shown to restrain that movement and disallow these mechanisms to take place. After a comprehensive examination of the structure by virtue of a hands-on mock-up model, analytical analysis and employment of a graphic kinematic methods, the design process has converged into a geometrical standardisation of the tower design in question. By employing a shape an odd shape factor  $N$  whenever pin-jointed assemblies defined by the triangular pattern are concerned, the structure is known that kinematic aspects are negated and large, strain-free displacements are omitted. This statement has been reached by modelling a structure where vertical live and dead loads were disregarded and only proposed wind load actions were imposed. Thus, one can argue that by introducing loads at the top-most ring as wind loads are present would generate enough tension force and stabilize the ring, in that way nodal displacements would subside regardless of the shape factor. For the apex ring to maintain its form, it is crucial that it be subjected to substantial vertical loads continuously. Moreover, polygons with an even number of sides are more prone to uncontrolled nodal shifts, necessitating a higher level of stabilizing tensile force to ensure structural integrity.

The suggested findings also hold importance for the construction process. The building method for such structures involves the sequential installation of diagonal and ring elements. When employing an even-sided polygon for the ring element, the initial segment, representative to the structure shown in Figure 5.8, cannot withstand lateral forces, such as those from ladders, standing construction workers, or temporarily placed items. This scenario induces strain-free nodal movement, negatively affecting the connections through significant rotational movements of members. This situation places undue stress on the connections, potentially leading to their failure as timber-steel connections are not entailing high levels of rotational stiffness. Thus, employing odd sided polygons would allow temporary stages of the tower to withstand any work or accidental lateral loads to be taken not by bending of the connection but by pure axial tension and compression of members.

---

After reviewing provided outcomes, one might suggest the placement of a curved ring at the most critical point of the tower, which is the apex. In that way the nodal movement would be restrained not only at the bottom (supports) but also at the top (by a stiff continuous ring). However, the topological and shape factor  $N$  influences on tower's kinematic nature might differ. Thus, following chapter explores the effect of these design adjustments on the tower structure following the triangular pattern.

# 6

## Stiffness Studies of the Triangular Pattern

### 6.1. Curvature

Geometrical variable related to the curvature of the tower and its effect on the tower's global stiffness and efficiency shall be investigated in this section. The variable  $C$  as defined in previous Chapter 4 indicates the distance (in m) between the straight curve connecting the upper and lower platform rings and the surface of the tower.

#### 6.1.1. Tower stiffness in response to the proposed wind load profile

It has been determined that, for the triangular topology, choosing towers characterized by shape factors  $N$  with odd values (involving uneven sided polygons for rings) is a necessary design choice. Such towers consistently exhibit a rigid response to loading. Thus, for curvature assessment, shape factors take values  $N = 3, 5, 7, \dots$

For each tower variant, the curvature parameter  $C$  was iterated and maximum deflection values against wind loads that were most critical in direction are recorded. In such a way the variability of curvature and its influence on the global stiffness of towers with different shape factors is investigated and presented in Figure 6.1. It should be noted that the y-axis is on a logarithmic scale as some displacements take very high values. It can be observed first that the most stable and stiff response to proposed wind loads is shown by the tower with the shape factor  $N = 3$ . Varying curvature  $C$  did not impose that great of an influence on assembly's ability to withstand loads as displacement values did not vary that much regardless if the shape was a hyperboloid or rather tending to a barrel one. This again can be attributed to the fully triangular composition of this structure. A highly favorable feature of this stable shape is to withstand loads fully by axial elongation/contraction. On the contrary, whenever the shape factor  $N$  was increasing to values higher than 3, the variation in curvature  $C$  had a significant effect on its capacity to resist wind loads. For shape factors  $N = 5, 7$  and  $9$ , each structure seems to have

quite a specific range of curvature values at which the response to wind loads is rather stable and stiff. However, as the shape factor  $N$  increases, that range within which the tower maintains stiffness becomes narrower. This indicates that for a higher number of polygon sides in the tower design, the stiffness becomes more susceptible to variations in curvature  $C$  parameter. Outside of this range, the tower seems to exhibit substantial displacements that potentially correspond to a global buckling phenomenon (deformed shapes for decreasing and increasing curvature values  $C$  can be found in Figures 6.2 and 6.3). This behaviour is most pronounced at the top of the tower where the upper ring is not restrained or connecting to anything above and, thus, the deformability of it is higher in magnitude. Additionally, it also can be seen that the stiffness does decrease as the shape factor  $N$  grows (except for  $N = 9$  as the minimum displacement value is lower than that of a tower having  $N = 7$ ). Finally, it should be highlighted that for each tower, with increasing shape factor  $N$ , the stiffest design variant is represented by a increasing curvature values  $C$ . This means that the stiffest shape for towers with an increasing shape factor  $N$  is one tending to a winder hyperboloid (Figure 6.4).

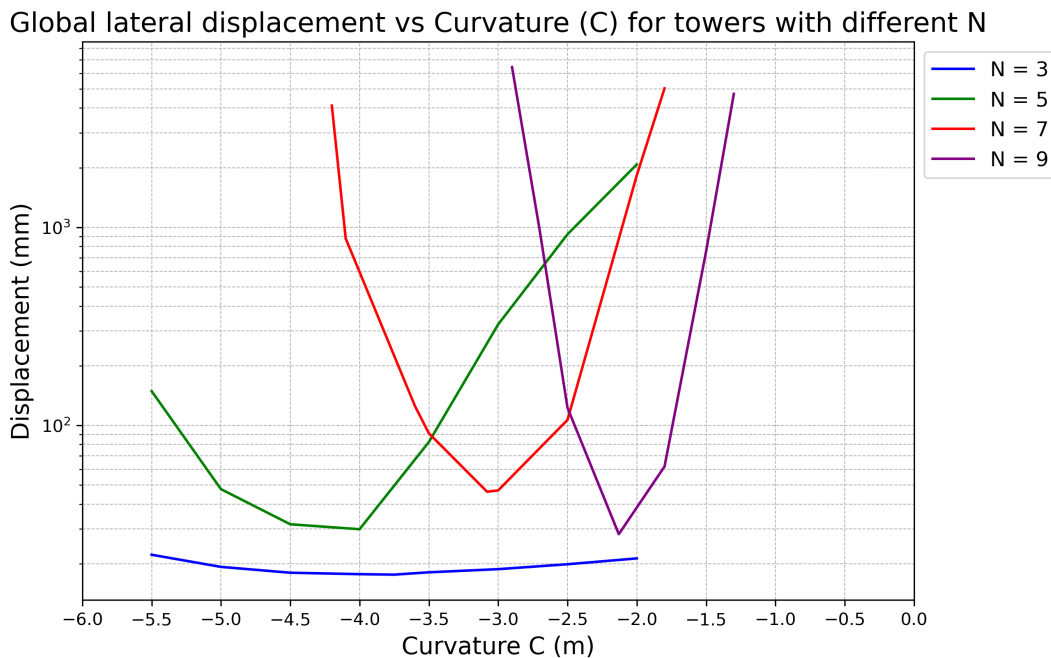


**Figure 6.1:** Towers with the triangular topology and different shape factors  $N$  and their response to wind loads whenever curvature  $C$  is adjusted. Results are displayed as global lateral displacements (in mm) against the curvature  $C$  (in m).

Stiffest design variants for every shape factor  $N$  and their corresponding performance parameters are provided in Table 6.1. It can be observed that that the displacements in general increase as the shape factor  $N$  becomes larger. An additional performance characteristic is introduced which is the strain energy, measured in kNm. This metric provides insights in the change in the elastic energy when the structure is subjected to wind loads. Specifically, the tower that absorbs less energy for a given loading case deforms less and the distribution of forces within each member and node is more uniform. Ultimately, low strain energy indicates a more material efficient design. Thus, from Table 6.1 it can be read that the values associated with strain energy does increase as shape factor  $N$  becomes larger. This can allude to a potential conclusion that towers with a higher number of polygon sides for its ring do perform in a less material-efficient manner. However, this study does not account for mass changes for tower structures taking a different shape factor. As it can be seen and understood from Table 6.1

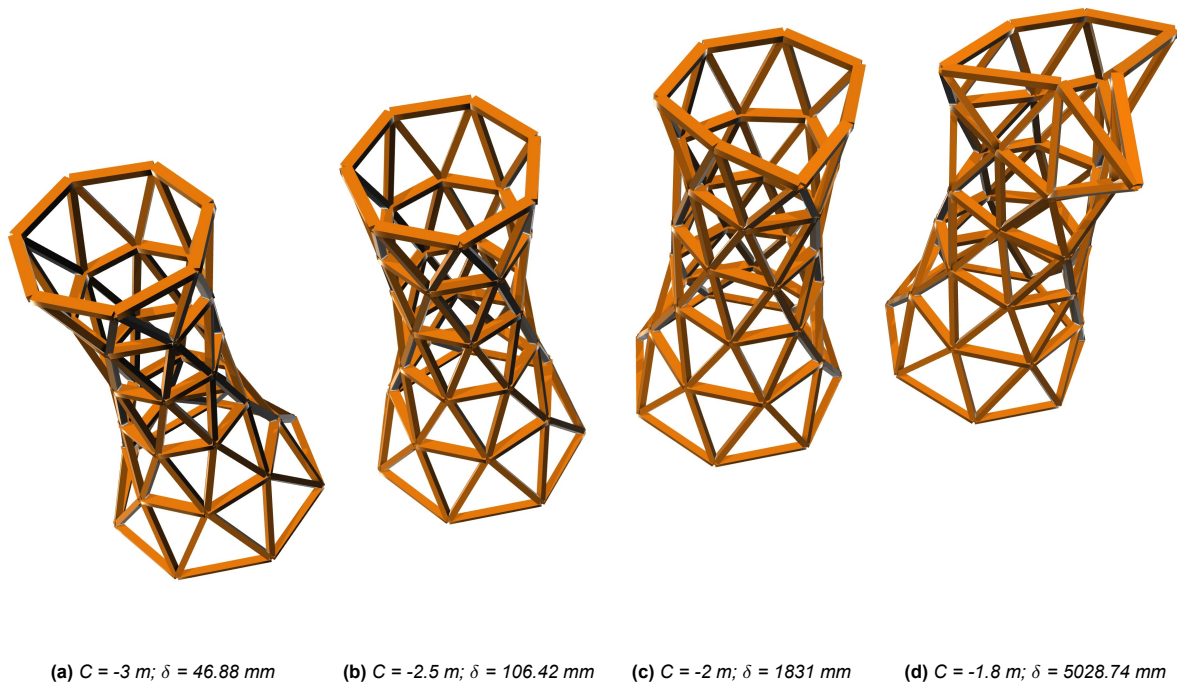
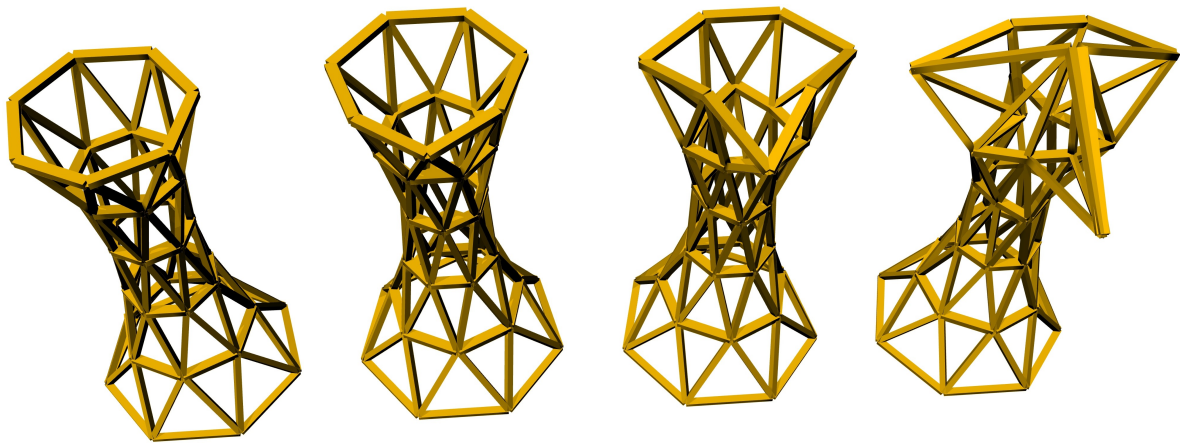


**Figure 6.2:** Illustration of the deformed tower variant employing a shape factor  $N = 7$  with its curvature variable  $C$  being increased (tower is widening). It can be observed that when the structure is subjected to the proposed wind profile, its deformed shape is quite rapidly approaching global buckling, while becoming less hyperbolic with just a little increase in curvature. It is of essence to note that the depicted deformations are on a 1:1 scale with actual displacements. Sub captions inform about the employed curvature variable  $C$  along with the corresponding global displacement  $\delta$ .

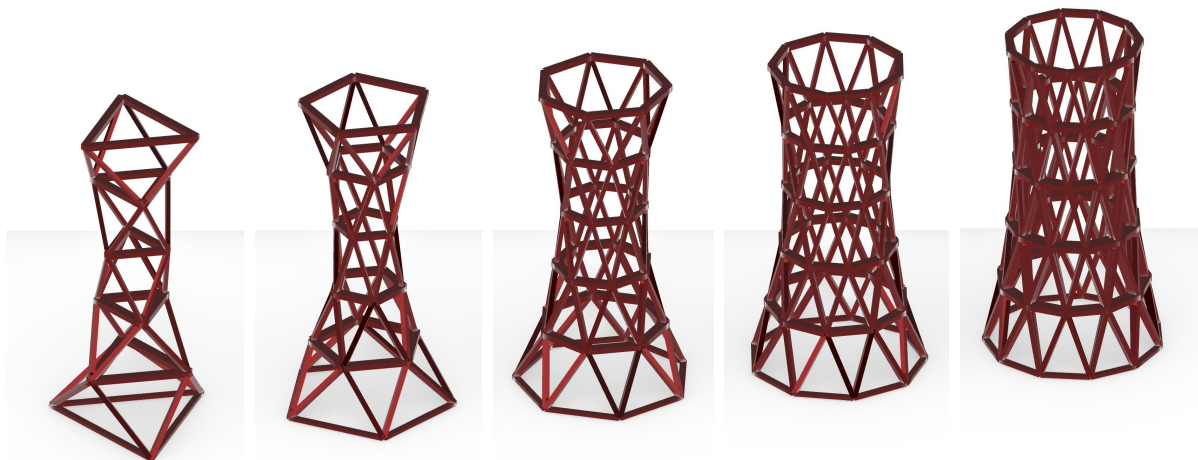
that throughout this analysis diagonal and ring members for each design variant were of the same size and mass increased along with the shape number  $N$ . As  $N$  grows, the stiffest configuration is becoming less hyperbolic (more of a barrel-like shape) and in turn results in a higher requirement for material. However, this can be accounted for as member sizes can be re-adjusted and scaled in such a way to make all tower variants achieve constant mass. The mass applied was equivalent to the design of the tower having a shape factor  $N = 7$ , which was equal to  $m = 66.76 \text{ t}$ . Performance metrics after this adjustment are shown in Table 6.2. It can be seen that discrepancy in strain energy and displacements is even more pronounced, evident (and visualized in Figure 6.5). Consequently, it can be inferred that the most efficient and sought after design aspects while taking into consideration mass and stiffness can be achieved by minimizing shape factor  $N$ . In addition, a very practical aspect is the number of nodes within the structure, that engineers usually strive to minimize as it corresponds to a more economic design. Thus, a lower shape factor  $N$  also translates to a more cost-effective design choice.

In terms of the overall hyperbolic shape and its rather stiff nature exemplified by these findings could be explained by simulating a fixed cantilever subjected to lateral loads and its shape in the lower half resembling one of the bending moment resulting from such loading conditions. It should be noted as well that given that the curvature is moving away from the cylindrical shape, the total surface area decreases along with projected wind loads. Moreover, due to their double curvature, hyperboloid structures facilitate the distribution of both vertical and horizontal forces. This feature guarantees that load concentrations are less prevalent throughout the assembly, resulting in a more balanced and efficient load transfer. These characteristics provide rationale behind the how hyperbolic shape deems structures more stable and



(a)  $C = -3.6 \text{ m}$ ;  $\delta = 124.85 \text{ mm}$     (b)  $C = -4.1 \text{ m}$ ;  $\delta = 877.53 \text{ mm}$     (c)  $C = -4.2 \text{ m}$ ;  $\delta = 4114.20 \text{ mm}$     (d)  $C = -4.3 \text{ m}$ ;  $\delta = 13207.31 \text{ mm}$

**Figure 6.3:** Illustration of the deformed tower variant employing a shape factor  $N = 7$  with its curvature variable  $C$  being decreased (tower is narrowing). It can be observed that when the structure is subjected to the proposed wind profile, its deformed shape is very rapidly approaching global buckling, while becoming more hyperbolic with just a little decrease in curvature. It is of essence to note that the depicted deformations are on a 1:1 scale with actual displacements. Sub captions inform about the employed curvature variable  $C$  along with the corresponding global displacement  $\delta$ .



(a)  $N = 3$ ;  $C = -3.75 \text{ m}$     (b)  $N = 5$ ;  $C = -4.14 \text{ m}$     (c)  $N = 7$ ;  $C = -3.08 \text{ m}$     (d)  $N = 9$ ;  $C = -2.13 \text{ m}$     (e)  $N = 11$ ;  $C = -1.53 \text{ m}$

**Figure 6.4:** Illustration of towers with varying shape factors. These variants represent the structure that has shown stiffest response to wind loads. It can be seen that as the shape factor  $N$  grows, the stiffest response is associated with tower shapes that become increasingly more cylindrical with their respective curvature  $C$  values increasing.

stiff under proposed loading conditions. However, the impact of the hyperboloid seems to diminish with higher shape factor  $N$  as stiffest configuration is one approaching a barrel-like shape. Nevertheless, a more contributing aspect here becomes the diminishing angle at which each ring element connects to a node, deeming the ring more deformable. Stability is maintained for these shapes with higher  $N$  by keeping diagonal members arriving at each node at less acute angles and retaining a more cylindrical profile. 'Snapping through' problem is reduced in this case as nodes are collectively kept within the

**Table 6.1:** Stiffest shape of towers taking different shape factors  $N$  and their respective results relating to global displacement, strain energy and mass. It should be noted that mass is not constant as same size members are used to construct the ring and diagonal elements.

N	C (m)	Displacement (mm)	Strain Energy (kNm)	Wind (deg)	Mass (t)
3	<b>-3.75</b>	<b>17.60</b>	0.86	31	41.21
5	<b>-4.14</b>	<b>27.91</b>	1.06	270	52.56
7	<b>-3.08</b>	<b>46.16</b>	1.36	90	66.76
9	<b>-2.13</b>	<b>28.17</b>	1.59	230	80.22
11	<b>-1.53</b>	<b>40.65</b>	2.12	152	92.52
15	<b>-0.81</b>	<b>59.57</b>	3.38	267	115.67

**Table 6.2:** Stiffest shape of towers taking different shape factors  $N$  and their respective results relating to global displacement, strain energy and mass. It should be noted that mass is being kept constant. This measurement does inform about the design variant exhibiting the most efficient structural behaviour.

N	C (m)	Displacement (mm)	Strain Energy (kNm)	Wind (deg)	Mass (t)
3	<b>-3.75</b>	<b>10.13</b>	0.47	31	67.47
5	<b>-4.14</b>	<b>20.50</b>	0.77	270	66.04
7	<b>-3.08</b>	<b>27.04</b>	1.36	90	66.76
9	<b>-2.13</b>	<b>33.55</b>	1.91	230	65.87
11	<b>-1.53</b>	<b>58.52</b>	3.10	152	67.09
15	<b>-0.81</b>	<b>105.93</b>	6.09	267	66.2

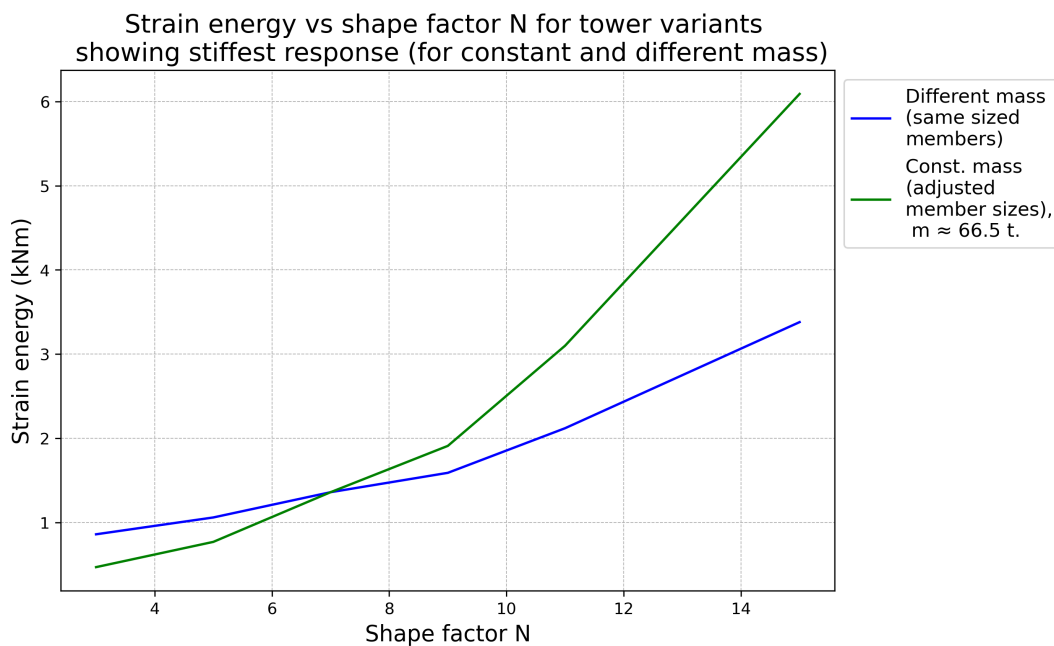


**Figure 6.5:** Towers variants showcasing the stiffest response to wind loads and different shape factors  $N$  and their respective strain energy (kNm). Findings inform about the most efficient design as strain energy indicate how much structure is affected by external loads. Lowest strain energy correspond to an efficient design. After adjusting structures to maintain constant mass for varying  $N$ , discrepancies in efficiency become even more apparent.

same plane characterised by lower overall curvature and reduced level of nodal force eccentricity.

### 6.1.2. Tower stiffness in response to simplified point loads

In order to showcase the importance of utilization of wind loads taking a non-uniform profile, an analysis is performed that showcases how a tower with a triangular topology responds whenever subjected to uni-directional loads applied at each node. This is done as to prove the extent to which the structure's behaviour is effected by loading conditions.

By taking a tower and subjecting it to point loads as illustrated in Figure 6.6, the effect of change in curvature  $C$  on the stiffness of designs with different shape factors  $N$  is recorded. In this comparative study, it should be noted that a total load of 500 kN is arbitrarily selected and divided per every node within each structure in order to ensure uniformity in testing conditions. Additionally, a constant mass is allocated per every tower design regardless of what shape factor  $N$  or curvature  $C$  is employed. Thus, in Figure 6.7 the results are displayed and it can be observed first hand that all tower designs regardless of the geometric configuration of rings, be they even or odd-sided polygons (even or odd  $N$ ), the response to uni-directional point loads is always stiff and stable. This observation and results do not agree completely with findings provided in Section 5.1 as no kinematic mechanisms are observed. Nevertheless, these loading conditions do not align with ones relating to critical, instability-inducing force vectors presented in Figure 5.6. However, there is still a distinction between towers with shape factors  $N = 4$  and  $N = 6$  as their displacement curve contains variability and fluctuations. On the contrary, tower structures with shape factors taking odd values like  $N = 3, 5$  and  $7$  are depicted with a curve that is way smoother. This still reinforces assertions made in previous sections about the reliability and stability of towers taking triangular topology. Specifically, towers, characterised by even-valued shape factors  $N$ , are less stable and predictable in response compared to ones showcasing odd-valued  $N$ . Additionally, as the curvature  $C$  grows the displacement values do decrease generally for towers except for one characterised by shape factor  $N = 3$ , which tends to show that displacements do grow as the shape becomes more of a barrel-like one for this configuration. However, the most essential point to note here is the fact that tower variants with the shape factor  $N = 5$  and  $N = 6$  perform most favorably as their displacement values are lowest overall. Nevertheless, the structure featuring pentagon rings ( $N = 5$ ) does appear to be a more desirable choice as it exhibits more predictable and linear response.

Overall, this test showcases that the choice of the wind profile in accordance with the 'Eurocode' guidelines does enrich the analysis of towers characterised by the triangular topology. By exposing the structure to non-uni-directional force vectors that represent a heavily unfavorable case, the outcomes do highlight design limitations in a more pronounced fashion. Highly adverse loading scenarios force the design process to converge into a narrow space of tower design possibilities. Given that these options satisfy proposed design criteria, the procedure indeed reaches the most optimal choice. On the contrary, in case of a simplified point load case, the design space does not seem to narrow down as the influence of changing curvature  $C$  (or which curvature  $C$  for a hyperboloid yields best results) is not that apparent for these anti-prism towers taking different shape factors  $N$ . Ultimately, it is of importance for a designer to emulate real-life loading conditions as closely as possible as such choice quite rapidly produces the most effective and favorable design outcome.

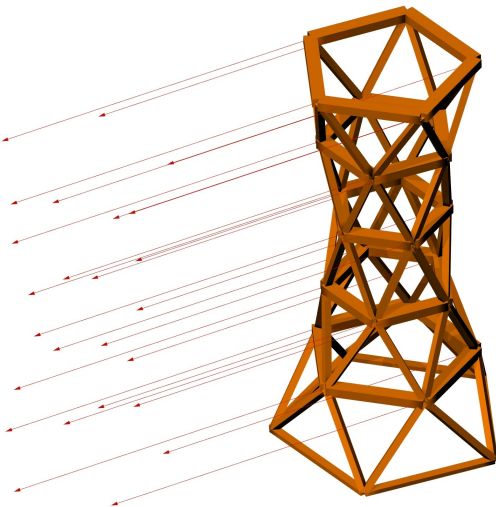


Figure 6.6: Illustration of the nodal point loads applied to the tower.

Displacements vs curvature C  
for towers with varying N subjected to horizontal  
nodal point loads (mass is kept constant at  $m = 66.65 \text{ t}$ )

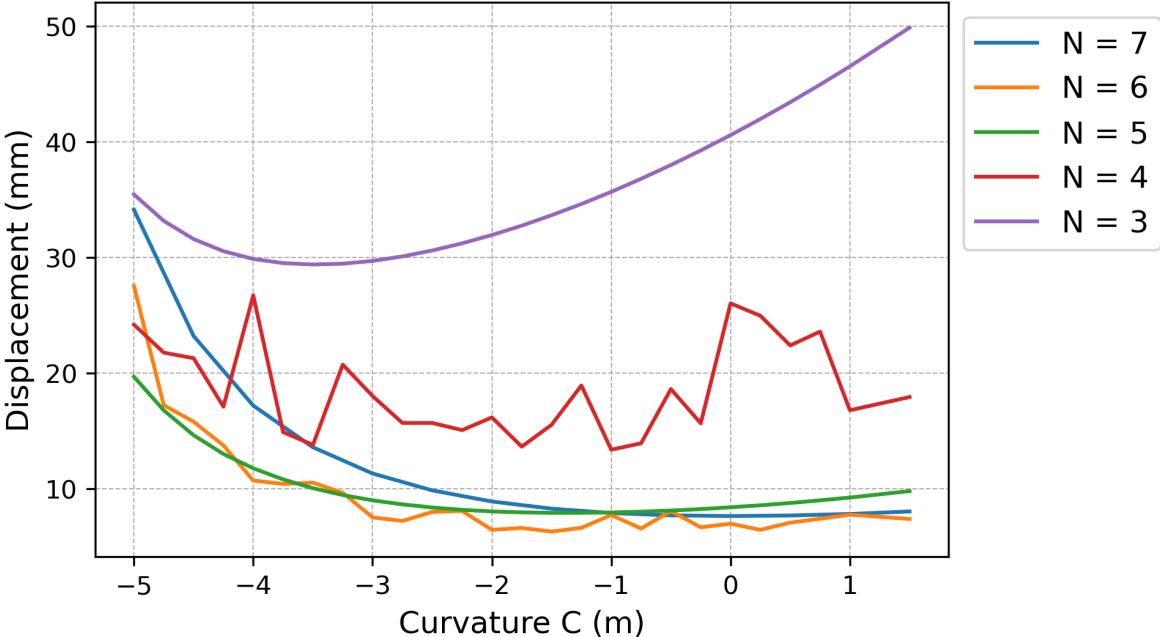
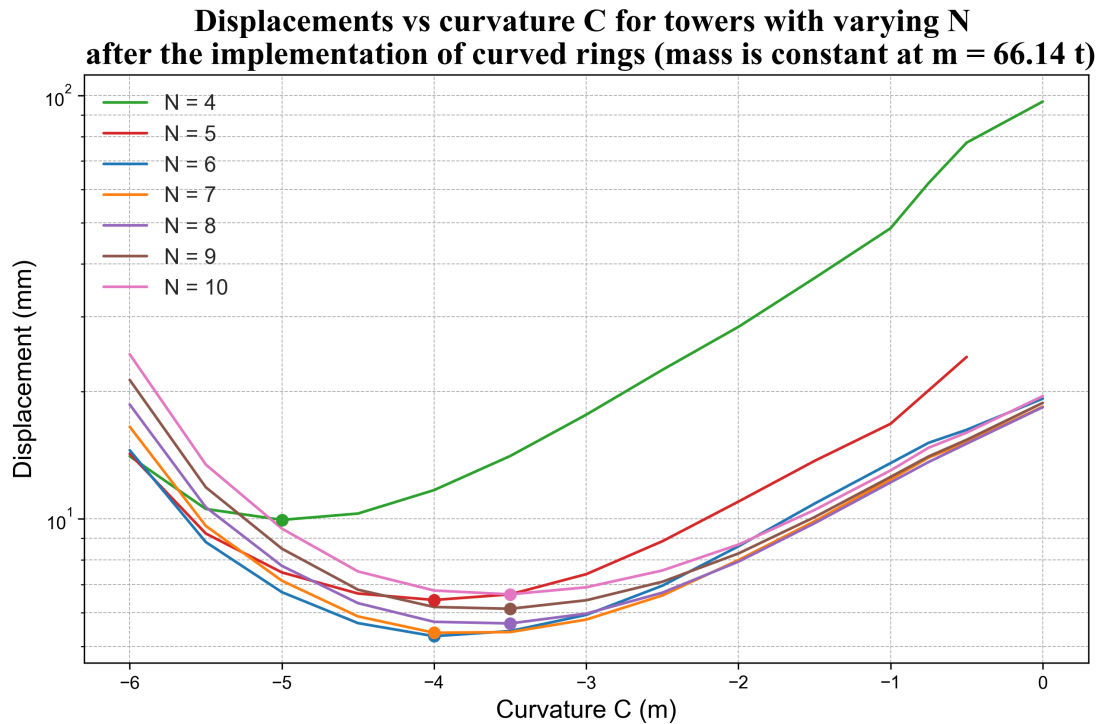


Figure 6.7: Tower variants with different shape factor N after being subjected to horizontal nodal point loads. The curvature C is varied for every design variant and displacements are recorded. It can be observed that all design variants exhibit a stable and stiff response to this simplified loading case.

## 6.2. Curved ring elements

The occurring instability and kinematic mechanisms observed in towers following a triangular topology and specific shape factors  $N$  necessitates the inclusion of elements to address this limitation and perhaps restrict the free (non-strain inducing) nodal movement within each ring. Thus, the proposed deployment of curved circular rings as a replacement for the one composed from straight pin jointed members. This modification also brings benefits in terms of the assembly's constructability. Instead of converging six straight members at a unified joint, this configuration allows continuous passage of circular rings through the joint. Meanwhile, four diagonal members connect to the ring from both the top and bottom. For this new configuration, the curvature variable  $C$  has been iterated for tower designs taking different shape factors  $N$ . It is of importance to note that loading conditions are representative of the wind profile in accordance with the 'Eurocode' guidelines, and a more detailed elaboration can be found in Chapter 4. Thus, Figure 6.8 depicts how the new design with different shape factors  $N$  responds to lateral wind loads while curvature  $C$  is iterated. It can be viewed that all design variants exhibit a stable and stiff response for this loading case. As curvature  $C$  grows, there appears to be a trend of increasing tower stiffness, which then converges to a consistent level (indicated by  $C = -3.61 m$ ). By glancing at the placement of markers (representative of the lowest displacement value for a given shape factor  $N$ ), it can be stated that for each shape factor  $N$ , there is a particular hyperbolic tower shape which results in a stiffest behaviour (see Figure 6.9). Furthermore, tower designs that exhibit the lowest overall displacement values are characterized by shape factors of either  $N = 6$  or  $N = 7$ . Finally, as the curvature increases (the global shape is approaching a barrel-like one), the stiffness of all tower designs have shown to decrease quite substantially.

Reported findings suggest that the incorporation of curved continuous rings omits the incidence or probability of global buckling, an effect which was more pronounced at the tower's apex, as illustrated in Figures 6.2 and 6.3. Instead, the structure now showcases a more uniform deformation, closely resembling that of a fixed cantilever as displayed in Figure 6.10. Focusing on the markers representing the lowest displacement in Figure 6.8, and analysing the most stiff tower variant across various shape factors  $N$  in terms of strain energy, it is evident in Table 6.3 that the tower structure with the greatest material efficiency continues to be characterised by the shape factor  $N = 6$ . This assembly showed lowest values in displacement and in strain energy, although differences between these metrics among all towers are minimal. Thus, for this curved ring configuration, designers do not require to emphasize the performance and efficiency aspects whenever the shape factor  $N$  surpasses 5. Figure 6.11 illustrates findings from Table 6.3 along with the scenario whenever the tower takes lower mass (44.23 t instead of 65.14 t due to slimmer members). This is done to emphasise a greater discrepancy in efficiency among tower structures defined by different shape factors  $N$ . As it should be expected, for both scenarios, shape factor  $N = 6$  prevails as the most favorable design choice. Finally, it is imperative to conduct a comparative study of towers utilizing solid curved rings and those equipped with segmented rings. By ensuring that both new and old tower configurations are compared fairly and comprehensively, the mass is kept constant at approximately  $m \approx 65.5 t$ . The constant mass is enforced by adjusting member cross-sections accordingly in relation to the change of total length when a new configuration of the structure is achieved. The improvement in efficiency and stiffness of towers equipped with solid curved rings over segmented rings in earlier designs is well illustrated in Figure 6.12. The introduction of this innovation leads to significant decrease in both displacement and strain energy metrics. Therefore, it is evident that solid curved rings are a huge upgrade in the tower's design.



**Figure 6.8:** Tower variants with different shape factor  $N$  after the implementation of curved ring members while maintaining constant mass. The curvature  $C$  is iterated for every design variant and displacements are recorded. It can be observed that all design variants exhibit a stable and stiff response to this loading case. As curvature ( $C$ ) grows, there appears to be a trend of decreasing tower stiffness, which then converges to a consistent level. Markers indicate the lowest displacement recorded for towers with different shape factors  $N$ . Note that the y - axis (displacements) is scaled logarithmically.

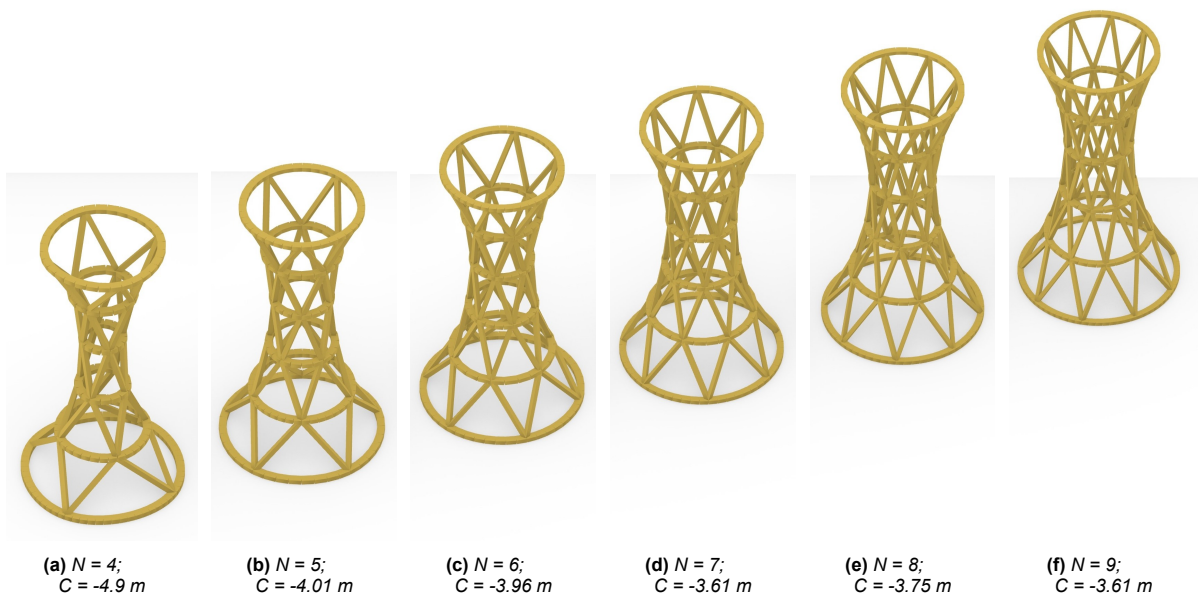


**Figure 6.9:** Illustration of towers (constant mass) with varying shape factors after the implementation of curved rings. These variants represent the structure that has shown stiffest response to wind loads. It can be seen that as the shape factor  $N$  grows, the stiffest response is associated with tower shapes that steadily converge into a hyperboloid with a curvature value  $C = -3.61$  (also described in Table 6.3).

The introduction of curved, smooth rings has drastically affected the stiffness of the structure. The values for displacement have improved significantly from those for assemblies free of curved elements.

The benefit of using smooth, uninterrupted rings is that they help stiffen the structure by absorbing the in-plane bending moment brought forward under the influence of the wind profile, while the structure is squeezed (see figure 6.13). Additionally, as kinematic mechanisms associated with the segmented towers defined by a triangular topology have a free top level component, thus, even by placing a single ring at the top, the structure becomes immobilized and any free nodal displacement is restricted.

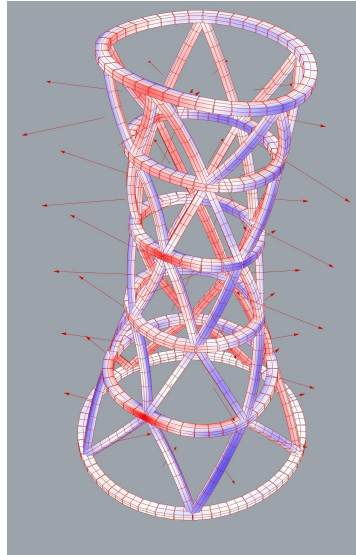


**Figure 6.10:** Deformed shape of the tower with curved rings, after exposure to the proposed wind profile (as indicated by the red arrows). It can be seen that that global shape does not tend to any instabilities and tower deforms laterally as a unit. This is due to immense in-plane stiffness facilitated by the solid ring, which resists loading in bending. Blue colour indicates members in tension while red represents members in compression. It is important to state that the illustrated deformation has been magnified 400 times compared to the actual values.

**Table 6.3:** Stiffest shape of towers taking different shape factors  $N$  and their respective results relating to global displacement, strain energy and mass after the implementation of curved ring members. It should be noted that mass is being kept constant. This measurement does inform about the design variant exhibiting the most efficient structural behaviour. It can be observed that these results indicate that this design variant significantly more efficient in comparison to the results relating to designs with segmented rings (see Table 6.2

N	C (m)	Displacement (mm)	Strain Energy (kNm)	Wind (deg)	Mass (t)
4	<b>-4.9</b>	<b>9.88</b>	0.29	140	65.14
5	<b>-4.01</b>	<b>6.37</b>	0.28	54	65.14
6	<b>-3.96</b>	<b>5.23</b>	0.25	46	65.14
7	<b>-3.61</b>	<b>5.15</b>	0.29	63	65.14
8	<b>-3.75</b>	<b>5.59</b>	0.28	124	65.14
9	<b>-3.61</b>	<b>6.02</b>	0.32	101	65.14
10	<b>-3.61</b>	<b>6.52</b>	0.34	171	65.14

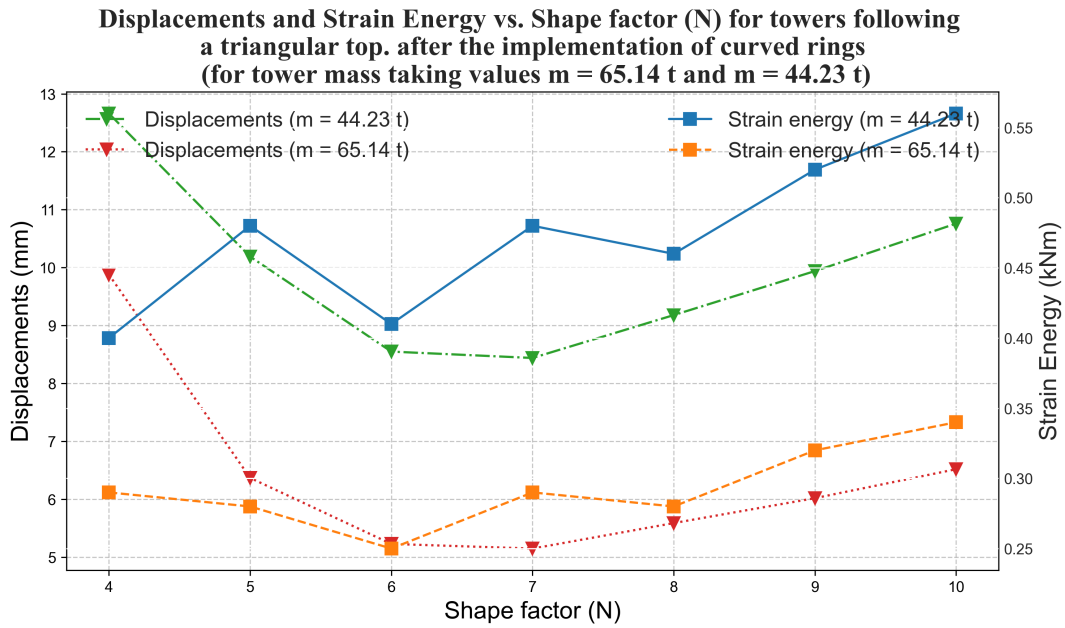


**Figure 6.11:** Displacements and strain energy plotted against the shape factor  $N$ . Each marker represent the stiffest tower with curved rings shape for every  $N$  derived from Table 6.3 while the mass is kept constant at  $m = 65.14 t$ . Additionally, for comparative purposes the mass of the tower has been reduced to  $m = 44.23 t$  and metrics were recorded again. Findings indicate that regardless of the mass, the most efficient behaviour has been exhibited by the tower design characterised by  $N = 6$  as strain energy and displacements are lowest in this case.

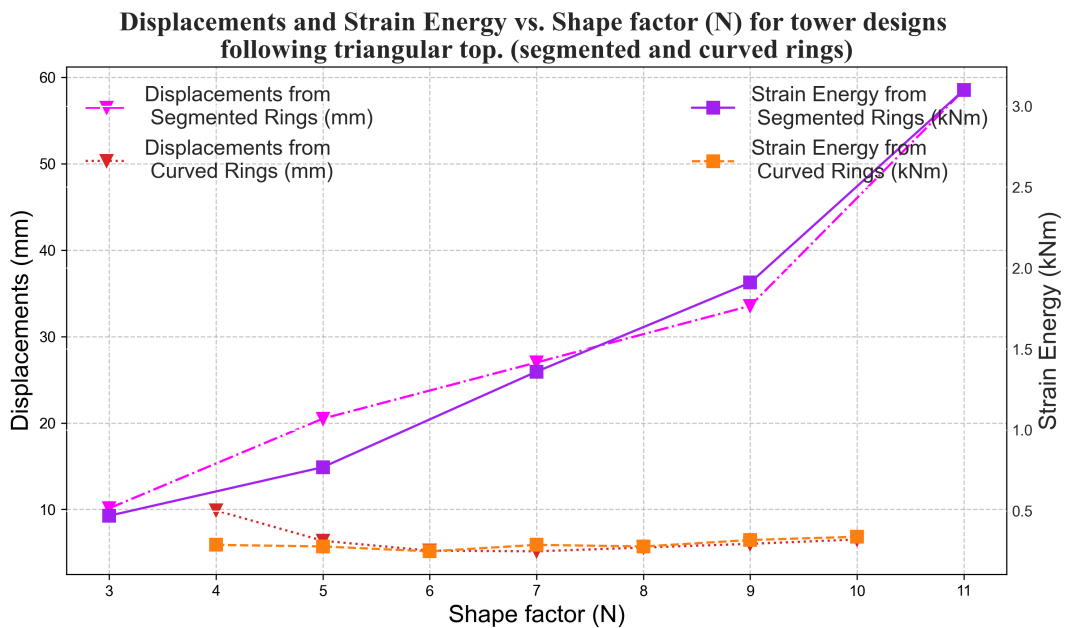


**Figure 6.12:** In the this plot, displacements and strain energy are graphed against the shape factor  $N$ . Each data point represents the configuration with the highest stiffness for a given  $N$ , adhering to a triangular topology with curved and segmented rings, as detailed in Tables 6.3 and 6.2. This analysis maintains a constant mass of approximately  $m \approx 66t$  for each tower configuration, facilitating a direct comparison of the impact of curvature  $C$  on displacement and strain energy characteristics. It can be seen that after the implementation of curved rings into tower design, strain energy and displacement drops down by on average a factor of 5 to 7.

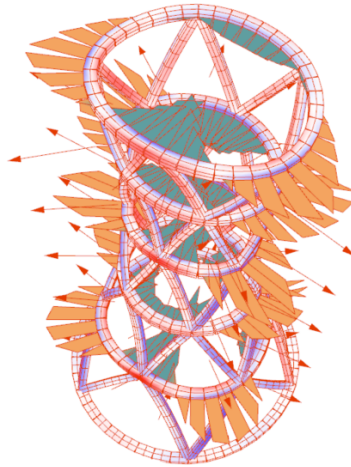


**Figure 6.13:** Illustration of restorative bending moments within curved rings to counter-act the squeezing action exerted by the wind load. Red arrows indicate wind load profile for each face of the tower.

### 6.3. Elaboration on results and discussion

#### TO BE CORRECTED

This chapter has provided a thorough parametric study concerning the effects that certain combinations of curvature  $C$  and shape factor  $N$  holds on tower's stiffness against proposed wind profile. The initial segment of the research focused on the structure composed of triangular topology and segmented rings. The findings suggests that the stiffness of the tower is highly sensitive to variations in curvature  $C$ , with the range leading to minimal displacements being notably limited. This implies a critical relationship between the curvature of the structure and its overall stability, highlighting the importance of precise curvature control in the design and construction of such variants of towers.

The main insight from this section is the heightened structural stiffness due to the tower's hyperboloid geometric shape. This configuration was proven to enhance global stiffness, as the most minimal displacement levels were observed with curvatures  $C$  remaining under 0 m across various shape factors  $N$ . This underlines the significant influence of the hyperboloid shape in optimizing the tower's structural resilience. In terms of further elaboration of this structural behavior, it's observable that in a two-dimensional view, the hyperboloid essentially represents an arch mirrored along its axis, which is subjected to wind forces. By modelling this simplified arch in 'Karamba3D' environment, shown in Figure 6.14, one can observe that the benefit of this set-up is a balanced incorporation of beam members (diagonals) as well as horizontal posts (ring members) to find equilibrium against imposed point loads. Through utilization of a catenary arch that resembles best the shape of the moment line of a straight beam subjected to equivalent loads, the most optimal stiffness characteristics are achieved. Compression in the arch reduces loads on horizontal posts (which have their own spring stiffness), thus, global displacements are reduced. This analogy translates well in attempts to justify obtained results that verify the hyperboloid shape as beneficial for tower's lateral stiffness. One should note, however, that this simplification does not completely capture the essence of actual modelled loading conditions which entail non-uniform wind profile acting upon the representative mesh of the tower as loads do increase along the height of the tower and vary significantly along its diameter. Additionally, this example uses

point loads acting horizontally and not perpendicularly in relation to the surface.

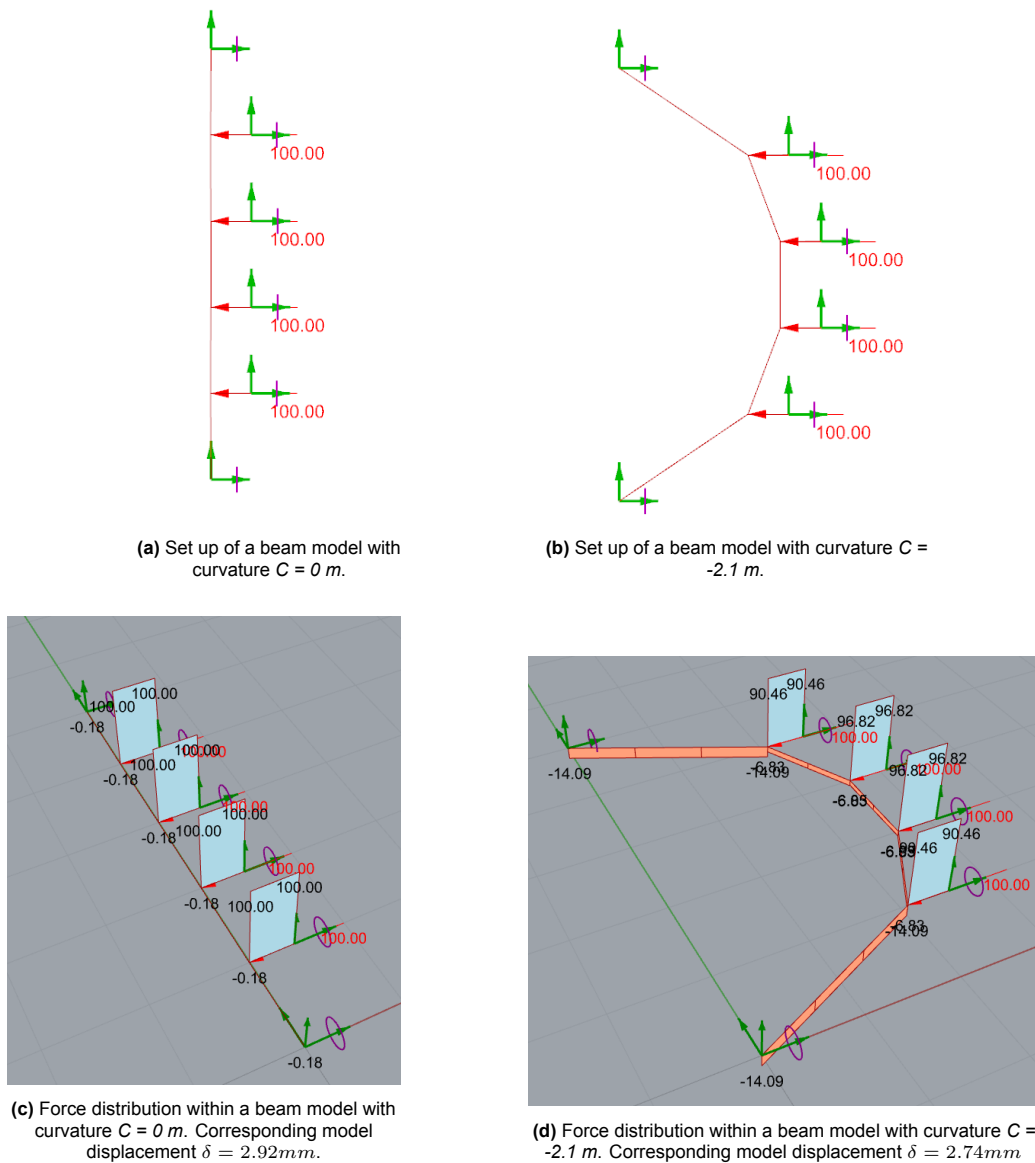


**Figure 6.14:** Simplification of the hyperboloid by projecting it to a 2D plane as an arch. Horizontal posts represent ring (circumferential) members, which in this case can be perceived as springs with a certain stiffness.

A further iteration of the model is required and is shown in Figure 6.15. In this instance, loads are acting perpendicular to the surface of the arched beam as force vectors re-adapt with the changing curvature. Enhancing the model's accuracy, horizontal supports have been substituted with inclined ones, linked to both the supports and the beam via pinned joints extending to the beam's end (where the free end of the tower is positioned). In this way, the simplification includes angles at which circumferential members join diagonal members within the tower structure. In order to replicate closely orientation and length of ring members corresponding to different shape factors  $N$ , associated polygons are drawn next to each point where rings connect to diagonals. Different shape factors yield different length and orientation of inclined posts, which in turn decide the stiffness of an equivalent spring. Figure 6.16 displays the representative configuration of inclined bars associated to shape factors  $N$ , and the resulting stiffness

of an equivalent spring subjected to a point load. When the shape factor  $N$  grows, the two bars that constitute a ring in the tower act as a spring with diminishing stiffness. This occurs as the angle ( $\alpha$ ) between the bars enlarges, affecting the equivalent stiffness due to the influence of the squared cosine component in the stiffness formula. The insights gained in this chapter align with the equivalent stiffness model, affirming that larger shape factors indeed have a detrimental effect on the overall stiffness of the tower.

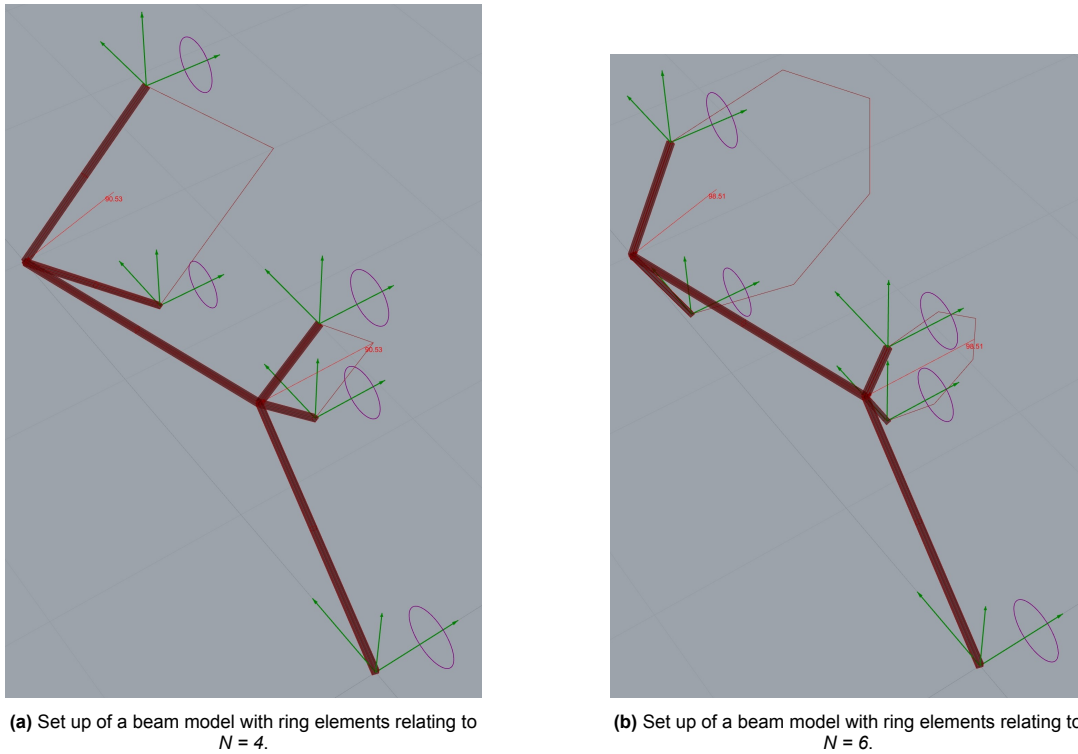


**Figure 6.15:** A more elaborate explanatory arch beam model providing representative ring elements that do re-adjust in orientation and length in accordance with the shape factor  $N$  utilized. Note that loads are applied directly and perpendicular to the shape of the tower arch. Note that green arrows and a purple circle indicate degrees of freedom of simple pinned supports.

Additionally, relating the component of curvature into this equivalent stiffness model, it is observable that with the growth of  $C$  in magnitude (tower shape is more hyperbolic), the diameter of the enclosing circle is reducing, in turn affecting the length of the ring member. Thus, Figure 6.17 shows the growth of the stiffness of the equivalent spring as the radius of the tower ring is diminishing. This is true for all shape factors. Such a feature again justify the shape of the hyperboloid as a beneficial one in terms of the global stiffness.

The occurrence of large deformations whenever curvature  $C$  would be quite too large (resembling a really narrow tower structure) or too small (a barrel shape) especially at the top ring (as portrayed in Figures 6.2 and 6.3) can be attributed to the fact that wind loads are always acting perpendicular to the surface of the tower. By modelling a simple beam and spring configuration, one can view that for large curvatures, the load at the top acts away from the stiffest direction of the spring, thus, the upper beam is rotating around a fixed hinge to which a way stiffer spring connects. The higher stiffness of the spring in the middle part stems from the reduced bar length contributing to higher equivalent stiffness, as shown in Figure 6.17. As the tower's shape becomes less curved, the middle spring's

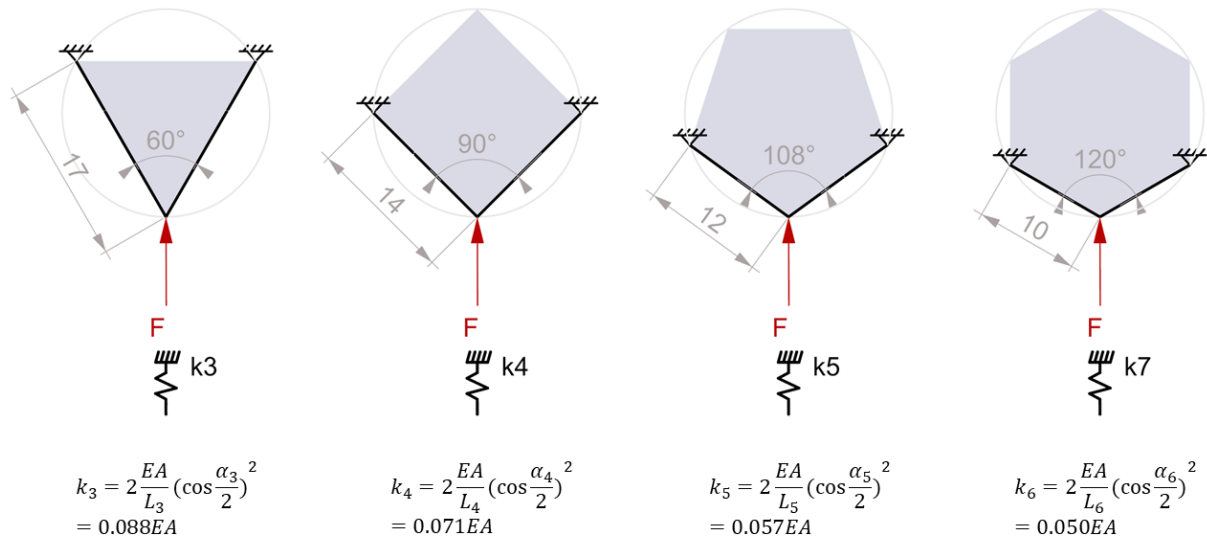
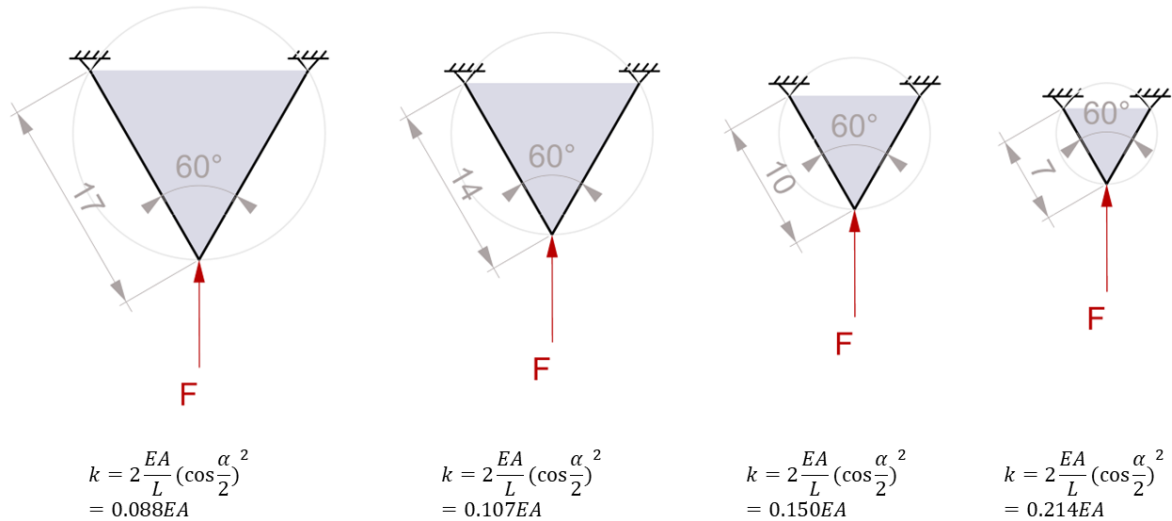


**Figure 6.16:** Representative spring models for tower rings taking different shape factors. All units are in m.

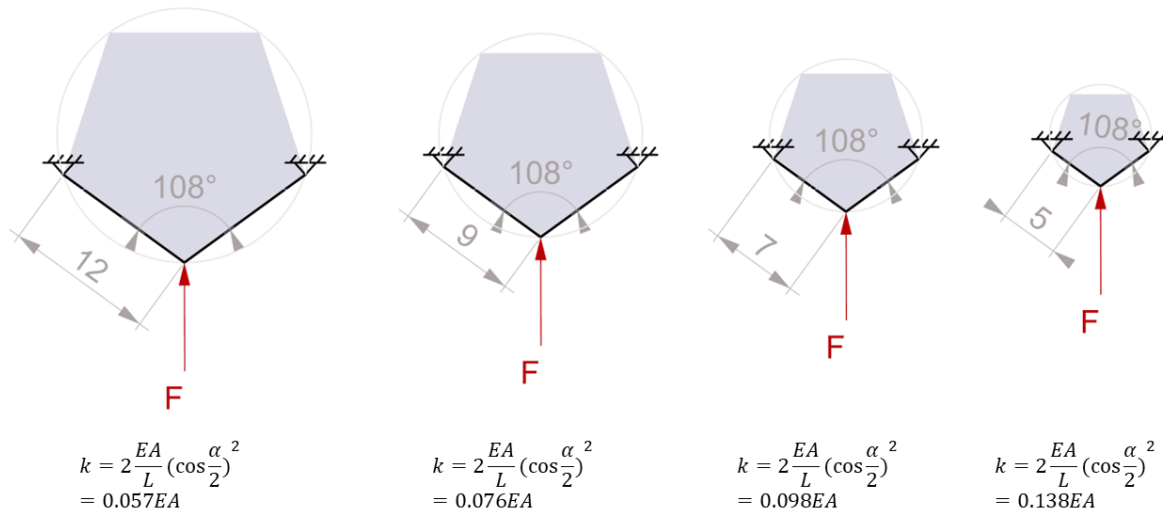
stiffness reduces. At the same time, the point loads on the structure increase. This is because as the tower starts to resemble a barrel shape, its surface area expands, leading to an increase in the wind forces it encounters. Thus, global displacements evidently grow, notably at the top, where point load direction still does not fully align with the stiffest direction of the spring. Moreover, higher wind pressure coefficient related to increasing height impose higher forces on the ring at the apex. Hence, The most optimal curvature stiffness wise encapsulates the configuration that attracts the least amount of wind at the top and at the lowest angle, while maintaining desirable level of stiffness in the central part of the tower.

Regarding the utilization of curved rings, this design component provides an solution to a diminishing ring stiffness observed in the previous design iterations. Maintaining a high ring stiffness at all times does result in significantly reduced displacements for all shape factors, as it is shown in Figure 6.12. However, in the same graph, one can view that displacements are quite large for a tower with a shape factor  $N = 3$  and  $N = 4$ . As circular beams resist loads by bending, span lengths of discrete ring elements (distance between vertices) do determine the stiffness of an equivalent spring. Figure 6.23 illustrates a rather low level of stiffness exhibited by the assembly with a shape factor  $N = 3$  as the resulting arch has significant length and rise (height). However, the stiffness grows with higher  $N$  and approaches its optimum at  $N = 7$  as detailed in Table 6.3.

This parametric study has shown the innate relationship between geometry and structural behaviour of the tower structure following a triangular pattern. The primary takeaway is the necessity to employ a hyperboloid configuration whenever the global shape of the tower is concerned. This design aspect brings sought after stiffness qualities regardless of the ring configuration (segmented or curved). In addition, aiming for a shape factor within the range of  $N = 5$  and  $N = 7$  would also yield lower global displacements. The optimal curvature  $C$  that enhances the structural stiffness of the tower is dependent on the design choice between segmented rings or a curved ring configuration. For the latter approach, as documented in Table 6.3 and depicted in Figure 6.8, a curvature of approximately 3.61 meters is identified as the most advantageous for stiffness, applicable particularly when the shape factor  $N$  ex-



(a) Set up of a beam model with ring elements relating to  $N = 3$ .



(b) Set up of a beam model with curvature  $C = -2.1 m$ .

**Figure 6.17:** A more elaborate explanatory arch beam model providing representative ring elements that do re-adjust in orientation and length in accordance with the shape factor  $N$  utilized. Note that loads are applied directly and perpendicular to the beam.

ceeds 7. Conversely, for designs that incorporate segmented rings, an increase in the shape factor corresponds to a stiffer structural response at a reduced curvature, aligning with a tower profile that more closely resembles a barrel shape. The underlying principle for this phenomenon is not completely understood to the core by the author. Nevertheless, it can be hypothesized that the diminishing stiffness of the top ring, as the shape factor grows, is so pronounced that a greater curvature forces this element to displace quite substantially. Thus, for higher shape factors, the tower assembly finds itself to be most optimal when wind load vector at the top ring is as horizontal as possible even though the total load on the tower is higher, despite an overall increase in the load experienced by the tower.

It should be noted that mass has been kept constant throughout this parametric stiffness study by re-adjusting member sizes in accordance to the total element length within the structure. For example, shape factor  $N = 10$  will yield thinner members than  $N = 5$ . Therefore, for towers employing curved

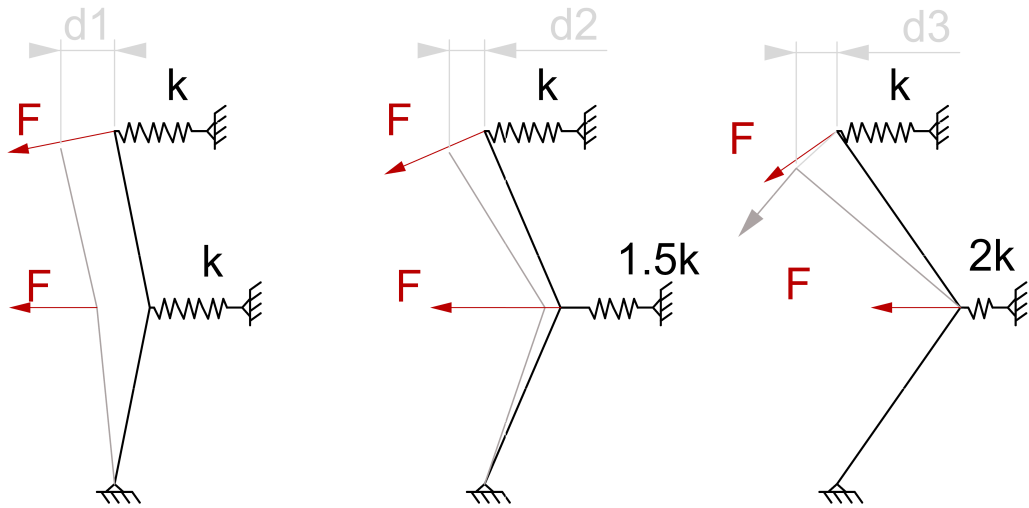


Figure 6.18: Set up of a beam model with ring elements relating to  $N = 3$ .



Figure 6.19: Set up of a beam model with curvature  $C = -2.1$   $m$ .



Figure 6.20: Set up of a beam model with curvature  $C = -2.1$   $m$ .

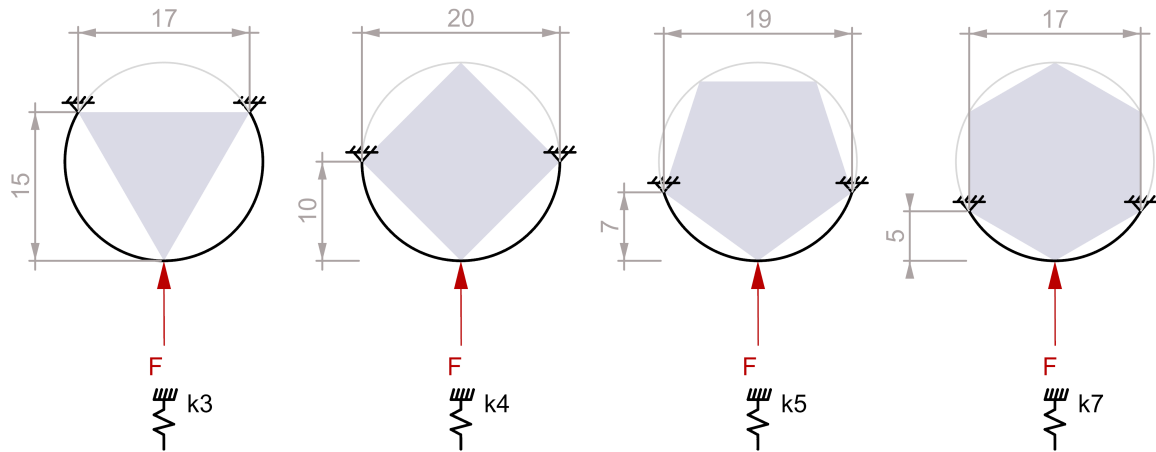


Figure 6.21: Set up of a beam model with curvature  $C = -2.1$   $m$ .

Figure 6.22: A more elaborate explanatory arch beam model providing representative ring elements that do re-adjust in orientation and length in accordance with the shape factor  $N$  utilized. Note that loads are applied directly and perpendicular to the beam.

rings, it can be stated that after the tower structure is exceeding shape factor  $N = 7$ , thinning members reduce the stiffness of the structural arch, thus, displacements grow.

In terms of recommendations for designing these kind of the timber towers employing a triangular pattern with segmented or curved rings, the process should focus on utilizing wind loads characterised by a non-uni-directional, and non-uniform in magnitude profiles. This choice enabled to re-create the



**Figure 6.23:** Given the implementation of curved (circular) rings, the spring model relies on bending of curved elements. All units are in m.

most unfavorable loading case that allowed to discover shapes that yield most sought after performance metrics in terms of stiffness.

For designing timber towers that feature triangular patterns with either segmented or curved rings, it is advisable to design by imposing wind load profiles that are neither unidirectional nor uniform in intensity. By simulating the most adverse loading scenarios with these complex wind patterns (following guidelines provided by Dutch building code NEN-EN 13782:2015, titled "Temporary structure - Tents Safety.") one can identify the tower geometries that offer the most desirable stiffness characteristics. By simply imposing uni-directional point loads of arbitrary magnitude on each node, the findings would be harshly different: the most optimal shape would be close of a barrel one with quite high stiffness characteristics. However, the proposed wind profile allowed a more intricate, challenging yet more fruitful exploration of the most optimal design.

# 7

## Stiffness Studies of the Custom Pattern

In this chapter, the analysis of the tower is presented, considering a custom pattern whose geometry and composition were described in Chapter 4. The analysis particularly dives into curvature effects on the tower's performance, particularly in connection to the overall global (lateral) stiffness when subjected to the presented wind profile as well as simplified loads later on. The effect of segmented and curved rings is also studied.

### 7.1. Curvature Influences

Similarly as before the analysis shall compare global displacement values (in mm) for towers (with different  $N$ ) against the varying curvature  $C$  values. It should also be noted that for towers with each distinct shape factors  $N$  the most unfavorable wind direction has been applied by reaching maximum displacement.

In Figure 7.1, the results from the modeling analysis are illustrated. A pattern akin to that observed in towers with triangular topology is evident: lower curvature values ( $C$ ) are associated with substantially higher displacements. This indicates that at low  $C$  values, global buckling is likely to occur, associated to the tower adopting a more constricted hyperboloidal shape. Towers exhibiting a deformed shape due to low curvature values, denoted as  $C$ , are showcased in Figure 7.2. The most robust response to the proposed wind load profile is observed in towers with curvature values ranging from  $C = -4 m$  to  $C = -3 m$ , applicable across all shape factors, or  $N$ . In Figure 7.1, markers on the graph represent minimum displacements recorded for towers with different  $N$  values. Interestingly, as curvature  $C$  increases, there is a corresponding rise in displacement values. However, the overall response of the towers maintains stable, as these displacement values are relatively low compared to ones of towers characterised by a narrow hyperboloid. Towers exhibiting a deformed shape due to higher curvature values, denoted as  $C$ , are showcased in Figure 7.3. Ultimately, the specific shape factor, referred to as  $N$ , which appears to yield the most stiff reaction in the tower structure marked by custom topology, is identified as  $N = 3$ . This conclusion is drawn from the fact that the most minimal curve in Figure 7.1 corresponds with

the polygon ring configuration denoted by this specific shape factor. Meanwhile for all the other shape factors, the stiffness seems to reduce as  $N$  is growing.

For the interpretation of this data, one can immediately tell that the triangular tubular shape, which is consistently kept throughout the height of the tower provides a favorable effect on its stiffness. Triangular ring does not seem to cause global buckling at the top of the tower whenever the shape of the structure approaches a narrow hyperboloid as triangle is not a deformable shape. With the growth of the shape factor  $N$ , the approach angle of members to the node takes on a less acute angle. In addition, the susceptibility of the top ring to deformation increases with the number of nodes within it, thus, increasing the likelihood of snap-through phenomenon. This event is more likely to occur in the upper ring, which is unconstrained and free to move. This is particularly evident under the impact of the wind load profile, which imposes a compressive squeezing effect on the ring (can be observed in Figure 7.2). As curvature  $C$  increases, leading to a more cylindrical form of the tower, the observed rise in displacement across all shape factors  $N$  may not be singularly due to a decrease in the structure's stiffness. Instead, it could be related to an increase in the total surface area, which consequently attracts more wind, resulting in a greater load imposed upon the structure. Thus, as the curvature decreases from  $C = 0\text{ m}$ , the wind load effects drop as well, while the most optimal balance between structural stiffness and loading magnitude is achieved. Table 7.1, in which stiffest responses for each shape factor  $N$  has been recorded along with their respective displacement and strain energy. By inspecting the data, the most optimal range for  $C$  is identified additionally with the fact that indeed the shape factor  $N = 3$  yields most the favorable and efficient structural behaviour given that the mass for every design variant is kept constant at  $m = 65.27\text{ t}$ .

**Table 7.1:** Stiffest shape of towers taking different shape factors  $N$  and their respective results relating to global displacement, strain energy and mass. It should be noted that mass is being kept constant. This measurement does inform about the design variant exhibiting the most efficient structural behaviour.

<b>N</b>	<b>C (m)</b>	<b>Displacement (mm)</b>	<b>Strain Energy (kNm)</b>	<b>Wind (deg)</b>	<b>Mass (t)</b>
3	<b>-3.61</b>	<b>6.69</b>	0.3	31	65.27
4	<b>-2.82</b>	<b>8.4</b>	0.43	0	65.27
5	<b>-4.08</b>	<b>11.56</b>	0.47	54	65.27
6	<b>-4.1</b>	<b>13.59</b>	0.52	34	65.27
7	<b>-3.7</b>	<b>16.13</b>	0.72	68	65.27
8	<b>-3.75</b>	<b>18.7</b>	0.8	138	65.27
9	<b>-3.41</b>	<b>22.21</b>	1.05	35	65.27

Regarding the comparative study to be performed between the tower designs previously inspected, which followed a triangular topology equipped with segmented and curved rings, and the custom topology tower design built with segmented rings, Figure 7.4 displays the displacements and strain energy of the stiffest responses observed in each tower design. These tower responses change in accordance with the different shape factor values  $N$ . It should be noted that the mass for all these design variants has been kept the same. Hence, the deep blue and cyan curves correspond to the tower configurations with the custom topology, indicating that those configurations are more material efficient if compared to the one with a triangulated topology with segmented rings, shown with the purple and pink curves. Nonetheless, they seem to be less efficient than ones with a triangular topology using curved rings, shown with the orange and red curves. The higher efficiency and stiffness levels associated with designs following a custom pattern can be related with the fact that the tower does not follow an antiprism

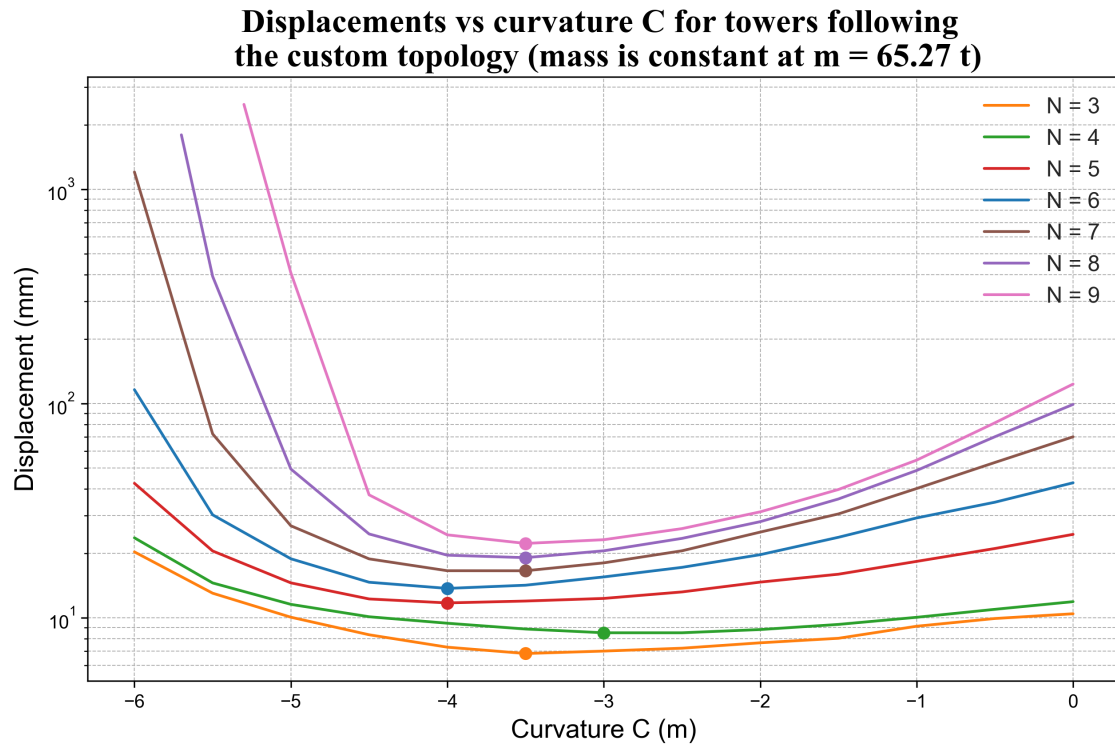


**Figure 7.1:** The plot examines tower variants adhering to a custom topology, characterized by varying shape factors ( $N$ ), while maintaining a constant mass and segmented rings. The curvature ( $C$ ) of each design variant is iteratively changed, and the associated displacements are recorded. Similar to observations in the triangular topology, lower curvature values ( $C$ ) tend to result in dramatically increased displacements. The stiffest tower response to the proposed wind profile was identified at curvatures ranging from  $C = -4$  meters to  $C = -3$  meters. Markers on the graph indicate the lowest displacement recorded for towers with different shape factors ( $N$ ). It is important to note that the y-axis, representing displacements, is scaled logarithmically.

configuration (in case of the triangular topology with segmented rings), for which the positioning of the ring is alternated at every level. Thus, in case of the custom topology, the top most ring is more restrained as the cross-section of the tower does not alter from bottom to the apex while diagonal crossings maintain the deformation less achievable. This is not the case for tower designs following the triangular topology with segmented rings as the top ring is free to deform and have unrestrained nodal movement. Figure 7.5 portrays four tower variants characterised by different curvatures placed side-by-side to highlight the difference in ring placement which culminates in a global buckling experienced by the tower following a triangular topology and a rather stiff and stable response shown by the structure defined by custom topology. Thus, the susceptibility to localized nodal movement that the triangular topology brings for the tower design is evident. It should be noted that the global buckling also occurs in case of towers defined by the custom topology when curvature is lowered at the certain value. However, the associated  $C$  when this happens is way lower than that of designs following a triangular topology (as it can be seen in Figures 6.1 and 7.1).

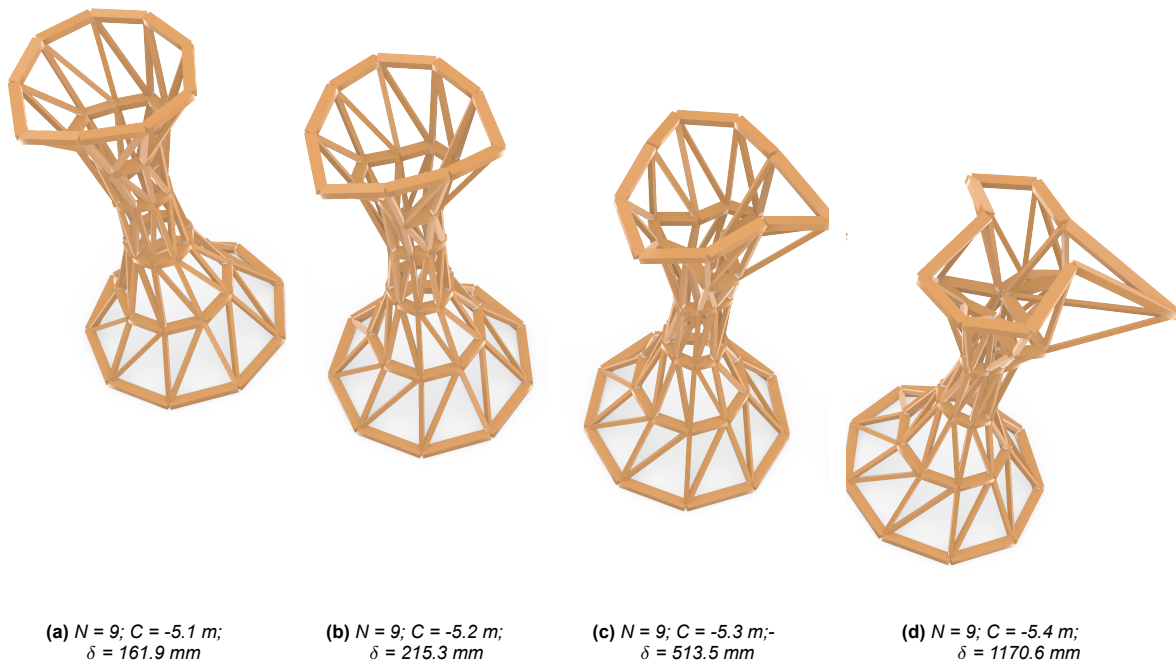


**Figure 7.2:** The figure presents a deformed tower variant, distinguished by a custom topology that incorporates a shape factor  $N = 9$ . This variant undergoes a change in its curvature variable  $C$ , resulting in a narrowing structure. It can be observed that when the structure is subjected to the proposed wind profile, its deformed shape is very rapidly approaching global buckling, while becoming more hyperbolic with just a little decrease in curvature. A crucial aspect of this illustration is the true-to-scale representation of deformations, mirroring the actual displacements. Additionally, sub-captions are provided to indicate the employed curvature variable ( $C$ ) and the corresponding global displacement ( $\delta$ ).

## 7.2. Curved Rings

The inclusion of curved rings for the tower design following the custom topology is presented in this section. Similarly as before this adjustment removes segmented rings (characterised by straight members) and introduces curved continuous rings. After subjecting the structure to the proposed wind load profile, varying the curvature  $C$ , recording the displacement for structures following a different shape factor  $N$ , the results are displayed in Figure 7.6. It can be viewed that regardless of the curvature  $C$  or shape factor  $N$ , the structure responds to wind in a stable and relatively stiff manner as depicted displacements are rather low and do not vary as much. This is to be expected as curved rings provide the in-plane stiffness to the structure which in turn decreases lateral displacement. The maintenance of the circular shape induces the ring to resist the loading in bending. It should be noted that a certain curvature range starting from  $C = -3.5 \text{ m}$  to  $C = -2.5 \text{ m}$  provides stiffest configurations for all shape factors  $N$ . It should also be noted that with the growth of  $N$ , the stiffness follows along and increases. This could be explained by the fact that as more nodes are introduced within the ring, the tower gains a more continuous outer skin (skeleton) where material is distributed more evenly, thus, facilitating a more uniform force flow along members. This effect is observed even if the mass is maintained constant for this tower variant throughout this study. The force distribution within the tower's skeleton is illustrated in Figure 7.7, where compressive elements are marked by blue and tensile ones are indicated by red.

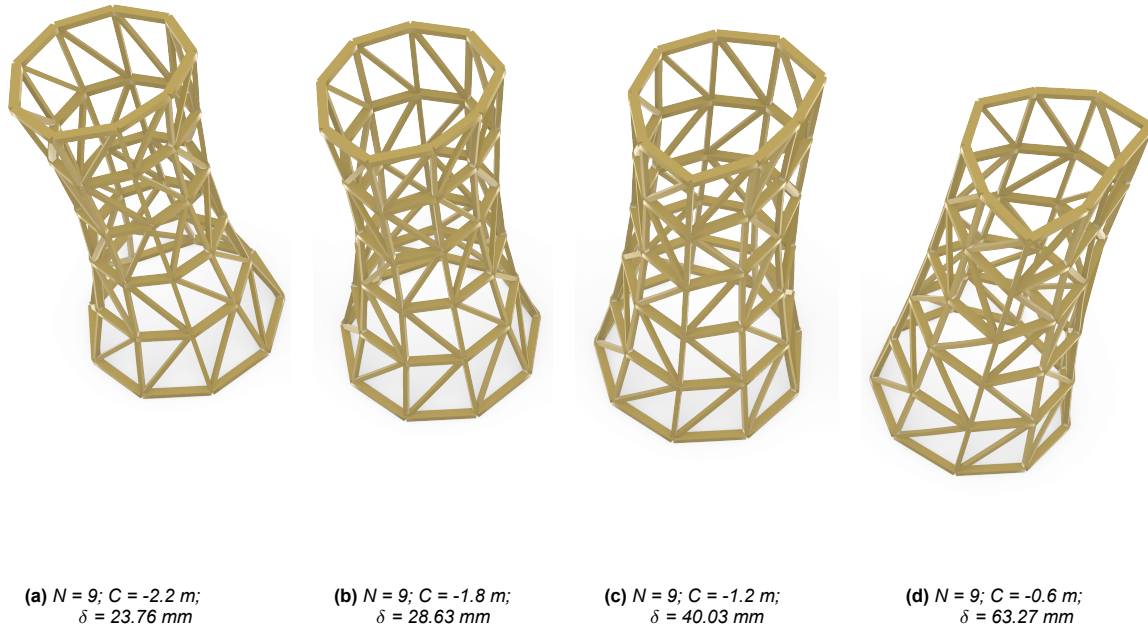


**Figure 7.3:** This illustration displays a custom topology tower variant characterized by a shape factor ( $N = 9$ ), where the curvature variable ( $C$ ) is increased, causing the tower to widen. When this structure is exposed to the proposed wind load profile, it demonstrates stable behavior, as indicated by relatively low displacements. As the tower adopts a more cylindrical shape, it presents a flatter surface to the oncoming wind, which appears to facilitate easier displacement. This effect becomes more pronounced in a fully cylindrical form, where the wind profile's squeezing action is markedly noticeable. It's important to highlight that the deformations shown here are illustrated at a scale of 1:30 compared to the actual displacements. Sub-captions provide details about the used curvature variable ( $C$ ) and the associated global displacement ( $\delta$ ).

To offer a comprehensive comparative analysis in relation to what has been studied so far, Table 7.2 and Figures 7.8 and 7.9 provide an overview of stiffest responses for this configuration and how does it compare to the other tower set ups previously analyzed. It can immediately be noticed the improvement in stiffness and strain energy metrics indicating a more efficient use of material given that the mass after this design adjustment has not been altered. However, as Figure 7.9 highlights, this proposed tower design does not showcase superior efficiency in relation to what has been demonstrated by the tower following a triangular topology and fitted with curved rings. This is indicated by a higher positioning of green and dark green curves than the orange ones. Recorded lower strain energy and displacement by the latter does inform the reader that the most effective design choice to resist the suggested wind load profile can be clearly identified.

In order to understand the discrepancy between these two tower designs in terms structural performance, one should take into account the composition of elements that link the rings in each tower. A brief comparative analysis using a simplified point load application was conducted on both tower configurations in order to comprehend this variance in structural performance. A total load of 500 kN has been divided into nodal forces for this specific purpose. Regarding the custom topology tower variant, the structure is made up of both vertical and diagonal members, in contrast with the triangular topology tower, which is exclusively made up of diagonal elements, as illustrated in Figure 7.10. Thus, the con-

**Displacements and Strain Energy vs. Shape factor (N)  
for towers following triangular top. (segmented and curved rings)  
as well as custom top. (segmented rings)  
while keeping mass constant at  $m = 66.5\text{ t}$ .**

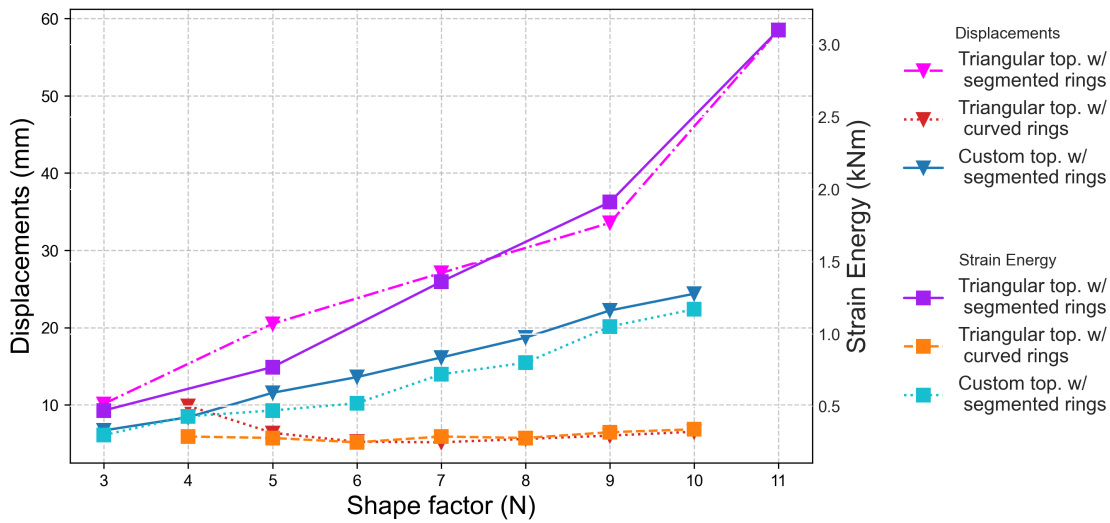


**Figure 7.4:** In the this plot, displacements and strain energy are graphed against the shape factor  $N$ . Each data point represents the configuration with the highest stiffness for a given  $N$ , adhering to a triangular topology with curved and segmented rings as well as custom topology with segmented rings. This analysis maintains a constant mass of approximately  $m \approx 66.5\text{t}$  for each tower configuration, facilitating a direct comparison of the impact of curvature  $C$  on displacement and strain energy characteristics. Newly studied tower design following a custom top. appears to exhibit more advantageous stiffness and strain energy characteristics compared to what has been observed in designs following a triangular top. (featuring segmented rings).

**Table 7.2:** Stiffest shape of towers (custom top. with curved rings) taking different shape factors  $N$  and their respective results relating to global displacement, strain energy and mass. It should be noted that mass is being kept constant. This measurement does inform about the design variant exhibiting the most efficient structural behaviour.

N	C (m)	Displacement (mm)	Strain Energy (kNm)	Wind (deg)	Mass (t)
3	-2.39	10.33	0.83	89	65.2
4	-2.82	7.32	0.45	45	65.2
5	-3.31	7.74	0.39	95	65.2
6	-3.31	7.61	0.38	67	65.2
7	-3.31	7.95	0.39	93	65.2
8	-3.01	8.24	0.46	69	65.2
9	-3.31	8.55	0.45	91	65.2
10	-2.81	8.92	0.56	181	65.2

figuration of these longitudinal members does influence the distribution of forces within the structure. For the custom topology, as shown in Figure 7.10, vertical members are observed to bear a significant portion of the load as they provide the shortest force path to supports, while diagonal members appear to be under-utilized. A rather consistent diagonal member pattern is observed in towers following a triangular topology, which allows a more homogeneous force distribution along the skeleton of the tower. Force distribution in equivalent tower designs characterised by custom and triangular topology is depicted in Figure 7.11. From two towers displayed in Figure 7.10, it should be noted that  $N$ ,  $C$  and mass characteristics are kept the same for both assemblies with the resulting displacements being  $\delta = 10.88\text{mm}$  in case of the custom topology and  $\delta = 9.26\text{mm}$  for the triangular one. It is noticeable that vertical members experience disproportionately higher stresses, thus, resulting higher strains render

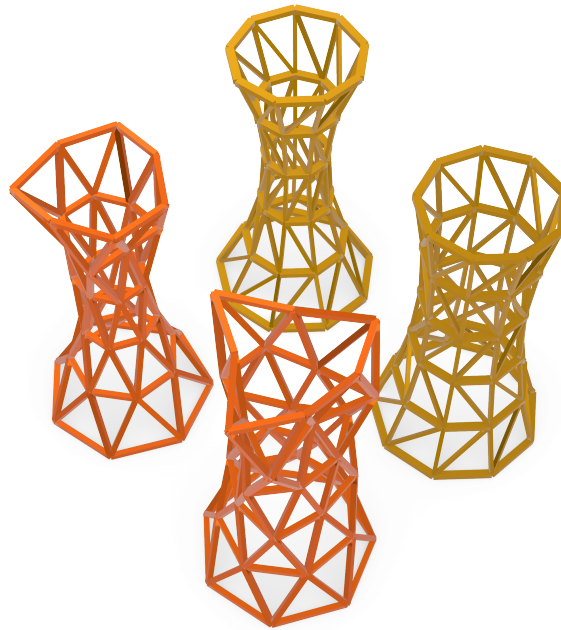


**Figure 7.5:** Custom topology (light brown) and triangular topology (orange) towers equipped with curved rings and the corresponding shape with the configuration that is narrowing ( $C = -3.9 m$ ) and widening ( $C = -2.2 m$ ) overall shape. It should be noted that the scale of the model is magnified 5 times in relation to real calculated displacements. It is observable how custom topology tower does not permit any ring deformations for a wider range of curvatures as the overall tubular configuration of the tower remains even and linear from bottom to top. In contrast, the tower with an antiprism composition, following a triangular topology, seems to provide more freedom of movement for the topmost rings.

the towers characterised by custom top. less stiff in comparison.

### 7.3. Discussion and elaboration on findings

This chapter conducts stiffness study of the tower structure following custom pattern. The investigation focused on understanding how alterations in the curvature  $C$  could influence the stiffness of the tower. In examining this particular configuration, it's clear from the beginning that opting for this pattern naturally enhances both the stiffness and stability characteristics of the structure, as for all shape factors  $N$ , displacements were within reasonable limit. This could be attributed to the placement of bracing at every rectangular opening via diagonal members as well as a non-alternating ring placement within the structure. This design aspect restricts free nodal movement, an issue more prevalent for structures characterised by a triangular pattern, at the apex in particular. Thus, towers defined by the custom pattern do not experience disproportionate displacements in the top ring. Instead the structure deforms and bends more uniformly, resembling that of a cantilever. However, for high shape factors, displacements at the top do become more pronounced, but this behaviour is associated with very small or large curvature values.

Previously observed with the triangular configuration, the spring stiffness of the rings diminishes with higher shape factors, thus, displacements do increase along with more vertices along the ring polygon. However, the stiffest response has been shown by structures with  $N = 3$ , a feature that was not evident for towers defined by the triangular pattern whenever segmented rings are utilized. This could be

**Displacements vs curvature  $C$  for towers following the custom topology after inclusion of curved rings (mass is constant at  $m = 65.20$  t)**

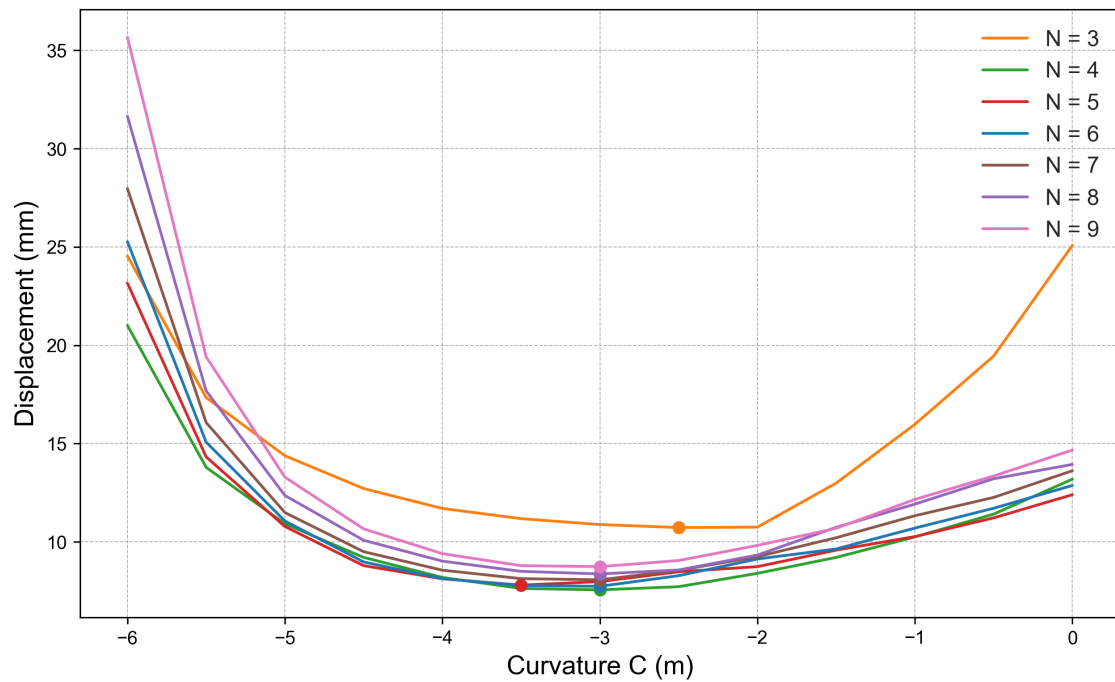


**Figure 7.6:** The plot examines tower variants adhering to a custom topology equipped with curved rings, characterized by varying shape factors ( $N$ ), while maintaining a constant mass. The curvature ( $C$ ) of each design variant is iteratively changed, and the associated displacements are recorded. As expected, all tower variants respond to wind profile in a stiff and stable manner with displacements showing a rather minimal variation. The stiffest tower response was identified at curvatures ranging from  $C = -3.5$  meters to  $C = -2.5$  meters. Markers on the graph indicate the lowest displacement recorded for towers with different shape factors ( $N$ ). It is important to note that the y-axis, representing displacements, is scaled logarithmically.

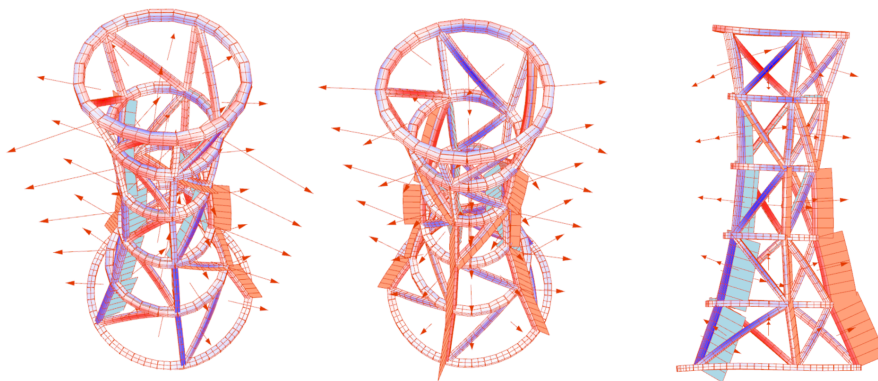


**Figure 7.7:** Illustration of force distribution within the structure defined by the custom top. (with curved rings). Following the application of wind load, the front side of the tower dealing with the positive pressure undergoes tension (indicated in blue), meanwhile the opposite side, facing the negative pressure, experiences compression (highlighted in red). Additionally, it can be observed that the lower part of the tower is undergoing larger forces than the top.

explained by varying ring positions in plan-view of the triangular pattern and a consistent placement of rings in case of a custom pattern, as shown in Figure 7.12. Triangular pattern enables only half of the rings to resist load in axial member compression, while the rest react to loading in bending, which is a less stiff response. As the shape factor increases, the span length of the rings responding

**Displacements and Strain Energy vs. Shape factor (N)  
for towers following triangular top. (curved rings)  
as well as custom top. (segmented and curved rings)  
while keeping mass constant at  $m = 66\text{ t}$ .**

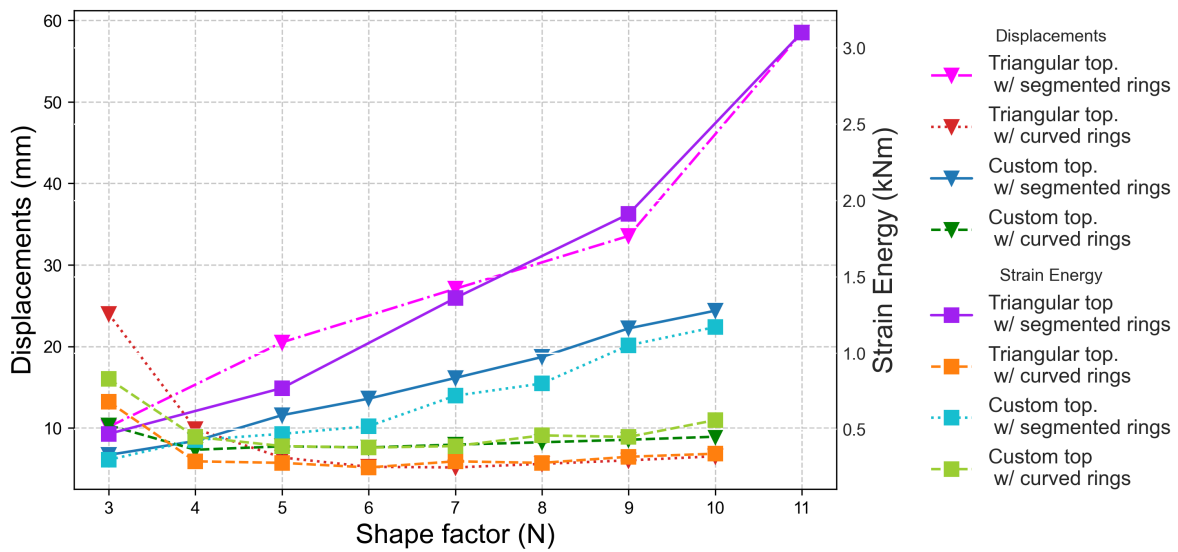


**Figure 7.8:** In this plot, displacements and strain energy are graphed against the shape factor  $N$ . Each data point represents the configuration with the highest stiffness for a given  $N$ , adhering to a triangular topology with curved and segmented rings as well as custom topology with segmented and curved rings. This analysis maintains a constant mass of approximately  $m \approx 66\text{ t}$  for each tower configuration, facilitating a direct comparison of the impact of curvature  $C$  on displacement and strain energy characteristics. Newly studied tower design following a custom top. with curved rings (green and dark green curves) appears to exhibit less advantageous stiffness and strain energy characteristics compared to what has been observed in designs following a triangular top. (featuring curved rings) indicated by red and orange curves.

through bending decreases, yet the equivalent stiffness of the springs in the remaining members also diminishes. The most stiff response is observed when there is an optimal mix of stiffness in the rings subjected to bending and the equivalent spring stiffness of the bars in alignment. Regarding the custom pattern, the consistent and aligned ring placement throughout the height of the structure ensures that bars consistently bear loads through axial compression. As a result, the equivalent spring stiffness is at its peak when the shape factor  $N$  is at its minimum. This is because the spring's stiffness is directly influenced by the shape factor, a relationship illustrated in Figure 6.16.

Similarly as before, towers with higher shape factors are found to exhibit the most optimal shape in terms of stiffness whenever curvature  $C$  values are lower in magnitude (the tower silhouette is more like a barrel). This does not align with the simplified bar 'Karamba3D' model presented in Section 6.3. Typically, as the equivalent spring stiffness of ring elements is reduced (higher shape factor  $N$ ), the bar model tends to find its optimal shape characterised by increased curvature. It is, therefore, recommended for future academic and research projects to investigate this property further with preserving the wind load profile established.

As regards the introduction of curved rings, the stiffness of the structure has risen substantially, as it was the case for structures following triangular pattern. Variants with lower shape factors did exhibit lower stiffness, which correlates with the arched beam model and the equivalent spring stiffness at the ring, as illustrated in Figure 6.23. However, received results did showcase worse stiffness characteristics than the counterpart employing triangular pattern, albeit by a marginal difference. Finally, as shape

**Displacements and Strain Energy vs. Shape factor (N)  
for towers following triangular top. (curved rings)  
as well as custom top. (segmented and curved rings)  
while keeping mass constant at  $m = 66$  t.**

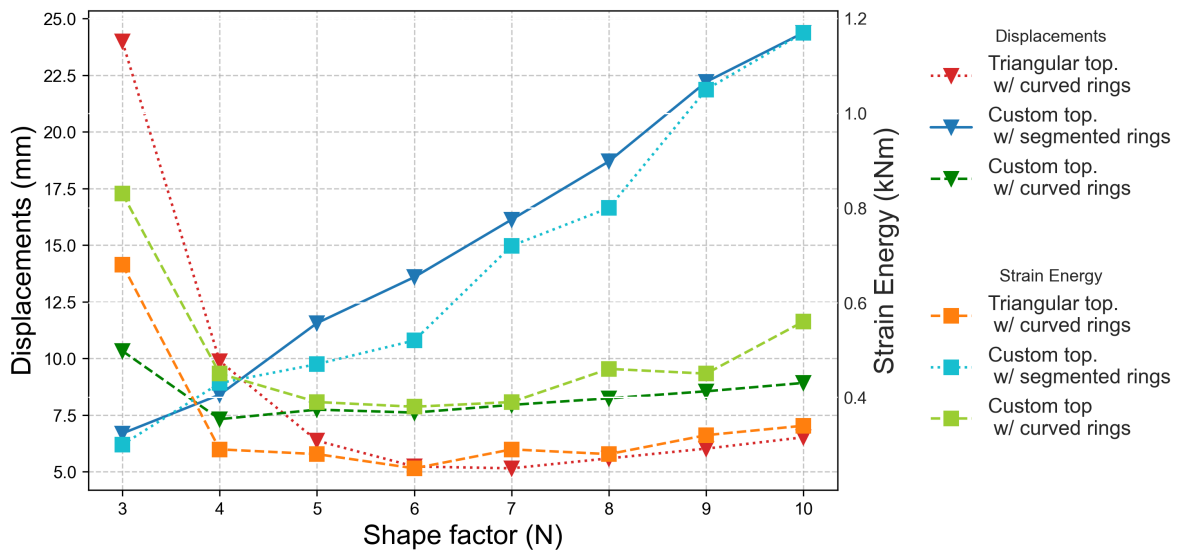


**Figure 7.9:** In this plot, displacements and strain energy are graphed against the shape factor  $N$ . Each data point represents the configuration with the highest stiffness for a given  $N$ , adhering to a triangular topology with curved rings as well as custom topology with segmented and curved rings. This plot serves as a closer examination of the three curves representing the most stiff and efficient designs, enabling a more accurate assessment of their relation.

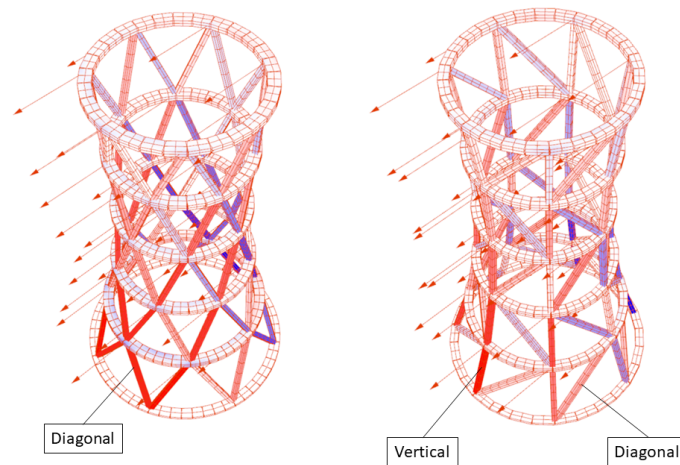


**Figure 7.10:** Illustration of members being in stress within structures characterized by the custom topology equipped with curved rings (right) along with the triangular topology also featuring curved rings (left). Both structures are characterized by  $C = -2$  and  $N = 7$  while mass is kept the same for both. A clear distinction can be noticed between the distribution of stresses in these assemblies as vertical members do take disproportionately higher amount of loads compared to the diagonal ones in case of the custom top. A more uniform force distribution is evident in case of the triangular topology.

factors are increased, the most optimal tower configuration with curved rings was defined by a curvature that was within the range of  $-3.31$  m to  $-2.81$  m. Thus, increasing the number of vertices around the perimeter of the ring did not affect the most optimal silhouette of the tower. This can be explained by the unchanging stiffness of the ring as curvature is evolving.

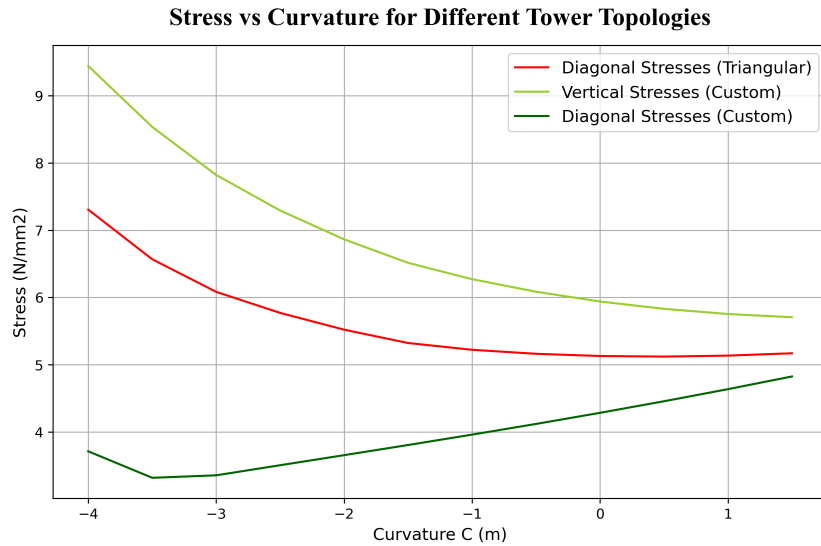


**Figure 7.11:** Average stresses against the variance in curvature  $C$  in vertical and respective diagonal members for towers following custom and triangular topology. The uneven distribution of loads in assemblies of custom pattern leads to excessive stress on vertical members and diagonal ones under-utilized. This is not the case for triangular topology as the average stress amount in its diagonals are less than that defined by the light green curve. This feature allows tower structures defined by the triangular topology to experience lower strains and resist loads in a more stiff manner.

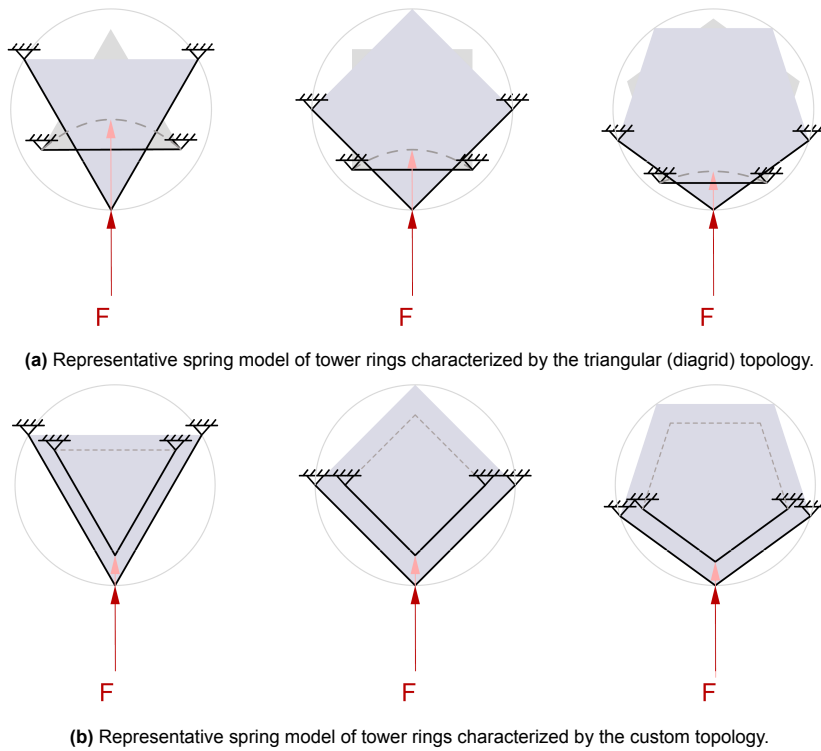
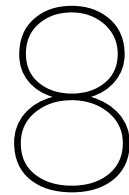


**Figure 7.12:** The tower stiffness is influenced by the arrangement of rings for different topologies, particularly when considering diverse shape factors denoted by  $N$ .

This study applies the concept of maintaining a constant mass and same cross-sections across various member groups within this tower’s topology. However, the fact (presented in Figure 7.11) that vertical and diagonal members experience varying stress levels suggests a potential adjustment. Specifically, it shows that the diagonal members might have been modelled with smaller cross-sections, whereas the

vertical elements could benefit from larger ones, all while maintaining the same mass of the structure. By employing this principle, it is thought by the author that towers equipped with curved rings, after this adjustment, should show improved stiffness compared to those with a triangular topology, especially considering small differences in displacement currently observed and presented in Figure 7.9.



# Materialization

## 8.1. Feasibility Study of the Initial Connection Design

The conducted parametric study involving topological and curvature influences has reduced the design space and informs following procedures about the most feasible and favorable tower configuration as regards the resistance to the proposed wind load profile. Drawing insights from the data provided in Figures 7.8 and 7.9, the analysis of performance metrics indicates that the triangular topology with curved rings is the favorable design choice. Regarding the suggested shape factor  $N$ , the evidence recommends that a value of  $N = 6$  offers optimal stiffness and material efficiency. However, considering the buildability perspective, an  $N = 5$  configuration results in fewer nodes (from 36 to 30), thereby reducing the number of necessary connections for design and installation, ultimately leading to a decrease in the required steel. This adjustment would not alter the performance of the design to a high degree as the variation in stiffness and strain energy between towers defined by these shape factors is still quite minimal. In terms of the curvature  $C$  value to be employed to achieve the most optimal shape, study findings also recommend the value  $C = -4 m$  (as outlined in Table 6.3). This value provides the most favorable lateral stiffness characteristics given the use of material throughout the structure and the magnitude of the wind load applied to it.

Therefore, as the global configuration has been set, the main concerns remains the introduction of dead and live loads resulting from the self-weight, platforms at every ring level and visitors. By applying the loading conditions as presented in Chapter 4, compressive forces arise in diagonal members as portrayed in Figure. Thus, the meeting point between diagonals and solid curved members becomes the focus of the next steps of the realization process. The design of connections within the tower is of essence, given that the transfer of forces between diagonal and curved members remains unaddressed, with only the modeled degrees of freedom being considered thus far. By obtaining the order of magnitude of force to be transmitted via diagonals and ring members, one can start implementing connection modelling, which entails an effective use of steel components like plates and bolts.

The initial step is to recognise a crucial node within the system of elements where force magnitude

is highest. By glancing at Figure 8.1, one can delineate diagonals within the 'Karamba3D' output subjected to highest compressive stresses indicated by colour red. The magnitude of these effects at the lowest ring is presented in Figure 8.1. As it can be recognised, upper diagonals are subjected to a compressive force of around 350 kN, while the lower ones are experiencing a force of around 520 kN.

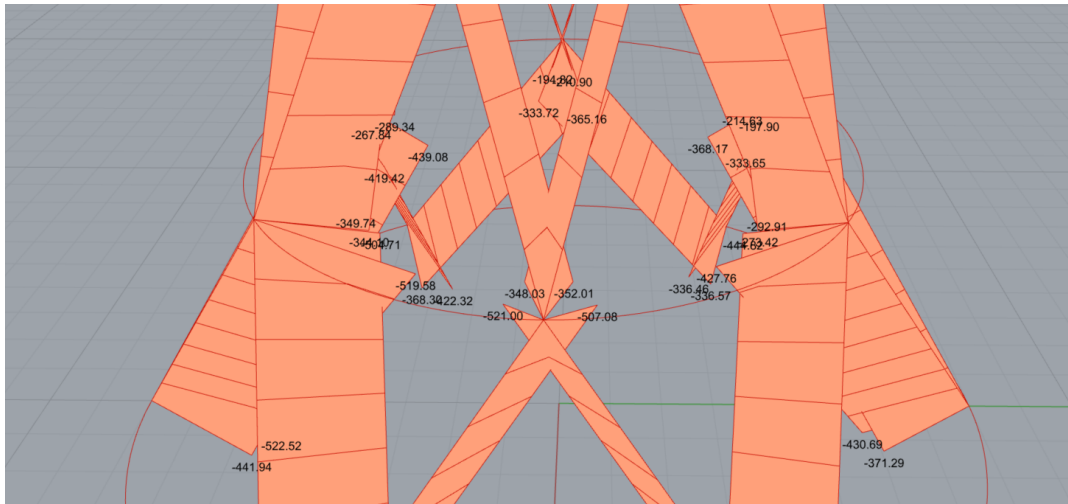
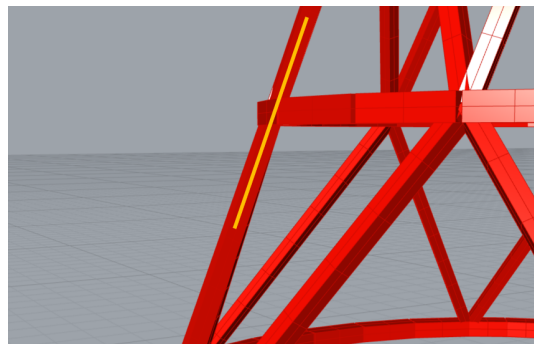


**Figure 8.1:** The lowest set of nodes experiences compressive forces. In this case live, permanent and wind loads are applied with relevant safety factors.

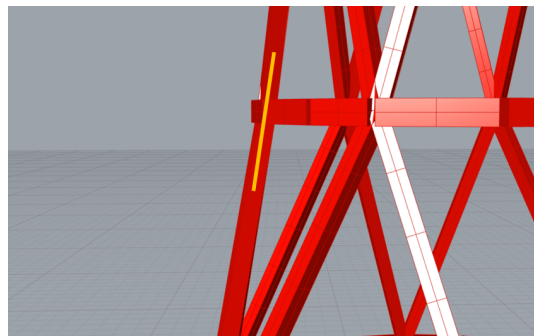
In order to preserve the continuity of solid glulam rings, the concept of the connection aimed at an incision through the circumferential element in which a steel plate could be inserted through. This plate would serve as a slotted plate on which lower and upper diagonal elements can be accommodated and jointed with bolts. In this way, by virtue of a double shear plane bolted timber steel plate connection and a long steel plate, the compressive force transfer between upper and lower diagonal members can be realized and transferred. The initial design of the connection from side and front view is presented in Figure 8.4. Note that the plate here is kept straight while diagonals abut at the node in same plane. The thickness of the proposed plate is 20 mm, while the choice of material is S355 steel. It is of importance to note that the angle at which diagonals connect to the ring shall should be kept identical as to avoid any significant kinks in the connecting steel plate. This would result in eccentricity in the force line leading to disequilibrium of forces meeting at that kink. To address this issue, it would be necessary to add a plate underneath the circular ring, secured with bolts. This addition would help in evenly distributing the forces at the bend, ensuring stability (Figure 8.3). This, however, would introduce potentially high transverse (perpendicular to the grain) forces on the timber element, which is an unfavorable loading scenario in terms of weaker timber characteristics. In addition, given the tower is not in use and therefore live loads are not present, tensile forces develop in diagonal members due to high wind loads on the windward side. By observing this effect in Figure 8.3, the resolved force in the protruding plate would be tensile. This is of essence, the tensile force acts on the ring in a direction that's perpendicular to the wood grain. These effects have to be taken into account by strategic placement of bolt rows. In case of compressive or tensile effects, the bolt row should be placed as far away from either edge as possible in order to avoid splitting of timber laminae. To reduce the force perpendicular to the grain and omit the need for plate bolted to the circular ring, the curvature of the tower is required to be altered to  $C = -4.2 \text{ m}$  to allow diagonal members join the ring at the same angle (or plane) as illustrated in Figure 8.2. In such a way the insertion plate is preserved as straight as possible and transmission of forces

is done without any eccentricities and kinks. However, this adjusted curvature  $C$  does not reflect the most favorable design in terms of lateral stiffness as presented in Figure 6.8. Thus, it can be stated that there is a direct dependency of connection design and force perpendicular to the grain of circular rings to the curvature parameter  $C$ .

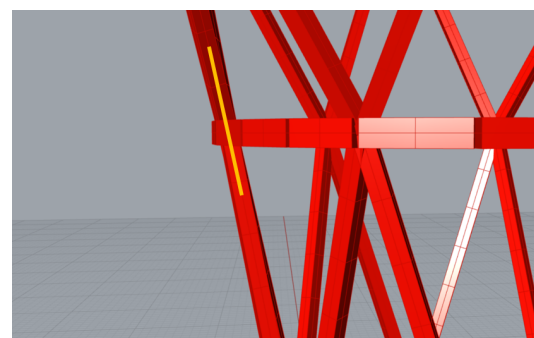
Additional concerns arise given that the curved (circular) ring is exposed to bending moments. As it was reviewed in 2.1.4 and presented in Figure 2.5, these effects will induce transverse (perpendicular to the grain) tensile stresses in the middle portion of the ring cross-section. Caution in design process should be taken to address these effects which might cause stress concentrations in the insertion plate hole or bolted holes.



(a) Lower ring diagonals.



(b) Middle ring diagonals.



(c) Upper ring diagonals.

**Figure 8.2:** Illustration of an altered tower configuration in terms of curvature as to allow upper and lower diagonal members to connect to the ring in a straight line in relation to one another.

Regarding the stability of the plate, the initial analysis and modelling of this element through employ-

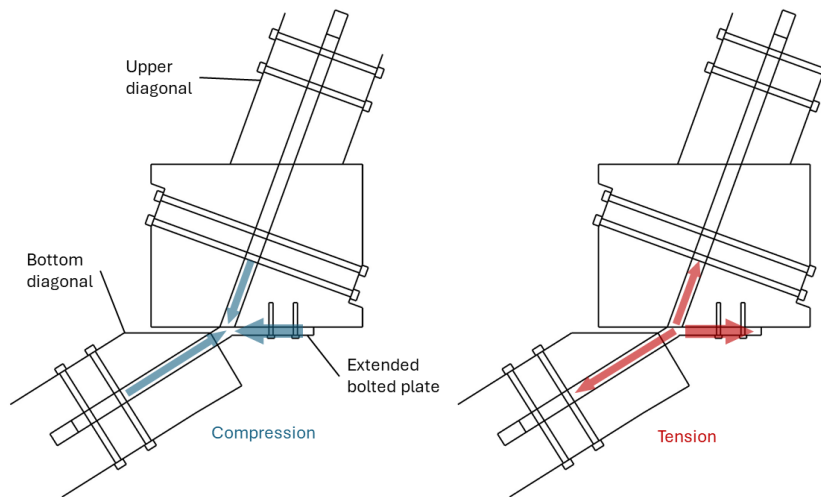


**Figure 8.3:** Due to certain curvature of the tower silhouette, diagonals do not abut at the node in the same plane, thus a kink in the connecting plate should be introduced.

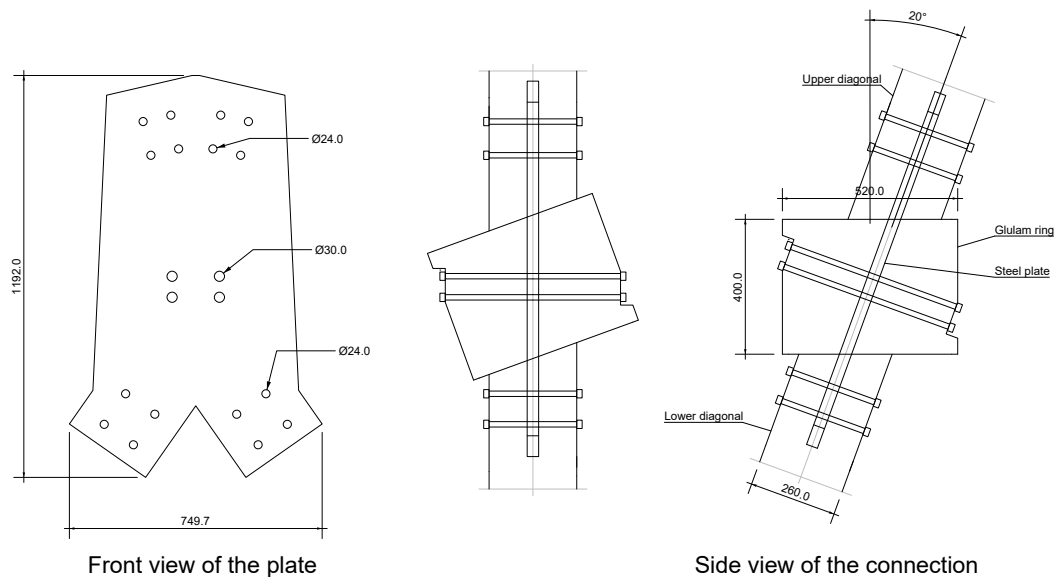


**Figure 8.4:** Drafted representation of the steel timber connection employing a longer steel plate accommodating timber diagonals via drilled bolts. Dimensions of members are taken to be arbitrary as the strength of the steel plate is to be investigated. It should be noted that this connection relates to lowest platform ring node, where force magnitude was evident to be the highest.

ment of IDEAS StatiCA software disregarded the contribution of embedding timber ring which would reinforce the plate laterally. Thus, the resulting buckling factors understandably were critically low (results are given in F). In addition, the software utilized cannot enforce more intricate boundary conditions for diagonal members that are connected to the plate. However, a deeper examination of this kind of connection and its stability could also consider how the steel plate is embedded within the timber circular ring. Furthermore, when modeling timber as a material, is of essence to model it in a way that represents its anisotropic nature and the direction of its grain.

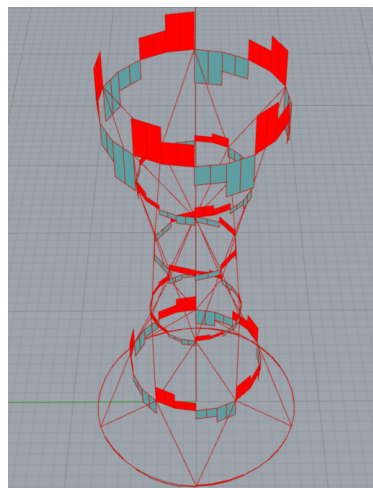
Another concern related to the global design of towers featuring curved members is the emergence of torsional stresses within rings after subjecting the structure to dead and live loads resulting from pedestrians and platform self-weight (Figure 8.6). This effect was not evident in previous chapters as towers were subjected to wind actions solely, while dead and live loads were negated. Figure 8.5 illustrates two tower configurations of towers defined by a triangular topology: the first employs curved rings throughout, while the second features segmented rings with a curved ring placed at the top. These both configurations are examined with a shape factor of  $N = 5$  and a curvature of  $C = -4.2$  m, investigating the torsional moments produced by dead and live loads subjected to the ring members through platforms. It is observed that the application of loads on curved members at each level allow for torsional moments to arise, especially for rings with higher radii (larger area of applied loads) and longer spans (directly correlated to a lower shape factor  $N$ ). The reason for this effect is the change of the center line along which the loads are applied across the span of a single ring member. Given the occurrence of these torsional moments, the design should be taking that into account and evaluate the allowable torsional stresses within circular glulam members since the load is spread around the ring's perimeter. A practical way to mitigate these stresses can involve situating and resting observational decks or staircases nearer supports within the ring span, as it implies only specific areas of the ring would be suitable for bearing loads.

This section provided a qualitative review of the timber - steel connection that would be implemented in case a triangular (diagrid) topology tower featuring curved (circular) rings is chosen. Having comprehended the complexity of such a connection, it becomes clear that designing this component would be an intricate and detailed process, especially due to its complex nature provided by the curved ring. Having said that, this level of detail falls beyond the scope of this research. Alternatively, the research proposes a look at alternative and more straightforward connection solutions that would be implemented in different tower design variants.

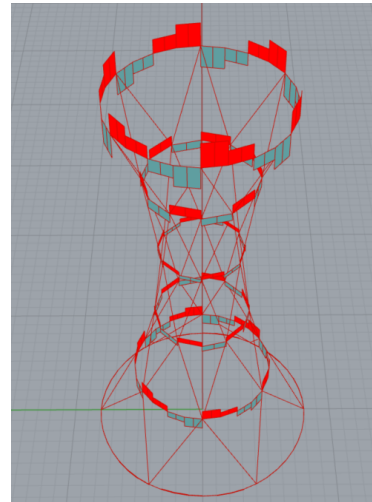
## 8.2. Alternative Connection Design Explorations

The idea of continuous ring to be employed for the design of the tower structure has been welcomed due to resulting levels of lateral stiffness being highly favorable in comparison to designs characterised by segmented rings. However, as it was mentioned previously at the end of Chapter 5, the introduction of curved continuous ring at the top of the tower, where ring deformation is most prevalent (especially for designs following a triangular topology) would still yield relatively favorable outcomes in terms of global lateral stiffness. While top ring is placed at the top of the tower, the rest of the structural member configuration remains segmented. A relevant reference project previously reviewed in Chapter 2 is the watch tower in Kootwijkerzand in the Dutch province of Gelderland, which incorporates segmented members throughout its configuration (Figure 8.7). However, the tower relies on in-plane stiff platforms (especially the one at the top) to supplement the structure with overall stability. Thus, the choice of ring at the top would negate the need to have a permanent platform placed at the apex. In terms of connections, both tower geometries (or topologies), antiprism (diagrid) or prism (custom) would have six straight members abutting at the joint.

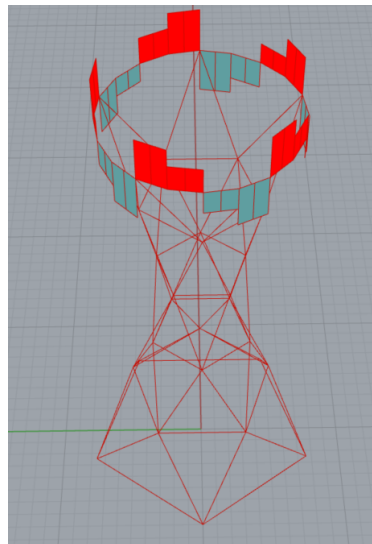
Unlike for design variants employing curved (circular) rings, no torsional effects and moments are ev-



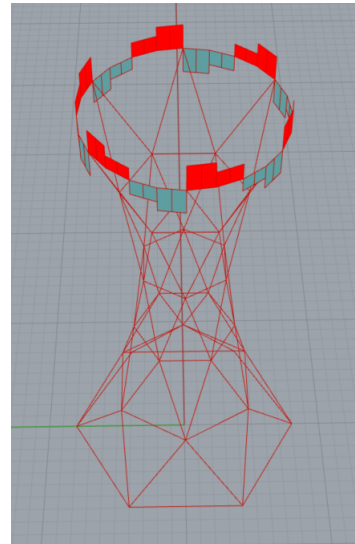
(a) Effects of torsion within the tower with curved rings ( $N = 5$ ).



(b) Effects of torsion within the tower with curved rings ( $N = 6$ ).



(c) Effects of torsion within the tower with segmented rings and a curved one at the top ( $N = 5$ ).



(d) Effects of torsion within the tower with segmented rings and a curved one at the top ( $N = 6$ ).

**Figure 8.5:** Comparison of torsional effects on towers with curved and segmented rings. It should be noted that the scale of moment lines on 'Karamba3D' component 'Beamview' is set to 0.1.

ident for segmented ring members after subjecting it to live and dead loads. The concept of pinned jointed segmented structure serves valuable in such a design iteration as bolted steel-timber connections are not ones to bear and resist these moments. Therefore, following design phases will prioritize addressing and diminishing the impacts of torsional and bending moments near connections. However, given the significant radius of the top ring (and the platform), this characteristic leads to larger distributed aerial forces (stemming from live and dead loads) on the ring. As illustrated in Figures 8.5c and 8.5d, these conditions result in torsional moments concentrated around the ring's support points. The susceptibility to torsional failure in curved ring elements is confirmed by the outputs from the 'Beaver' timber structural analysis plug-in, as displayed in Figure 8.6. Thus, the same practical approach could be applicable for this component: either avoid using this ring for platforms where loads would be transferred directly to its diameter or distribute the loads closer to supports. Naturally, if the

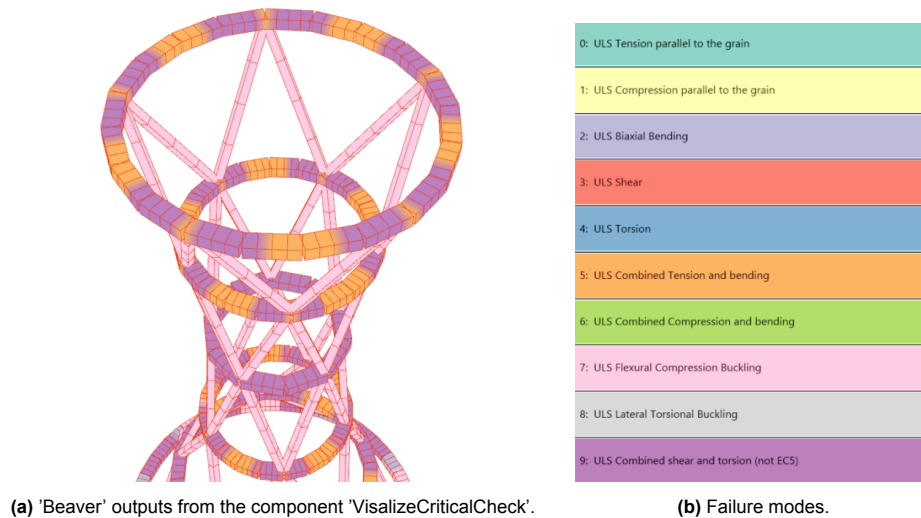


**Figure 8.6:** 'Beaver' plug-in outputs displaying critical failure modes in which certain glulam sections throughout the tower might fail. It can be seen that ring elements are highly susceptible to failure as utilization for that failure mechanism is the highest.

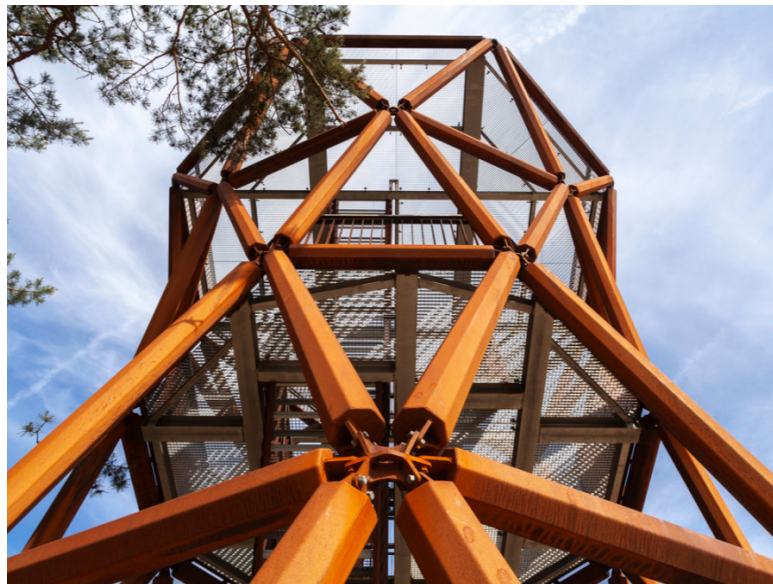


**Figure 8.7:** Watch tower in Kootwijkersand and the connection design employed to join 6 steel members (NatureScanner 2024).

decision is made to spread loads around the ring's perimeter, the main consideration for designing the top flexurally stiff ring becomes the combined effects of in-plane bending and torsion. This aspect has to be taken into account in the design process. Therefore, for this design exploration a choice has been made use this ring for platforms where loads would be transferred directly to its diameter. This design choice yields the more unfavorable scenario which will supplement the design of members underneath as well as connections. A more detailed assessment of the circular glulam ring at the top regarding associated connection design, combined torsional and bending effects is warranted.

By employing a flexurally stiff ring at the top, the lateral stiffness of the tower are still unknown for both topologies. Thus, the following subsections shall briefly investigate lateral stiffness characteristics against the suggested wind load profile of towers following triangular (diagrid) and custom topologies

with the proposed new ring configuration. In the detailed design of the structure's connections, the new and altered tower variant that exhibits best lateral stiffness characteristics shall be implemented.

### 8.2.1. Triangular Topology

This subsection provides an overview of lateral stability characteristics of a tower defined by the triangular topology, following the introduction of the new ring placement. The structure to be examined is illustrated in Figure 8.8.

For this analysis, the aspect of mass consistency throughout the project has to be taken into account as to identify the most material efficient design variant. Thus, all tower configurations going through varying shape factors  $N$  and curvature  $C$  shall maintain the same mass of approx. 65 t. The proposed weight of the structure would lead to bulkier members. Nonetheless, as previously noted, the primary focus remains the comparison of stiffness of various design options within this analysis. Thus, after performing the wind load assessment on the proposed structure, Figure 8.9 provides resulting global displacement values for towers taking different shape factors  $N$  while curvature  $C$  is changing. By looking at the graph, it can be said that introducing a curved ring at the top of the tower, does improve the segmented triangular configuration in terms of stability (compared to what has been observed in Figure 5.1) as towers characterised by an even values shape factor  $N$  exhibits comparatively lower displacements. Nevertheless, configurations of towers with smaller curvature values,  $C$ , can show abrupt jumps in displacements. Whenever the curvature increases, the rather cylindrical, or a wider hyperboloid shape, the tower tends to show stable and stiff response to wind loads.

In general, incorporating a flexurally stiff ring does not match the observation that towers with a triangular pattern only show kinematic mechanisms or sudden increases in displacements when associated with even shape factors  $N$ . It's evident that also towers equipped with rectangular or hexagonal rings can achieve stable outcomes if a flexurally stiff ring at the top is implemented. Therefore, it becomes clear that kinematic mechanisms become apparent in towers where the top rings are unrestrained and composed of segmented (pin-jointed) members.

**Table 8.1:** Stiffest shape of towers (triangular top. with segmented rings and a curved ring a the top) taking different shape factors  $N$  and their respective results relating to global displacement, strain energy and mass. It should be noted that mass is being kept constant. This measurement does inform about the design variant exhibiting the most efficient structural behaviour.

<b>N</b>	<b>C (m)</b>	<b>Displacement (mm)</b>	<b>Strain Energy (kNm)</b>	<b>Wind (deg)</b>	<b>Mass (t)</b>
3	-4.48	12.22	0.46	149	65.09
4	-3.61	7.49	0.37	25	65.09
5	-1.94	9.47	0.89	80	65.09
6	0.87	11.56	1.40	79	65.09
7	1.49	12.09	1.70	90	65.09

Additionally, by reading the Table 8.1, it can be perceived that with an increasing shape factor  $N$ , the stiffest response is shown by an ever increasing curvature  $C$ . This indicates that for a larger number of nodes within the ring, the cylinder or even a barrel becomes the stiffest tower shape against proposed wind profile. This feature is true despite the fact that barrel and cylinder shapes attract more wind than



**Figure 8.8:** A sample tower following the triangular topology having segmented rings and a curved ring at the top. This configuration has a shape factor  $N = 6$  and a curvature  $C = -4 m$ .

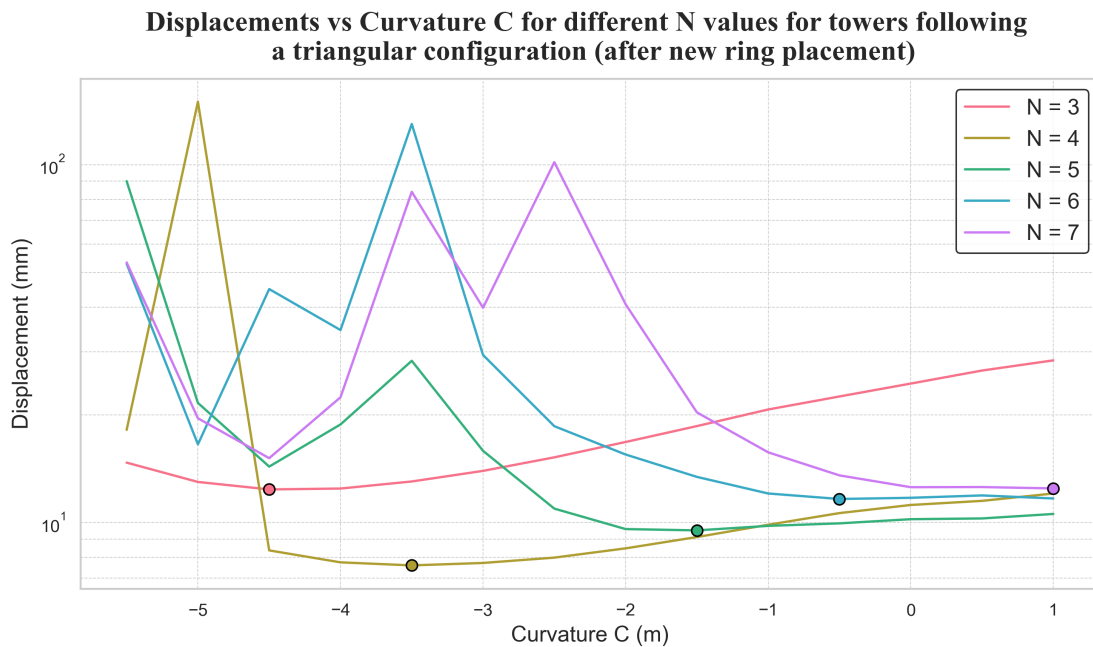


**Figure 8.9:** The plot examines tower variants adhering to a triangular topology equipped with segmented rings with a curved ring at the apex, characterized by varying shape factors ( $N$ ), while maintaining a constant mass. The curvature ( $C$ ) of each design variant is iteratively changed, and the associated displacements are recorded. It is important to note that the y-axis, representing displacements, is scaled logarithmically. Markers indicate the stiffest response for every shape factor.

a narrow hyperboloid. Finally, the stiffest response is shown by towers taking the shape factor  $N = 4$  or  $N = 5$ .

Similarly as before, these findings shall be compared with those obtained from previous chapters. Figure 8.10 displays stiffest response for different configurations for every shape factor  $N$ . It can be seen that by introducing a stiffening ring at the top, this new tower set up shows improvement from the one following a custom topology (with segmented rings). However, it does seem to be less stiff than ones equipped with curved rings at every level. Additionally, in the same fashion as for other tower set ups,

stiffness does reduce as shape factor  $N$  is growing. It should be noted that in this specific graph, strain energy findings are negated for better readability and due to its close correlation to displacements.

**Displacements vs. Shape factor (N)  
for tower stiffest responses for different configurations.**

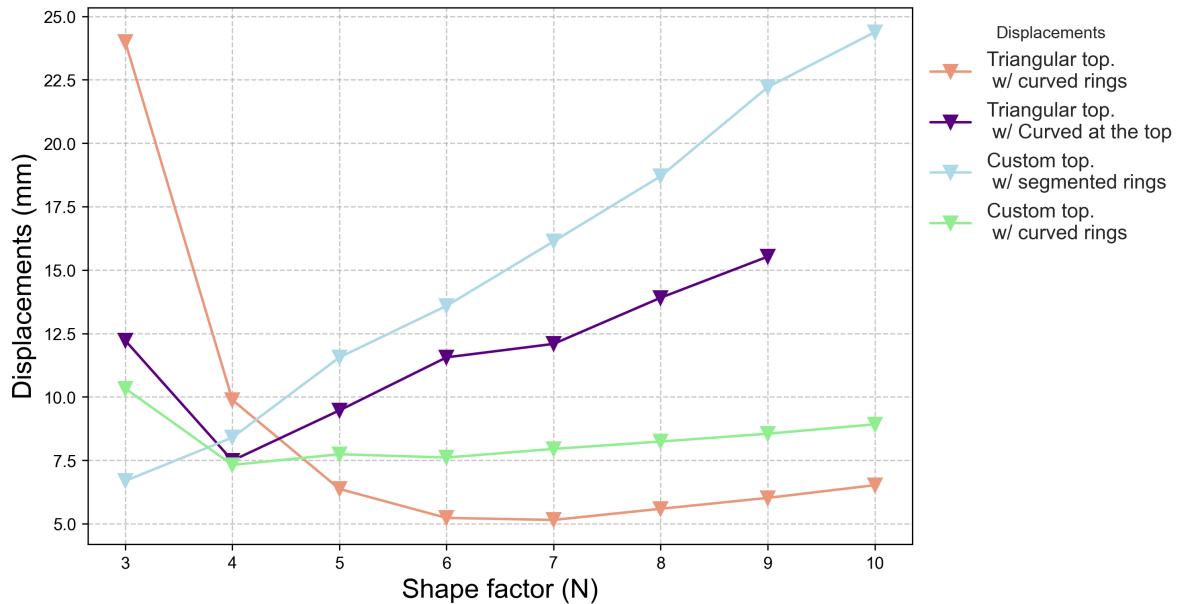


**Figure 8.10:** In this plot, displacements are graphed against the shape factor  $N$ . Each data point represents the configuration with the highest stiffness for a given  $N$ , adhering to a triangular topology with a curved ring at the top as well as all the other configurations that showed favorable stiffness metrics. This analysis maintains a constant mass of approximately  $m \approx 65t$  for each tower configuration, facilitating a direct comparison of the impact of curvature  $C$  on displacement.

### 8.2.2. Custom topology

This subsection provides an overview of lateral stability characteristics of a tower defined by the custom topology, following the introduction of the new ring placement. Similarly as before the analysis shall compare global displacement values (in mm) for towers (with different  $N$ ) against the varying curvature  $C$  values. It should also be noted that for towers with each distinct shape factors  $N$  the most unfavorable wind direction has been applied by reaching maximum displacement. The tower configuration following the custom pattern (curved ring at the top) is presented in Figure 8.11.

After performing the wind load assessment on the proposed structure, Figure 8.12 provides resulting global displacement values for towers taking different shape factors  $N$  while curvature  $C$  is changing. By inspecting the graph, one can delineate that all tower variants show stiffest response at lower curvature  $C$  values. This is quite a contrasting feature in comparison to what has been observed for structures adapting a triangular pattern. Additionally, shape factors  $N$  that resulted in stiffest responses can be seen to be  $N = 4$  and  $N = 5$ . Throughout the graph, it can be observed that all responses were stable and rather predictable as no displacement jumps are evident (unlike the tower defined by a triangular pattern).

Additionally, by reading the Table 8.2, it can be perceived that with an increasing shape factor  $N$ , the



**Figure 8.11:** A sample tower following the custom topology having segmented rings and a curved ring at the top. This configuration has a shape factor  $N = 5$  and a curvature  $C = -4 m$ .

stiffest response is related to a curvature that converges to a value that is close to one observed previously in Tables 6.3 and 7.2 ( $C \approx 3.6 m$ ). This indicates that for a larger number of nodes within the ring, the structure finds its own stiffest global configuration that resembles a narrow hyperboloid. It does correlate with the fact that narrower hyperboloid attracts less wind as projected area of the mesh is reduced.

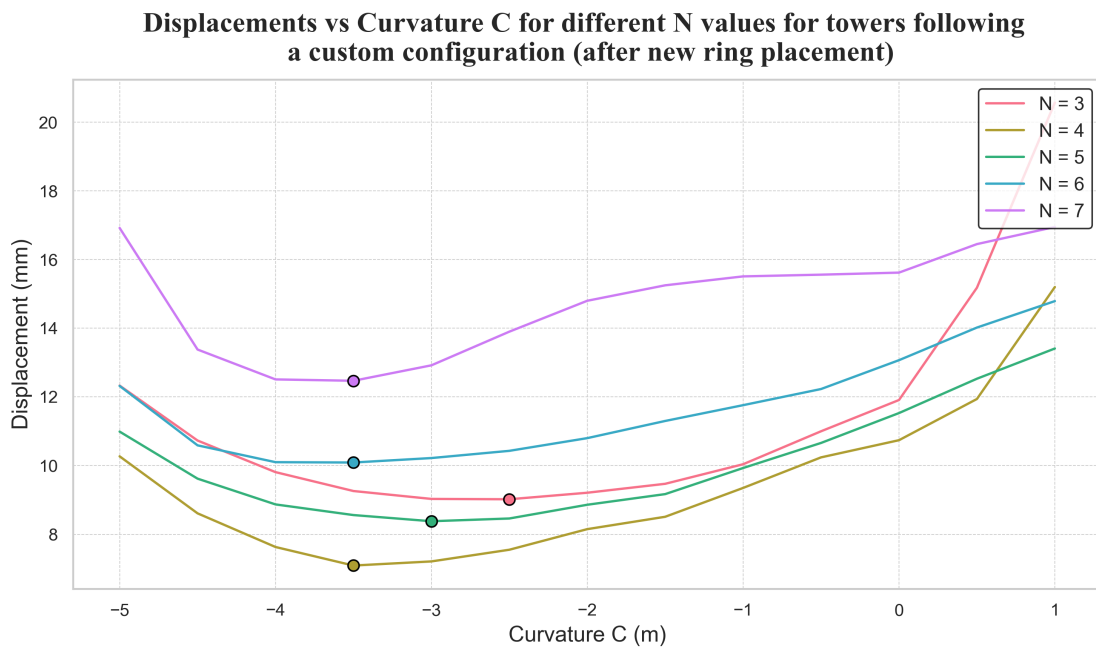


**Figure 8.12:** The plot examines tower variants adhering to a custom topology equipped with segmented rings with a curved ring at the apex, characterized by varying shape factors ( $N$ ), while maintaining a constant mass. The curvature ( $C$ ) of each design variant is iteratively changed, and the associated displacements are recorded. Markers indicate the stiffest response for every shape factor.

Similarly as before, these findings shall be compared with those obtained from previous chapters. Figure 8.13 displays stiffest response for different configurations for every shape factor  $N$ . It can be seen that by introducing a stiffening ring at the top, this new tower set up shows improvement from the one

**Table 8.2:** Stiffest shape of towers (custom top., with segmented rings and a curved ring at the top) taking different shape factors  $N$  and their respective results relating to global displacement, strain energy, and mass. It should be noted that mass is being kept constant. This measurement does inform about the design variant exhibiting the most efficient structural behaviour.

N	C (m)	Displacement (mm)	Strain Energy (kNm)	Wind (deg)	Mass (t)
3	-2.81	8.00	0.42	77	65.04
4	-3.17	6.85	0.35	45	65.04
5	-3.01	8.28	0.52	126	65.04
6	-3.75	9.95	0.51	96	65.04
7	-3.61	12.30	0.64	68	65.04
8	-3.58	14.58	0.74	48	65.04
9	-3.31	16.94	0.93	74	65.04

following a custom topology (with segmented rings). However, it does seem to be less stiff than ones equipped with curved rings at every level. Additionally, in the same fashion as for other tower set ups, stiffness does reduce as shape factor  $N$  is growing. In terms of a direct comparison with the tower having equivalent ring placement as this one (triangular topology, indicated by a purple graph), the level of stiffness that the assembly with custom pattern has shown is slightly superior for certain shape factors (up to  $N < 7$ ). Thus, after the observed stability and improved stiffness characteristics after the implementation of stiffening ring at the top, the tower defined by the custom pattern emerges as a more favorable structural assembly.

**Displacements vs. Shape factor (N)  
for tower stiffest responses for different configurations.**

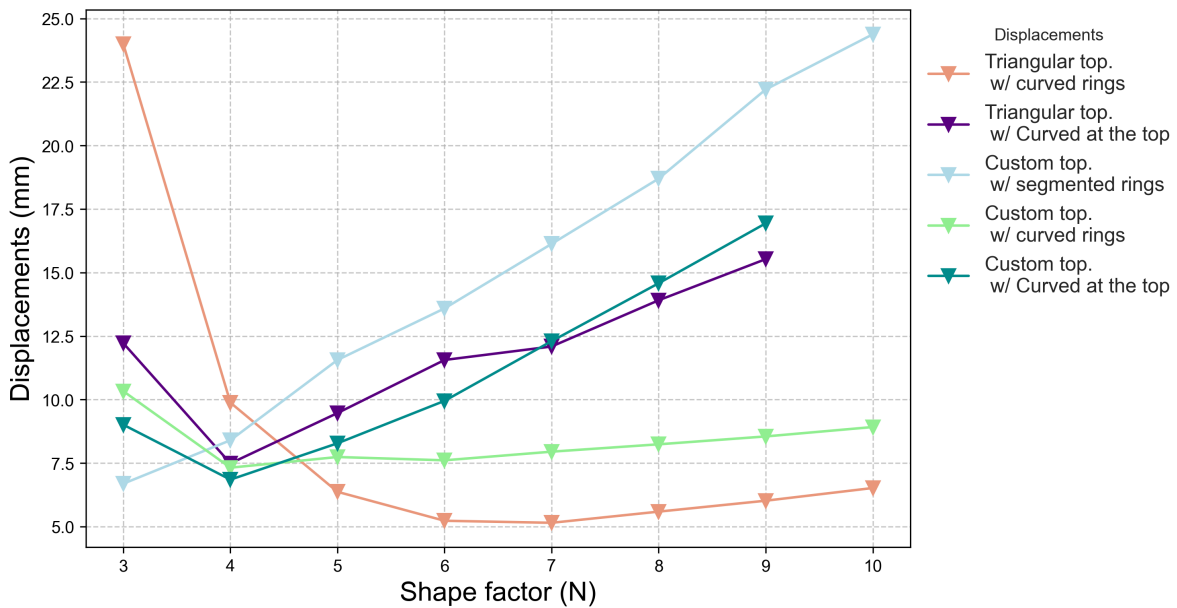


**Figure 8.13:** In the this plot, displacements are graphed against the shape factor  $N$ . Each data point represents the configuration with the highest stiffness for a given  $N$ , adhering to a custom topology with a curved ring at the top as well all the other configurations that showed favorable stiffness metrics. This analysis maintains a constant mass of approximately  $m \approx 65t$  for each tower configuration, facilitating a direct comparison of the impact of curvature  $C$  on displacement.

### 8.3. Determining the final design and optimizing member sizes

Following a thorough feasibility analysis of the novel tower design, which entails segmented (pin-jointed) rings throughout and a singular curved (circular) ring at the top, the definitive conclusion has been to adopt a configuration adhering to a custom pattern. This decision is based on the design's superior stiffness and stability, contrary to what has been observed in terms of triangular pattern. Hence, this section delves into the initial assessment of the connection design which would allow to realize the proposed tower design.

It is of essence to determine the appropriate shape factor  $N$  and curvature  $C$ . These parameters will lead the assembly process for the tower, whose connections are to be designed and assessed. By glancing at Figure 8.13, shape factors  $N = 4$  and  $N = 5$  do provide most favorable stiffness outcomes. However, knowing that a square ( $N = 4$ ) segmented circumferential ring does have longer spans than the one employing a pentagon ( $N = 5$ ) or hexagon ( $N = 6$ ), this aspect becomes crucial when live and permanent loads are introduced on each ring segment. The application of live and dead loads (which were presented in Chapter 4) are illustrated in Figure 8.14 bearing in mind that platform loads are distributed on ring elements via line loads.



**Figure 8.14:** Applied live and dead loads stemming from a platform at every ring level. Red areas indicate the potential placement of platforms and where live and dead loads are distributed initially.

Reducing span length would result in lower sagging moments on each ring segment as well as vertical loads that ought to be transferred by vertical ones. In addition, fewer vertical members would be required to support the tower at the bottom, which may introduce concerns related to buckling due to high compressive forces. Thus, utilizing higher shape factors seem to be a more favorable design decision.

An additional factor to consider is the magnitude of force to be transferred within the connection. By assuming the curvature  $C = -3.5 \text{ m}$  (which is within the range that allowed for a stiffest response for most towers) and documenting resulting shear, vertical and horizontal forces to be transferred through the lowest (critical) node for towers taking different shape factors  $N$ , one can make estimations on the feasibility of each tower in terms of connection design (Figure 8.15 and Table 8.3). After inspecting the data, it could be stated that  $N = 5$  or  $N = 6$  provides the most favorable force distribution at the connection as more vertices within the ring does result in lower impact on members and, hence, nodes. This omits the need for larger cross-sections as spans are shortened from one node to the other (diminishing sagging moments). As the difference in force at connection between variants adopting  $N = 5$  and  $N = 6$  is not as large, the final configuration for a ring shall be the one of the pentagon as this choice reduces the amount of connections needed by 6 in comparison to the hexagon (less steel is required). Additionally, it can be observed that the force magnitude in diagonal members is comparatively lower than in vertical members for this configuration, as indicated by  $D_{x1}$  and  $D_{x2}$ . This feature will assist in determining member sizes as well as connection components at critical nodes.

It should also be noted that adopting a lower shape factor  $N$ , the angle at which members join at the node are not as sharp, thus, members are not as densely and closely placed in relation to one another. Thus, from the scheming point of view, the choice of  $N = 5$  is more favorable than  $N = 6$ .

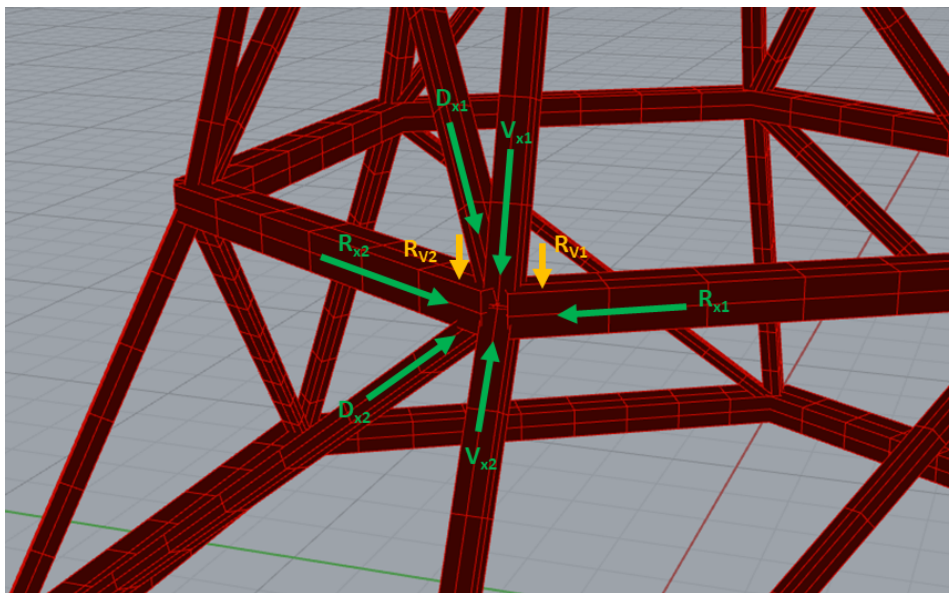


**Figure 8.15:** Illustration and annotation of forces acting on the most critical node. In this instance,  $N = 6$ ,  $C = -3.5 \text{ m}$ . It should be noted that in all cases there are 6 members joining at the node. This annotation is utilized to represent forces at nodes for towers with different  $N$  in Table 8.3. It should be noted that green colour indicates axial forces while colour yellow indicates shear forces imposed upon the connection.

After deciding on the shape factor ( $N = 5$ ) and curvature ( $C = -3.5 \text{ m}$ ), sizing of members is taken

**Table 8.3:** Representation of forces being transmitted to the most critical connection within different tower assemblies. Compressive forces are negative, while tensile are positive. It can be seen that there is a significant jump in compressive forces occurring in vertical member  $V_{x1}$  when shape factor  $N = 4$  is adopted.

<b>N</b>	$R_{x1}$ (kN)	$R_{x2}$ (kN)	$R_{v1}$ (kN)	$R_{v2}$ (kN)	$V_{x1}$ (kN)	$V_{x2}$ (kN)	$D_{x1}$ (kN)	$D_{x2}$ (kN)
4	-90.56	-90.56	-71.03	-71.03	-564.88	-786.13	-21.72	16.32
5	-102.08	-102.08	-67.01	-67.01	-475.62	-677.90	-35.89	30.34
6	-116.77	-105.75	-61.07	-61.07	-404.46	-584.71	22.47	-24.77

into account in order to find the most optimal solution that would satisfy ULS and SLS standards as proposed by Eurocode 5 (Steer 2001) and Dutch Annex of Eurocode 0 (Snijder and Steenberg 2020). As outlined in Chapter 4, the evaluation of the timber structure is facilitated by the 'Beaver' plug-in. This tool performs a structural analysis of a given timber structure, considering the ultimate limit state (ULS) across ten distinct categories and the serviceability limit state (SLS) in three categories, focusing on the deflection of individual members relative to their local axes. For the recording displacements globally as before, 'Karamba3D' outputs are utilized in this case. For SLS requirements, Table 8.4 and Table 8.5 provides limiting values that will be adopted for the tower design. Thus, for the tower design (which is assumed to be within an 'industrial building' category in Table 8.4) with a height  $H = 30\text{ m}$ , the limiting global displacement value becomes  $30/150 = 0.2\text{ m} = 200\text{ mm}$ .

**Table 8.4:** The recommended range of limiting values of deflections for beams with span  $l$  provided in Table 7.2 from Eurocode 5 (Steer 2001).

	$w_{inst}$	$w_{net,fin}$	$w_{fin}$
Beam on two supports	$l/300$ to $l/500$	$l/250$ to $l/350$	$l/150$ to $l/300$
Cantilevering beams	$l/150$ to $l/250$	$l/125$ to $l/175$	$l/75$ to $l/150$

**Table 8.5:** Limits for horizontal displacements (for characteristic combinations of actions) as detailed in EN 1990, cl. A1.4.2 (Snijder and Steenberg 2020).

<b>Number of storeys</b>	<b>Building (part)</b>	<b>Limit of horizontal displacement</b>
1	Industrial building	$u \leq H/150$
	Other buildings	$u \leq H/300$
2 or more	Per storey	$u_i \leq H_i/300$
	Whole building	$u \leq H/500$
Parapet at the location of a height difference	Upper edge and baluster together	$u \leq 20\text{ mm}$

Thus, after obtaining unity checks in all three categories (ULS, SLS for local displacements and SLS for global displacements), the on-going design procedure investigates most suitable member sizes that would deem the structure optimized for its mass. To accommodate the observation that diagonal and vertical members lower down in the structure experience higher stresses stemming from both vertical

and lateral loads, for optimization purposes these members have been divided into two categories: those in the upper section and those in the lower section. Figure 8.16 illustrates the distinction of two sections. An exception is made for ring elements where three sections have been proposed and portrayed in Figure 8.16. This division reflects the impact of ring radius, which yields higher potential live and dead area loads. The optimization process adjusts the cross-section of each member group to arrive at the most material efficient solution and satisfy ULS and SLS (global and local) requirements. The process involved adjusting or reducing timber member cross-section dimensions until utilization in all three categories were close to a limiting value of 1. Thus, Table 8.6 presents final tower design geometry, topology and member size characteristics that define the optimized structure against wind, live and dead loads. Consequently, Figures 8.17 and 8.18 displays resulting ULS and SLS (local) outputs for the assembly of timber members within the tower structure obtained through 'Beaver' plugin in 'Grasshopper' environment.

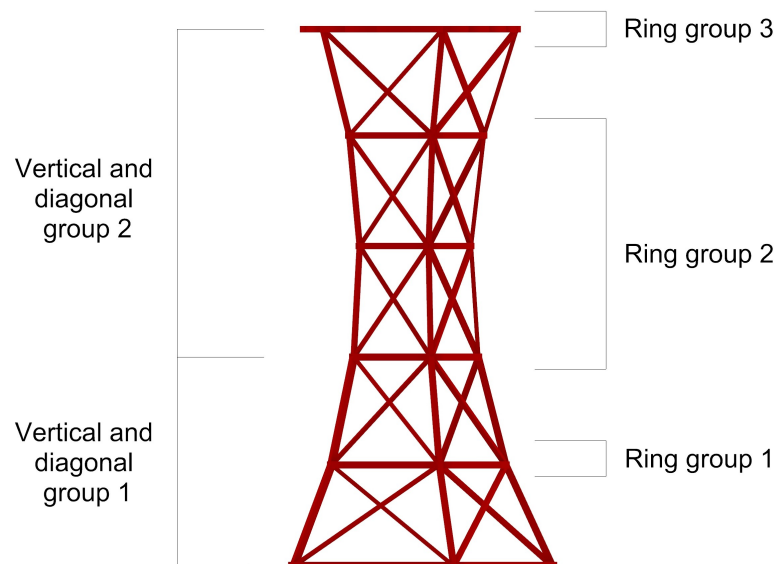


**Figure 8.16:** Division of members for optimization.

Table 8.6 offers detailed critical utilization values for the structure relating to ULS and SLS (local and global) conditions. Hence, it can be inferred that the local Serviceability Limit State (SLS) condition primarily governs the tower's design criteria, especially in relation to the lower ring elements. These components, because of their extended spans and the significant areal loads from the larger platform, deflect to levels near the permissible limits.

**Table 8.6:** A comprehensive overview of tower's specifications relating to dimensions, strength and SLS characteristics (local and global), final geometrical parameters and materials of choice.

<b>Dimensions of Structural Elements</b>		
<b>Element group</b>	<b>Height (H) in mm</b>	<b>Width (W) in mm</b>
Vertical 1	320	280
Vertical 2	280	240
Diagonal 1	320	200
Diagonal 2	400	160
Ring 1	400	560
Ring 2	320	450
Ring 3	440	620
<b>Mass</b>		28.10 t

<b>Load Capacities</b>		
<b>Element</b>	<b>ULS</b>	<b>SLS (Local)</b>
Vertical	0.84	0.42
Diagonal	0.84	0.82
Ring	0.62	0.93

<b>Parameter</b>	<b>Value</b>
Shape factor $N$	5
Curvature $C$	-3.5 m
Displacement	35.05 mm
SLS	0.175

<b>Material</b>	<b>Type</b>
Timber	GL28h
Steel	S355

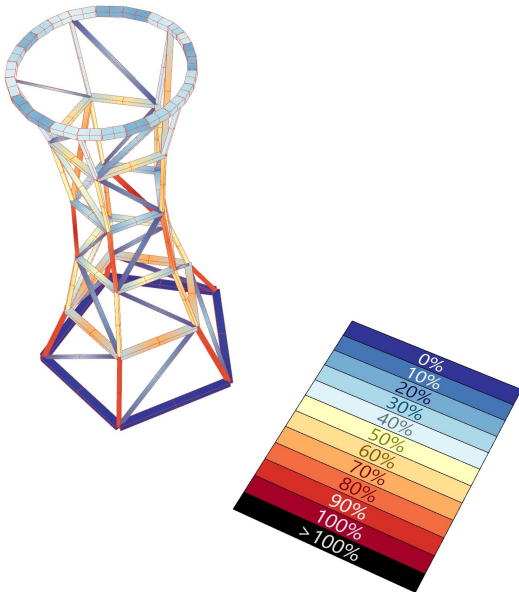


Figure 8.17: ULS unity check for all timber members within the final design of the tower.

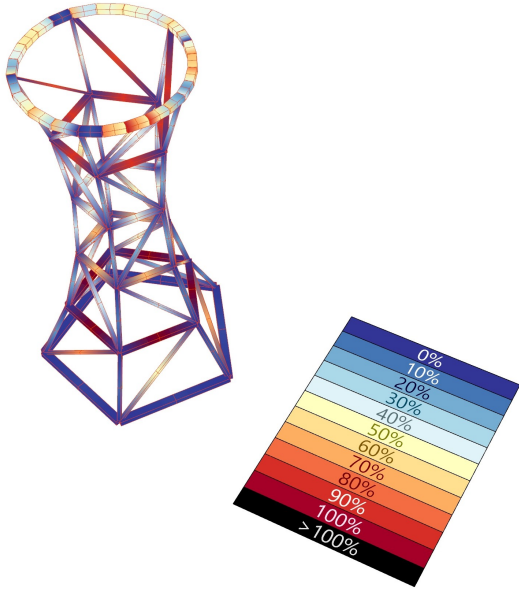


Figure 8.18: SLS (local) unity check for all timber members within the final design of the tower.

## 8.4. Connection detailing

### 8.4.1. Stiffness Considerations and Geometry of the Connection

Following the acquisition of the tower’s final overall geometry, material selection, and sizing of its members, the next step involves evaluating how the elastic slip modulus could impact the tower’s global

lateral stiffness. Within 'Karamba3D' plug-in this characteristic can be defined by adjusting the 'Beam-joints' component and providing translational stiffness values in its local x direction at the end of each members within the structure. In this case, diagonal, vertical and segmented ring members are the ones whose end joint translational stiffnesses would be altered. Since the curved ring member at the top is assumed to be continuous, the joints connecting each discrete unit that comprises it are set to possess infinite translational stiffness. Thus, the resulting global displacement after adjusting slip modulus of each joint is presented in Figure 8.19. As it can be anticipated, there is a rise in the global lateral displacement values in response to a decrease in the elastic slip modulus. However, in order to maintain the tower within the allowable limit (indicated by a red line in Figure 8.19), the required elastic slip modulus at ends of each member has to be at least 27.74 kN/mm.

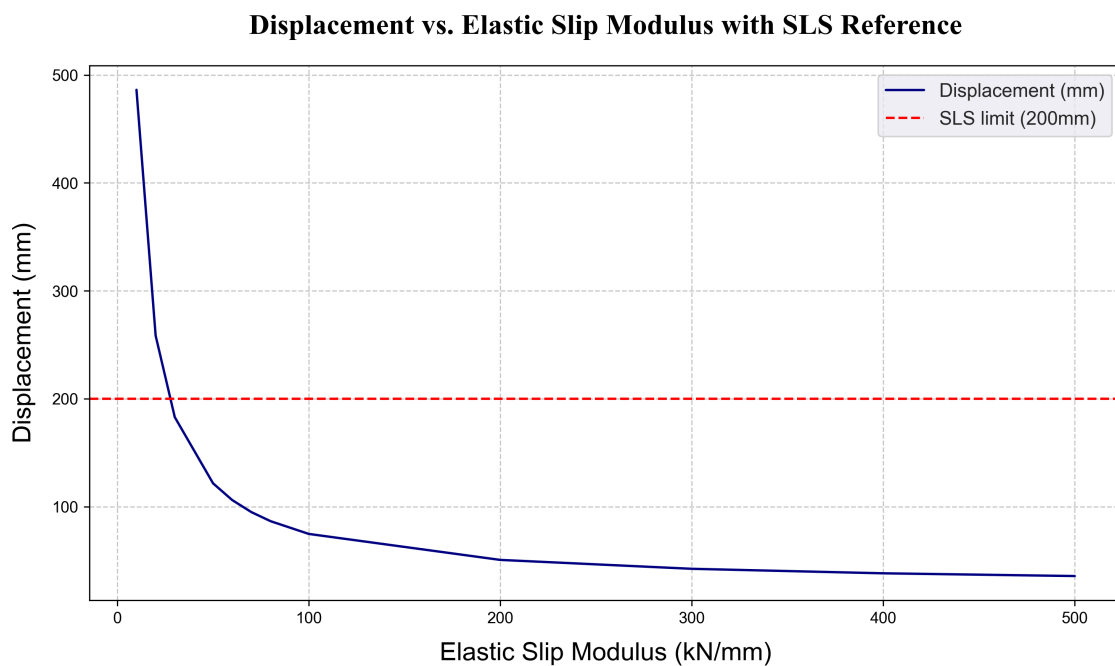


**Figure 8.19:** Illustration of members based on their critical and governing failure category in ULS.

After establishing connection requirements that would deem the tower structure adhering to proposed SLS requirements, the next step involves proceeding with the detailing phase, which will outline the schematic configuration of the connection. After inspecting the critical node at the lowest ring element, member cross-sections and angles of orientation as well as loads imposed upon the connection (as detailed in Table 8.3), the initial configuration in 2D of the connection can be drafted and provided in Figure 8.20. The design incorporates six steel plates linked to a steel tube, which is internally reinforced along its diameter with an extra set of plates. These reinforcements are oriented to align with the principal force vectors acting upon the critical node. The steel tube does provide improved stability against buckling. Dimensions and types of bolts are detailed within the drawing. Six external plates are slotted inside rectangular timber members and bolted through. For vertical and ring members, due to the high magnitude of forces to be transferred (Table 8.3) two plates are inserted into those elements as to reduce the susceptibility to buckling of these steel members. However, as forces in diagonal members are lower in value, steel plates may protrude more as buckling might not be critical in that case. Additionally, this provides more favorable spacing of these members. Members are annotated

in Figure 8.20 in sync with the labelling provided in Figure 8.15. To gain a better feel for dimensions and angles of inclination for each plate, Figure 8.21 provides a 3D representation of the proposed connection design.

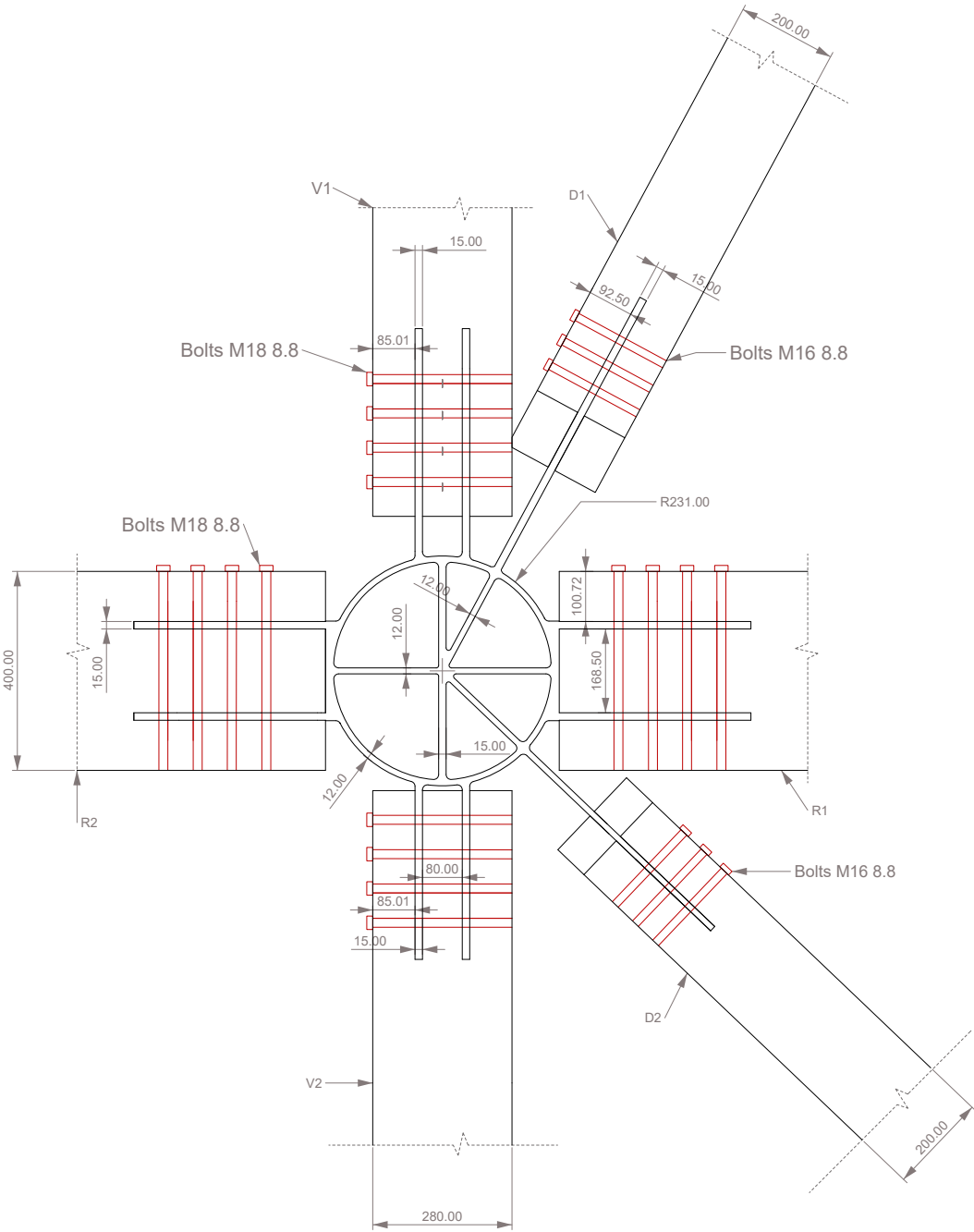
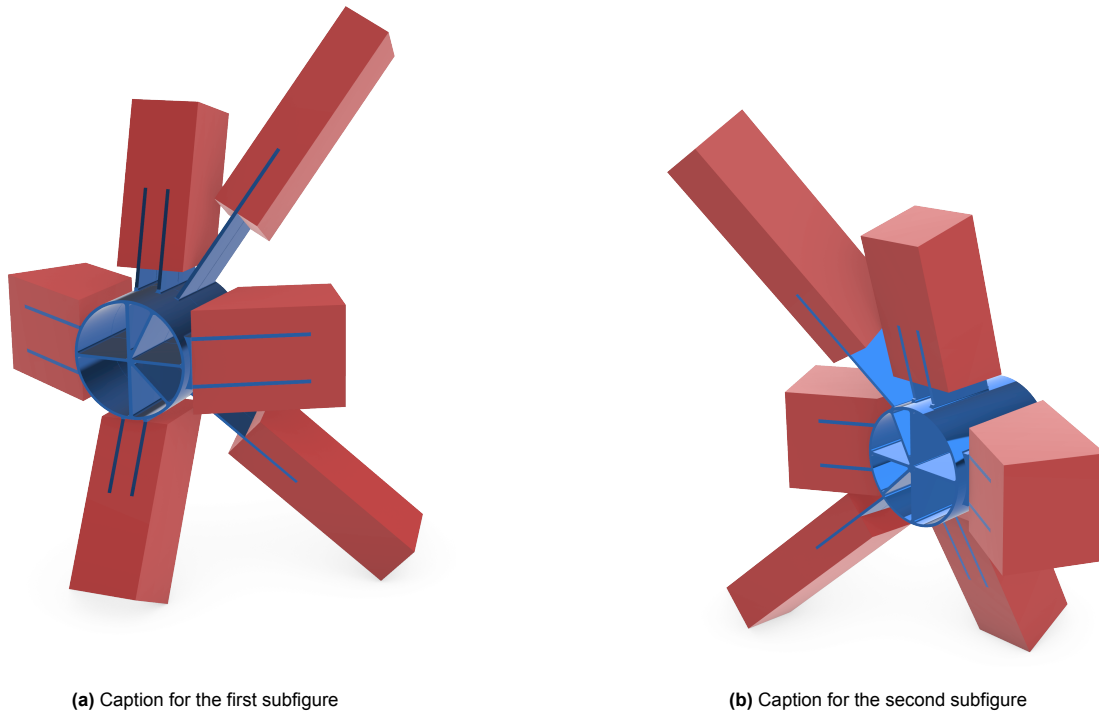


Figure 8.20: Front view of the connection. All values are in mm.

Following the outline of the steel-timber connection’s overall geometry, a detailed evaluation of each member and the respective plates in respect to its slip modulus and strength capacity is subsequently undertaken. The lower vertical member, denoted as V2, is recognised as the most crucial element



**Figure 8.21:** Perspective view of the proposed connection design. Red blocks indicate glulam members

according to the findings presented in Table 8.3. The total design compressive force to be taken by this timber-steel connection component is:  $F_{Ed} = -677.90 \text{ kN}$ . Hence, the subsequent subsections will provide analytical and finite element analysis of the connection in terms of its lateral stiffness, stability and strength.

#### 8.4.2. Analytical Assessment of the connection in SLS and ULS in accordance with Eurocode 5

##### Elastic slipping modulus assessment of the critical fastener connection

The multiple fastener connection as it is present in the vertical member V2, is equipped with 9 bolts and with multiple shear planes (due to two plates being utilized). Thus, for this component, the prescribed minimum distances and spacing are set in accordance with the guidelines provided in Eurocode 5. General characteristics for chosen bolt (fastener) type can be found in Table 8.7, while glulam (GL28h) material properties are provided in Table 8.8.

In this case, minimum distances and spacings are computed based on equations provided in Table 8.9:

$$a_1 = (4 + |\cos \alpha|) \cdot d = (4 + |\cos 0^\circ|) \cdot 18 \text{ mm} = 90 \text{ mm} \quad (8.1)$$

$$a_2 = 4 \cdot d = 4 \cdot 18 \text{ mm} = 72 \text{ mm} \quad (8.2)$$

**Table 8.7:** Fastener Specifications

Parameter	Value
Fastener diameter $d$	18 mm
Steel class	8.8
Elastic limit $f_{y,b}$	660 MPa
Characteristic tensile strength $f_{u,b}$	830 MPa
Number of rows $n_{rows}$	3
Number of bolts per row: $n$	3

**Table 8.8:** Material properties for GL28h class in accordance with EN 14080:2013.

Property	GL28h	Property	GL28h
		$E_{0,g,mean}$ (MPa)	12600
		$E_{0,g,05}$ (MPa)	10500
$f_{m,g,k}$ (MPa)	28	$E_{90,g,mean}$ (MPa)	300
$f_{t,0,g,k}$ (MPa)	22.3	$E_{90,g,05}$ (MPa)	250
$f_{t,90,g,k}$ (MPa)	0.5	$G_{g,mean}$ (MPa)	650
$f_{c,0,g,k}$ (MPa)	28	$G_{g,05}$ (MPa)	540
$f_{c,90,g,k}$ (MPa)	2.5	$G_{r,mean}$ (MPa)	65
$f_{v,g,k}$ (MPa)	3.5	$G_{r,05}$ (MPa)	54
$f_{r,g,k}$ (MPa)	1.2	$\rho_{g,k}$ (kg/m <sup>3</sup> )	425
		$\rho_{g,mean}$ (kg/m <sup>3</sup> )	460

$$a_{3,t} = \max(7 \cdot d, 80 \text{ mm}) = \max(7 \cdot 18 \text{ mm}, 80 \text{ mm}) = 126 \text{ mm} \quad (8.3)$$

$$a_{3,c} = 4 \cdot d = 4 \cdot 18 \text{ mm} = 72 \text{ mm} \quad (8.4)$$

$$a_{4,t} = \max((2 + 2 \cdot \sin \alpha) \cdot d, 3 \cdot d) = \max((2 + 2 \cdot \sin 0^\circ) \cdot 18 \text{ mm}, 3 \cdot 18 \text{ mm}) = 54 \text{ mm} \quad (8.5)$$

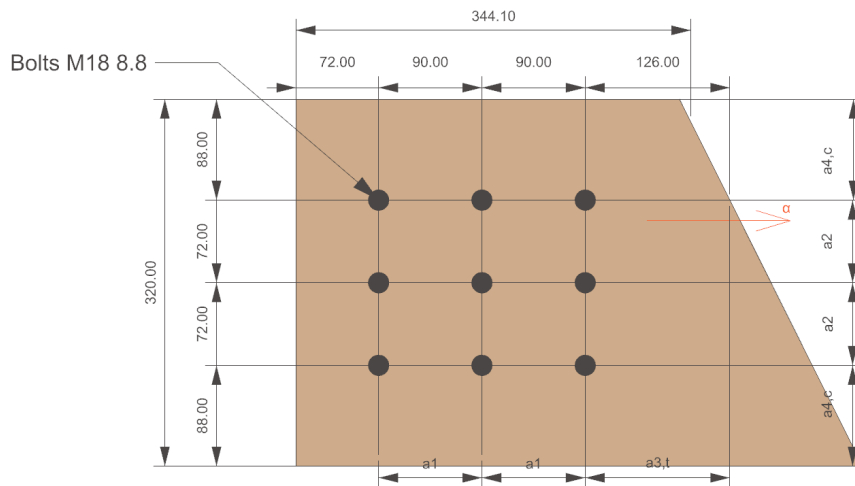
$$a_{4,c} = 3 \cdot d = 3 \cdot 18 \text{ mm} = 54 \text{ mm} \quad (8.6)$$

Note that for  $\alpha = 0^\circ$ , the cosine is 1 and the sine is 0. Therefore,  $|\cos \alpha| = 1$  and  $\sin \alpha = 0$ .

After establishing spacing and edge distances, the following computations aim at determining the stiffness per shear plane in accordance with Eurocode 5. Thus, to estimate the stiffness of each shear plane of the connection, it is necessary to use the average density of glued laminated timber GL28h with a mean density  $\rho_m = 460 \text{ kg/m}^3$  according to EN 14080. For a multiple shear plane fastener connection, it is of importance to decompose the component into inner and outer parts with two shear

**Table 8.9:** Minimum values of spacing and edge and end distances for bolts as detailed in Table 8.4 from Eurocode 5.

Spacing and end/edge distances (see Figure 8.7)	Angle $\alpha$	Minimum spacing or end/edge distance
$a_1$ (parallel to grain)	$0^\circ \leq \alpha \leq 360^\circ$	$(4 +  \cos \alpha )d$
$a_2$ (perpendicular to grain)	$0^\circ \leq \alpha \leq 360^\circ$	$4d$
$a_{3,t}$ (loaded end)	$-90^\circ \leq \alpha \leq 90^\circ$	$\max(7d; 80 \text{ mm})$
$a_{3,c}$ (unloaded end)	$90^\circ \leq \alpha \leq 270^\circ$	$4d$ (for $90^\circ \leq \alpha < 150^\circ$ ) $(1 + 6 \sin \alpha)d$ (for $150^\circ \leq \alpha < 210^\circ$ ) $(1 + 6 \sin \alpha )d$ (for $210^\circ \leq \alpha \leq 270^\circ$ )
$a_{4,t}$ (loaded edge)	$0^\circ \leq \alpha \leq 180^\circ$	$\max[(2 + 2 \sin \alpha)d; 3d]$
$a_{4,c}$ (unloaded edge)	$180^\circ \leq \alpha \leq 360^\circ$	$3d$

**Figure 8.22:** Resulting distances and spacing of the connection.  $\alpha$  direction denotes compressive force orientation which is aligned with the grain direction in this case. All values are in mm.

planes each as illustrated in Figure 8.23. The slip modulus in the serviceability limit state per fastener and shear plane is obtained by Eq. (7.1) in Eurocode 5:

$$K_{\text{ser}} = \rho_m^{1.5} \cdot d/23 = 460^{1.5} \cdot 18/23 = 8488.65 \text{ N/mm} \quad (8.7)$$

For the timber-steel multiple fastener connection with 9 bolts and 4 shear planes and under consideration of 7.1(3) in Eurocode, this yields:

$$k_{\text{type}} = \begin{cases} 1 & \text{for timber/timber} \\ 2 & \text{for timber/steel or timber/concrete} \end{cases} \quad (8.8)$$

$$K_{\text{ser},J} = n_{\text{plan}} \cdot n_{\text{org}} \cdot k_{\text{type}} \cdot K_{\text{ser}} = 4 \cdot 9 \cdot 2 \cdot 8488.65 = 611.18 \text{ kN/mm} \quad (8.9)$$

For the stiffness in inner part, called IN:

$$K_{\text{ser},J,\text{IN}} = n_{\text{plan}} \cdot n_{\text{org}} \cdot k_{\text{type}} \cdot K_{\text{ser}} = 2 \cdot 8 \cdot 2 \cdot 8488.65 = 407.45 \text{ kN/mm} \quad (8.10)$$

For the stiffness in outer part, called OUT:

$$K_{ser,J,OUT} = n_{plan} \cdot n_{org} \cdot k_{type} \cdot K_{ser} = 1 \cdot 8 \cdot 2 \cdot 8488.65 = 152.80 \text{ kN/mm} \quad (8.11)$$

Hence, the resulting design slip modulus or lateral stiffness of the fastener connection exceeds the minimum required limit as the utilization of the connection is:

$$\frac{27.74 \text{ kN/mm}}{611.18 \text{ kN/mm}} = 0.045 < 1.000 \quad (8.12)$$



**Figure 8.23:** Decomposition of the connection with four shear planes into connections with two shear planes (Sandhaas et al. 2018).

To assess the critical joint in terms of ULS, general characteristics of the connection are required. The embedding strength is given by the characteristic density of timber GL28h according to EN 14080 and Equation (8.32) in Eurocode 5, which yields:

$$f_{h,0,k} = 0.082 \cdot (1 - 0.01 \cdot d) \cdot \rho_k = 0.082 \cdot (1 - 0.01 \cdot 18) \cdot 440 = 29.58 \text{ MPa}$$

The rope effect is calculated by the timber compression under the flat washer as:

$$F_{ax,Rk} = \frac{\pi}{4} (D_{ext}^2 - D_{int}^2) \cdot 3 \cdot f_{c,90,k} = \frac{\pi}{4} (50^2 - 18^2) \cdot 3 \cdot 2.5 = 12817 \text{ N}$$

The yield moment of the bolt is calculated according to Equation (8.30) in Eurocode 5:

$$M_{y,Rk} = 0.3 \cdot f_{u,k} \cdot d^{2.6} = 0.3 \cdot 830 \cdot 18^{2.6} = 456991.22 \text{ Nmm}$$

#### Capacity of a single dowel

Starting from the proposed dimensions in Figure 8.20 with side member thicknesses  $t_1 = 85 \text{ mm}$  and thickness of the inner member  $t_2 = 80 \text{ mm}$ , the capacity of a connection with steel plates constituting

the external elements of a connection with two shear planes (part IN) can be determined according to Eq. (8.13) in Eurocode 5 (concerning failure modes  $l$  and  $m$ ):

$$F_{v,Rk,Jhs} = \min \left\{ \begin{array}{l} 0.5 \cdot f_{h,0,k} \cdot t_2 \cdot d, \\ \frac{2.3 \cdot \sqrt{M_{y,Rk} \cdot f_{h,0,k} \cdot d}}{m} \end{array} \right. \quad (8.13)$$

Application of these design equations for the inner (IN) part results in:

$$F_{v,Rk,Jhs,IN} = \min \left\{ \begin{array}{l} 0.5 \cdot 29.58 \cdot 80 \cdot 18, \\ 2.3 \cdot \sqrt{456991.22 \cdot 26.52 \cdot 18} \end{array} \right. \quad (8.14)$$

$$F_{v,Rk,IN} = 21301.63 \text{ N} \quad (8.15)$$

The capacity of a connection with a steel plate comprising the central element of a connection with two shear planes (part OUT) is computed in accordance with Eq. (8.11) in Eurocode 5 (concerning failure modes  $f$ ,  $g$  and  $h$ ):

$$F_{v,Rk,Jhs} = \min \left\{ \begin{array}{l} f_{h,1,k} \cdot t_1 \cdot d, \\ f_{h,1,k} \cdot t_1 \cdot d \left( \sqrt{2 + \frac{4 \cdot M_{y,Rk}}{f_{h,1,k} \cdot d \cdot t_1^2}} - 1 \right), \\ 2.3 \cdot \sqrt{M_{y,Rk} \cdot f_{h,1,k} \cdot d} \end{array} \right. \quad (8.16)$$

Application of the design equations for the OUT part leads to:

$$F_{v,Rk,Jhs,OUT} = \min \left\{ \begin{array}{l} 29.58 \cdot 85 \cdot 18 = 45265.96 \text{ N} \\ 29.58 \cdot 85 \cdot 18 \left( \sqrt{2 + \frac{4 \cdot 456991.22}{29.58 \cdot 18 \cdot 85^2}} - 1 \right) = 25948.36 \text{ N} \\ 2.3 \cdot \sqrt{456991.22 \cdot 29.58 \cdot 18} = 35880.47 \text{ N} \end{array} \right\} = 25948.36 \text{ N} \quad (8.17)$$

The capacity of half of the connection is acquired by mode 5 ( $m + g$ ):

$$F_{v,Rk,pb,OUT} = F_{v,Rk,Jhs,IN} + F_{v,Rk,Jhs,OUT} = 21301.63 + 25948.36 = 47249.99 \text{ N} \approx 48 \text{ kN} \quad (8.18)$$

### Splitting failure

The brittle capacity, taking into account several fasteners in a row, is acquired in accordance with Eq. (8.1) and (8.34) in Eurocode 5 by:

$$F_{v,ef,Rk} = n_{plate} \cdot \sum_{i=1}^{n_{rows}} n_{ef} \cdot F_{v,p,Rk,Jhs} \quad (8.19)$$

where

$$n_{ef} = \min \left\{ \begin{array}{l} n \\ n^{0.9} \sqrt[4]{\frac{a_1}{13d}} \end{array} \right. = \min \left\{ \begin{array}{l} 4 \\ 4^{0.9} \sqrt[4]{\frac{90}{13 \cdot 18}} \end{array} \right. = 2.74 \quad (8.20)$$

and thus

$$F_{v,ef,Rk} = 2 \cdot 3 \cdot 2.74 \cdot 48 = 789.12kN \quad (8.21)$$

The capacity going along the row of fasteners of the central component of the connection accumulates to:

$$F_{v,ef,Rk,IN} = \frac{789.12}{48} \cdot 21.30 = 350.17kN \quad (8.22)$$

and the capacity along the row of fasteners of the outer parts of the connection amounts to:

$$F_{v,ef,Rk,OUT} = \frac{789.12}{48} \cdot \frac{25.94}{2} = 213.23kN \quad (8.23)$$

### Plastic failure

In the scenario where the connection is able to reach the plastic limit without brittle failure, the rope effect can be included to the capacity per shear plane as provided here:

$$F_{v,Rk} = F_{v,Rk,Jhs} + \min \left\{ \frac{F_{ax,Rk}}{4}, 0.25 \cdot F_{v,Rk,Jhs,IN} \right\} + \min \left\{ \frac{F_{ax,Rk}}{4}, 0.25 \cdot F_{v,Rk,Jhs,OUT} \right\} = 48 + 2 \cdot 3.2 = 53.65kN \quad (8.24)$$

The maximum characteristic plastic capacity of the connection can be derived to be:

$$F_{v,Rk} = n_{plate} \cdot \sum_{i=1}^{n_{rows}} n \cdot F_{v,Rk} = 2 \cdot 3 \cdot 3 \cdot 53.65 = 965.86kN \quad (8.25)$$

whereby the plastic capacity of the central part amounts to:

$$F_{v,Rk,IN} = \frac{965.86}{53.65} \cdot (21.30 + 3.20) = 441.11kN \quad (8.26)$$

and the plastic capacity of one of the outer parts amounts to:

$$F_{v,Rk,OUT} = \frac{965.86}{53.65} \cdot \frac{(25.94 + 3.20)}{2} = 262.38kN \quad (8.27)$$

### Summary of the analytical assessment

Therefore, to offer an overview of the computed outcomes, Table 8.10 presents the essential strength and stiffness characteristics of the multi-fastener connection that includes 9 bolts.

Parameter	Value	Design Requirement	Utilization
Plastic failure: $F_{v,Rk}$	965.86 kN	677.90 kN	0.70
Splitting failure: $F_{v,ef,Rk}$	789.12 kN	677.90 kN	0.86
Stiffness: $K_{ser,J}$	611.18 kN/mm	27.74 kN/mm	0.04

**Table 8.10:** Summary of failure modes, stiffness, design requirements, and utilization.

It can be observed that the steel-timber joint with multiple fasteners and shear planes have sufficient strength and stiffness to satisfy ULS and SLS requirements for the tower. The utilization figures detailed in Table 8.10 suggest there is some room to optimize the joint design, resulting in more efficient use of

materials. Approaching a more optimal utilization ratio, which is closer to 1, may involve re-adjusting the configuration, such as reducing the number of bolt rows, choosing bolts with reduced diameters, or using steel of a lower grade. An investigation of the steel-timber joint in the V2 member should ideally include an analysis for block shear failure scenario, given that the V2 member may be subjected to tension forces in cases where the tower structure bears no live or dead loads coming from platforms. The bolt spacing and edge distanced did account for a scenario where the timber member V2 might be exposed to tensile forces by employing a loaded end parameter  $a_{3,t} = 126mm$  (Figure 8.22). However, due to the limited time frame designated for this thesis, it is of necessity to exclude this aspect of the assessment.

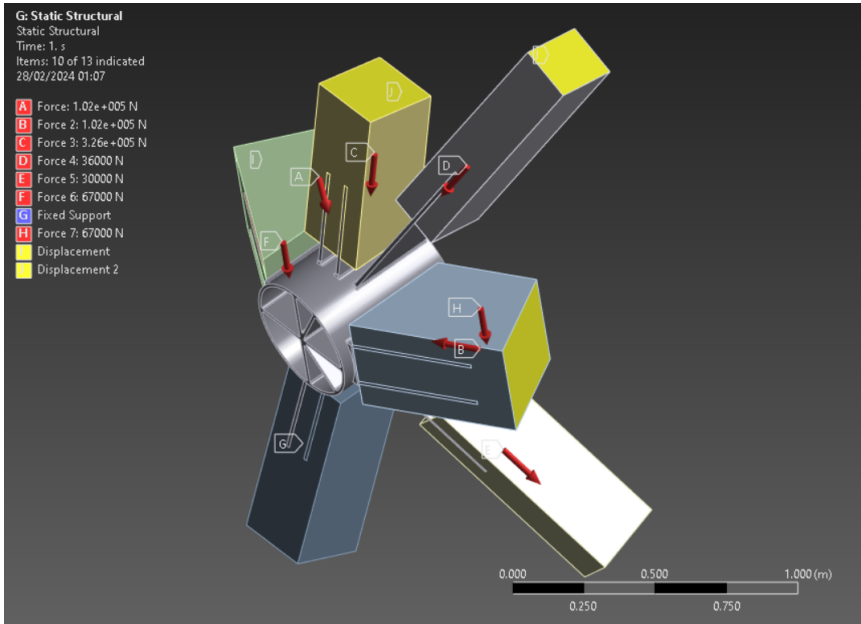
The following part of the connection examination will focus on an evaluation of the stability and resistance to buckling in the updated connection design by employment of a Finite Element Analysis (FEA) tools.

### 8.4.3. Finite Element Analysis of the steel part of the connection

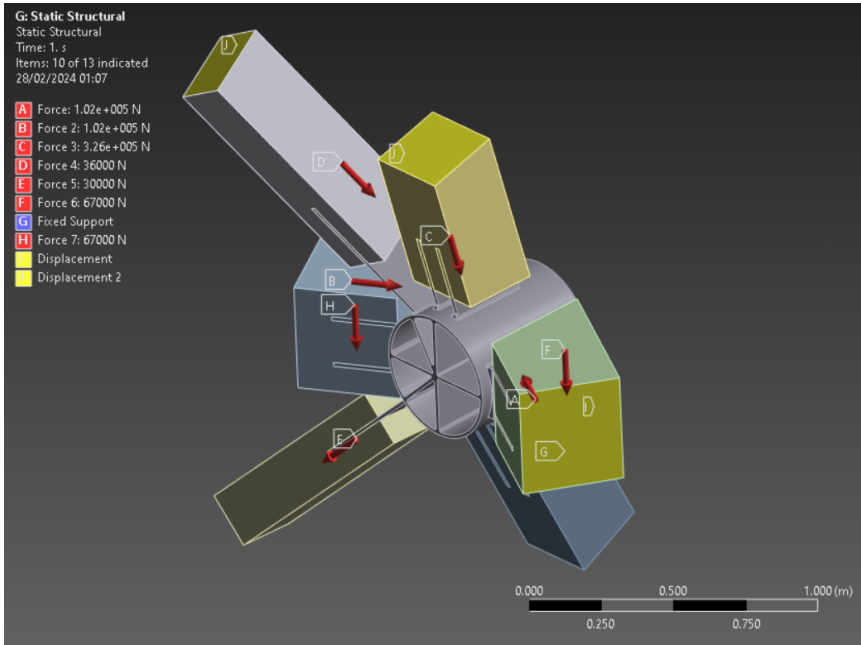
The geometry displayed in Figure 8.21 has been imported into 'ANSYS FEA' software and analysed by employing Finite Element Method (FEM). The choice of this analysis software is based on its powerful functionality in terms of analysis non-conventional geometries and configurations while 'IDEA StatiCa' is mostly limited to pre-defined and standardized member cross-sections and connectivities. In addition, this software does allow to model anisotropic materials like timber.

Red timber blocks referred in the aforementioned image are modelled as timber by incorporating glulam GL28h characteristics displayed in Table 8.8. Thus, it is of importance to model the material by selecting 'Orthotropic Elasticity' option under Linear Elastic toolbar and defining Young's modulus, Poisson's ratio and shear modulus to be different along the local X, Y and Z directions. When considering that the external steel plates are inserted into the timber blocks, assigning orthotropic properties to the glue-laminated timber beams can in turn enhance the reinforcing effect to some degree on the steel plates through these wooden elements. Thus, this feature would reduce buckling lengths of steel plates, especially of those associated with vertical members V1 and V2 as the force to be transmitted is the highest there. Boundary conditions, as illustrated in Figure 8.24, specify that the end surfaces of the timber blocks are constrained, limiting their displacement along the local y and z axes. As regards the load imposition on plates, it has been modelled that the bonded area between timber blocks and steel plates would be placed around the centre point of associated bolt rows.

Therefore, by running a linear 'Eigenvalue Buckling' and 'Static Structural' analysis, the resulting buckling factors and associated shapes can be observed in Figure 8.25, while equivalent stresses within the steel part are illustrated in Figure 8.26. By employing the tubular section, buckling factors for all deformed shapes are above the conservative limit of 15, which allows to rely on the plastic analysis of steel sections of group 1 and group 2 as detailed by IDEA StatiCa (2024). This marks a considerable improvement in terms of stability compared to the section previously designed and considered (Figure 8.4). In terms of equivalent (von-Mises) stresses in the tubular section, it appears that stress concentrations are generally absent. Nevertheless, one might observe these stress concentrations at the lower part of the connection, particularly where slotted plates are joined to the tubular section. This possibly



(a)



(b)

Figure 8.24: Set-up of the connection model by enforcing restraints and loading conditions.

could be improved by increasing the fillet radius, although it might cause challenges concerning the stress flow within the section due to welds, which would be done off-site.

### 8.5. Construction considerations

An important design feature of the tower structure that improved stiffness characteristics have been the ring at the top. In modelling the ring, it has been assumed that it is continuous and non-segmented.

This is implemented by allowing every discrete member comprising it to be connected by rigid joints. However, the diameter of this ring is 12 m, thus, it is a geometrical parameter limiting this type of member to be transported by the truck in one piece. This transportation and construction limitation shall be addressed by splitting the ring into 3 segments (splines) at certain points within the structure and allowing these members to be transported by the cargo box of the truck. Limiting cargo dimensions in the Netherlands are provided by European Parliamentary Research Service (2014), which indicate the limiting height of the cargo to be 4 m, 2.55 meters in width while the length of it should not exceed 12 m. It can be viewed in Figure 8.27 that resulting splines are almost within permissible limits defined by European Parliamentary Research Service (2014). The height exceedance of 0.35 m is recognised and shall be taken into account by possibly utilizing an open cargo platform on the truck.

The structural design involves split ring segments that are interconnected through joints, which allow rotations around the local z-axis, corresponding to in-plane rotation. Concerning other restraints, including different rotational directions and translations, are restricted in order to ensure the desirable level of stiffness within the structure. Modelled joints of the ring are displayed in Figure 8.28, while one should note the positioning of the joint, which is roughly aligned with the point of contraflexure or inflection point within the ring. In this point, moments around the local y axis (sagging and hogging) are close to zero. In this way, the designed connection at that node is required to transfer minimal amounts of bending moment. Thus, the material usage, such as steel bolts and plates, is effectively reduced. Regarding the impact on tower's structural performance, resulting updated ULS and SLS values are provided in Table 8.11 while in-plane moments within the ring before and after the split of it are provided in Figure 8.29. It is evident and anticipated that allowing in-plane rotations at the top curved ring would have a slight detriment to the overall stiffness of the tower as global lateral displacements rose to 41.14 mm from the previous 34.72 mm. However, increased in-plane moments did not affect the ULS general utilization value (which remained constant at 0.56) as curved rings did not represent to the most critical member within the assembly. To be precise, though, the utilization as regards the ULS at the top ring did increase from 0.14 to 0.17 as 'Combined Tension and Bending' remained the critical failure mode associated with this member.

**Table 8.11:** Structural Performance Metrics for the Tower after implementing split ring at the top.

<b>Metric</b>	<b>Value</b>
Displacement	41.14 mm
SLS (Global)	0.20
Max. ULS	0.84
Max. SLS (Local)	0.93

## 8.6. Discussion

This chapter provides a description of a detailed design process that delves into the materialization and assembly of the tower. The most optimal design does not only fulfill standardized requirements related to global stiffness characteristics, but to member strength, stability (ULS) as well as connection detailing and scheming considerations. A key example of an iterative design processes was the fact that the most optimal and feasible design outcome was not dictated solely by the parametric lateral stiffness study findings. Instead, practical real-world considerations, particularly regarding the application of vertical loads and timber-steel connections dictated the design outcome. The primary assessment tool for timber was the 'Beaver' plug-in, which proved to be instrumental in ensuring that the design stays within permissible limits dictated by Eurocode 5. The author believes that this tool will become integral to civil engineering design practices in the near future. Its utility will extend beyond academia into the professional realm, thanks to its capability to immediately assess timber structures across 10 design categories (provided in Chapter 4). The main limitation of the software remains its inability to assess more unconventional timber cross-sections, like circular, for example. In addition, the tool does not precisely indicate displacement values for individual members, rather, it only produces SLS unity check results. Finally, the formatting of the final report could be re-structured for enhanced readability.

The first design exploration approached the tower variant that was considered the most optimal in terms of lateral stiffness analysis: triangular (diagrid) pattern featuring curved (circular) rings. The further analysis of the tower requires to apply live and dead loads to the structure stemming from the platform at each ring. The decision to integrate an insertion within the ring was motivated by the requirement to maintain the continuity of this element. This approach allows for the inclusion of a steel plate that connects diagonal members from both the bottom and top. The qualitative analysis of the concept of this connection concluded the complexity of this joint. Further research is warranted to assess the feasibility and the strength of this connection via the implementation of FEA tools. This is required as to examine how the steel plate interacts with the timber it is embedded in, as well as with the bolts drilled in the vicinity of it. The most important takeaway was that the straightness of the insertion plate necessitates major curvature variable  $C$  adjustments to force upper and lower diagonal members to meet the node in the same plane. This introduces an additional variable in the design process whenever as the connection configuration is directly implicated by the global geometrical variable.

By omitting curved rings, that impose quite a challenging level of connectivity of adjacent members, the design process implemented segmented ring configuration with one curved ring at the top. In terms of the pattern, the custom one emerged as primary one due to its high levels of stiffness when mostly segmented rings compose the tower. Due to high loads to be transmitted at the bottom of the structure, which might lead to localized buckling of steel members within the potential connection, this design procedure proposed a tubular steel component with radially placed external and internal plates that align with timber members to be joined. Knowing that this connection configuration requires quite a significant amounts of steel, the number of nodes within the structure had to be lowered (reduced shape factor  $N$ ) even though this topology parameter is not the one suggested by the parametric stiffness study conducted in this chapter. However, these design alterations pose an importance of developing multiple final design options since the whole array of performance criteria will not be satisfied evenly greatly by one singular tower configuration. By weighing the importance of each requirement, the selection

process iteratively weaves between different design variants by sacrificing one performance metric for the merit of the other until one feasible and optimal choice can be presented. The top circular ring remains unchanged, as it has been noted in previous observations that for such towers, the largest displacements occur at the unconstrained ring at the apex. Hence, employing a member with high flexural stiffness would assist in mitigating these displacements. In addition, the absence of upper diagonal members at that ring does simplify the potential design of the connection as only two diagonals from below are required to be attached. This would potentially involve a steel plate that is partially inserted into the ring and drilled through to minimize the chance of stress concentrations caused by transverse tension (in plane bending moments) in the ring's middle section. Naturally, this design implementation should be evaluated and checked to ensure it does not lead to tensile cracks if the insertion plate is selected.

In terms of finding the most optimal member size distribution, it should be noted that this characteristic is highly dependent on the pattern to be selected for the final design. As regards the custom pattern, a noticeable aspect of this configuration is the fact that vertical members are loaded significantly more than the diagonal ones, as detailed in Table 8.3. This drove the design process to thicken vertical posts while thinner diagonal members are proposed as part of the optimized structure. By reducing the cross-section of diagonals, the scheming of the connection becomes less complex by allowing closer placement of vertical elements (V1 and V2) to the tubular steel section. In this way, the buckling lengths of external steel plates outside the tubular section are reduced via the reinforcement provided by vertical timber sections as well as the lowered position of bolt rows within that plate (Figure 8.20). Meanwhile diagonal members can be connected via a longer and more slender steel plate since forces to be transmitted there are less considerable. In contrast, employing triangular configuration would impose a challenging placement of diagonal members that both bear significant vertical forces and arrive at the node at an angle, which is quite acute, especially for higher shape factors. Placement of those elements would necessitate longer steel plates connected to beams via fasteners, which in turn increase buckling lengths and susceptibility to local instability phenomenon. In general, the bolted nature of the connection does provide a possibility for a disassembly as welding on-site is not required. However, the proposed section is still of a high geometrical complexity and would be a costlier option in terms of production and the amounts of material required. In addition, tight spaces between welded plates for vertical members might introduce extra complexity in welding process.

Concerning the elastic slip modulus, the proposed connection design demonstrates strong performance for multiple shear plane fastener connection at members V1 and V2. Nonetheless, a comprehensive stiffness assessment should also include double shear fastener connections at members R1, R2, D1, and D2. Although it is hypothesized with considerable conviction that lateral stiffness characteristics in these components will meet standardized requirements, conducting the same elastic slip modulus evaluation is essential for a complete analysis.

Assembly considerations also accounted for dimensions of tower members, which does seem to cause much of an issue when segmented ring members are concerned due to their low length. However, topmost ring component is geometrically a continuous circle with a rather large diameter. This poses a logistical challenge as these dimensions cannot be fulfilled by a regular truck cargo box. Thus, splitting of the ring into three splines did solve the issue. However, spline connectivity and detailing of the joint also would need to be addressed in the ensuing design processes as the updated structural model

specified that spline nodes cannot transmit in-plane (around local z-axis) moments. This design choice was made as means to reduce the amount of steel required for a node that would be rigid otherwise. Revised structural model did not get affected by such a substantial degree from this change as global displacements got increased by a marginal amount.

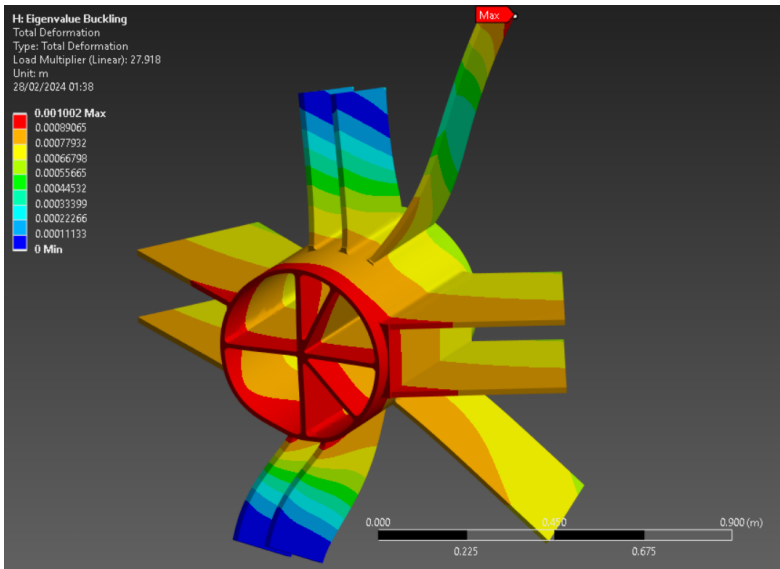
It should be noted that this analysis did not present the final tower detail ready for construction as the top most ring still is required to be assessed individually due to combined torsional and in-plane bending moment effects as well as connection designs. Another aspect for this is the load case which assumes a certain placement of platforms within the structure. This scenario remains still suggestive, as previously mentioned. The tower's design could incorporate alternative functionalities within its load-bearing framework, such as spiral staircases going through the tower's full height. These elements would need to be assessed individually in more detailed phases of the design process.

The placement of the top most ring here reflects the necessity of constraining the top most part of the structure and, thus, enhancing stiffness of the tower. Alternatively, this could also be done via placement of in-plane bracing or placement of a platform which is a stiff diaphragm given the top most ring is polygonal (not flexurally stiff). However, these solutions have to be applied permanently throughout the tower's lifetime in order to preserve gained stiffness effects. Meanwhile the incorporation of a stiff ring at the apex ensures stability at all times while presenting opportunities for creative uses, such as installing transparent glass roofs (which are not desirable to provide stiffness) or designing platforms that cover half of the ring's space, equipped with openings placed arbitrarily. In other words, it could be stated that the functional versatility of the tower is heightened by preserving the flexurally stiff ring and that is quite important in architectural terms.

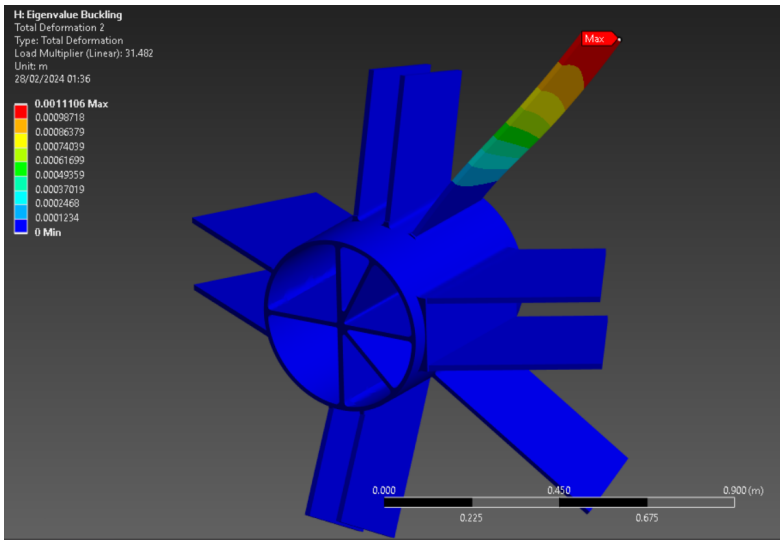
When considering the area available for functions on platforms influenced by various shape factors  $N$ , it logically makes sense that platforms with triangular configurations would yield the least area. As the number of sides increases, moving closer to a circular form, the platform area also grows. Yet, an optimal balance is found when using a shape factor of  $N = 5$ . Beyond this value the incremental area gain for platforms with additional sides becomes less substantial as detailed in Table 8.12. By employing higher shape factors, the considerations related to higher number of nodes, thus, heightened costs of construction shall become governing.

Shape factor	Normalized Area
N = 3	1.00
N = 4	1.54
N = 5	1.83
N = 6	2.00
N = 7	2.11

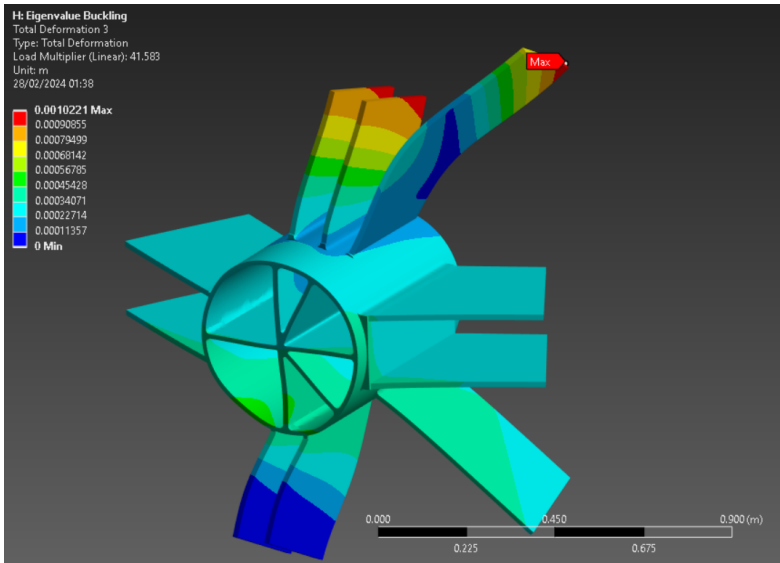
**Table 8.12:** Normalized areas of platforms provided by different shape factors  $N$ .



(a) Load multiplier (buckling factor): 27.918

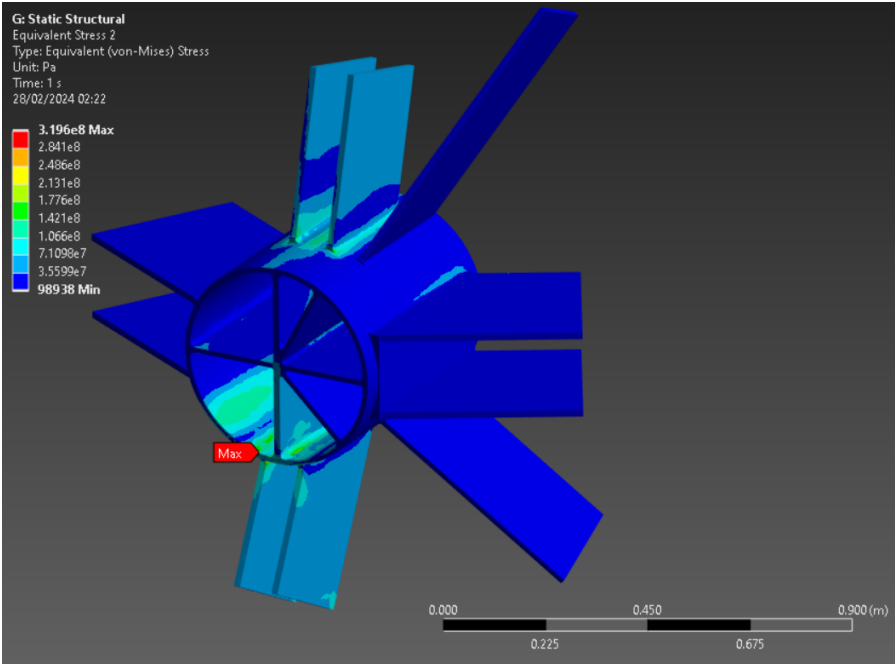


(b) Load multiplier (buckling factor): 31.482

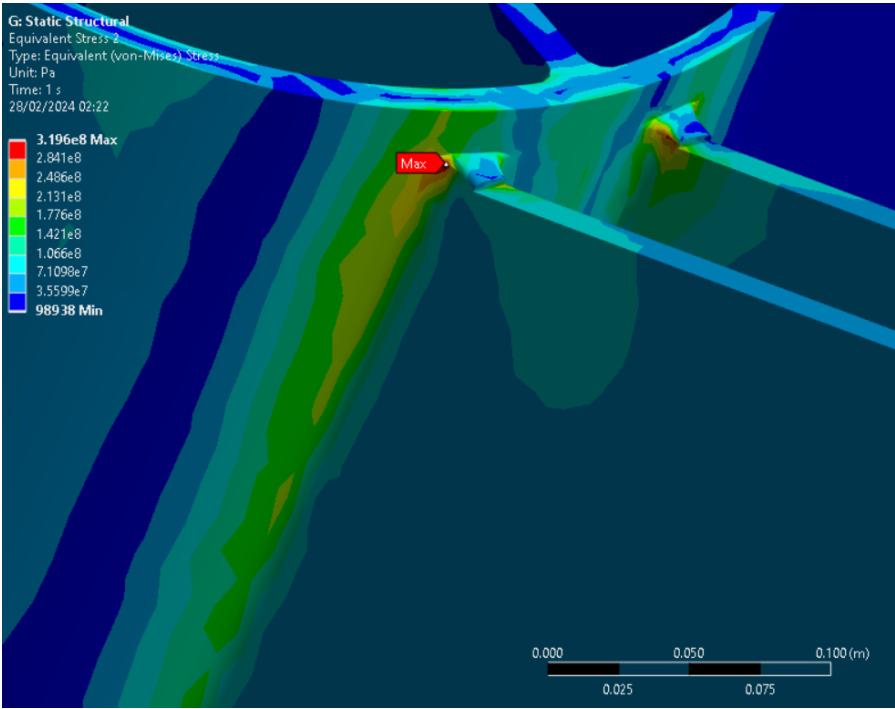


(c) Load multiplier (buckling factor): 41.583

**Figure 8.25:** Resulting buckling shapes of the steel component after being subjected to compressive member forces. Each image corresponds to a different buckling factor. The scale is 1:200.



(a) Maximum stress: 319 MPa



(b) A close up of the stress concentration occurring at a fillet section between the plate and tubular section.

**Figure 8.26:** Equivalent (von-Mises) stresses occurring within the steel component after being subjected to compressive member forces. Image in (b) shows the section with higher stress concentrations developing at the onset of two lower plates, which are exposed to highest compressive loads transmitted from member

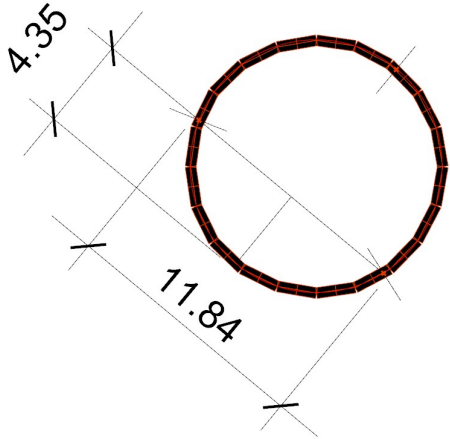


Figure 8.27: Split ring segments and dimensions of the largest segment. All values are in m.

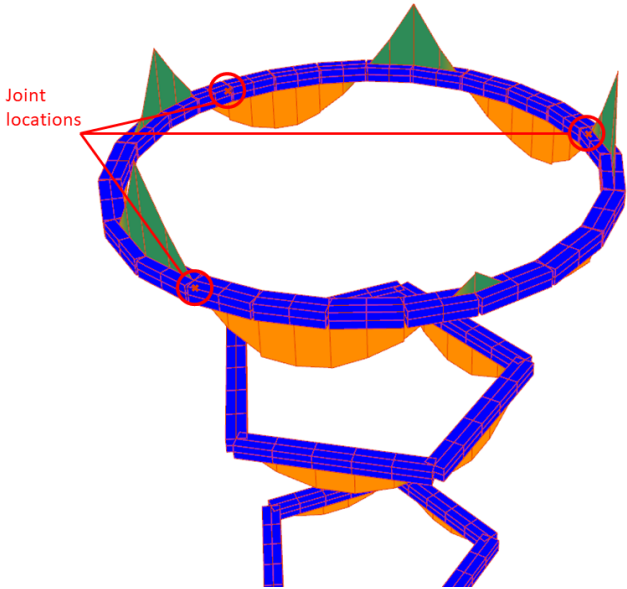


Figure 8.28: Split ring segments and their respective joint placement in relation to sagging and hogging moments. Joints are placed at points of inflexion.

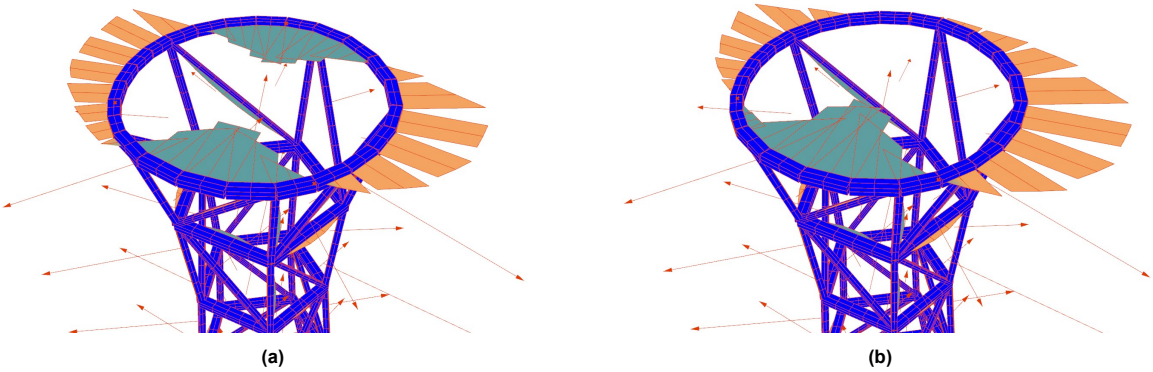


Figure 8.29: Bending moments around the local z-axis (in-plane) within the top ring before (a) and after (b) splitting the ring at said joint locations. The scale of the moment line is 0.13 kNm to m in the 'BeamView' component. Notice the points of zero moment within the member as these are represented by the placement of joints where splices meet.

# 9

## Conclusions

### 9.1. Conclusions and Recommendations

The aim of this thesis project was to devise a global geometry of a timber observational tower, whose parameters and their impact on its lateral stiffness and stability is to be investigated and documented. The need to preserve tower's adaptability and multi-functionality throughout its lifespan has identified the skeleton (or the main body) as the critical and singular element in providing the necessary stiffness and strength features. Without the need to rely on the potential placement of platform at certain levels (which would dramatically increase stiffness against the wind), the versatility of this structure is heightened.

The generation of geometry successfully captured two predominant shapes (antiprism and prism) defined by two topologies: triangular (diagrid) and a custom one. Tower framework was devised by fully segmented vertical and diagonal members that changed direction at every node coming up. The curvature ( $C$ ) determined the skewness of the hyperboloid, while shape factor  $N$  described the density of the grid through number of vertices in each ring. The introduction of circular rings in addition to the segmented ones for every tower variant has been effectively accomplished.

In terms of the effect that the change in topological parameters might have on tower's stability, the important outcome has been encountered regarding the segmented ring tower configuration following a triangular (diagrid) pattern. After subjecting the tower to proposed wind load profile, it has been discovered that assemblies defined by even valued shape factors  $N$  exhibit kinematic indeterminacy. This indicates that at the tower's summit, the nodes can move without causing strain, a phenomenon which is referred to as kinematic mechanisms. The discovery has been verified by employing analytical and graphic kinematics methods, supplemented by building a representative mock-up model of the tower. Even though these methods have consistently determined whether the structure was kinematically determinate, they differed in the level of clarity and intuition they provide to engineers regarding the nature of emerging instabilities. The kinematic nature of towers with the diagrid pattern and segmented rings do inform design practices about potential limitations concerning structural integrity and ease of con-

struction. It is highly advised in this case to refrain from designing towers emulating antiprism shape if the the shape factor  $N$  is even in order to avoid instabilities arising from such a choice at the apex of the tower. Instabilities could force joints lacking in rotational stiffness to counteract this motion, an outcome that is generally unwanted.

The following investigations into how topology and curvature affects the performance aimed to identify the tower design that is both the stiffest and most material-efficient. This was achieved by forcing each potential configuration to maintain the same mass, accomplished by adjusting the sizes of the members accordingly. It has been concluded that for tower structures employing segmented circumferential (ring) elements, custom pattern exhibited the most stiff and stable response against wind loads, characterised by a shape factor  $N = 3$  and curvature  $C = -3.61 m$  with the associated displacements of 6.69 mm. A more generalized outcome relating to topology and the use of segmented rings is that towers emulating prism shape (or a post and beam configuration) are more stable and laterally stiff than ones defined by an antiprism (diagrid pattern). As per curved ring configurations, towers defined by the triangular topology has been showcasing highest level of stiffness as the most optimal geometry was characterised by the shape factor  $N = 7$  and curvature  $C = -3.61 m$  with the associated displacements of 5.15 mm. It should be noted that displacement values shall serve more for a comparative view than to reflect the fully optimized tower configuration. The hyperboloid tower shape has been confirmed to significantly increase stiffness in response to specific wind load profiles that followed standardized guidelines for enclosed and pitched structures (tents). In addition, the shape factor has been recorded to influence global displacement values a great deal. For tower assemblies equipped with both types of rings, substantial shape factors ( $N > 7$ ) were associated with increasingly lower stiffness. The effect of curvature and shape factors on stiffness was illustrated and justified by simplified spring and arch models.

The final part of the thesis project aimed at achieving the most optimal tower geometry and delve into the materialization of it. The first optimal configuration derived from prior analysis, was the one employing curved rings and following a triangular pattern. However, the qualitative analysis concerning the feasibility of the connection yielded the corresponding complexity of such a connection relating to its direct dependence on global geometrical parameters (curvature,  $C$ ) and how it would impact the interaction with the curved ring.

Alternative design explorations focused on the re-evaluation of the shape and topology of the tower. The decision was taken to add a flexurally stiff ring at the top of the structure, while keeping the remaining rings polygonal. Studies examining stiffness in towers, after making this adjustment for both topologies, revealed that towers characterized by the custom pattern — employing segmented rings and a single curved ring at the top — demonstrated lower displacements. Interestingly, from previous observations, the topmost unrestrained ring for tower designs following a triangular topology has been an issue if an even valued shape factor  $N$  has been selected. After the implementation a flexurally stiff ring, towers represented by any polygonal ring shape have been able to exhibit stable behaviours. This finding highlights the necessity of restraining nodal movement at the apex of the tower and stabilize the structure. Therefore, the implementation of flexurally stiff rings at every level (which was quite a prevalent design choice for Shukov towers in attempts to reach stability) is not necessary for structures defined by an antiprism shape (or triangular topology).

The tower featuring a custom pattern, which includes a curved ring at its summit and segmented rings in other sections has been selected for further assessment in terms of connection design. The use of segmented rings facilitates accommodation of all six members at the node, ensuring a clash-free assembly. This is achieved through the implementation of steel plate fasteners equipped with single or multiple shear planes. Resulting tower configuration has been optimized for mass by reducing member cross-sections until utilization values for ULS and SLS for timber were satisfactory. The size of the structural members was largely influenced by the topology which was chosen. Specifically, the custom pattern required larger cross-sections for vertical members due to their role in bearing both dead and live vertical loads. On the contrary, the diagonal members, which basically contributed to stability and stiffness experienced less substantial forces, did not need as large cross-sections. Overall the sizing did not influence stiffness characteristics as much as primary governing factor was the ultimate limit state.

For the final design the shape factor that was determined to be ideal for the design is  $N = 5$ . The curvature associated with this design was measured at  $C = -3.5$  meters. Additionally, the final SLS (global) metric achieved was 0.2, and the global lateral displacement observed was 41.44 millimeters. The final value for mass of timber used was  $m = 28.10$  t. For this prismatic structure, the main load bearing component is the vertical member while diagonals are essential for providing stiffness. The necessity and role of the flexurally stiff ring in maintaining the structure's top stability are being questioned also. It's pondered whether that stability might also be achieved through the installation of a platform functioning as a stiff diaphragm or through simple bracing. Yet, the functional flexibility of a curved ring is highlighted. Thus, it is recommended for its ability to offer an open space for various functional and architectural interpretation.

## 9.2. Future Work

The main limitation of this project and that one that specifically is relevant for larger scale timber construction projects like this is the user comfort. Wind forces can cause timber towers to experience dynamic loads, leading to horizontal movements that may yield discomfort or annoyance for the people inside. This effect, known as vibration serviceability failure, specifically concerns the building's sway perception, underscoring the essence of taking into account these dynamic responses in design. Considering the height and reduced mass of the tower, this issue would rapidly become highly emphasised. To draw parallels with similar projects, Camp Adventure Tower in Denmark, Zealand, which employs a hyperboloid shape has posed a similar issue of user induced dynamic loading, which became a governing factor leading design choices. However, steel was selected for its construction, characterised by a higher weight than timber (Arup 2024). Thus, future research should concentrate on determining the leading factors in terms of topology, curvature and member sizes that would render the structure to exhibit an acceptable performance. However, there is a promise for hyperboloid timber structures in regards to providing sought after user comfort outcomes. Trinh and H. Zhang (2021) have conducted a comprehensive evaluation of a 200 m timber diagrid (triangular) structure in hyperboloid form and presented its dynamic performance to be more superior than that of a traditionally braced or diagrid convex shaped alternatives. Thus, these finding suggests a significant potential for hyperboloid timber structures to also fulfill vibration serviceability requirements, while material efficiency is still maintained. Although it is highly suspected that the mass of the structure would rise to in order to absorb and

dampen the energy from wind forces more effectively. Additionally, regarding connection design to address dynamic considerations, high rigidity is not a favorable factor as certain movement should be allowed in order to accommodate energy dissipation and avoid stress concentrations. These aspects should guide the ensuing research of these segmented hyperboloid timber structures.

An additional consideration is the standardization of acquired results that would guide the design of similar hyperboloid structures characterised by varying platform ring radii and total height. Thus far, the current research methodology aimed at investigating a tower silhouette with said parameters being pre-determined. Therefore, this study does not propose a universal solution for the design of hyperboloid timber structures that would have more adjustable and variable geometry. The current study acknowledges the structural stiffness benefits offered by a hyperboloid shape compared to cylindrical or convex configurations, especially under non-uniform wind load profiles. Further potential research shall investigate the acquisition of generalized geometrical relationships between certain parameters that would yield the most favorable stiffness characteristics for towers of different height as well as upper platform radius. The latter factor is proven to be of considerable relevance as regards the stiffness performance of the studied structure.

# References

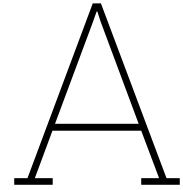
- Akbarzadeh, Masoud, Tom Van Mele, and Philippe Block (2015). "On the equilibrium of funicular polyhedral frames and convex polyhedral force diagrams". In: *Computer-Aided Design* 63, pp. 118–128.
- ANSYS, Inc. (2023). *What is Finite Element Analysis?* Accessed: 2023-03-19. URL: <https://www.ansys.com/simulation-topics/what-is-finite-element-analysis> (visited on 03/19/2023).
- Apolinarska, Aleksandra Anna (2018). "Complex timber structures from simple elements: Computational design of novel bar structures for robotic fabrication and assembly". PhD thesis. ETH Zurich.
- Arehart, Jay H et al. (2021). "Carbon sequestration and storage in the built environment". In: *Sustainable Production and Consumption* 27, pp. 1047–1063.
- Arets, E.J.M.M. et al. (2011). *Global wood production: assessment of industrial round wood supply from forest management systems in different global regions*. Tech. rep. 1808. Alterra, Wageningen-UR.
- Arsenev (June 2009). *The World's First Hyperboloid Lattice Shell Structure*. Own work. Russian engineer and architect Vladimir Shukhov was the first in the world to invent and use in construction hyperboloid towers. For the 1896 All-Russia industrial and art exhibition in Nizhniy Novgorod Shukhov built the steel lattice 37-meter tower, which became the first hyperboloid structure in the world. The astonishing hyperboloid lattice structure caused delight of the European specialists ("The Nijni-Novgorod exhibition: Water tower, room under construction, springing of 91 feet span", "The Engineer" magazine, 1897, No 19.3 - P.292-294).
- Arup (2024). *Camp Adventure Tower*. <https://www.arup.com/projects/camp-adventure-tower>. Accessed: 2024-02-28.
- Beckh, Matthias (2015). *Hyperbolic structures: Shukhov's lattice towers-forerunners of modern lightweight construction*. John Wiley & Sons.
- Blaß, Hans Joachim and Carmen Sandhaas (2017). *Timber engineering-principles for design*. KIT Scientific Publishing.
- Cajmatz, Karin (2017). "View of Wood-Structural Concepts for an Observation Tower Displaying the Potential of Timbe". In.
- Calladine, Christopher R (1978). "Buckminster Fuller's "tensegrity" structures and Clerk Maxwell's rules for the construction of stiff frames". In: *International journal of solids and structures* 14.2, pp. 161–172.
- Capital Value (2020). *Housing shortage in the Netherlands will rise to 415,000 homes in 2024*. Accessed: 2024-02-28. URL: <https://www.capitalvalue.nl/en/news/housing-shortage-in-the-netherlands-will-rise-to-415000-homes-in-2024>.
- Cicerone, Silvestro et al. (Jan. 2021). "Arbitrary pattern formation on infinite regular tessellation graphs". In: *Proceedings of the 22nd International Conference on Distributed Computing and Networking*, pp. 56–65.
- Cindy, Manou and Janneke (2024). *Wandelroute Kootwijkerzand Staatsbosbeheer*. <https://wandel-enopdeveluwe.nl/wandelroute/kootwijkerzand-wandelroute-kootwijk/>. Accessed: 2024-03-12.
- Cromwell, Peter R (1997). *Polyhedra*. Cambridge University Press.

- Doe, John (2021). "Design of Curved Glulam Beams According to ANSI/AWC NDS". In: *Structural Analysis and Design Software*.
- Ebielmaj (Sept. 2014). *Gliwice, maszt radiostacji*. Polish. [https://commons.wikimedia.org/wiki/File:Maszt\\_04.JPG](https://commons.wikimedia.org/wiki/File:Maszt_04.JPG). Accessed: 2024-03-08.
- Elnasri, Ibrahim et al. (2007). "Shock enhancement of cellular structures under impact loading: Part I Experiments". In: *Journal of the Mechanics and Physics of Solids* 55.12, pp. 2652–2671.
- English, Elizabeth C (2005). "Vladimir Shukhov and the invention of hyperboloid structures". In: *Structures Congress 2005: Metropolis and Beyond*, pp. 1–9.
- European Parliamentary Research Service (Apr. 2014). *Weights and dimensions of road vehicles in the EU*. <https://epthinktank.eu/2014/04/10/weights-and-dimensions-of-road-vehicles-in-the-eu/>. Accessed: [insert current date here].
- Eversmann, Philipp, Fabio Gramazio, and Matthias Kohler (2017). "Robotic prefabrication of timber structures: towards automated large-scale spatial assembly". In: *Construction Robotics* 1.1-4, pp. 49–60.
- Fine Stay Slovenia (2024). *Visit The Pyramidenkogel Observation Tower in Klagenfurt, Austria*. <https://finestayslovenia.com/whattosee/pyramidenkogel-observation-tower-austria/>. Accessed: 2024-03-12.
- Frame (2013). *Observation Tower on the Pyramidenkogel*. <https://frameweb.com/article/observation-tower-on-the-pyramidenkogel>. Accessed: 2024-03-12.
- Grünbaum, Branko and Geoffrey Colin Shephard (1987). *Tilings and patterns*. Courier Dover Publications.
- Guo, Yan-Lin et al. (2018). "Experimental and numerical studies of instability mechanism and load resistance of rhombic grid hyperboloid-latticed shells under vertical load". In: *Engineering Structures* 166, pp. 167–186.
- Gursel, A Petek et al. (2014). "Life-cycle inventory analysis of concrete production: A critical review". In: *Cement and Concrete Composites* 51, pp. 38–48.
- Hart, Jim and Francesco Pomponi (2020). "More timber in construction: Unanswered questions and future challenges". In: *Sustainability* 12.8, p. 3473.
- Herzog, Thomas et al. (2004). *Timber Construction Manual*. Accessed via ProQuest Ebook Central. Walter de Gruyter GmbH. URL: <https://ebookcentral-proquest-com.tudelft.idm.oclc.org/lib/delft/detail.action?docID=1075578>.
- hsbcad (2024). *Pyramidenkogel | Client Cases*. <https://fr.hsbcad.com/cases/pyramidenkogel>. Accessed: 2024-03-12.
- IDEA StatiCa (2023). *Steel*. Accessed: 2023-03-19. URL: <https://www.ideastatica.com/steel> (visited on 03/19/2023).
- (2024). *Steel joint buckling analysis*. Accessed: 2024-02-28. URL: <https://www.ideastatica.com/support-center/buckling-analysis>.
- IEA (2020). "Energy Efficiency 2020". In: *IEA, 2020*. URL: <https://www.iea.org/reports/energyefficiency-2020>.
- Jenssen, Dag (2012). *Seljord Watch Tower / Rintala Eggertsson Architects*. <https://www.archdaily.com/212966/seljord-watch-tower-rintala-eggertsson-architects>. Accessed: 2024-03-12.
- Jockwer, Robert and André Jorissen (2018). "Stiffness and deformation of connections with dowel-type fasteners". In: *Design of Connections in Timber Structures* 95.
- Jockwer, Robert, Vera Öberg, et al. (2023). "TOWARDS ADAPTABILITY AND CIRCULARITY OF TIMBER BUILDINGS". In: *World Conference on Timber Engineering (WCTE 2023)*.

- Johan, Ryan et al. (2019). "Building intelligence through generative design". In: *Proceedings of the 24th International Conference of the Association for Computer-Aided Architectural Design Research in Asia (CAADRRIA)*. Vol. 1, pp. 371–380.
- Johansen, Knut W (1949). "Theory of timber connections". In: *International Assoc. of Bridge and Structural Engineering Publication 9*, pp. 249–262.
- Kuśnierz, Kazimierz (2003). *Wiadomości Konserwatorskie [Conservation News]*. Polish. Ed. by Kazimierz Kuśnierz. <https://www.zeriba.pl/wkjhoc/wk/wk14.pdf>. Accessed: 2024-03-08. Warsaw: Stowarzyszenie Konserwatorów Zabytków [Association of Monument Conservators].
- Lackner, Markus and Michael Vodicka (2013). "The World's Tallest Wooden Observation Tower: Design for Durability". In: *Advanced Materials Research 778*. Accessed: 2024-03-12, pp. 1028–1033. ISSN: 1662-8985. DOI: 10.4028/www.scientific.net/AMR.778.1028.
- Liddell, Ian (2015). "Frei Otto and the development of gridshells". In: *Case Studies in Structural Engineering 4*, pp. 39–49. ISSN: 2214-3998. DOI: <https://doi.org/10.1016/j.csse.2015.08.001>. URL: <https://www.sciencedirect.com/science/article/pii/S2214399815300011>.
- Liew, Andrew et al. (2018). "Load-path optimisation of funicular networks". In: *Meccanica 53*, pp. 279–294.
- Lorusso, Claudia (2012). *Wood Beton has realized the Strand East Tower in London*. <https://www.archilovers.com/stories/1184/wood-beton-has-realized-the-strand-east-tower-in-london.html>. Accessed: 2024-03-12.
- Maxwell, J Clerk (1870). "I.—on reciprocal figures, frames, and diagrams of forces". In: *Earth and Environmental Science Transactions of the Royal Society of Edinburgh 26.1*, pp. 1–40.
- McRobie, Allan et al. (2017). "Graphic kinematics, visual virtual work and elastographics". In: *Royal Society open science 4.5*, p. 170202.
- Milner, Henry Robert (2009). "Sustainability of engineered wood products in construction". In: *Sustainability of construction materials*. Elsevier, pp. 184–212.
- NatureScanner (2024). *Radio Kootwijk*. <https://www.naturescanner.nl/europa/nederland/radio-kootwijk>. Accessed: 15-February-2024.
- Nidheesh, PV and M Suresh Kumar (2019). "An overview of environmental sustainability in cement and steel production". In: *Journal of cleaner production 231*, pp. 856–871.
- Nonenmacher, R. A. (2008). *Hexagonal Prism BC*. [https://commons.wikimedia.org/wiki/File:Hexagonal\\_Prism\\_BC.svg](https://commons.wikimedia.org/wiki/File:Hexagonal_Prism_BC.svg). Accessed: 2024-03-15.
- Ong, C.B. (2015). "7 - Glue-laminated timber (Glulam)". In: *Wood Composites*. Ed. by Martin P. Ansell. Woodhead Publishing, pp. 123–140. ISBN: 978-1-78242-454-3. DOI: <https://doi.org/10.1016/B978-1-78242-454-3.00007-X>. URL: <https://www.sciencedirect.com/science/article/pii/B978178242454300007X>.
- Oval, Robin (2019). "Topology Finding of Patterns for Structural Design". PhD thesis. Université Paris-Est.
- Paris Agreement, Paris (2015). "Paris agreement". In: *report of the conference of the parties to the United Nations framework convention on climate change (21st session, 2015: Paris)*. Retrieved December. Vol. 4. HeinOnline, p. 2017.
- Pellegrino, Sergio (1993). "Structural computations with the singular value decomposition of the equilibrium matrix". In: *International Journal of Solids and Structures 30.21*, pp. 3025–3035.
- Prandini, Renan, João Tavares Pini, and Márcio Sartorelli Venâncio de Souza (2023). "BEAVER: A PARAMETRIC DESIGN FRAMEWORK FOR TIMBER ENGINEERING". In:

- Przemieniecki, JS (1968). "Discrete-element methods for stability analysis of complex structures". In: *The Aeronautical Journal* 72.696, pp. 1077–1086.
- Ranger Truss (2024). *Hardwood vs Softwood - Which is Better for Timber Construction Projects?* <https://rangertruss.com/blog/hardwood-vs-softwood-which-is-better-for-timber-construction-projects/>. Accessed: 2024-03-23.
- Rankine, WJ Macquorn (1864). "XVII. Principle of the equilibrium of polyhedral frames". In: *The London, Edinburgh, and Dublin Philosophical Magazine and Journal of Science* 27.180, pp. 92–92.
- Sandhaas, Carmen et al. (2018). "Design of connections in timber structures". In: *Shaker-Verlag GmbH*.
- Schlaich, Jorg and Kurt Schafer (1991). "Design and detailing of structural concrete using strut-and-tie models". In: *Structural Engineer* 69.6, pp. 113–125.
- Schlaich, Jörg and Ingo Schober (2005). "Freeform glass roofs". In: *Structures Congress 2005: Metropolis and Beyond*, pp. 1–13.
- Schoenberg, Frederic (2011). "Tessellations". In.
- Shitanaka, Atsushi, Takahira Aoki, and Tomohiro Yokozeki (2019). "Comparison of buckling loads of hyperboloidal and cylindrical lattice structures". In: *Composite Structures* 207, pp. 877–888.
- Smulski, S. (2004). "SOLID WOOD PRODUCTS | Structural Use of Wood". In: *Encyclopedia of Forest Sciences*. Ed. by Jeffery Burley. Oxford: Elsevier, pp. 1318–1327. ISBN: 978-0-12-145160-8. DOI: <https://doi.org/10.1016/B0-12-145160-7/00047-8>. URL: <https://www.sciencedirect.com/science/article/pii/B0121451607000478>.
- Snijder, HH and HMG Steenbergen (2020). *Steel Design 1: Structural Basics*. John Wiley & Sons.
- Steer, PJ (2001). "EN1995 Eurocode 5: Design of timber structures". In: *Proceedings of the Institution of Civil Engineers-Civil Engineering*. Vol. 144. 6. Thomas Telford Ltd, pp. 39–43.
- Stewart, Gilbert W (1973). *Introduction to matrix computations*. Elsevier.
- Tedeschi, Arturo (2011). "Intervista a David Ruten". In: *MixExperience Tools1 (in Italian and English)*. Naples, Italy: MixExperience, pp. 28–29.
- Thiel, Cassandra L et al. (2013). "A materials life cycle assessment of a net-zero energy building". In: *Energies* 6.2, pp. 1125–1141.
- Tomruen (Feb. 2006). *Hexagonal Antiprism*. [https://commons.wikimedia.org/wiki/File:Hexagonal\\_antiprism.png](https://commons.wikimedia.org/wiki/File:Hexagonal_antiprism.png). Accessed: 2024-03-16.
- Trinh, Lien and Hong Zhang (2021). "The 200 m timber tower-A study of building geometry and construction feasibility". In.
- United Nations, Org. (2020). "United Nations, Population". In: *United Nations, 2022*. URL: <https://www.un.org/en/globalissues/population>.
- Vakarel (May 2006). *Drawing of former wooden radio tower Ismaning*. [https://commons.wikimedia.org/wiki/File:Sendeturm\\_Ismaning.gif](https://commons.wikimedia.org/wiki/File:Sendeturm_Ismaning.gif). Original drawing by Vakarel. Accessed on: 2024-03-08.
- Vasiliev, VV, VA Barynin, and AF Rasin (2001). "Anisogrid lattice structures—survey of development and application". In: *Composite structures* 54.2-3, pp. 361–370.
- Versteeg Conlledo, Jacob (2022). "A computational study on the application of efficient dual structural systems for achieving desirable comfort levels in timber high-rise structures". In.
- Vries, Peter de (2005). *Observation Tower in Holmers Halkenbroek*. Award-winning wooden lookout tower constructed by Tentech featuring a hyperboloid structure made from thinned wood, with a design emphasizing replaceability and sustainable use of materials. Architectural and structural design, engineering, and project management were provided by Tentech. Tentech. URL: <https://tentech.nl/en/textile-architecture/observation-tower/>.

- Vries, Peter A. de and Wolfgang F. Gard (2006). *Small Diameter Round Wood Observation Tower*. Research Report. Faculty of Civil Engineering and Geosciences, Timber Structures and Wood Technology. Delft, The Netherlands: Delft University of Technology.
- Woodubuy (2022). *How to measure sawn timber and PSE*. Website. Accessed: June 6, 2023. URL: <http://www.woodubuy.com>.
- Xia, Liang and Piotr Breitkopf (2015). "Multiscale structural topology optimization with an approximate constitutive model for local material microstructure". In: *Computer Methods in Applied Mechanics and Engineering* 286, pp. 147–167.
- Xiao, Lijun et al. (2020). "A multi-cell hybrid approach to elevate the energy absorption of micro-lattice materials". In: *Materials* 13.18, p. 4083.
- Yang, LI et al. (2023). "Layout design of thin-walled structures with lattices and stiffeners using multi-material topology optimization". In: *Chinese Journal of Aeronautics* 36.4, pp. 496–509.
- Yoon, Young-Cheol et al. (2018). "Sustainable design for reinforced concrete columns through embodied energy and CO2 emission optimization". In: *Energy and Buildings* 174, pp. 44–53.
- Zhang, Yihui et al. (2009). "Deformation and failure mechanisms of lattice cylindrical shells under axial loading". In: *International Journal of Mechanical Sciences* 51.3, pp. 213–221.
- Zimmer, Ernst (1950). *Ismaning Transmitter – Structurae*. <https://structurae.net/en/media/39853-ismaning-transmitter>. Accessed: 2024-03-08.



## Grasshopper scripts

This is the link to associated Grasshopper scripts for the generation of both patterns: custom and triangular. Keep in mind that Karamba3D, Beaver and Pufferfish plug-ins are required to access full functionality of this script. In addition, to enable Python scripting with packages, the Rhino Remote plug-in is necessary. The dropbox link:

[Grasshopper Scripts for Custom and Triangular Patterns](#)

# B

## Singular Value Decomposition Code in Python

The following code provides the process of performing SVD for an equilibrium matrix. The resulting matrices denoted by  $S$ ,  $U$  and  $V$  are acquired.

```
1
2 import rhinoscriptsyntax as rs
3 import ghpythonlib.treehelpers as th
4
5 import scriptcontext
6 import ghpythonremote
7
8 # Assuming that 'numpy' and 'rpy' are already available in the remote environment
9 np = scriptcontext.sticky['numpy']
10 rpy = scriptcontext.sticky['rpy']
11 rpyc = scriptcontext.sticky['rpyc']
12
13
14 import Rhino
15 import Grasshopper
16
17 # Input: DataTree to convert
18 input_tree = x # Replace with your actual DataTree
19
20 # Function to convert DataTree to a flat list
21 def tree_to_list(tree):
22     flat_list = []
23     for i in range(tree.BranchCount):
24         branch = tree.Branch(i)
25         flat_list.extend(branch)
26     return flat_list
27
28
29
30 output_flat_list = tree_to_list(input_tree)
```

```
31 output_matrix = [output_flat_list[i:i + num_columns] for i in range(0, len(output_flat_list),
    num_columns)]
32
33 # SVD calculation
34 U_local, S_local, Vt_local = np.linalg.svd(output_matrix)
35
36 # Convert S_local to a list
37 S_local_list = S_local.tolist()
38
39 # Output: List
40 print(S_local_list)
41 a = S_local_list
42
43 print('U')
44 print(U_local.tolist())
45
46 print('Vt')
47 print(Vt_local.tolist())
48
49 print('n_r=')
50 print len(U_local)
51
52 print('n_c=')
53 print len(Vt_local)
```



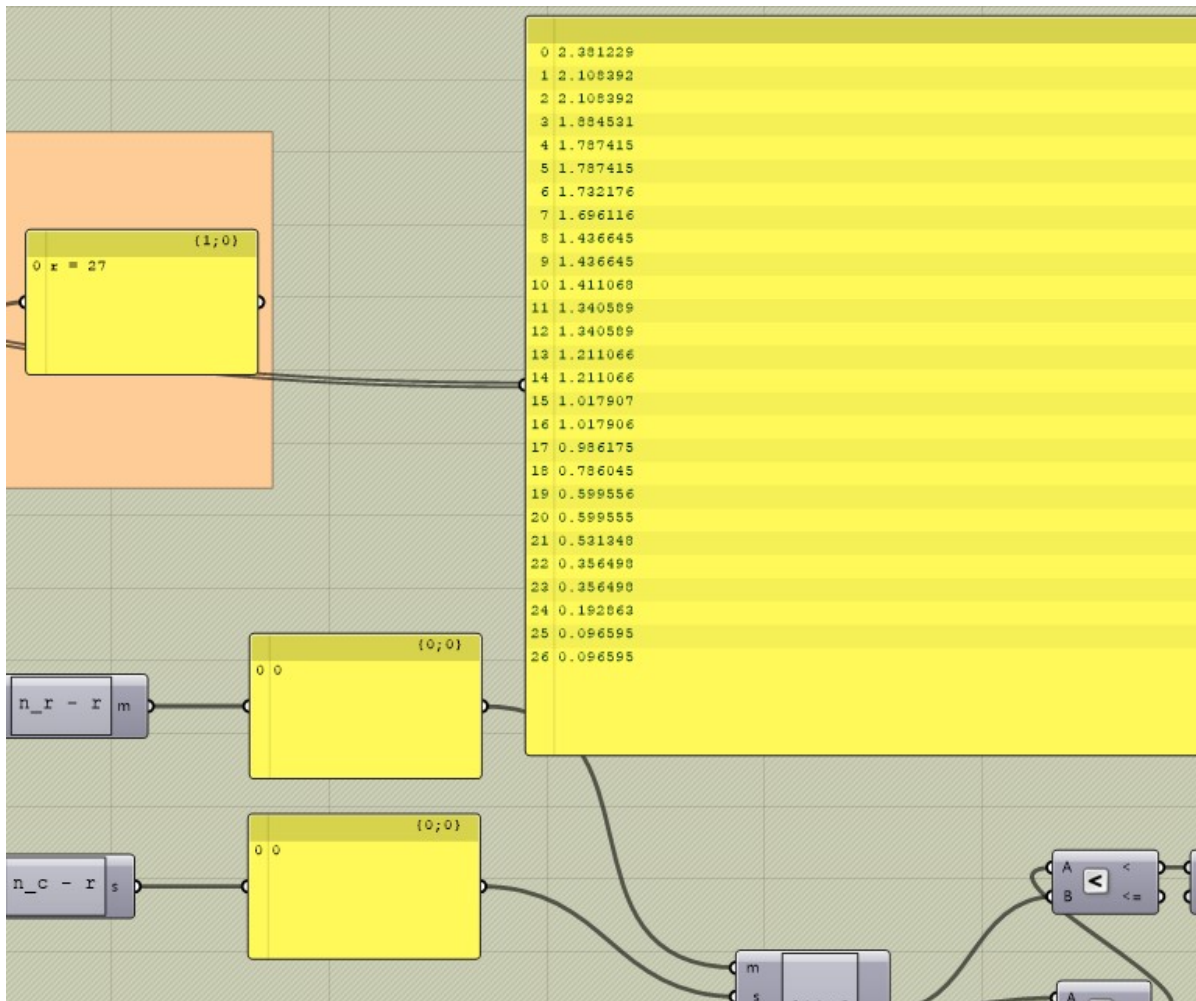


**Figure C.2:** The rank and resulting values of numbers of kinematic mechanisms and states of self-stress related to tower defined by the **triangular pattern** and  $N = 3$  while having 4 rings in total. This outcome confirms that this structure is **kinematically determinate**.

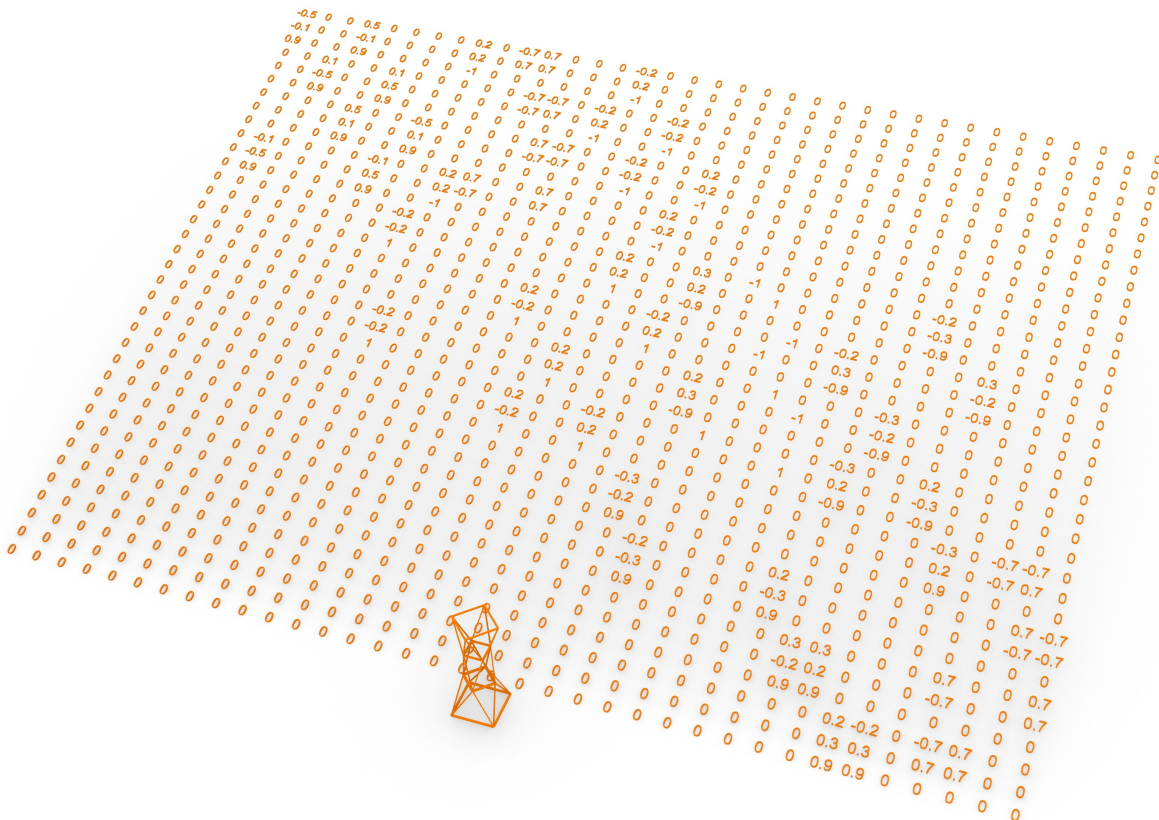


**Figure C.3:** Equilibrium matrix of the tower defined by the **triangular pattern** and  $N = 4$  while having 4 rings in total.

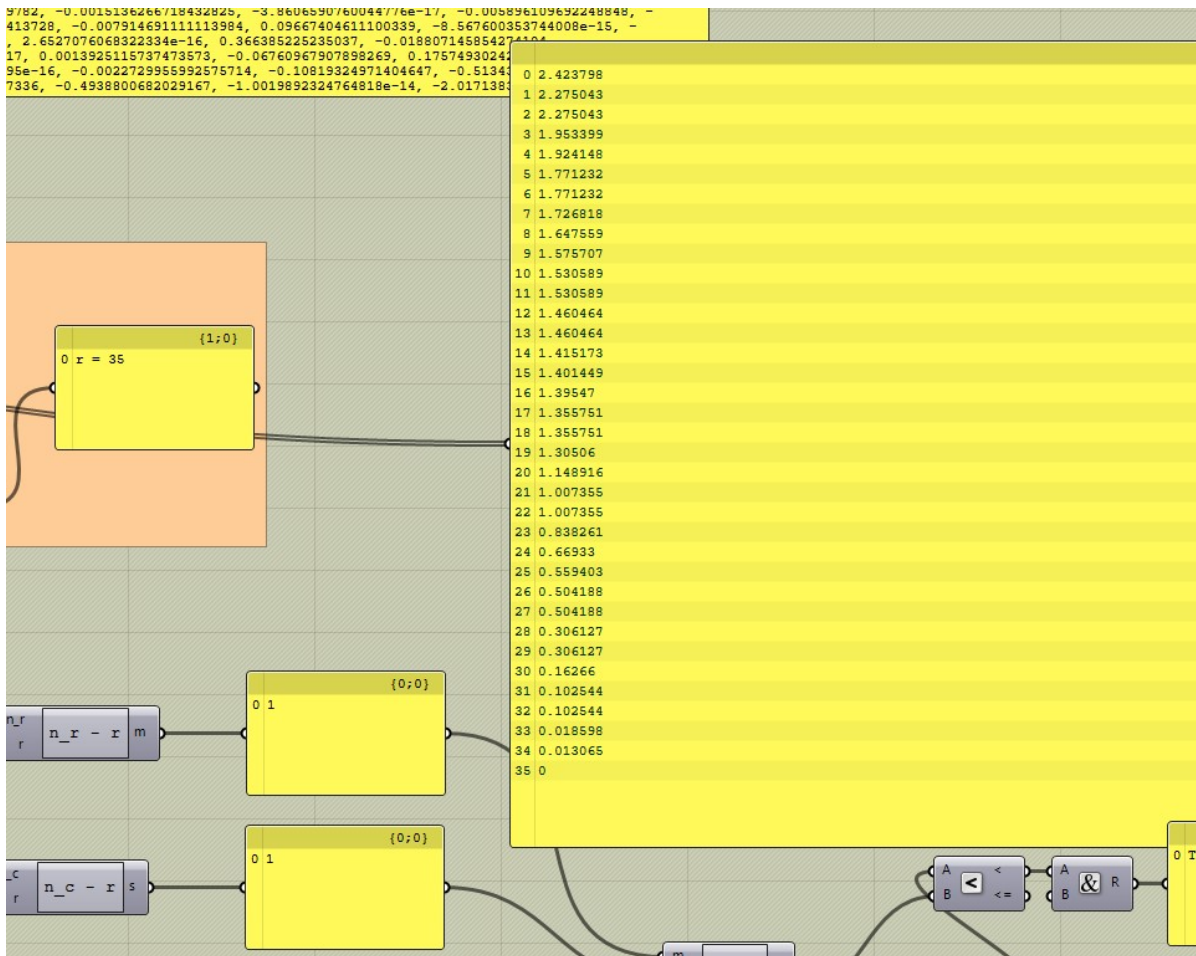


**Figure C.4:** The rank and resulting values of numbers of kinematic mechanisms and states of self-stress related to tower defined by the **triangular pattern** and  $N = 4$  while having 4 rings in total. This outcome confirms that this structure is **kinematically indeterminate**.



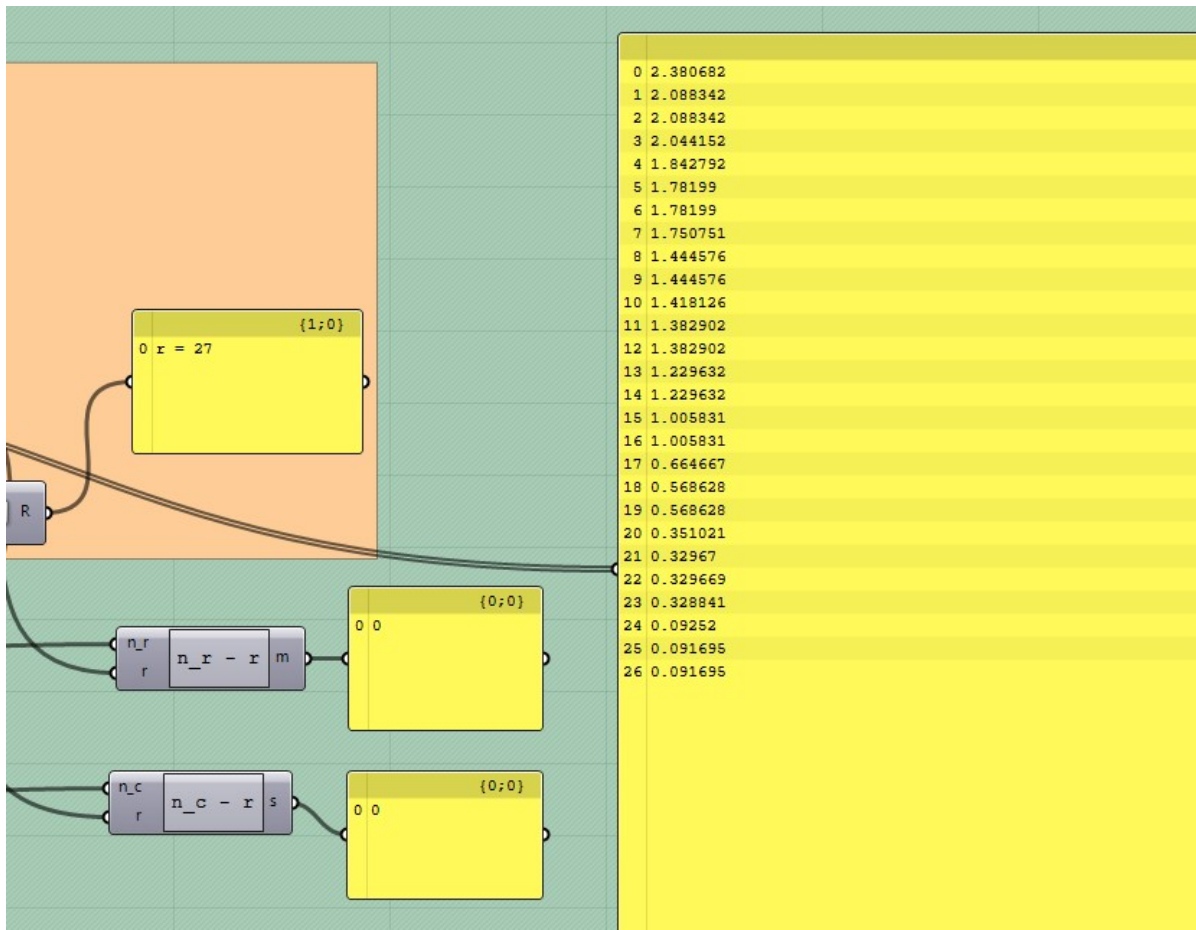


**Figure C.6:** The rank and resulting values of numbers of kinematic mechanisms and states of self-stress related to tower defined by the **custom pattern** and  $N = 3$  while having 4 rings in total. This outcome confirms that this structure is **kinematically determinate**.

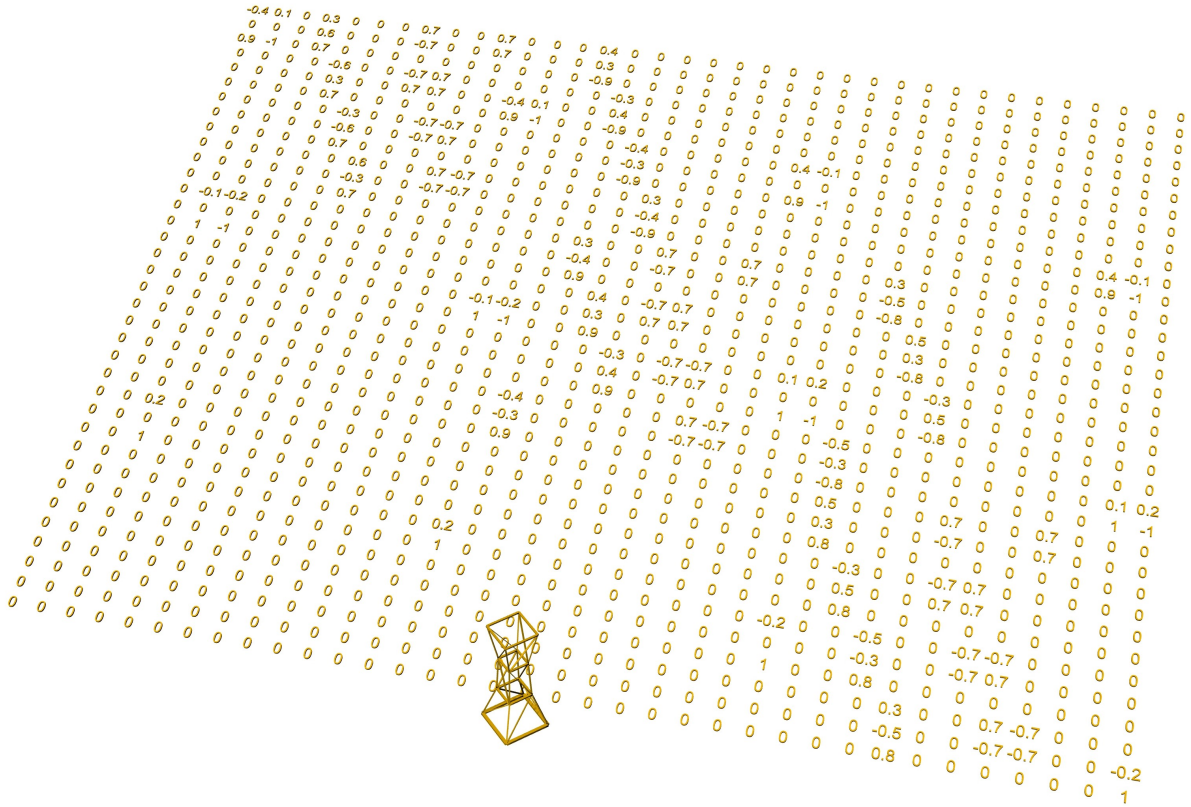


Figure C.7: Equilibrium matrix of the tower defined by the custom pattern and  $N = 4$  while having 4 rings in total.

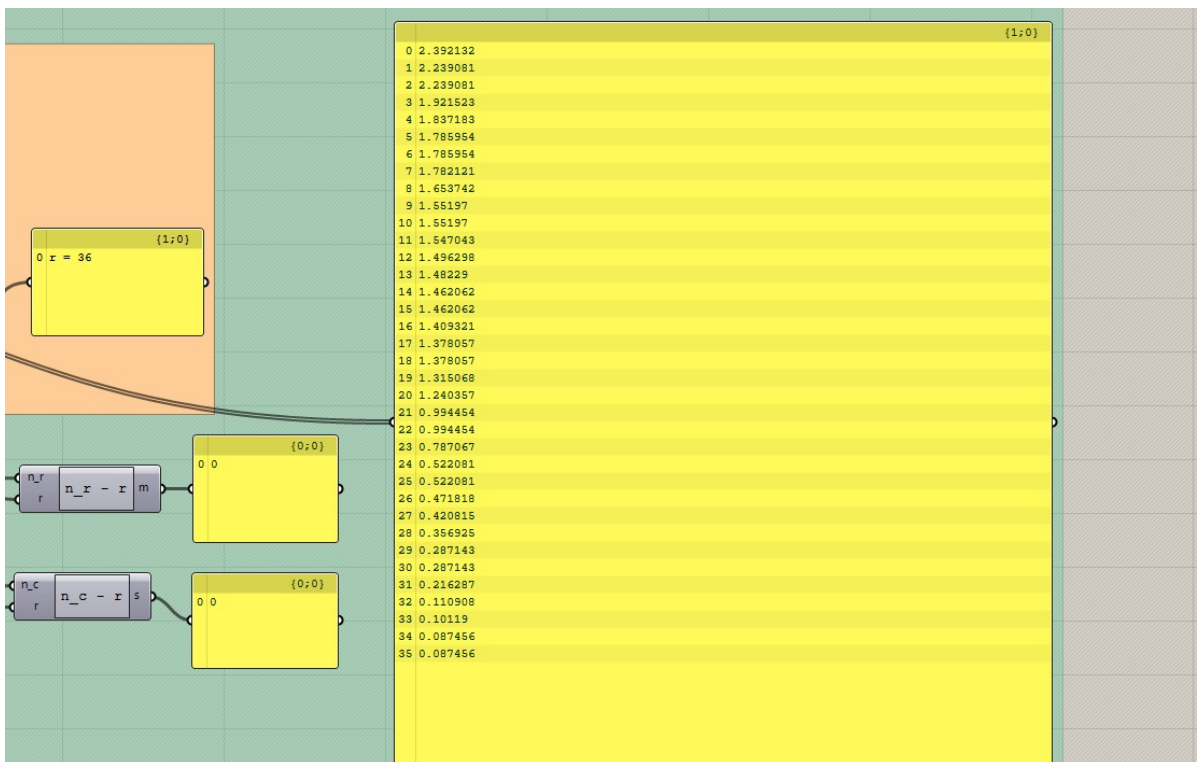
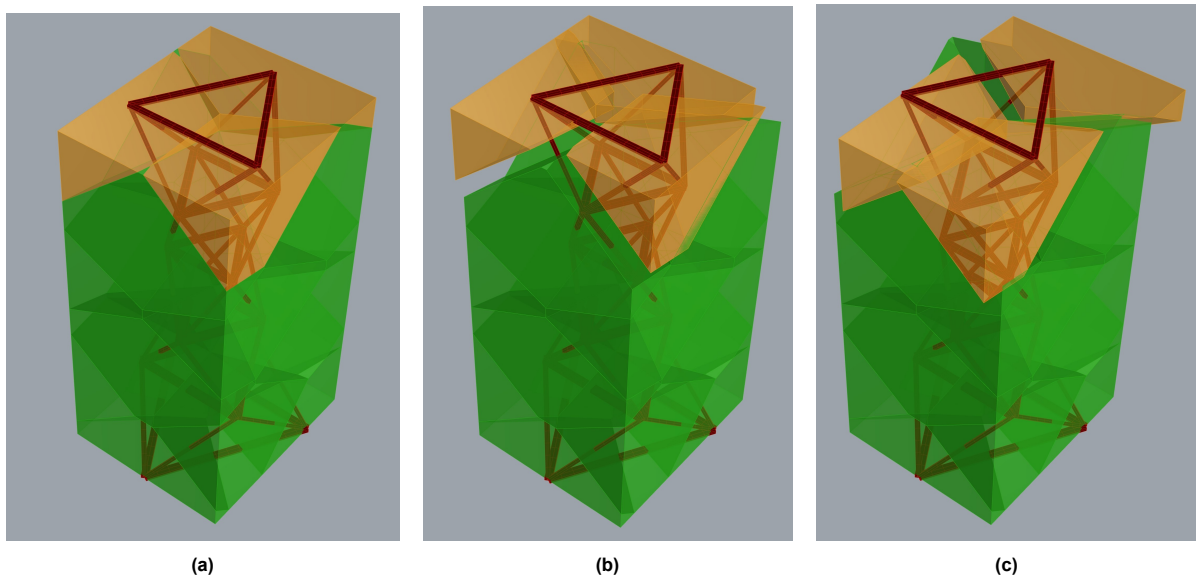


Figure C.8: The rank and resulting values of numbers of kinematic mechanisms and states of self-stress related to tower defined by the custom pattern and  $N = 4$  while having 4 rings in total. This outcome confirms that this structure is kinematically determinate.

# D

## Graphic kinematics of other tower configurations

The following are reciprocal force cells of towers following triangular and custom patterns. These variants are multi-levelled and, thus, there are more reciprocal cells corresponding to each node.



**Figure D.1:** Reciprocal cells of the tower defined by the triangular topology and  $N = 3$ . At the topmost ring the cells are unable to shift without separation or overlapping to their adjacent counterpart. Thus, the structure is kinematically determinate.

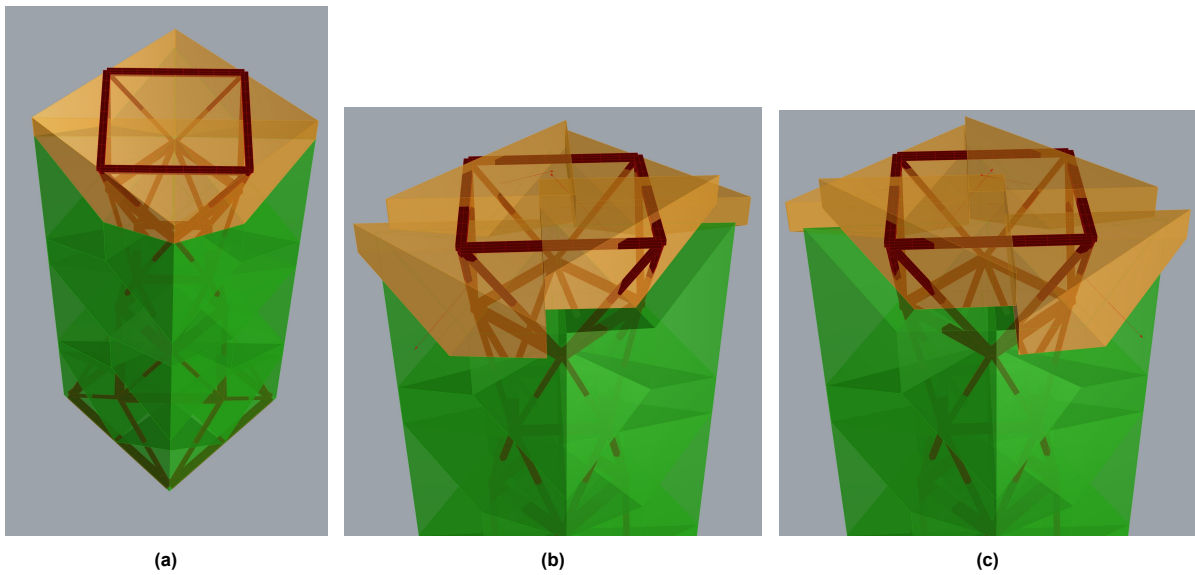


**Figure D.2:** Reciprocal cells of the tower defined by the triangular topology and  $N = 4$ . At the topmost ring the cells are able to shift without separation or overlapping to their adjacent counterpart. Thus, the structure is kinematically indeterminate.

# E

## Beaver plug-in reports for member groups in the final design.

### E.1. The most critical vertical member

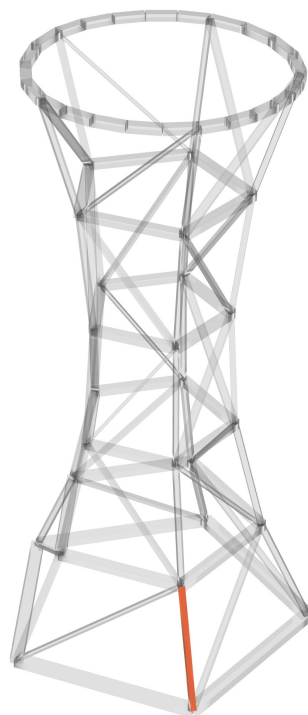


**Figure E.1:** Vertical members for which Beaver calculation reports are generated.

The following is the Beaver report detailing structural calculations for the vertical member highlighted in Figure E.1. Note that the member is assessed at 3 parts: at the start of it, the middle and the end,

thus, three reports are generated per each part containing calculations in 10 categories.

```
1
2 Tension along the grain acc. to EC5 6.1.2 | N = -678471.81
3 sigN = -7.57
4 Kmod = 0.90
5 Ym = 1.25
6 ft0d = 16.06
7 R0 = 0.00
8
9 Compression along the grain acc. to EC5 6.1.4 | N = -678471.81
10 sigN = -7.57
11 Kmod = 0.90
12 Ym = 1.25
13 fc0d = 20.16
14 R1 = 0.38
15
16 Bending acc. to EC5 6.1.6 | Wy = 0.00
17 Wz = 0.00
18 fmk = 28.00
19 Myd = 0.00
20 Mzd = 0.00
21 sigMy = 0.00
22 Kmod = 0.90
23 Ym = 1.25
24 fmd = 20.16
25 Km = 0.70
26 R2y = 0.00&R2z = 0.00
27
28 Shear acc. to EC5 6.1.7 | kcrit = 0.67
29 Vy = -101.56
30 Vz = -2511.31
31 A = 0.09
32 sigVy = 0.00
33 sigVz = -0.04
34 R3y = 0.00&R3z = 0.02
35
36 Torsion acc. to EC5 6.1.8 |
37 It = 0.00
38 Kshape = 1.17
39 Mt = 0.00
40 SigMt = 0.00
41 Kmod = 0.90
42 Ym = 1.25
43 fvd = 2.52
44 R4 = 0.00
45
46 Combined Bending and Axial Tension acc. to EC5 6.2.3 | A = 0.09
47 Wy = 0.00
48 Wz = 0.00
49 Nd = -678471.81
50 Myd = 0.00
51 Mzd = 0.00
52 sigN = -7.57
53 sigMy = 0.00
54 sigMz = 0.00
```

```
55 Kmod = 0.90
56 Ym = 1.25
57 ft0d = 16.06
58 fmd = 20.16
59 Km = 0.70
60 R5y = 0.00&R5z = 0.00
61
62 Combined Bending and Axial Compression acc. to EC5 6.2.4 | A = 0.09
63 Wy = 0.00
64 Wz = 0.00
65 Nd = -678471.81
66 Myd = 0.00
67 Mzd = 0.00
68 sigN = -7.57
69 sigMy = 0.00
70 sigMz = 0.00
71 Kmod = 0.90
72 Ym = 1.25
73 fc0d = 20.16
74 fmd = 20.16
75 Km = 0.70
76 R6y = 0.14&R6z = 0.14
77
78 Compression or combined Compression and Bending acc. to EC5 6.3.2 (buckling about both axes
   considered) | A = 0.09
79 Wy = 0.00
80 Wz = 0.00
81 Nd = -678471.81
82 Myd = 0.00
83 Mzd = 0.00
84 sigN = -7.57
85 sigMy = 0.00
86 sigMz = 0.00
87 ly = 6.22
88 lz = 6.22
89 ry = 0.09
90 rz = 0.08
91 lampi = 0.02
92 lamy = 67.33
93 lamz = 76.95
94 lamyrel = 1.11
95 lamzrel = 1.26
96 ky = 1.15
97 kz = 1.35
98 kyc = 0.68
99 kzc = 0.55
100 Kmod = 0.90
101 Ym = 1.25
102 fc0d = 20.16
103 fmd = 20.16
104 Km = 0.70
105 R7y = 0.55&R7z = 0.68
106
107 Bending or combined Bending and Compression acc. to EC5 6.3.3 (lateral torsional buckling
   considered) | A = 0.09
108 Wy = 0.00
109 Wz = 0.00
```

```
110 Nd = -678471.81
111 Myd = 0.00
112 Mzd = 0.00
113 sigN = -7.57
114 sigMy = 0.00
115 sigMz = 0.00
116 ly = 6.22
117 lz = 6.22
118 ry = 0.09
119 rz = 0.08
120 lampi = 0.02
121 lamy = 67.33
122 lamz = 76.95
123 lamyrel = 1.11
124 lamzrel = 1.26
125 ky = 1.15
126 kz = 1.35
127 kyc = 0.68
128 kzc = 0.55
129 ltb = 6.22
130 lefy = 6.22
131 lefz = 6.22
132 sigMcrity = 322.62
133 sigMcritz = 481.57
134 lammy = 0.29
135 lammz = 0.24
136 kcridy = 1.00
137 kcridz = 1.00
138 Kmod = 0.90
139 Ym = 1.25
140 fc0d = 20.16
141 fmd = 20.16
142 Km = 0.70R8y = 0.68&R8z = 0.55
143
144 Combined Torsion and Shear - Not speciefied in EC5 (Maximum Shear Utilization Ratio + Torsion
    Utilization Ratio) | R9 = R3max + R4 = 0.02
145
146
147
148 Tension along the grain acc. to EC5 6.1.2 | N = -678471.81
149 sigN = -7.57
150 Kmod = 0.90
151 Ym = 1.25
152 ft0d = 16.06
153 R0 = 0.00
154
155 Compression along the grain acc. to EC5 6.1.4 | N = -678471.81
156 sigN = -7.57
157 Kmod = 0.90
158 Ym = 1.25
159 fc0d = 20.16
160 R1 = 0.38
161
162 Bending acc. to EC5 6.1.6 | Wy = 0.00
163 Wz = 0.00
164 fmk = 28.00
165 Myd = -3904.86
```

```
166 Mzd = 157.92
167 sigMy = 0.82
168 Kmod = 0.90
169 Ym = 1.25
170 fmd = 20.16
171 Km = 0.70
172 R2y = 0.04&R2z = 0.03
173
174 Shear acc. to EC5 6.1.7 | kcrit = 0.67
175 Vy = 0.00
176 Vz = 0.00
177 A = 0.09
178 sigVy = 0.00
179 sigVz = 0.00
180 R3y = 0.00&R3z = 0.00
181
182 Torsion acc. to EC5 6.1.8 |
183 It = 0.00
184 Kshape = 1.17
185 Mt = 0.00
186 SigMt = 0.00
187 Kmod = 0.90
188 Ym = 1.25
189 fvd = 2.52
190 R4 = 0.00
191
192 Combined Bending and Axial Tension acc. to EC5 6.2.3 | A = 0.09
193 Wy = 0.00
194 Wz = 0.00
195 Nd = -678471.81
196 Myd = -3904.86
197 Mzd = 157.92
198 sigN = -7.57
199 sigMy = 0.82
200 sigMz = 0.04
201 Kmod = 0.90
202 Ym = 1.25
203 ft0d = 16.06
204 fmd = 20.16
205 Km = 0.70
206 R5y = 0.00&R5z = 0.00
207
208 Combined Bending and Axial Compression acc. to EC5 6.2.4 | A = 0.09
209 Wy = 0.00
210 Wz = 0.00
211 Nd = -678471.81
212 Myd = -3904.86
213 Mzd = 157.92
214 sigN = -7.57
215 sigMy = 0.82
216 sigMz = 0.04
217 Kmod = 0.90
218 Ym = 1.25
219 fc0d = 20.16
220 fmd = 20.16
221 Km = 0.70
222 R6y = 0.18&R6z = 0.17
```

```
223
224 Compression or combined Compression and Bending acc. to EC5 6.3.2 (buckling about both axes
      considered) | A = 0.09
225 Wy = 0.00
226 Wz = 0.00
227 Nd = -678471.81
228 Myd = -3904.86
229 Mzd = 157.92
230 sigN = -7.57
231 sigMy = 0.82
232 sigMz = 0.04
233 ly = 6.22
234 lz = 6.22
235 ry = 0.09
236 rz = 0.08
237 lampi = 0.02
238 lamy = 67.33
239 lamz = 76.95
240 lamyrel = 1.11
241 lamzrel = 1.26
242 ky = 1.15
243 kz = 1.35
244 kyc = 0.68
245 kzc = 0.55
246 Kmod = 0.90
247 Ym = 1.25
248 fc0d = 20.16
249 fmd = 20.16
250 Km = 0.70
251 R7y = 0.60&R7z = 0.71
252
253 Bending or combined Bending and Compression acc. to EC5 6.3.3 (lateral torsional buckling
      considered) | A = 0.09
254 Wy = 0.00
255 Wz = 0.00
256 Nd = -678471.81
257 Myd = -3904.86
258 Mzd = 157.92
259 sigN = -7.57
260 sigMy = 0.82
261 sigMz = 0.04
262 ly = 6.22
263 lz = 6.22
264 ry = 0.09
265 rz = 0.08
266 lampi = 0.02
267 lamy = 67.33
268 lamz = 76.95
269 lamyrel = 1.11
270 lamzrel = 1.26
271 ky = 1.15
272 kz = 1.35
273 kyc = 0.68
274 kzc = 0.55
275 ltb = 6.22
276 lefy = 6.22
277 lefz = 6.22
```

```
278 sigMcrity = 322.62
279 sigMcritz = 481.57
280 lammy = 0.29
281 lammz = 0.24
282 kcrity = 1.00
283 kcritz = 1.00
284 Kmod = 0.90
285 Ym = 1.25
286 fc0d = 20.16
287 fmd = 20.16
288 Km = 0.70R8y = 0.68&R8z = 0.58
289
290 Combined Torsion and Shear - Not speciefied in EC5 (Maximum Shear Utilization Ratio + Torsion
    Utilization Ratio) | R9 = R3max + R4 = 0.00
291 Tension along the grain acc. to EC5 6.1.2 | N = -678471.81
292 sigN = -7.57
293 Kmod = 0.90
294 Ym = 1.25
295 ft0d = 16.06
296 R0 = 0.00
297
298 Compression along the grain acc. to EC5 6.1.4 | N = -678471.81
299 sigN = -7.57
300 Kmod = 0.90
301 Ym = 1.25
302 fc0d = 20.16
303 R1 = 0.38
304
305 Bending acc. to EC5 6.1.6 | Wy = 0.00
306 Wz = 0.00
307 fmk = 28.00
308 Myd = 0.00
309 Mzd = 0.00
310 sigMy = 0.00
311 Kmod = 0.90
312 Ym = 1.25
313 fmd = 20.16
314 Km = 0.70
315 R2y = 0.00&R2z = 0.00
316
317 Shear acc. to EC5 6.1.7 | kcrit = 0.67
318 Vy = 101.56
319 Vz = 2511.31
320 A = 0.09
321 sigVy = 0.00
322 sigVz = 0.04
323 R3y = 0.00&R3z = 0.02
324
325 Torsion acc. to EC5 6.1.8 |
326 It = 0.00
327 Kshape = 1.17
328 Mt = 0.00
329 SigMt = 0.00
330 Kmod = 0.90
331 Ym = 1.25
332 fvd = 2.52
333 R4 = 0.00
```

```
334
335 Combined Bending and Axial Tension acc. to EC5 6.2.3 | A = 0.09
336 Wy = 0.00
337 Wz = 0.00
338 Nd = -678471.81
339 Myd = 0.00
340 Mzd = 0.00
341 sigN = -7.57
342 sigMy = 0.00
343 sigMz = 0.00
344 Kmod = 0.90
345 Ym = 1.25
346 ft0d = 16.06
347 fmd = 20.16
348 Km = 0.70
349 R5y = 0.00&R5z = 0.00
350
351 Combined Bending and Axial Compression acc. to EC5 6.2.4 | A = 0.09
352 Wy = 0.00
353 Wz = 0.00
354 Nd = -678471.81
355 Myd = 0.00
356 Mzd = 0.00
357 sigN = -7.57
358 sigMy = 0.00
359 sigMz = 0.00
360 Kmod = 0.90
361 Ym = 1.25
362 fc0d = 20.16
363 fmd = 20.16
364 Km = 0.70
365 R6y = 0.14&R6z = 0.14
366
367 Compression or combined Compression and Bending acc. to EC5 6.3.2 (buckling about both axes
      considered) | A = 0.09
368 Wy = 0.00
369 Wz = 0.00
370 Nd = -678471.81
371 Myd = 0.00
372 Mzd = 0.00
373 sigN = -7.57
374 sigMy = 0.00
375 sigMz = 0.00
376 ly = 6.22
377 lz = 6.22
378 ry = 0.09
379 rz = 0.08
380 lampi = 0.02
381 lamy = 67.33
382 lamz = 76.95
383 lamyrel = 1.11
384 lamzrel = 1.26
385 ky = 1.15
386 kz = 1.35
387 kyc = 0.68
388 kzc = 0.55
389 Kmod = 0.90
```

```
390 Ym = 1.25
391 fc0d = 20.16
392 fmd = 20.16
393 Km = 0.70
394 R7y = 0.55&R7z = 0.68
395
396 Bending or combined Bending and Compression acc. to EC5 6.3.3 (lateral torsional buckling
    considered) | A = 0.09
397 Wy = 0.00
398 Wz = 0.00
399 Nd = -678471.81
400 Myd = 0.00
401 Mzd = 0.00
402 sigN = -7.57
403 sigMy = 0.00
404 sigMz = 0.00
405 ly = 6.22
406 lz = 6.22
407 ry = 0.09
408 rz = 0.08
409 lampi = 0.02
410 lamy = 67.33
411 lamz = 76.95
412 lamyrel = 1.11
413 lamzrel = 1.26
414 ky = 1.15
415 kz = 1.35
416 kyc = 0.68
417 kzc = 0.55
418 ltb = 6.22
419 lefy = 6.22
420 lefz = 6.22
421 sigMcrity = 322.62
422 sigMcritz = 481.57
423 lammy = 0.29
424 lammz = 0.24
425 kcridy = 1.00
426 kcridz = 1.00
427 Kmod = 0.90
428 Ym = 1.25
429 fc0d = 20.16
430 fmd = 20.16
431 Km = 0.70R8y = 0.68&R8z = 0.55
432
433 Combined Torsion and Shear - Not speciefied in EC5 (Maximum Shear Utilization Ratio + Torsion
    Utilization Ratio) | R9 = R3max + R4 = 0.02
```

## E.2. The most critical vertical member

In the same way, the most critical diagonal member and its calculations are provided in this section.

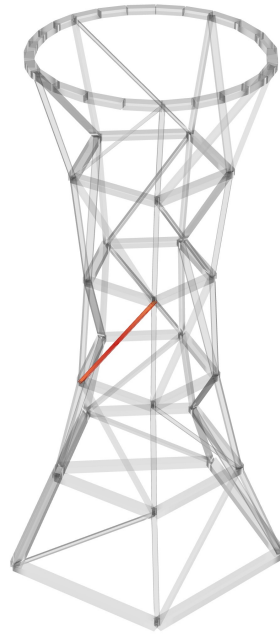


**Figure E.2:** The most critical diagonal member for which Beaver calculation reports are generated.

```
1
2 Tension along the grain acc. to EC5 6.1.2 | N = -119873.69
3 sigN = -1.87
4 Kmod = 0.90
5 Ym = 1.25
6 ft0d = 16.06
7 R0 = 0.00
8
9 Compression along the grain acc. to EC5 6.1.4 | N = -119873.69
10 sigN = -1.87
11 Kmod = 0.90
12 Ym = 1.25
13 fc0d = 20.16
14 R1 = 0.09
15
16 Bending acc. to EC5 6.1.6 | Wy = 0.00
17 Wz = 0.00
18 fmk = 28.00
19 Myd = 0.00
20 Mzd = 0.00
21 sigMy = 0.00
22 Kmod = 0.90
23 Ym = 1.25
```

```
24 fmd = 20.16
25 Km = 0.70
26 R2y = 0.00&R2z = 0.00
27
28 Shear acc. to EC5 6.1.7 | kcrit = 0.67
29 Vy = -1904.20
30 Vz = 2039.03
31 A = 0.06
32 sigVy = -0.04
33 sigVz = 0.05
34 R3y = 0.02&R3z = 0.02
35
36 Torsion acc. to EC5 6.1.8 |
37 It = 0.00
38 Kshape = 1.38
39 Mt = 0.00
40 SigMt = 0.00
41 Kmod = 0.90
42 Ym = 1.25
43 fvd = 2.52
44 R4 = 0.00
45
46 Combined Bending and Axial Tension acc. to EC5 6.2.3 | A = 0.06
47 Wy = 0.00
48 Wz = 0.00
49 Nd = -119873.69
50 Myd = 0.00
51 Mzd = 0.00
52 sigN = -1.87
53 sigMy = 0.00
54 sigMz = 0.00
55 Kmod = 0.90
56 Ym = 1.25
57 ft0d = 16.06
58 fmd = 20.16
59 Km = 0.70
60 R5y = 0.00&R5z = 0.00
61
62 Combined Bending and Axial Compression acc. to EC5 6.2.4 | A = 0.06
63 Wy = 0.00
64 Wz = 0.00
65 Nd = -119873.69
66 Myd = 0.00
67 Mzd = 0.00
68 sigN = -1.87
69 sigMy = 0.00
70 sigMz = 0.00
71 Kmod = 0.90
72 Ym = 1.25
73 fc0d = 20.16
74 fmd = 20.16
75 Km = 0.70
76 R6y = 0.01&R6z = 0.01
77
78 Compression or combined Compression and Bending acc. to EC5 6.3.2 (buckling about both axes
  considered) | A = 0.06
79 Wy = 0.00
```

```
80 Wz = 0.00
81 Nd = -119873.69
82 Myd = 0.00
83 Mzd = 0.00
84 sigN = -1.87
85 sigMy = 0.00
86 sigMz = 0.00
87 ly = 7.55
88 lz = 7.55
89 ry = 0.12
90 rz = 0.05
91 lampi = 0.02
92 lamy = 65.40
93 lamz = 163.51
94 lamyrel = 1.08
95 lamzrel = 2.69
96 ky = 1.12
97 kz = 4.23
98 kyc = 0.70
99 kzc = 0.13
100 Kmod = 0.90
101 Ym = 1.25
102 fc0d = 20.16
103 fmd = 20.16
104 Km = 0.70
105 R7y = 0.13&R7z = 0.70
106
107 Bending or combined Bending and Compression acc. to EC5 6.3.3 (lateral torsional buckling
    considered) | A = 0.06
108 Wy = 0.00
109 Wz = 0.00
110 Nd = -119873.69
111 Myd = 0.00
112 Mzd = 0.00
113 sigN = -1.87
114 sigMy = 0.00
115 sigMz = 0.00
116 ly = 7.55
117 lz = 7.55
118 ry = 0.12
119 rz = 0.05
120 lampi = 0.02
121 lamy = 65.40
122 lamz = 163.51
123 lamyrel = 1.08
124 lamzrel = 2.69
125 ky = 1.12
126 kz = 4.23
127 kyc = 0.70
128 kzc = 0.13
129 ltb = 7.55
130 lefy = 7.55
131 lefz = 7.55
132 sigMcrity = 69.41
133 sigMcritz = 1084.47
134 lammy = 0.64
135 lammz = 0.16
```

```
136 kcrity = 1.00
137 kcritz = 1.00
138 Kmod = 0.90
139 Ym = 1.25
140 fc0d = 20.16
141 fmd = 20.16
142 Km = 0.70R8y = 0.70&R8z = 0.13
143
144 Combined Torsion and Shear - Not speciefied in EC5 (Maximum Shear Utilization Ratio + Torsion
    Utilization Ratio) | R9 = R3max + R4 = 0.02
145
146 Tension along the grain acc. to EC5 6.1.2 | N = -118532.19
147 sigN = -1.85
148 Kmod = 0.90
149 Ym = 1.25
150 ft0d = 16.06
151 R0 = 0.00
152
153 Compression along the grain acc. to EC5 6.1.4 | N = -118532.19
154 sigN = -1.85
155 Kmod = 0.90
156 Ym = 1.25
157 fc0d = 20.16
158 R1 = 0.09
159
160 Bending acc. to EC5 6.1.6 | Wy = 0.00
161 Wz = 0.00
162 fmk = 28.00
163 Myd = 3849.73
164 Mzd = 3595.17
165 sigMy = 0.90
166 Kmod = 0.90
167 Ym = 1.25
168 fmd = 20.16
169 Km = 0.70
170 R2y = 0.12&R2z = 0.14
171
172 Shear acc. to EC5 6.1.7 | kcrit = 0.67
173 Vy = 0.00
174 Vz = 0.00
175 A = 0.06
176 sigVy = 0.00
177 sigVz = 0.00
178 R3y = 0.00&R3z = 0.00
179
180 Torsion acc. to EC5 6.1.8 |
181 It = 0.00
182 Kshape = 1.38
183 Mt = 0.00
184 SigMt = 0.00
185 Kmod = 0.90
186 Ym = 1.25
187 fvd = 2.52
188 R4 = 0.00
189
190 Combined Bending and Axial Tension acc. to EC5 6.2.3 | A = 0.06
191 Wy = 0.00
```

```
192 Wz = 0.00
193 Nd = -118532.19
194 Myd = 3849.73
195 Mzd = 3595.17
196 sigN = -1.85
197 sigMy = 0.90
198 sigMz = 2.11
199 Kmod = 0.90
200 Ym = 1.25
201 ft0d = 16.06
202 fmd = 20.16
203 Km = 0.70
204 R5y = 0.00&R5z = 0.00
205
206 Combined Bending and Axial Compression acc. to EC5 6.2.4 | A = 0.06
207 Wy = 0.00
208 Wz = 0.00
209 Nd = -118532.19
210 Myd = 3849.73
211 Mzd = 3595.17
212 sigN = -1.85
213 sigMy = 0.90
214 sigMz = 2.11
215 Kmod = 0.90
216 Ym = 1.25
217 fc0d = 20.16
218 fmd = 20.16
219 Km = 0.70
220 R6y = 0.13&R6z = 0.14
221
222 Compression or combined Compression and Bending acc. to EC5 6.3.2 (buckling about both axes
      considered) | A = 0.06
223 Wy = 0.00
224 Wz = 0.00
225 Nd = -118532.19
226 Myd = 3849.73
227 Mzd = 3595.17
228 sigN = -1.85
229 sigMy = 0.90
230 sigMz = 2.11
231 ly = 7.55
232 lz = 7.55
233 ry = 0.12
234 rz = 0.05
235 lampi = 0.02
236 lamy = 65.40
237 lamz = 163.51
238 lamyrel = 1.08
239 lamzrel = 2.69
240 ky = 1.12
241 kz = 4.23
242 kyc = 0.70
243 kzc = 0.13
244 Kmod = 0.90
245 Ym = 1.25
246 fc0d = 20.16
247 fmd = 20.16
```

```
248 Km = 0.70
249 R7y = 0.25&R7z = 0.82
250
251 Bending or combined Bending and Compression acc. to EC5 6.3.3 (lateral torsional buckling
    considered) | A = 0.06
252 Wy = 0.00
253 Wz = 0.00
254 Nd = -118532.19
255 Myd = 3849.73
256 Mzd = 3595.17
257 sigN = -1.85
258 sigMy = 0.90
259 sigMz = 2.11
260 ly = 7.55
261 lz = 7.55
262 ry = 0.12
263 rz = 0.05
264 lampi = 0.02
265 lamy = 65.40
266 lamz = 163.51
267 lamyrel = 1.08
268 lamzrel = 2.69
269 ky = 1.12
270 kz = 4.23
271 kyc = 0.70
272 kzc = 0.13
273 ltb = 7.55
274 lefy = 7.55
275 lefz = 7.55
276 sigMcrity = 69.41
277 sigMcritz = 1084.47
278 lammy = 0.64
279 lammz = 0.16
280 kcrity = 1.00
281 kcritz = 1.00
282 Kmod = 0.90
283 Ym = 1.25
284 fc0d = 20.16
285 fmd = 20.16
286 Km = 0.70R8y = 0.76&R8z = 0.17
287
288 Combined Torsion and Shear - Not speciefied in EC5 (Maximum Shear Utilization Ratio + Torsion
    Utilization Ratio) | R9 = R3max + R4 = 0.00
289
290 Tension along the grain acc. to EC5 6.1.2 | N = -117190.68
291 sigN = -1.83
292 Kmod = 0.90
293 Ym = 1.25
294 ft0d = 16.06
295 R0 = 0.00
296
297 Compression along the grain acc. to EC5 6.1.4 | N = -117190.68
298 sigN = -1.83
299 Kmod = 0.90
300 Ym = 1.25
301 fc0d = 20.16
302 R1 = 0.09
```

```
303
304 Bending acc. to EC5 6.1.6 | Wy = 0.00
305 Wz = 0.00
306 fmk = 28.00
307 Myd = 0.00
308 Mzd = 0.00
309 sigMy = 0.00
310 Kmod = 0.90
311 Ym = 1.25
312 fmd = 20.16
313 Km = 0.70
314 R2y = 0.00&R2z = 0.00
315
316 Shear acc. to EC5 6.1.7 | kcrit = 0.67
317 Vy = 1904.20
318 Vz = -2039.03
319 A = 0.06
320 sigVy = 0.04
321 sigVz = -0.05
322 R3y = 0.02&R3z = 0.02
323
324 Torsion acc. to EC5 6.1.8 |
325 It = 0.00
326 Kshape = 1.38
327 Mt = 0.00
328 SigMt = 0.00
329 Kmod = 0.90
330 Ym = 1.25
331 fvd = 2.52
332 R4 = 0.00
333
334 Combined Bending and Axial Tension acc. to EC5 6.2.3 | A = 0.06
335 Wy = 0.00
336 Wz = 0.00
337 Nd = -117190.68
338 Myd = 0.00
339 Mzd = 0.00
340 sigN = -1.83
341 sigMy = 0.00
342 sigMz = 0.00
343 Kmod = 0.90
344 Ym = 1.25
345 ft0d = 16.06
346 fmd = 20.16
347 Km = 0.70
348 R5y = 0.00&R5z = 0.00
349
350 Combined Bending and Axial Compression acc. to EC5 6.2.4 | A = 0.06
351 Wy = 0.00
352 Wz = 0.00
353 Nd = -117190.68
354 Myd = 0.00
355 Mzd = 0.00
356 sigN = -1.83
357 sigMy = 0.00
358 sigMz = 0.00
359 Kmod = 0.90
```

```
360 Ym = 1.25
361 fc0d = 20.16
362 fmd = 20.16
363 Km = 0.70
364 R6y = 0.01&R6z = 0.01
365
366 Compression or combined Compression and Bending acc. to EC5 6.3.2 (buckling about both axes
      considered) | A = 0.06
367 Wy = 0.00
368 Wz = 0.00
369 Nd = -117190.68
370 Myd = 0.00
371 Mzd = 0.00
372 sigN = -1.83
373 sigMy = 0.00
374 sigMz = 0.00
375 ly = 7.55
376 lz = 7.55
377 ry = 0.12
378 rz = 0.05
379 lampi = 0.02
380 lamy = 65.40
381 lamz = 163.51
382 lamyrel = 1.08
383 lamzrel = 2.69
384 ky = 1.12
385 kz = 4.23
386 kyc = 0.70
387 kzc = 0.13
388 Kmod = 0.90
389 Ym = 1.25
390 fc0d = 20.16
391 fmd = 20.16
392 Km = 0.70
393 R7y = 0.13&R7z = 0.68
394
395 Bending or combined Bending and Compression acc. to EC5 6.3.3 (lateral torsional buckling
      considered) | A = 0.06
396 Wy = 0.00
397 Wz = 0.00
398 Nd = -117190.68
399 Myd = 0.00
400 Mzd = 0.00
401 sigN = -1.83
402 sigMy = 0.00
403 sigMz = 0.00
404 ly = 7.55
405 lz = 7.55
406 ry = 0.12
407 rz = 0.05
408 lampi = 0.02
409 lamy = 65.40
410 lamz = 163.51
411 lamyrel = 1.08
412 lamzrel = 2.69
413 ky = 1.12
414 kz = 4.23
```

```
415 kyc = 0.70
416 kzc = 0.13
417 ltb = 7.55
418 lefy = 7.55
419 lefz = 7.55
420 sigMcrity = 69.41
421 sigMcritz = 1084.47
422 lammy = 0.64
423 lammz = 0.16
424 kcridy = 1.00
425 kcritz = 1.00
426 Kmod = 0.90
427 Ym = 1.25
428 fc0d = 20.16
429 fmd = 20.16
430 Km = 0.70R8y = 0.68&R8z = 0.13
431
432 Combined Torsion and Shear - Not speciefied in EC5 (Maximum Shear Utilization Ratio + Torsion
    Utilization Ratio) | R9 = R3max + R4 = 0.02
```

## E.3. The most critical ring member

The most critical ring member and its calculations are provided in this section.

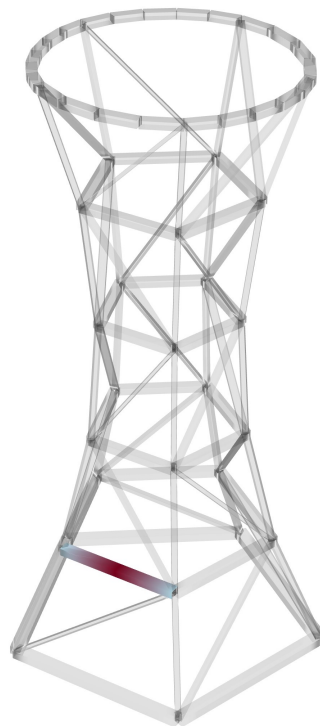


**Figure E.3:** The most critical ring member for which Beaver calculation reports are generated.

```
2 Tension along the grain acc. to EC5 6.1.2 | N = -126080.75
3 sigN = -0.56
4 Kmod = 0.90
5 Ym = 1.25
6 ft0d = 16.06
7 R0 = 0.00
8
9 Compression along the grain acc. to EC5 6.1.4 | N = -126080.75
10 sigN = -0.56
11 Kmod = 0.90
12 Ym = 1.25
13 fc0d = 20.16
14 R1 = 0.03
15
16 Bending acc. to EC5 6.1.6 | Wy = 0.01
17 Wz = 0.02
18 fmk = 28.00
19 Myd = 0.00
20 Mzd = 0.00
21 sigMy = 0.00
22 Kmod = 0.90
23 Ym = 1.25
24 fmd = 20.16
25 Km = 0.70
26 R2y = 0.00&R2z = 0.00
27
28 Shear acc. to EC5 6.1.7 | kcrit = 0.67
29 Vy = -4929.19
30 Vz = -81426.50
31 A = 0.22
32 sigVy = -0.03
33 sigVz = -0.54
34 R3y = 0.01&R3z = 0.22
35
36 Torsion acc. to EC5 6.1.8 |
37 It = 0.01
38 Kshape = 1.11
39 Mt = 0.00
40 SigMt = 0.00
41 Kmod = 0.90
42 Ym = 1.25
43 fvd = 2.52
44 R4 = 0.00
45
46 Combined Bending and Axial Tension acc. to EC5 6.2.3 | A = 0.22
47 Wy = 0.01
48 Wz = 0.02
49 Nd = -126080.75
50 Myd = 0.00
51 Mzd = 0.00
52 sigN = -0.56
53 sigMy = 0.00
54 sigMz = 0.00
55 Kmod = 0.90
56 Ym = 1.25
57 ft0d = 16.06
58 fmd = 20.16
```

```
59 Km = 0.70
60 R5y = 0.00&R5z = 0.00
61
62 Combined Bending and Axial Compression acc. to EC5 6.2.4 | A = 0.22
63 Wy = 0.01
64 Wz = 0.02
65 Nd = -126080.75
66 Myd = 0.00
67 Mzd = 0.00
68 sigN = -0.56
69 sigMy = 0.00
70 sigMz = 0.00
71 Kmod = 0.90
72 Ym = 1.25
73 fc0d = 20.16
74 fmd = 20.16
75 Km = 0.70
76 R6y = 0.00&R6z = 0.00
77
78 Compression or combined Compression and Bending acc. to EC5 6.3.2 (buckling about both axes
   considered) | A = 0.22
79 Wy = 0.01
80 Wz = 0.02
81 Nd = -126080.75
82 Myd = 0.00
83 Mzd = 0.00
84 sigN = -0.56
85 sigMy = 0.00
86 sigMz = 0.00
87 ly = 6.34
88 lz = 6.34
89 ry = 0.12
90 rz = 0.16
91 lampi = 0.02
92 lamy = 54.90
93 lamz = 39.22
94 lamyrel = 0.90
95 lamzrel = 0.64
96 ky = 0.94
97 kz = 0.72
98 kyc = 0.84
99 kzc = 0.95
100 Kmod = 0.90
101 Ym = 1.25
102 fc0d = 20.16
103 fmd = 20.16
104 Km = 0.70
105 R7y = 0.03&R7z = 0.03
106
107 Bending or combined Bending and Compression acc. to EC5 6.3.3 (lateral torsional buckling
   considered) | A = 0.22
108 Wy = 0.01
109 Wz = 0.02
110 Nd = -126080.75
111 Myd = 0.00
112 Mzd = 0.00
113 sigN = -0.56
```

```
114 sigMy = 0.00
115 sigMz = 0.00
116 ly = 6.34
117 lz = 6.34
118 ry = 0.12
119 rz = 0.16
120 lampi = 0.02
121 lamy = 54.90
122 lamz = 39.22
123 lamyrel = 0.90
124 lamzrel = 0.64
125 ky = 0.94
126 kz = 0.72
127 kyc = 0.84
128 kzc = 0.95
129 ltb = 6.34
130 lefy = 6.34
131 lefz = 6.34
132 sigMcrity = 1012.83
133 sigMcritz = 369.11
134 lammy = 0.17
135 lammz = 0.28
136 kcridy = 1.00
137 kcridz = 1.00
138 Kmod = 0.90
139 Ym = 1.25
140 fc0d = 20.16
141 fmd = 20.16
142 Km = 0.70R8y = 0.03&R8z = 0.03
143
144 Combined Torsion and Shear - Not speciefied in EC5 (Maximum Shear Utilization Ratio + Torsion
    Utilization Ratio) | R9 = R3max + R4 = 0.22
145
146 Tension along the grain acc. to EC5 6.1.2 | N = -126356.77
147 sigN = -0.56
148 Kmod = 0.90
149 Ym = 1.25
150 ft0d = 16.06
151 R0 = 0.00
152
153 Compression along the grain acc. to EC5 6.1.4 | N = -126356.77
154 sigN = -0.56
155 Kmod = 0.90
156 Ym = 1.25
157 fc0d = 20.16
158 R1 = 0.03
159
160 Bending acc. to EC5 6.1.6 | Wy = 0.01
161 Wz = 0.02
162 fmk = 28.00
163 Myd = -129052.82
164 Mzd = 7812.28
165 sigMy = 8.64
166 Kmod = 0.90
167 Ym = 1.25
168 fmd = 20.16
169 Km = 0.70
```

```
170 R2y = 0.44&R2z = 0.32
171
172 Shear acc. to EC5 6.1.7 | kcrit = 0.67
173 Vy = 0.00
174 Vz = 0.00
175 A = 0.22
176 sigVy = 0.00
177 sigVz = 0.00
178 R3y = 0.00&R3z = 0.00
179
180 Torsion acc. to EC5 6.1.8 |
181 It = 0.01
182 Kshape = 1.11
183 Mt = 0.00
184 SigMt = 0.00
185 Kmod = 0.90
186 Ym = 1.25
187 fvd = 2.52
188 R4 = 0.00
189
190 Combined Bending and Axial Tension acc. to EC5 6.2.3 | A = 0.22
191 Wy = 0.01
192 Wz = 0.02
193 Nd = -126356.77
194 Myd = -129052.82
195 Mzd = 7812.28
196 sigN = -0.56
197 sigMy = 8.64
198 sigMz = 0.37
199 Kmod = 0.90
200 Ym = 1.25
201 ft0d = 16.06
202 fmd = 20.16
203 Km = 0.70
204 R5y = 0.00&R5z = 0.00
205
206 Combined Bending and Axial Compression acc. to EC5 6.2.4 | A = 0.22
207 Wy = 0.01
208 Wz = 0.02
209 Nd = -126356.77
210 Myd = -129052.82
211 Mzd = 7812.28
212 sigN = -0.56
213 sigMy = 8.64
214 sigMz = 0.37
215 Kmod = 0.90
216 Ym = 1.25
217 fc0d = 20.16
218 fmd = 20.16
219 Km = 0.70
220 R6y = 0.44&R6z = 0.32
221
222 Compression or combined Compression and Bending acc. to EC5 6.3.2 (buckling about both axes
    considered) | A = 0.22
223 Wy = 0.01
224 Wz = 0.02
225 Nd = -126356.77
```

```
226 Myd = -129052.82
227 Mzd = 7812.28
228 sigN = -0.56
229 sigMy = 8.64
230 sigMz = 0.37
231 ly = 6.34
232 lz = 6.34
233 ry = 0.12
234 rz = 0.16
235 lampi = 0.02
236 lamy = 54.90
237 lamz = 39.22
238 lamyrel = 0.90
239 lamzrel = 0.64
240 ky = 0.94
241 kz = 0.72
242 kyc = 0.84
243 kzc = 0.95
244 Kmod = 0.90
245 Ym = 1.25
246 fc0d = 20.16
247 fmd = 20.16
248 Km = 0.70
249 R7y = 0.47&R7z = 0.35
250
251 Bending or combined Bending and Compression acc. to EC5 6.3.3 (lateral torsional buckling
    considered) | A = 0.22
252 Wy = 0.01
253 Wz = 0.02
254 Nd = -126356.77
255 Myd = -129052.82
256 Mzd = 7812.28
257 sigN = -0.56
258 sigMy = 8.64
259 sigMz = 0.37
260 ly = 6.34
261 lz = 6.34
262 ry = 0.12
263 rz = 0.16
264 lampi = 0.02
265 lamy = 54.90
266 lamz = 39.22
267 lamyrel = 0.90
268 lamzrel = 0.64
269 ky = 0.94
270 kz = 0.72
271 kyc = 0.84
272 kzc = 0.95
273 ltb = 6.34
274 lefy = 6.34
275 lefz = 6.34
276 sigMcrity = 1012.83
277 sigMcritz = 369.11
278 lammy = 0.17
279 lammz = 0.28
280 kcrity = 1.00
281 kcritz = 1.00
```

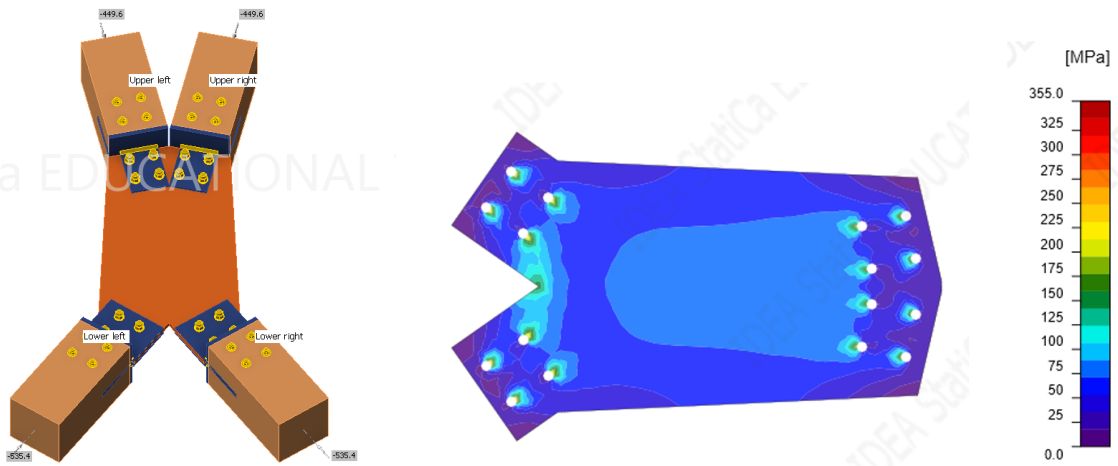
```
282 Kmod = 0.90
283 Ym = 1.25
284 fc0d = 20.16
285 fmd = 20.16
286 Km = 0.70R8y = 0.23&R8z = 0.33
287
288 Combined Torsion and Shear - Not speciefied in EC5 (Maximum Shear Utilization Ratio + Torsion
    Utilization Ratio) | R9 = R3max + R4 = 0.00
289
290 Tension along the grain acc. to EC5 6.1.2 | N = -126632.78
291 sigN = -0.57
292 Kmod = 0.90
293 Ym = 1.25
294 ft0d = 16.06
295 R0 = 0.00
296
297 Compression along the grain acc. to EC5 6.1.4 | N = -126632.78
298 sigN = -0.57
299 Kmod = 0.90
300 Ym = 1.25
301 fc0d = 20.16
302 R1 = 0.03
303
304 Bending acc. to EC5 6.1.6 | Wy = 0.01
305 Wz = 0.02
306 fmk = 28.00
307 Myd = 0.00
308 Mzd = 0.00
309 sigMy = 0.00
310 Kmod = 0.90
311 Ym = 1.25
312 fmd = 20.16
313 Km = 0.70
314 R2y = 0.00&R2z = 0.00
315
316 Shear acc. to EC5 6.1.7 | kcrit = 0.67
317 Vy = 4929.19
318 Vz = 81426.50
319 A = 0.22
320 sigVy = 0.03
321 sigVz = 0.54
322 R3y = 0.01&R3z = 0.22
323
324 Torsion acc. to EC5 6.1.8 |
325 It = 0.01
326 Kshape = 1.11
327 Mt = 0.00
328 SigMt = 0.00
329 Kmod = 0.90
330 Ym = 1.25
331 fvd = 2.52
332 R4 = 0.00
333
334 Combined Bending and Axial Tension acc. to EC5 6.2.3 | A = 0.22
335 Wy = 0.01
336 Wz = 0.02
337 Nd = -126632.78
```

```
338 Myd = 0.00
339 Mzd = 0.00
340 sigN = -0.57
341 sigMy = 0.00
342 sigMz = 0.00
343 Kmod = 0.90
344 Ym = 1.25
345 ft0d = 16.06
346 fmd = 20.16
347 Km = 0.70
348 R5y = 0.00&R5z = 0.00
349
350 Combined Bending and Axial Compression acc. to EC5 6.2.4 | A = 0.22
351 Wy = 0.01
352 Wz = 0.02
353 Nd = -126632.78
354 Myd = 0.00
355 Mzd = 0.00
356 sigN = -0.57
357 sigMy = 0.00
358 sigMz = 0.00
359 Kmod = 0.90
360 Ym = 1.25
361 fc0d = 20.16
362 fmd = 20.16
363 Km = 0.70
364 R6y = 0.00&R6z = 0.00
365
366 Compression or combined Compression and Bending acc. to EC5 6.3.2 (buckling about both axes
      considered) | A = 0.22
367 Wy = 0.01
368 Wz = 0.02
369 Nd = -126632.78
370 Myd = 0.00
371 Mzd = 0.00
372 sigN = -0.57
373 sigMy = 0.00
374 sigMz = 0.00
375 ly = 6.34
376 lz = 6.34
377 ry = 0.12
378 rz = 0.16
379 lampi = 0.02
380 lamy = 54.90
381 lamz = 39.22
382 lamyrel = 0.90
383 lamzrel = 0.64
384 ky = 0.94
385 kz = 0.72
386 kyc = 0.84
387 kzc = 0.95
388 Kmod = 0.90
389 Ym = 1.25
390 fc0d = 20.16
391 fmd = 20.16
392 Km = 0.70
393 R7y = 0.03&R7z = 0.03
```

```
394
395 Bending or combined Bending and Compression acc. to EC5 6.3.3 (lateral torsional buckling
      considered) | A = 0.22
396 Wy = 0.01
397 Wz = 0.02
398 Nd = -126632.78
399 Myd = 0.00
400 Mzd = 0.00
401 sigN = -0.57
402 sigMy = 0.00
403 sigMz = 0.00
404 ly = 6.34
405 lz = 6.34
406 ry = 0.12
407 rz = 0.16
408 lampi = 0.02
409 lamy = 54.90
410 lamz = 39.22
411 lamyrel = 0.90
412 lamzrel = 0.64
413 ky = 0.94
414 kz = 0.72
415 kyc = 0.84
416 kzc = 0.95
417 ltb = 6.34
418 lefy = 6.34
419 lefz = 6.34
420 sigMcrity = 1012.83
421 sigMcritz = 369.11
422 lammy = 0.17
423 lammz = 0.28
424 kcrity = 1.00
425 kcritz = 1.00
426 Kmod = 0.90
427 Ym = 1.25
428 fc0d = 20.16
429 fmd = 20.16
430 Km = 0.70R8y = 0.03&R8z = 0.03
431
432 Combined Torsion and Shear - Not speciefied in EC5 (Maximum Shear Utilization Ratio + Torsion
      Utilization Ratio) | R9 = R3max + R4 = 0.22
```

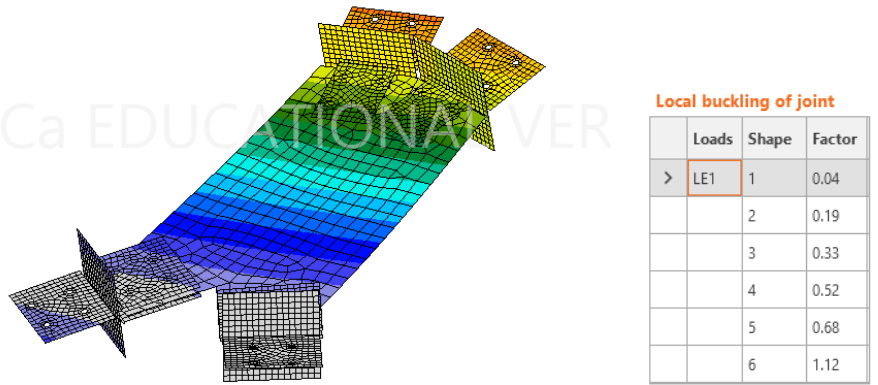
F

IDEASTatiCA analysis outputs of the  
first connection design



(a) Initial connection overview.

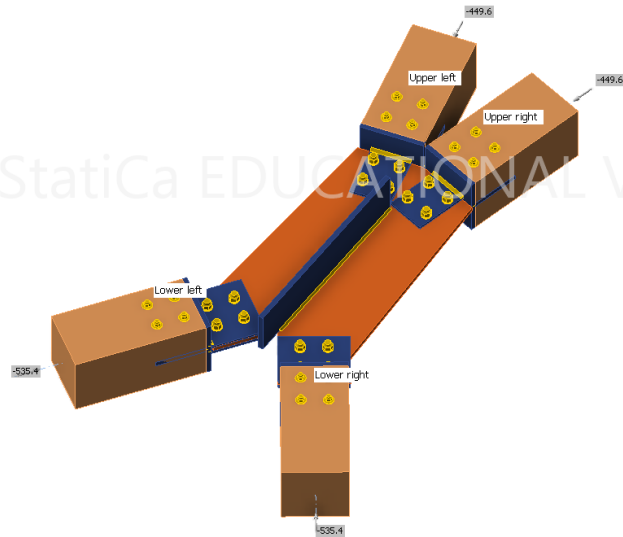
(b) Stress distribution in the connection plate.



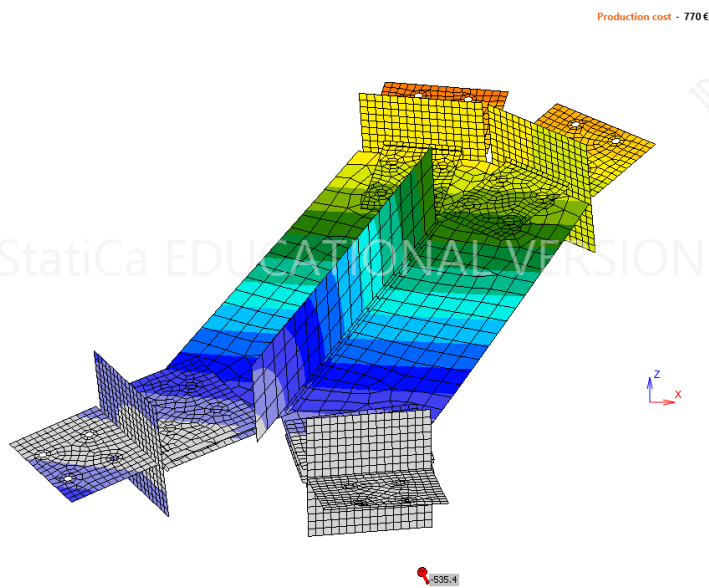
(c) Deformed shape of the connection plate relating to the lowest buckling factor.

(d) Buckling factors  $\alpha_{crit}$  for a given loading case.

**Figure F.1:** Structural analysis of the steel plate connection and results relating to strength capacity and stability.



(a) Altered connection overview.



(b) Deformed shape of the connection plate with stiffener.

**Local buckling of joint**

	Loads	Shape	Factor
>	LE1	1	0.06
		2	0.20
		3	0.35
		4	0.60
		5	0.68
		6	1.25

(c) Buckling factors  $\alpha_{crit}$  for a given loading case.

**Figure F.2:** Structural analysis of the steel plate connection and results relating to strength capacity and stability after implementing a stiffener plate.